Development of *in vitro* 3D white adipose cell culture models for investigating white adipose cell biology and genetics of fat distribution



Keanu Paphiti

A thesis submitted for the degree of Doctor of Philosophy

2025

Radcliffe Department of Medicine

St Hugh's College, University of Oxford





Declaration

I, Keanu Paphiti, confirm that the work presented in this thesis is my own. Where information has been derived from other sources, I confirm that it has been clearly indicated in the thesis.

Acknowledgements

I would like to thank my MRC Harwell Supervisors, Professor Roger Cox and Dr Alexander Graham, for their support and belief in this project. Roger showed genuine interest and enthusiasm, and additionally made the substantial purchase of the Mosquito instrument which was essential for this work. Alex provided vital training when I first joined MRC Harwell, and he ensured I was in a position to continue this project following his departure. I appreciate his mentorship and for creating a friendly working environment.

My colleague Dr Ying Bai supported me during the closure period at Harwell, making the day-to-day working environment much more enjoyable. I appreciate all the occasions we would chat in the lab and the knowledge she would freely impart.

I would like to thank my OCDEM Supervisors, Professor Fredrik Karpe, Professor Leanne Hodson and Dr Katherine Pinnick, for facilitating my move to OCDEM and for making me feel welcome. Fredrik and Katherine supported me with their extensive knowledge of adipose tissue biology and assisted with navigating technical issues and structuring the project. Leanne supported me in pastoral aspects and liaised with MRC Harwell for continued support and equipment loans.

Outside of Supervision, there are many people at OCDEM I would like to thank, including Amy Barrett, Elspeth Johnson and Dr Nellie Loh for volunteering their help in the lab. A special thank you to Daniel Phillips for his work and guidance with the RNA-sequencing results analysis, who continued to help after his departure from OCDEM.

To my friends back home, thank you for providing a sense of normality when I would visit.

Above all, I am eternally grateful to my Mum and Stepdad, who have provided endless support. I think they have experienced the ups and downs of this journey with me, and have steadfastly provided encouragement during the low periods. Their work here is done.

Note on the closure of the Mammalian Genetics Unit and project changes

The project was originally an industrial collaboration (iCASE) with OxSyBio Ltd, a former synthetic tissue company, but prior to my project starting they went into liquidation. A key member of their staff transferred to MRC Harwell and was one of my initial Supervisors. He remained with MRC Harwell for approximately 6 months, and then resigned during the first COVID lockdown.

The COVID pandemic caused the temporary closure of the MRC Harwell labs for extended periods on more than one occasion. There were also periods of heavily restricted working conditions throughout. During this period, I also had to vacate my accommodation in Oxford and return to my family home to work remotely.

Following on from this, the MRC took the decision to close the Mammalian Genetics Unit (MGU) at Harwell and my main Supervisor, Professor Roger Cox, decided to take retirement. I was advised that I would need to move to another lab in Oxford and seek new Supervisors.

I approached Professor Leanne Hodson at the Oxford Centre for Diabetes Endocrinology and Metabolism (OCDEM), and was kindly offered to join her and Professor Fredrik Karpe's lab. This move inevitably caused some disruption whilst the essential equipment necessary for my project was moved from Harwell to OCDEM, and the equipment loan agreements drawn up. It also involved a realignment of my project with new elements added.

Table of contents

Declaration 1
Acknowledgements 2
Note on the closure of the Mammalian Genetics Unit and project changes 3
Table of contents 4
List of figures 10
List of tables 13
Abstract 14
1 Background 18
1.1 Human adipose tissue structure and function 18
1.2 Lipogenesis and lipolysis 20
1.3 Heterogeneity among white adipose depots 22
1.4 Dysfunction of white adipose tissue 23
1.5 Adipose tissue distribution and risk of cardiometabolic disease 25
1.6 Lipodystrophy syndromes 26
1.6.1 Familial partial lipodystrophy type 2 28
1.6.2 Models for the study of lipodystrophy 28
1.7 Transcriptional regulation of adipogenesis 29
1.8 Challenges of studying adipocytes 31
1.9 Modelling adipose tissue *in vitro* 32
1.10 3D adipocyte models 33
1.10.1 Scaffold-based approaches 33
1.10.2 Scaffold-free methods 34
1.10.3 Microfluidic platforms 34
1.11 Concluding remarks 38
1.12 Thesis aims 39
2 Methods 40
2.1 Preparation of reagents for spheroid fabrication 40
2.1.1 Sterile oil preparation 40
2.1.2 Fmoc dipeptide solution preparation 40
2.1.3 Hydrogel-based matrix preparation 41
2.2 Automation of spheroid fabrication and culture 41
2.2.1 Cellular droplet production 41
2.2.2 Automated liquid handling of spheroids 42
2.3 Assessment of spheroid viability and lipid content by high-content imaging 43
2.3.1 Viability assay 43
2.3.2 Lipid phenotyping assay 44

2.4 Spheroid size determination 44
2.5 Human cell culture 45
2.5.1 Background 45
2.5.1.1 Generation of depot-specific preadipocyte lines 45
2.5.5.2 Generation of doxycycline-inducible cell lines for LMNA overexpression studies 45
2.5.2 Maintenance of preadipocyte lines in 2D culture 46
2.5.3 Freezing cells 46
2.5.4 Thawing cells 47
2.6 Adipogenic differentiation 47
2.7 Doxycycline-induction of EGFP and LMNA expression 48
2.7.1 Preparation of doxycycline stock solution 48
2.7.2 Doxycycline treatment 48
2.8 RNA applications 49
2.8.1 RNA isolation from 2D cultures of preadipocytes 49
2.8.2 cDNA Synthesis 49
2.8.3 Single nucleotide polymorphism (SNP) genotyping 50
2.9 Histology of spheroids and adipose tissue samples 51
2.9.1 Automatic sample processing, wax embedding and sectioning 51
2.9.2 H&E staining 52
2.10 Statistical analysis 53
3 Development of a high-throughput spheroid model of mouse white adipose tissue 54
3.1 Introduction 54
3.1.1 Background 54
3.1.2 Chapter aims 56
3.2 Specific methods 57
3.2.1 Mouse stromal vascular fraction cell isolation and culture 57
3.2.2 Spheroid culture and adipogenic differentiation using automated liquid handling 58
3.2.3 Measurement of glycerol, FFA and adiponectin concentrations in culture media 58
3.2.4 Immunofluorescence staining of perivascular cells in spheroids 59
3.2.5 Plasma membrane staining 59
3.2.6 Confocal and lightsheet imaging 59
3.2.7 Quantification of mouse adipocyte sizes 60
3.3 Results 61
3.3.1 Optimisation of mouse SVF spheroid production 61

3.3.2 Spheroid culturing and cell viabilities 64
3.3.3 Investigating cell types present within undifferentiated spheroids..... 66
3.3.4 Assessment of adipogenesis 67
3.3.5 Secreted metabolite and adipokine concentrations 70
3.3.6 Investigating adipogenesis using global heterogeneous *Rreb1* knockout mice 72
3.3.6.1 Quantification of adipocyte sizes in mouse WAT depots 72
3.3.6.2 Characterisation of Rreb1 haploinsufficient spheroids..... 75
3.4 Discussion 78
3.4.1 Summary 81
4 Development of a human adipose tissue depot-specific 3D cell culture model 82
4.1 Introduction 82
4.1.1 Background 82
4.1.2 Chapter aims 83
4.2 Specific methods 83
4.2.1 2D cell plating and staining for lipid droplet imaging 83
4.2.2 Lipid droplet segmentation and size analysis 84
4.3 Results 85
4.3.1 Optimisation of human preadipocyte spheroid production 85
4.3.2 Characterisation of abdominal and gluteal DFAT spheroids during adipogenesis 88
4.3.3 3D culture improves differentiation of abdominal and gluteal DFAT cells 90
4.3.4 Histological analysis of spheroids 95
4.4 Discussion 99
4.4.1 Summary 101
5 Investigation of a familial partial lipodystrophy type 2 mutation on regional human adipose biology 102
5.1 Introduction 102
5.1.1 The *LMNA* gene and laminopathies 102
5.1.2 Chapter hypothesis 103
5.1.3 Chapter aims 103
5.2 Specific methods 104
5.2.1 Human leptin ELISA 104
5.2.2 Histological processing of human subcutaneous adipose tissue biopsies 104
5.2.3 Picrosirius red staining for detection of collagen fibres 105
5.2.4 Quantitative polymerase chain reaction (qPCR) 106
5.2.5 Doxycycline dose response curves 107

5.2.6 High-content imaging for quantification of adipogenesis levels in 2D cultures ……107
5.2.7 Measurement of intracellular triglyceride content 108
5.2.8 Proliferation experiments 109
5.2.9 Differential nuclear staining assay..... 109
5.2.10 EdU assay 110
5.2.11 High-throughput assessment of preadipocyte nuclear morphology 110
5.2.12 Lipid droplet staining of spheroids..... 110
5.3 Results..... 111
5.3.1 Examination of FPLD2 patients..... 111
5.3.1.1 Depot-specific leptin release 111
5.3.1.2 Body composition by DXA 113
5.3.1.3 Histological assessment of FPLD2 subcutaneous adipose tissue 114
5.3.4 Endogenous *LMNA* expression during differentiation of abdominal and gluteal DFAT cells 117
5.3.5 Induction of *LMNA* expression in preadipocytes..... 118
5.3.6 Expression of LMNA R482W reduced adipogenesis in both abdominal and gluteal adipocytes *in vitro* 120
5.3.7 Validation of high-content imaging for quantifying adipogenesis in 2D culture ……123
5.3.8 *LMNA* overexpression reduced abdominal but not gluteal preadipocyte proliferation *in vitro*..... 124
5.3.9 Overexpression of LMNA R482W increased nuclear shape defects in gluteal preadipocytes more than in abdominal preadipocytes..... 129
5.3.10 Characterisation of LMNA R482W mutant spheroids 134
5.4 Discussion 141
5.4.1 Adipogenesis 141
5.4.2 Nuclear morphology..... 143
5.4.3 Proliferation 144
5.4.4 ECM environment 146
5.4.5 Limitations 147
5.4.6 Summary 148
6 RNA-sequencing analysis of LMNA R482W adipose cells..... 149
6.1 Introduction..... 149
6.1.1 The role of lamins in regulating transcription: lamina-associated domains ... 149
6.1.2 Chromatin alterations in laminopathies 152
6.1.3 Transcription factors 155
6.1.3.1 Sterol-regulatory element binding protein..... 155
6.1.3.2 Specific protein 1 156

6.1.4 Epigenetic regulators 157
6.1.5 Regulation of transcription by LMNA R482W: a complex and incomplete picture 158
6.1.6 Chapter hypothesis 159
6.1.7 Chapter Aims 159
6.2 Specific methods 160
6.2.1 RNA sample quality control 160
6.2.2 EGFP PCR 160
6.2.3 RNA-seq data analysis 161
6.2.4 Functional enrichment analysis 162
6.3 Results 163
6.3.1 Quality control of the RNA-seq dataset 163
6.3.2 Abdominal cells show greater transcriptomic changes in response to LMNA R482W expression than gluteal cells 169
6.3.3 Identification of abdominal and gluteal distinct mutant DEGs 171
6.3.4 Pathway enrichment analysis 179
6.3.4.1 Depot comparisons in preadipocytes at day 0 of differentiation 179
6.3.4.2 Depot comparisons at day 7 of differentiation 183
6.3.4.3 Depot comparisons at day 14 of differentiation 187
6.3.5 Comparison of distinct mutant DEGs conserved across adipogenesis 191
6.3.5.1 Abdominal mutant DEGs conserved during adipogenesis were linked to collagen, apoptosis and included a PRC1 component 192
6.3.5.2 Gluteal mutant DEGs conserved during adipogenesis 193
6.3.6 Effects on PRC2 194
6.3.7 Verification of mutant DEG selection process 195
6.4 Discussion 199
6.4.1 Abdominal LMNA-R482W cells showed a striking upregulation of collagen-related genes 199
6.4.2 Altered ZF5 gene targets in abdominal LMNA mutant cells 200
6.4.3 Altered Wnt gene expression in gluteal LMNA-R482W cells 201
6.4.4 Lipid metabolism and Wnt signalling-associated genes were consistently downregulated during adipogenesis in gluteal mutant cells 204
6.4.5 Clues from PCDH10 expression – a possible link between LMNA, HOTAIR and PRC2? 206
6.4.6 Summary 209
7 General discussion and future perspectives 210
7.1 Automation of 3D adipose spheroid production 210
7.2 Validation of the murine adipose spheroid model 211
7.3 Depot-specific human 3D adipose models 212

7.4 Depot-specific effects of the LMNA R482W mutation in FPLD2 214
7.4.1 FPLD2: a gene expression model, structural model, or a combination of both? ……215
7.4.2 Effect of substrate stiffness on *LMNA* expression and mechanosignalling pathways..... 217
7.5 Future perspectives 218
7.5.1 Functional validation of FPLD2 candidate genes 218
7.5.2 Increasing the cellular complexity of the 3D adipose model 219
7.6 Concluding remarks 220
8 References……...221

List of figures

Figure 1.1. Adipose tissue structure and heterogeneity ……20

Figure 1.2. Cellular and structural changes during unhealthy adipose tissue expansion …….24

Figure 1.3. Genes mutated in monogenic forms of partial lipodystrophy ……27

Figure 1.4. Key genes involved in adipogenic differentiation ……...30

Figure 3.1. Steps for droplet-in-oil spheroid production ……55

Figure 3.2. Cellular droplet sizes after automated dispensing ……62

Figure 3.3. Reproducible spheroid formation in 96-well plates……..63

Figure 3.4. Representative bright field images of spheroids dislodging from hydrogel spheres……64

Figure 3.5. Cell viability assessment of spheroids generated using the Mosquito instrument at 100, 150, 200 and 250 nL dispense volumes……65

Figure 3.6. Immunofluorescence staining of undifferentiated SVF-derived spheroid……...66

Figure 3.7. Lipid phenotyping of spheroids during adipogenesis……68

Figure 3.8. Spheroid lipid droplet morphologies on day 7 of differentiation……69

Figure 3.9. Light sheet fluorescence microscopy images (3D rendering) of fused spheroid triplicate models on day 14 of differentiation……...70

Figure 3.10. Quantification of glycerol (a) and adiponectin (b) in 48-hour conditioned media from differentiated adipose spheroids……..71

Figure 3.11. Male *Rreb1* haploinsufficient mice display depot-specific reductions in adipocyte size (unpublished data (Yu, *et al*., 2024) from the Cox group)……..72

Figure 3.12. Relative frequency of adipocyte areas in *Rreb1* heterozygous knockout mice on a 60% high-fat diet (HFD) within 250 μm^2 bin divisions……74

Figure 3.13. Characterisation of *Rreb1* haploinsufficient spheroids during adipogenesis……76

Figure 3.14. Confocal imaging of *Rreb1* haploinsufficient spheroids on day 7 of adipogenesis……77

Figure 4.1. Optimisation of human abdominal and gluteal preadipocyte spheroid production …….....86

Figure 4.2. Viabilities of abdominal and gluteal preadipocyte 3D cultures two days post-production ……87

Figure 4.3. Differentiation of human abdominal and gluteal DFAT spheroids ……..89

Figure 4.4. Lipid phenotyping of abdominal and gluteal DFAT spheroids ……..90

Figure 4.5. Quantification of lipid droplet sizes in 2D and 3D cultures on day 11..……..92

Figure 4.6. Relative frequencies of lipid droplet diameters in abdominal and gluteal DFAT cells differentiated in 2D and 3D culture conditions, with or without fatty acid treatment ……93

Figure 4.7. Adiponectin secretion in 48-hour conditioned media from abdominal and gluteal DFAT spheroids on day 11 of differentiation……94

Figure 4.8. H&E staining of abdominal and gluteal DFAT spheroids during adipogenesis (days 0 and 14) ……..96

Figure 4.9. Higher magnification H&E images (400×) of abdominal and gluteal DFAT spheroids differentiated to day 14……97

Figure 4.10. Differentiated adipose spheroids showed no strong evidence for necrosis……..98

Figure 5.1. Depot-specific release of leptin in FPLD2 patients……...112

Figure 5.2. Histological assessment of subcutaneous abdominal and femoral adipose tissue from FPLD2 subjects……115

Figure 5.3. Picrosirius red staining images of subcutaneous abdominal and femoral adipose tissue from FPLD2 subjects ……116

Figure 5.4. Endogenous LMNA mRNA expression in abdominal and gluteal EGFP cells…..118

Figure 5.5. Doxycycline dose response curves of abdominal and gluteal Dox-inducible cell lines……119

Figure 5.6. Effect of WT and R482W LMNA overexpression on adipogenesis in abdominal and gluteal Dox-inducible cells……...121

Figure 5.7. Single nucleotide polymorphism (SNP) genotyping of Dox-inducible cell lines showing leaky LMNA R482W expression……..121

Figure 5.8. Validation of *in vitro* adipogenesis assay……...123

Figure 5.9. Effect of WT and R482W LMNA overexpression on proliferation of abdominal and gluteal Dox-inducible preadipocytes……..125

Figure 5.10. Cell doubling times of abdominal (a) and gluteal (b) preadipocytes after 48 hour doxycycline treatment at higher dosage (0.5 µg/mL)……...126

Figure 5.11. Differential nuclear staining assay on preadipocytes…….126

Figure 5.12. Quantification of abdominal and gluteal preadipocytes in S-phase of the cell cycle……127

Figure 5.13. Effect of WT and R482W LMNA overexpression on nuclear morphology in abdominal and gluteal preadipocytes during proliferation……...131

Figure 5.14. Higher doxycycline treatment exacerbated the nuclear morphology defects in gluteal preadipocytes overexpressing LMNA R482W……132

Figure 5.15. Effect of WT and R482W LMNA overexpression on nuclear roundness in confluent abdominal and gluteal preadipocytes……133

Figure 5.16. Representative bright field and fluorescent micrographs of abdominal and gluteal EGFP spheroids on days 0 and 14 of differentiation……135

Figure 5.17. Sizes of LMNA R482W mutant spheroids during *in vitro* differentiation…….135

Figure 5.18. Confocal imaging of lipid droplets in LMNA spheroids at day 12 of differentiation ……137

Figure 5.19. H&E staining of LMNA-R482W spheroids……..139

Figure 5.20. Collagen staining of LMNA-R482W spheroids……140

Figure 6.1. Lamina-associated domain (LAD)-mediated gene regulation……150

Figure 6.2. The two main models of laminopathies……..154

Figure 6.3. Multi-dimensional scaling (MDS) plots of RNA-seq dataset……164

Figure 6.4. Sample verification and genotyping……166

Figure 6.5. Depot-specific marker gene expression in abdominal and gluteal preadipocytes during differentiation……167

Figure 6.6. Adipogenic marker gene expression in abdominal and gluteal preadipocytes during differentiation……168

Figure 6.7. Total number of significant differentially expressed genes (DEGs) in LMNA-R482W mutant and LMNA-WT cells versus controls during adipogenic differentiation……170

Figure 6.8. UpSet plots showing the number of unique or shared DEGs between sets……..172

Figure 6.9. Comparison of day 0 abdominal and gluteal distinct LMNA mutant DEGs……179

Figure 6.10. Comparison of day 7 abdominal and gluteal distinct LMNA mutant DEGs……..183

Figure 6.11. Comparison of day 14 abdominal and gluteal distinct LMNA mutant DEGs……187

Figure 6.12. Comparison of day 0, 7 and 14 distinct LMNA mutant DEGs to find intersecting genes conserved across adipogenesis……..191

Figure 6.13. *EZH2* expression in abdominal and gluteal cells during differentiation……194

Figure 6.14. Number of overlapping DEGs dysregulated by LMNA R482W from independent analyses ……...…196

Figure 6.15. Volcano plots showing differentially expressed genes between LMNA-WT and LMNA-R482W cells……..197

Figure 6.16. Potential mechanism of PRC2 regulation and Wnt signalling in regional LMNA R482W-expressing adipose cells……...208

List of tables

Table 1.1. 3D mono- and co-culture models of adipose tissue……..….35

Table 2.1. Thermal cycler conditions for cDNA synthesis…….50

Table 2.2. qPCR conditions for *LMNA* SNP genotyping……50

Table 2.3. Automatic tissue processor conditions……..51

Table 2.4. Haematoxylin and eosin (H&E) staining……52

Table 3.1. Mosquito instrument dispensing qualities for volume settings……62

Table 5.1. Haematoxylin and picrosirius red staining of human adipose tissue and spheroid sections.…..……..105

Table 5.2. TaqMan assay probes used for qPCR……106

Table 5.3. Thermal cycling conditions for TaqMan Fast qPCR……...106

Table 5.4. 1% NP-40 lysis buffer composition……..108

Table 5.5. Clinical parameters of FPLD2 (LMNA p.R482W) and control subjects from *in vivo* physiological study (unpublished data, MRG group)……112

Table 5.6. Clinical parameters and DXA measurements of two FPLD2 subjects (*LMNA* p.R482W) compared with control subjects from the Oxford Biobank……113

Table 6.1. PCR component volumes……..160

Table 6.2. Thermocycling conditions for EGFP PCR……...161

Table 6.3. Top distinct DEGs in abdominal LMNA-R482W cells at day 0 of differentiation….173

Table 6.4. Top distinct DEGs in gluteal LMNA-R482W cells at day 0 of differentiation……...174

Table 6.5. Top distinct DEGs in abdominal LMNA-R482W cells at day 7 of differentiation….175

Table 6.6. Top distinct DEGs in gluteal LMNA-R482W cells at day 7 of differentiation……...176

Table 6.7. Top distinct DEGs in abdominal LMNA-R482W cells at day 14 of differentiation..177

Table 6.8. Top distinct DEGs in gluteal LMNA-R482W cells at day 14 of differentiation…….178

Table 6.9. Enriched terms for distinct abdominal LMNA-R482W DEGs at day 0.....182

Table 6.10. Enriched GO:BP terms for distinct gluteal LMNA-R482W DEGs at day 0……182

Table 6.11. Enriched terms for distinct abdominal LMNA-R482W DEGs at day 7……...185

Table 6.12. Enriched terms for distinct gluteal LMNA-R482W DEGs at day 7……186

Table 6.13. Enriched terms for distinct abdominal LMNA-R482W DEGs at day 14……188

Table 6.14. Top enriched transcription factor-binding motifs for distinct abdominal LMNA-R482W DEGs at day 14 ……..189

Table 6.15. Enriched terms for distinct gluteal LMNA-R482W DEGs at day 14……...190

Table 6.16. Enriched terms for abdominal LMNA-R482W DEGs conserved during adipogenesis …… 193

Development of in vitro 3D white adipose cell culture models for investigating white adipose cell biology and genetics of fat distribution

Keanu Paphiti

Radcliffe Department of Medicine; St Hugh's College, University of Oxford

A thesis presented for the degree of Doctor of Philosophy; Trinity Term 2025

Abstract

Cardiometabolic consequences of obesity are linked to white adipose tissue dysfunction, yet model systems to study the adipose organ are limited. Adipose biology is commonly studied using 2D cell culture systems, but these lack the complexity of *in vivo* tissue. 3D cell culture models more accurately reflect properties of *in vivo* tissue, therefore providing a valuable platform for future research. However, there are no standardised methods for 3D culture, with existing systems being labour-intensive and low-throughput, limiting their use in large-scale studies. Therefore, the aim of this DPhil was to develop and characterise high-throughput 3D adipose cell models utilising automation and to then apply these in studies of adipose tissue biology and genetics.

Initially, I further developed an established method for generating primary adipocyte spheroids from mouse subcutaneous white adipose tissue, by automating the spheroid production and evaluating requirements for spheroid cell numbers, effects of hypoxia, potential for adipogenic differentiation and adipokine secretion. This approach enabled more rapid and uniform spheroid formation at scale, thereby improving the reproducibility of spheroid sizes. Model validation with the *Rreb1* gene showed that *Rreb1* loss in primary preadipocytes reduced spheroid size and lipid accumulation during differentiation, reflecting the adipose tissue phenotype of *Rreb1* knockout mice and demonstrating the value of the *in vitro* spheroid model for mechanistic studies.

The 3D adipose culture system was then applied to immortalised human regional preadipocytes. Characterisation revealed depot-specific features such as larger lipid droplets in the gluteal spheroids compared to abdominal. A striking example of human adipose tissue dysfunction is familial partial lipodystrophy type 2 (FPLD2), which is typified by loss of gluteofemoral adipose tissue. The effects of a FPLD2-linked mutation in the *LMNA* gene (R482W) on abdominal and gluteal adipocyte biology were investigated using both 2D and 3D cell models. Overexpression of R482W-mutated LMNA caused a modest yet statistically significant reduction in lipid accumulation within cells from both depots cultured in 2D, with more pronounced effects detected in gluteal cells, which recapitulates patient phenotypes. In contrast, overexpression of wild-type LMNA in abdominal cells was associated with decreased proliferation in preadipocytes and enhanced their differentiation. Overexpression of both wild-type and mutant LMNA caused changes to nuclear morphology in preadipocytes derived from both depots. Notably, gluteal cells showed a much higher incidence of abnormal nuclear shapes upon overexpression of mutant LMNA.

Bulk RNA-sequencing was performed on LMNA R482W-expressing cells to further investigate FPLD2 disease mechanisms. This identified fibrosis as a likely pathogenic mechanism affecting abdominal cells, with upregulated collagen gene expression identified in 2D samples and collagen fibre accumulation observed in spheroids. Expression of genes involved in lipid uptake and metabolism, including *LPL*, were reduced in gluteal cells. Additionally, altered expression of Wnt pathway genes suggests that the mutation may, in part, influence adipogenesis by altering β-catenin levels, thus contributing to the regional differences in disease severity. A femoral subcutaneous biopsy from a patient with FPLD2 showed profound fibrotic changes supporting the *in vitro* findings.

In conclusion, this thesis describes the development and application of high-throughput 3D adipose tissue models, that provide improvements over conventional 2D and manual 3D approaches. The platform accommodates various sources of preadipocytes and delivers greater scalability, reproducibility and biological relevance for disease modelling. Gene expression profiles of LMNA R482W modified cell cultures provided insight into the depot-specific pathogenic effects in FPLD2. Further work is needed to characterise these genes to inform future therapeutic strategies.

~ Word count: approximately 45,000 ~

Common Abbreviations

A-V	Arterio-venous
BAT	Brown adipose tissue
BMI	Body mass index
BODIPY 493/503	4,4-difluoro-1,3,5,7,8-pentamethyl-4-bora-3a,4a-aiaza-s-indacene
C/EBP	CCAAT-enhancer binding protein
CAM	Calcein AM
CGL	Congenital generalised lipodystrophy
CVD	Cardiovascular disease
DEG	Differentially expressed gene
DFAT	Dedifferentiated fat
DMEM	Dulbecco's modified eagle medium
DNL	*De novo* lipogenesis
Dox	Doxycycline
DPBS	Dulbecco's phosphate-buffered saline
ECM	Extracellular matrix
EdU	5-ethynyl-2'-deoxyuridine
EGFP	Enhanced green fluorescent protein
ELISA	Enzyme-linked immunosorbent assay
FA	Fatty acid
FBS	Fetal bovine serum
FFA	Free fatty acid
FPLD2	Familial partial lipodystrophy type 2
GWA	Genome-wide association
gWAT	Perigondal white adipose tissue
H&E	Haematoxylin and eosin
H3K27me3	Trimethylation of histone H3 lysine 27
HFD	High-fat diet
HOX	Homeobox
iPSC	Induced pluripotent stem cell
iWAT	Inguinal white adipose tissue
kPA	Kilopascal
LAD	Lamina-associated domain
LFD	Low-fat diet

LMNA	Lamin A/C
LPL	Lipoprotein lipase
MCE	Mitotic clonal expansion
MSC	Mesenchymal stem cell
nL	Nanolitre
NL	Nuclear lamina
PBS	Phosphate-buffered saline
PFA	Paraformaldehyde
PI	Propidium iodide
PPARγ	Peroxisome proliferator-activated receptor gamma
PRC2	Polycomb repressive complex 2
PSR	Picrosirius red
qPCR	Quantitative polymerase chain reaction
RM3	Rat and mouse no. 3 breeding diet
RNA-seq	RNA-sequencing
Rreb1	Ras-responsive element binding protein
***Rreb1*$^{+/-}$**	Heterozygous *Rreb1* knockout mouse
***Rreb1*$^{+/+}$**	Wild-type *Rreb1* mouse
SD	Standard deviation
SEM	Standard error of the mean
SAT	Subcutaneous adipose tissue
SNP	Single nucleotide polymorphism
SREBP1	Sterol-regulatory element binding protein
SVF	Stromal vascular fraction
T2D	Type 2 diabetes
TF	Transcription factor
TG	Triglyceride
µL	Microlitre
ULGTA	Ultra-low gelling temperature agarose
µm	Micrometre
V-A	Veno-arterial
VAT	Visceral adipose tissue
w/v	Weight/volume
WAT	White adipose tissue
WT	Wild-type

1 Background

1.1 Human adipose tissue structure and function

Adipocytes are specialised lipid-storing cells that perform a wide range of physiological functions. They reside in adipose (fat) tissue, which accounts for approximately 20-25% of total body weight in normal weight people and is organised into distinct anatomical depots (Loskill, *et al*., 2017). Adipose tissue has important endocrine functions and secretes more than 600 bioactive compounds, including cytokines, growth factors, signalling lipids and microRNAs (Cao, 2013) (Scheja & Heeren, 2019). These substances play vital roles in regulating glucose homeostasis, insulin sensitivity, vascular tone, reproduction and immune responses (Maenhaut & Van de Voorde, 2011) (Kershaw & Flier, 2004).

Adipose tissue is divided into two types: white adipose tissue (WAT) and brown adipose tissue (BAT). These are further categorised based on their anatomical location as either subcutaneous adipose tissue (SAT), a layer located between the dermis and fascia, or visceral adipose tissue (VAT), which surrounds internal organs. SAT accounts for approximately 80% of total body fat and is primarily divided into abdominal and gluteofemoral depots (Passaro, *et al*., 2017). Additional specialised adipose tissue depots include dermal, bone marrow, and mammary, each exhibiting unique characteristics and functions (Zwick, *et al*., 2018). For instance, bone marrow adipose tissue (BMAT) is metabolically active and an important source of adiponectin during caloric restriction (Cawthorn, *et al*., 2014), contributing both to local bone homeostasis and systemic metabolic regulation (Zwick, *et al*., 2018).

Adipose tissue is highly heterogeneous in terms of both its cellular composition and function. While mature adipocytes account for ~90% of tissue volume (Corvera, 2021), it also comprises various non-adipocyte cell types. These include immature (undifferentiated) preadipocytes, fibroblasts, endothelial cells and various stem cells, collectively known as the stromal vascular fraction (SVF). The tissue also contains multiple immune cell types, such as macrophages, neutrophils and T-cells, contributing to its role as an immunological organ.

Recent advances in single cell RNA-sequencing (scRNA-seq) technology have enabled a deeper understanding of the cellular diversity within adipose tissue. This has shown that the composition of SVF differs across various adipose depots, as well as within individual depots, revealing distinct subpopulations of adipose stem and precursor cells (ASPCs) with specific functions (Vijay, *et al*., 2020) (Lazarescu, *et al*., 2025). For example, 'adipogenesis regulator' (Areg) cells have been identified, which perform non-adipogenic functions (Schwalie, *et al*., 2018). Mature adipocyte populations within the same depot also display heterogeneity in their function, with Bäckdahl *et al*. (2021) showing, through spatial transcriptomics, that human WAT contains three distinct adipocyte subpopulations classified by marker gene expression. One of these adipocyte subtypes, enriched in perilipin-1 and -4 expression, was linked to whole-body insulin sensitivity.

Similar to other tissues, WAT is organised into a complex 3D structure, comprising cells embedded within a soft extracellular matrix (ECM) composed predominantly of fibrous proteins (e.g. collagens and fibronectin), proteoglycans and polysaccharides (Ruiz-Ojeda, *et al*., 2019) (Jääskeläinen, *et al*., 2023). The ECM not only provides structural support but also regulates cell proliferation, adhesion, migration and differentiation by establishing concentration gradients of growth factors and signalling molecules. Within this 3D environment is a network of blood vessels, with each adipocyte typically surrounded by at least one capillary (Lijnen, 2008) (Ioannidou, *et al*., 2022a). This supplies cells with adequate oxygen and nutrients whilst allowing exchange of signalling molecules and metabolites to support inter-organ communication. Additionally, adipose tissue receives innervation from the sympathetic nervous system, which regulates lipid breakdown (lipolysis) through the release of noradrenaline.

The ECM undergoes continuous remodelling to accommodate tissue expansion or regression, giving adipose tissue a high degree of plasticity. These processes are regulated by adipose tissue macrophages (ATMs) and secreted metalloproteinases (MMPs), which degrade ECM components (Chavey, *et al*., 2003). MMP activity is modulated by tissue inhibitors of matrix

metalloproteinases (TIMPs), ensuring maintenance of ECM homeostasis. However, an imbalance between ECM production and degradation can result in excessive ECM accumulation (fibrosis), leading to adipocyte death and tissue dysfunction.

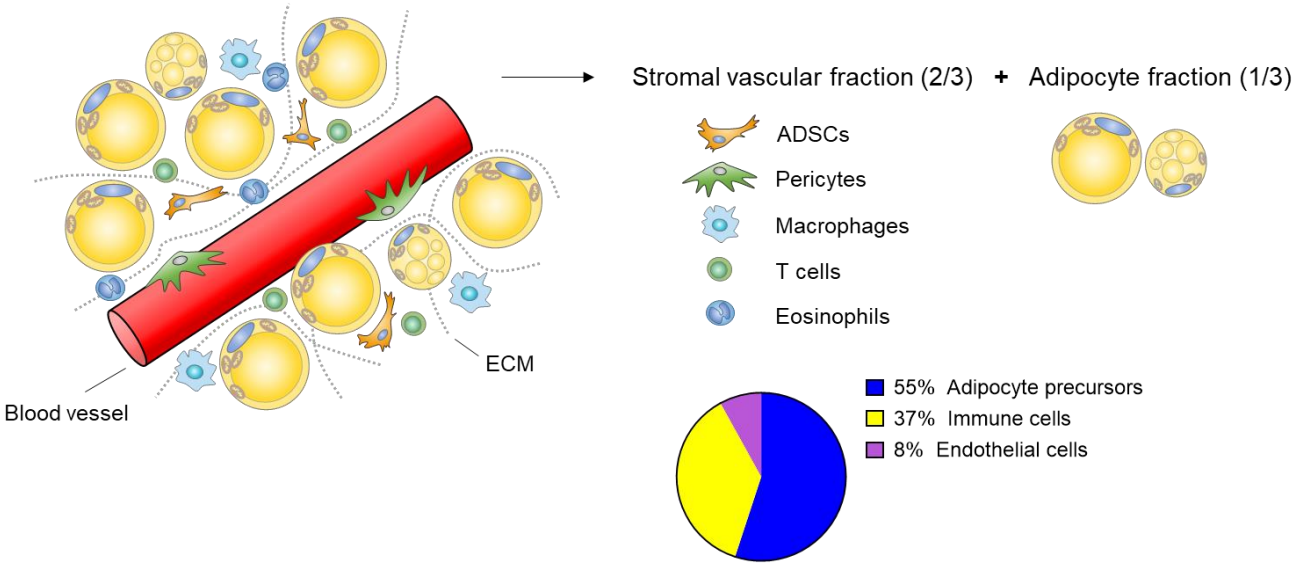


Figure 1.1. Adipose tissue structure and heterogeneity. Adipose tissue is comprised of multiple interacting cell types embedded in a complex 3D structure. The pie chart shows different cell types classified into three major groups within the stromal vascular fraction (SVF), as determined by Vijay *et al*. (2020) using single cell RNA-sequencing (scRNA-seq). Note that cell composition varies between species, adipose depots and different studies. Figure adapted from Constantin *et al*. (2020). Extracellular matrix (ECM), adipose-derived stem cells (ADSCs).

1.2 Lipogenesis and lipolysis

Adipocytes are divided into three main types: white, brown or beige, based on their distinct functions and morphological characteristics. White adipocytes are the most common and specialise in energy storage by accumulating neutral lipids, mainly triglycerides (TGs), within a single large unilocular lipid droplet. This droplet can occupy up to 90% of the cell volume and displaces the nucleus towards the cell's periphery, resulting in a characteristic 'signet ring' morphology (Arner & Rydén, 2022) (Church, *et al*., 2012).

The balance between lipid synthesis (lipogenesis) and lipolysis is crucial for fat accumulation. Adipocytes receive dietary lipids from circulating TG-rich lipoproteins through the action of lipoprotein lipase (LPL), a lipolytic enzyme present on the surfaces of capillary endothelial

cells (Yu & Ginsberg, 2005). Since TGs cannot cross cell membranes, LPL hydrolyses TGs in lipoproteins into free fatty acids (FFAs) and glycerol, allowing FFAs to enter adipocytes via protein-mediated transport for re-esterification and storage in cytosolic lipid droplets. A range of proteins regulate lipid droplet dynamics, including perilipin 1 (PLIN1) which coats the lipid droplet surface in adipocytes, regulating lipolysis in a phosphorylation-dependent manner (Yang & Mottillo, 2020). In the basal state, non-phosphorylated PLIN1 limits lipase access and sequesters CGI-58, thereby suppressing adipose triglyceride lipase (ATGL) activity and promoting triglyceride storage (Yang & Mottillo, 2020). Upon protein kinase A (PKA)-mediated phosphorylation, PLIN1 releases CGI-58 and facilitates hormone-sensitive lipase (HSL) recruitment, enabling coordinated triglyceride hydrolysis.

Alternatively, adipocytes can produce TGs via *de novo* lipogenesis (DNL), generating FFAs from non-lipid precursors (predominately carbohydrates) by converting acetyl coenzyme A into palmitate (16:0). Glucose is the main substrate for DNL, but adipocyte DNL may only contribute less than 4% of the total TG content in adipose tissue; the majority originates from dietary fat or circulating lipoproteins (Strawford, *et al*., 2004) (Rowland, *et al*., 2023). It is noteworthy that most *in vitro* studies use adipogenic differentiation protocols lacking exogenous FFAs, relying exclusively on DNL, which does not accurately reflect physiological conditions and may influence adipocyte function (Gamwell, *et al*., 2023).

Lipogenesis and lipolysis are regulated by hormonal signals. In the postprandial (fed) state, insulin secreted by pancreatic β-cells stimulates adipocyte lipogenesis by promoting translocation of glucose transporters to the plasma membrane. This increases glucose uptake enabling glycerol-3-phosphate synthesis to occur in parallel to fatty acid uptake, allowing new TGs to be synthesised (Santoro, *et al*., 2021). Insulin activates the transcriptional regulator, sterol-regulatory element binding protein 1 (SREBP1), which induces expression of lipogenic genes, and promotes LPL activity to increase fatty acid uptake from chylomicrons. It also simultaneously inhibits lipolysis by reducing HSL activity.

Lipolysis is a complex process involving numerous lipid droplet proteins, lipases and co-factors (Yang & Mottillo, 2020). During periods of increased energy demand catecholamines, such as noradrenaline, induce PKA-mediated phosphorylation of PLIN1 surrounding lipid droplets. This recruits ATGL and HSL, increasing lipolysis and FFA release from adipocytes. Circulating FFAs are then delivered to peripheral tissues, such as skeletal muscle, where they undergo β-oxidation to produce adenosine triphosphate (ATP).

Thus, WAT serves as body's primary energy reservoir, storing excess energy that can be rapidly mobilised to meet metabolic demands. Nearly all animal species possess adipose tissue (Gesta, *et al*., 2007), with one simple hypothesis being that it evolved to protect other organs that cannot tolerate lipid storage (Speakman & Elmquist, 2022). Notably, lipids provide more than twice the energy per gram compared to carbohydrates and, due to their hydrophobic properties, do not need to be stored with water, making them a highly concentrated and efficient fuel source (Speakman, 2018) (Carracedo, *et al*., 2013).

1.3 Heterogeneity among white adipose depots

White adipocyte size varies considerably (30-130 μm) depending on lipid content and is influenced by factors such as sex, age, body mass index (BMI) and genetics (Wronska & Kmiec, 2012). Adipocyte size is heterogeneous across fat depots, with individuals of healthy weight generally having larger abdominal SAT adipocytes than VAT (e.g. omental) adipocytes (Pellegrinelli, *et al*., 2016) (Ye, *et al*., 2022); this likely reflects the greater lipid storage capacity of SAT.

Adipocyte size is an important factor influencing metabolic health, with larger adipocytes shown to be less responsive to insulin and therefore associated with impaired glucose metabolism. Several studies have identified adipocyte enlargement (hypertrophy) as an independent risk factor for the onset of type 2 diabetes (T2D), regardless of overall adiposity or body fat distribution (Weyer, *et al*., 2000) (Lundgren, *et al*., 2007) (Lönn, *et al*., 2010).

In addition to differences in cell size, WAT depots exhibit distinct metabolic and functional characteristics, including divergent hormonal responses and secretory profiles. Visceral adipocytes have increased lipolysis and metabolic activity compared to subcutaneous adipocytes, with visceral depots releasing higher levels of pro-inflammatory hormones, such as resistin and visfatin (Coelho, *et al*., 2013) (Kershaw & Flier, 2004). In contrast, subcutaneous adipocytes secrete more anti-inflammatory factors, notably adiponectin, which has beneficial insulin-sensitising effects.

1.4 Dysfunction of white adipose tissue

WAT is widely distributed throughout the body, expanding or contracting in response to an organism's energy requirements. This expansion occurs through two main processes: hypertrophy (an increase in cell size) and hyperplasia (increased proliferation or recruitment of new preadipocytes) (Parlee, *et al*., 2014). Due to mature adipocytes being post-mitotic, it is necessary to generate new cells from adipocyte precursors within the SVF.

In adults, the number of adipocytes is relatively stable with an annual turnover rate of ~10% (Spalding, *et al*., 2008); however, during excessive tissue expansion, growth often occurs via hypertrophy rather than hyperplasia. Increased accumulation of WAT, as observed in obesity (BMI ≥ 30 kg/m^2), is associated with an elevated risk of developing diseases such as diabetes, cardiovascular disease (CVD), depression and cancer. Obesity is being increasingly recognised as a complex disease influenced by behavioural, genetic and socioeconomic factors. The increase in obesity levels is a growing concern, with approximately 43% of the global adult population classified as overweight or obese in 2022 (World Health Organization, 2025), projected to rise to 50% by 2050 (GBD 2021 Adult BMI Collaborators, 2025). A recent attempt to reclassify obesity is based on whether there are metabolic complications of the obese state rather than focusing strictly on the BMI cut-off (Rubino, *et al*., 2025).

Unhealthy adipose tissue expansion is accompanied by numerous cellular and structural changes including adipocyte hypertrophy, ECM remodelling and alterations in resident cell populations (Kusminski, *et al*., 2016). Enlarged adipocytes have an increased rate of basal lipolysis, which increases FFA levels in circulation. According to the 'lipid overflow hypothesis', when adipocytes reach their lipid storage capacity, excess lipids spill over into the plasma and accumulate in non-adipose tissues (Longo, *et al*., 2019). This ectopic lipid deposition causes cellular stress and metabolic disturbances (lipotoxicity) (Saponaro, *et al*., 2015). As adipose tissue is highly vascularised, inadequate blood supply during tissue expansion may also lead to hypoxia, contributing to cellular dysfunction (Kusminski, *et al*., 2016).

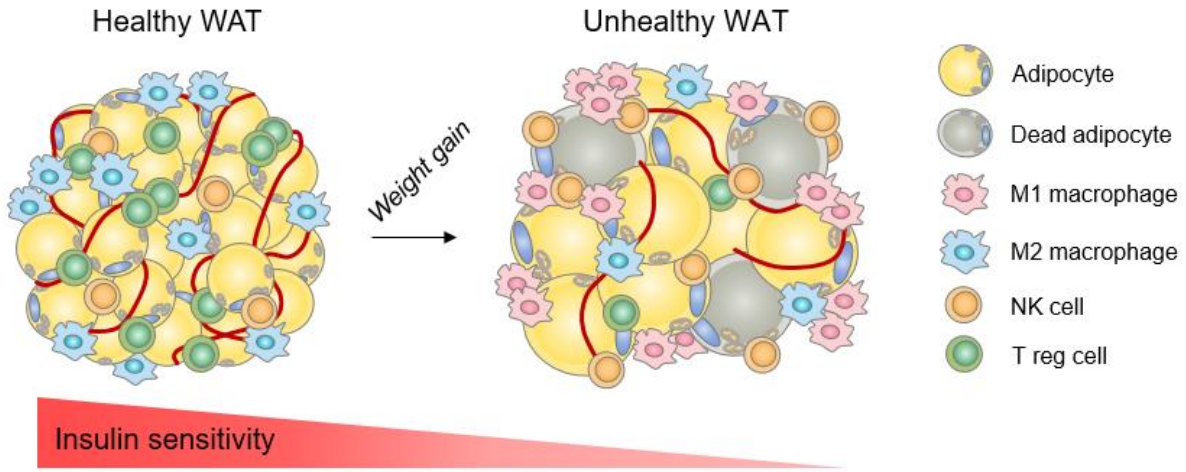


Figure 1.2. Cellular and structural changes during unhealthy adipose tissue expansion. Excessive adipocyte hypertrophy is associated with numerous structural and cellular changes in adipose tissue including inflammation, microvascular rarefaction and necrosis. Adapted from Kusminski *et al*. (2016).

Obesity is also characterised by increased production of inflammatory cytokines, promoting immune cell recruitment and activation, which includes M1 ATMs (Coelho, *et al*., 2013). These cells infiltrate the tissue and surround dying adipocytes, forming the 'crown-like' structures observed in histology (Kusminski, *et al*., 2016). Such processes are involved in fibrosis and inflammation, contributing to a low-grade systemic inflammatory state. The resulting metabolic syndrome characterised by hyperglycaemia, hypertension, dyslipidaemia and abdominal obesity increases CVD risk (Coelho, *et al*., 2013). Therefore, maintaining healthy adipose

levels is crucial, as both excess (obesity) and deficiency (lipodystrophy) contribute to metabolic disease (further discussed in section **1.6**).

1.5 Adipose tissue distribution and risk of cardiometabolic disease

Some individuals experience WAT expansion without adverse health effects, in a type of obesity known as ‘metabolically healthy obesity’ (MHO) (Karpe & Pinnick, 2015). It is recognised that the site of adipose tissue storage influences cardiometabolic disease risk and is a stronger predictor of CVD than BMI or total adiposity alone. This is exemplified by the typical 'apple' (android) and 'pear' (gynoid) body shapes commonly observed in men and women, respectively. Accumulation of subcutaneous adipose tissue in the upper-body is correlated with a higher risk of CVD, while lower-body storage is associated with a reduced risk and may provide metabolic benefits (Manolopoulos, *et al*., 2010). This suggests that regional differences in lipid storage and tissue expansion are important in determining CVD risk.

Adipocytes from these regions exhibit different patterns of expansion. Tchoukalova *et al*. (2010) performed a controlled weight gain experiment with serial adipose tissue biopsies and demonstrated that abdominal subcutaneous adipocytes favour expansion by hypertrophy, whereas lower-body adipocytes preferentially expand by hyperplasia. The greater gluteofemoral fat accumulation seen in premenopausal women is associated with a lower risk of metabolic disease, highlighting this depot’s protective role as a ‘metabolic sink’ capable of sequestering excess lipids over both short- and long-term periods. This may be due to the greater proliferative capacity of gluteofemoral preadipocytes and their ability to sequester more lipids, as adipocytes in this region are generally larger than those in the abdominal area.

Moreover, these depots vary in fatty acid uptake; a tracer study showed that abdominal adipose tissue extracts more TG from chylomicrons, while femoral adipose tissue shows less distinction between chylomicron- and very low-density lipoprotein (VLDL)-TGs (McQuaid, *et*

al., 2010a). The abdominal depot also contains a higher density of β-adrenergic receptors, resulting in increased rates of lipolysis compared to gluteal tissue (Wahrenberg, *et al*., 1989). Arner *et al*. (1991) showed that LPL activity is higher in abdominal tissue in men, whereas the gluteal depot shows higher LPL activity in women, despite mRNA levels being higher in abdominal in both sexes. Additionally, multiple studies have compared protein (Vogel, *et al*., 2019), mRNA (Karastergiou, *et al*., 2013) and microRNA (Rantalainen, *et al*., 2011) expression profiles between these depots, identifying differences such as the differential expression of homeobox (*HOX*) genes, which indicates distinct developmental programming.

1.6 Lipodystrophy syndromes

Insufficient fat storage resulting in metabolic abnormalities are best exemplified by lipodystrophy syndromes, a group of rare (estimated 1.3-4.7 cases per million) (Chiquette, *et al*., 2017) genetic or acquired conditions in which adipose tissue regresses or fails to form. However, it is acknowledged that lipodystrophy syndromes are likely underdiagnosed and subtle forms of the condition may exist (Mann & Savage, 2019). These are classified as generalised or partial, affecting either the whole-body or distinct anatomical regions. In congenital generalised lipodystrophy (CGL), near total adipose tissue loss is present from birth and leads to severe metabolic complications. CGL is caused by autosomal recessive mutations in multiple genes. For example, mutations in AGPAT2, encoding 1-acylglycerol-3-phosphate O-acyltransferase 2, cause CGL type 1; this enzyme catalyses the conversion of lysophosphatidic acid to phosphatidic acid, a critical step in triglyceride synthesis (Patni & Garg, 2015). In CGL type 2, BSCL2 is mutated, which encodes the endoplasmic reticulum protein seipin, a key regulator of adipocyte differentiation and lipid droplet biogenesis (Payne, et al., 2008).

In contrast to generalised forms of lipodystrophy, adipose tissue loss in familial partial lipodystrophy (FPLD) is typically less extensive but results in a characteristic loss of

metabolically protective lower-body fat and pathological fat redistribution. FPLD can be inherited in either an autosomal dominant or recessive manner. Seven main subtypes have been identified (Zammouri, *et al*., 2021) based on the mutated gene (**Figure 1.3**).

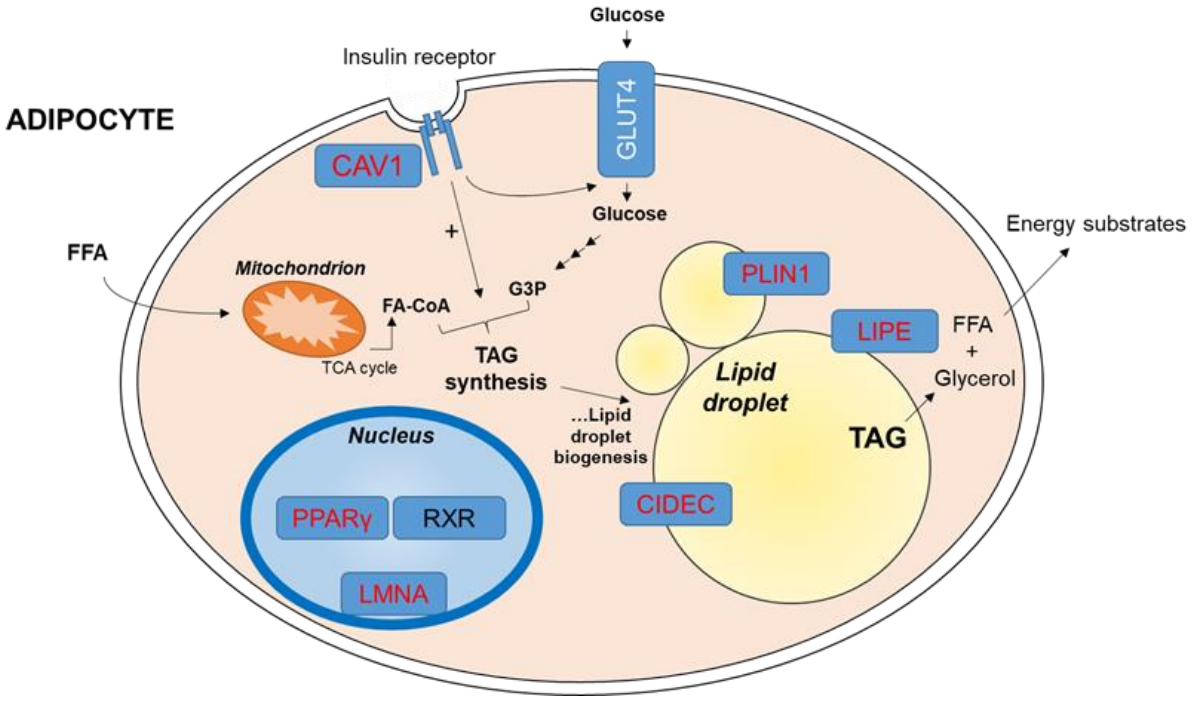


Figure 1.3. Genes mutated in monogenic forms of partial lipodystrophy. Genes involved in nuclear structure (*LMNA*) and adipocyte differentiation (*PPARγ*) are mutated in familial partial lipodystrophy (FPLD) types 2 and 3, respectively. Lipid droplet regulatory genes (*PLIN1*, *CIDEC* and *LIPE*) are mutated in FPLD2 types 4, 5 and 6, respectively. *CAV1* is mutated in FPLD7. FPLD type 1 is thought to have a polygenic etiology and is therefore not represented. Abbreviations: FFA, free fatty acid; FA-CoA, fatty acid-coenzyme A; TAG, triglyceride; G3P, glycerol-3-phosphate; TCA, tricarboxylic acid; RXR, retinoid X receptor. Adapted from Zammouri *et al*. (2021).

Both lipodystrophy and obesity, despite having contrasting effects on adipose tissue mass, may lead to similar metabolic health issues such as insulin resistance, fatty liver disease, pancreatitis and CVD (Mann & Savage, 2019). The accumulation of lipids in non-adipose organs is observed in both conditions and may result in lipotoxicity, demonstrating that maintaining adequate levels of adipose tissue is vital for metabolic health.

There are currently limited treatment options for lipodystrophy patients. The leptin analogue metreleptin is used to treat leptin deficiency in generalised lipodystrophy, but this is treating a symptom rather than the cause. A recent study using adeno-associated virus (AAV)-based gene therapy in a pre-clinical mouse model has shown promise as a potential treatment for generalised lipodystrophy by restoring adipose tissue development (Tiwari, *et al*., 2024).

1.6.1 Familial partial lipodystrophy type 2

Familial partial lipodystrophy type 2 (FPLD2; MIM 151660), or Dunnigan lipodystrophy, is a rare and serious form of lipoatrophy caused by autosomal dominant mutations in the *LMNA* gene encoding the nuclear protein lamin A/C (Shackleton, *et a*l., 2000). FPLD2 typically appears at puberty with progressive loss of subcutaneous adipose tissue from the limbs and lower-body; whilst adipose storage is often increased in the face, neck and visceral (e.g. intra-abdominal) regions. This is accompanied by metabolic disturbances including hyperinsulinaemia, dyslipidaemia, lower circulating leptin and hepatic steatosis (Worman, 2012) (Shin & Worman, 2022). FPLD2 patients are also at an increased risk of atherosclerosis and cardiovascular disease (Hegele, 2001).

Approximately 32% of FPLD2 cases are caused by a missense mutation (C > T) at nucleotide position 1444 in the *LMNA* gene (Jacob & Garg, 2006), which results in a basic arginine amino acid at residue 482 being replaced with a non-polar aromatic tryptophan (R482W). This mutation occurs within the C-terminal immunoglobulin-like domain of lamin A/C (Krimm, *et al*., 2002), with the 482 site being a mutational “hotspot” for FPLD2. The heterozygous *LMNA* R482W mutation is not predicted to alter protein conformation, but may alter protein interactions with DNA and transcription factors involved in adipocyte differentiation (Dhe-Paganon, *et al*., 2002) (Shin & Worman, 2022). However, it is currently not fully understood why certain adipose tissue depots are more severely affected by lamin A/C mutations in FPLD2.

1.6.2 Models for the study of lipodystrophy

Lipodystrophy types share mechanisms such as disrupted adipocyte development and abnormal lipid droplet regulation. Mouse models partly mimic disease features like reduced fat mass and liver fat accumulation, but species differences in fat distribution and disease onset limit direct comparisons to humans. *In vitro* human cellular models for investigating

lipodystrophy mechanisms are not well established, particularly for partial lipodystrophy, where not all adipose depots are affected equally. For example, familial partial lipodystrophy type 3 (FPLD3) normally presents with the retention of abdominal fat along with loss of lower-body fat. Whilst this condition presents with milder fat loss compared to FPLD2, it generally has more severe metabolic complications (Vasandani, *et al*., 2022). Understanding why adipocytes fail in lipodystrophy is vital to help develop novel treatments and gain deeper insights into adipose tissue biology. Patient-derived induced pluripotent stem cell (iPSC) models with specific genotypes or mutations have been used for studies (Friesen & Cowan, 2018), but the factors necessary to differentiate iPSCs into depot-specific adipocytes have yet to be determined, making it unclear which depot they represent.

1.7 Transcriptional regulation of adipogenesis

An intricate network of interacting transcription factors governs the differentiation of preadipocytes into mature lipid-loaded adipocytes (adipogenesis) (Shimano & Sato, 2017) (Payne, *et al*., 2009) (Moseti, *et al*., 2016) (Farmer, 2006). Central to this network is the nuclear hormone receptor peroxisome proliferator-activated receptor gamma (PPARγ), referred to as the ‘master regulator’ of adipogenesis; this designation is due to its expression being essential for fat cell development. PPARγ is activated by both fatty acids and synthetic ligands, such as thiazolidinediones, and interacts with retinoic acid receptor (RXR) to form a heterodimeric complex; this binds to DR-1 sites in the regulatory elements of target genes (Tontonoz & Spiegelman, 2008) (Chan & Wells, 2009) (Lefterova, *et al*., 2008). Examples of activated lipogenic genes are LPL, fatty acid binding protein 4 (FABP4) and acyl-CoA synthetase (ACS) (Moseti, *et al*., 2016). Lipid uptake and metabolism is accompanied by morphological changes in the fibroblastic precursor cell, which acquires a spherical shape due to increased lipid stores.

Transcription factors belonging to the CCAAT-enhancer binding protein (C/EBP) family also play an important role in this process, with C/EBPβ and δ expression increasing during very early adipogenesis; this in turn activates C/EBPα and PPARγ, which work co-operatively to activate lipogenic genes (Rosen, *et al*., 2000) (Madsen, *et al*., 2014). C/EBPα shares many transcriptional targets with PPARγ. C/EBPα and PPARγ engage in a positive feedback loop in which one TF activates the other, thereby enhancing and maintaining adipocyte differentiation **(Figure 1.4**).

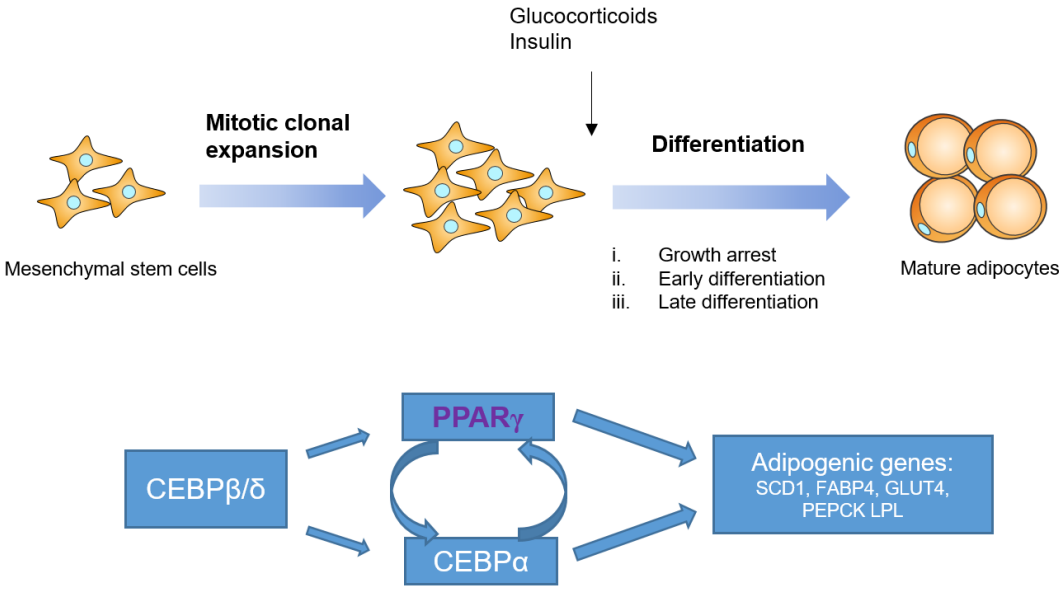


Figure 1.4. Key genes involved in adipogenic differentiation. When preadipocytes reach confluency *in vitro*, they become growth-arrested due to cell-cell contact inhibition. Upon stimulation by adipogenic cues, cells undergo approximately two rounds of synchronised cell cycle division (mitotic clonal expansion, MCE), after which they to cease to proliferate and begin differentiating. Key regulatory genes of adipogenesis are shown. Activation of PPARγ, for example by CEBPβ/δ, results in expression of adipocyte-specific genes giving rise to the mature adipocyte phenotype. PPARγ and CEBPα act cooperatively in this process. Figure adapted from Moseti *et al*. (2016).

1.8 Challenges of studying adipocytes

To date, genome-wide association (GWA) studies have identified hundreds of genetic loci associated with altered body fat distribution (measured by waist-to-hip ratio) and cardiometabolic traits (Loos & Kilpeläinen, 2018), many of which have yet to be functionally validated. Contributing factors are the expense of generating, housing and phenotyping mouse models, the inherent challenges of studying human adipose tissue *in vivo*, and the lack of physiologically relevant *in vitro* disease models.

Studying human adipose biology presents considerable challenges, primarily due to the complex nature of the tissue. Mature adipocytes are fragile and lipid-rich, making them difficult to maintain *in vitro*. Their high buoyancy and poor adherence to standard plastic culture surfaces further complicates long-term culturing. Additionally, as post-mitotic cells, mature adipocytes lack proliferative capacity, limiting their suitability for extended studies.

To overcome these limitations, researchers frequently isolate SVF from adipose tissue, typically from lipoaspirates or biopsies. The multipotent mesenchymal stem cells (MSCs) in this fraction can be expanded in culture and differentiated into adipocytes, providing a useful approach to study adipocyte function from donors with varying characteristics or genotypes *in vitro*.

However, the use of SVF cells is restricted by their declining adipogenic potential over successive passages. To address this, several immortalised preadipocyte cell lines and strains have been developed from primary human cells, including the Simpson Golabi Behmel Syndrome (SGBS) pre-adipocyte cell strain (Wabitsch, *et al*., 2001) used to study adipogenesis. These models can be cultured long-term and maintain robust adipogenic capacity across multiple passages. Each approach has its advantages and disadvantages. For example, while immortalised cell lines offer consistency and ease of use, they do not fully capture the cellular heterogeneity of SVF and are susceptible to ‘genetic drift’ over time.

1.9 Modelling adipose tissue *in vitro*

Adipose biology has traditionally been studied using *in vitro* 2D cell culture and *in vivo* models, such as transgenic mice. However, the latter are expensive, time-consuming and any mechanisms elucidated using non-human species may not be translatable to humans. As previously mentioned, adipose tissue composition and distribution differ between species; for instance, the visceral perigonadal depot found in mice does not have a human equivalent (Cohen, *et al*., 2013).

Although 2D cell culturing is inexpensive and offers ease of manipulation, it is limited by its lack of complexity. In these systems, cellular morphology is affected by adherence to rigid, artificial surfaces, which can cause cytoskeletal changes and alter the organisation of cell-surface receptors (Akhmanova, *et al*., 2015) (Duval, *et al*., 2017). Cells in 2D cultures receive relatively uniform exposure to nutrients and growth factors, unlike in tissues or 3D cultures where this varies. Additionally, cell-to-cell and cell-to-ECM contacts are greatly reduced in 2D culture. These differences influence many factors such as differentiation, viability, gene expression and response to external cues (Jensen & Teng, 2020).

3D cell culture systems provide more physiologically relevant conditions for the study of adipose biology, due to mimicking *in vivo* tissue structure. In mature white adipocytes *in vivo*, the presence of a unilocular lipid droplet promotes a spherical cell morphology. This is typically lost in 2D cultures, where cells exhibit multilocular lipid droplets that resemble those found in beige/brown adipocytes. In contrast, the unilocular morphology can be retained in 3D environments. For example, Hsiao *et al.* (2016) generated 3D hydrogel microfibers in which adipocyte precursors were differentiated into white unilocular adipocytes that could be maintained for up to 91 days. Furthermore, visceral preadipocytes are notoriously more difficult to differentiate *in vitro* compared to subcutaneous cells. Emont *et al.* (2015) demonstrated that this difference could be mitigated by the use of 3D culture techniques, differentiating visceral and subcutaneous murine preadipocytes in 3D collagen hydrogels, which enhanced lipid accumulation in visceral preadipocytes.

1.10 3D adipocyte models

Several researchers have developed 3D cell cultures of adipose tissue using a variety of techniques (**Table 1.1**). These models utilised different cell sources, including mouse and human immortalised or primary preadipocytes. Three of these techniques are described below.

1.10.1 Scaffold-based approaches

A widely used approach to develop 3D adipose models involves hydrogels, which are polymer networks that mimic the natural ECM environment by providing structural support to encapsulated cells. These can be of a natural or synthetic origin and are able to be modified to fine-tune their mechanical and biochemical properties.

For culturing and differentiating preadipocytes, various hydrogels of natural origin have been used as scaffolds including silk, collagen, alginate and commercial Matrigel™. Adipose tissue provides a soft environment (Young's modulus of ~2-4 kPa) (Li, *et al*., 2021) compared to the high stiffness of plastic substrates used in 2D culture, whereas the mechanical properties of hydrogels are much closer to the native tissue environment. Decellularised ECM scaffolds derived from adipose tissue samples have also been used to provide cells with substrates more closely resembling the structure and composition of native tissue (Dunne, *et al*., 2014).

Hydrogels have the additional benefit of their potential use in 3D bioprinting of complex cellular structures. Depending on its specific properties, a hydrogel may be used to form desired structures and then cross-linked or solidified using light, temperature or chemicals. This enables the fabrication of complex structures which can be functionalised with different cell types and used in regenerative medicine applications.

1.10.2 Scaffold-free methods

Scaffold-free approaches do not employ hydrogels but allow cells to aggregate by gravitational or magnetic forces. A benefit of choosing this approach is the relatively low cost of ultra-low attachment (ULA) plates, which have surfaces that prevent cell attachment, forcing cells to self-aggregate and form their own matrix environment. Methods requiring magnetic forces require introduction of magnetic nanoparticles into the cell cultures, which may interfere with cellular function.

1.10.3 Microfluidic platforms

Microfluidic devices are miniature systems that reflect *in vivo* conditions such as blood flow and chemical gradients. Simplistic microfluidic devices consist of two chambers enabling crosstalk of cells through a semi-permeable barrier. Recently, 'adipose tissue on chip' models have been developed for studying interactions between adipose cells and other cell types, such as macrophages, to investigate inflammatory responses (Zhu, *et al*., 2018) (Kongsuphol, *et al*., 2019). A limitation of microfluidic devices is the material from which they are fabricated, with polydimethylsiloxane (PDMS) having the disadvantage of absorbing compounds.

Table 1.1. 3D mono- and co-culture models of adipose tissue. A wide range of *in vitro* 3D models of adipose tissue have been described. Methods are categorised on production method into scaffold-based (involving the use of hydrogels for seeding 3D cultures on top or encapsulation), scaffold-free (excluding the use of hydrogels; examples include magnetic levitation, bioreactors and hanging-drop method), and microfluidic approaches which mimic physiological conditions by exposing cells to dynamic fluid flow (media perfusion). The description column shows if a combination of methodologies was employed. Abbreviations: white adipose tissue (WAT); subcutaneous adipose tissue (SAT); ultra-low attachment (ULA); brown adipose tissue (BAT); visceral adipose tissue (VAT); endothelial cell (EC); peripheral blood mononuclear cell (PBMC); adipose-derived stem cell (ADSC); extracellular matrix (ECM); mesenchymal stem cell (MSC); polydimethylsiloxane (PDMS); microbial transglutaminase (mTG); hyaluronic acid (HA).

Publication	3D Model	Cell source	Description	Applications
Method: Scaffold-free				
Muller *et al*. 2019	Vascularised human WAT	SVF isolated from human SAT	SVF cells seeded in ULA plates with continuous stirring. Cells aggregated to form spheroids which were transferred to Matrigel™, also stirred.	Vascularised adipose spheroids formed chimeric vessels when engrafted into immune deficient mice.
Taylor *et al*. 2020	Murine VAT containing immune cells	SVF isolated from mouse VAT	SVF cells seeded in ULA plates.	
Klingelhutz *et al*. 2018	Human WAT Mouse WAT and BAT	Immortalised human subcutaneous pre-adipocytes Primary SVF cells isolated from: • Human SAT (skin-derived) • Neonatal mouse SAT and VAT	Cellularised droplets dispensed on underside of lid, inverted and incubated in a humidified chamber. Resultant spheroids transferred to ULA plates.	Tested adipose spheroid responses during differentiation to environmental toxins.
Naderi *et al*. 2014	Human adipose tissue	Primary human MSCs isolated from: • Abdominal adipose tissue • Umbilical cords from full-term placentas	Cells seeded in Terasaki plates, inverted and incubated to form 'microtissues'. These were transferred to 96-well plates or centrifuge tubes in spinning bioreactor.	
Daquinag *et al*. 2013	Vascularised mouse WAT	Murine cell lines: • 3T3-L1 cells • GFP-expressing bEND.3 ECs Mouse SVF from SAT and VAT (intraperitoneal depot)	Cells magnetised by the attachment of nanoshuttles and aggregated into spheroids (adiospheres) by magnetic forces.	

Publication	3D Model	Cell source	Description	Applications
Method: Scaffold-based				
Emont *et al*. 2015	Mouse SAT and VAT	Mouse SVF isolated from inguinal and perigonadal adipose depots	Pre-adipocytes cultured in a rat tail type I collagen matrix, polymerised at 37°C neutral pH.	
Nishijima-Matsunobu *et al*. 2013	Human or rat adipose liver co-culture	Hepatocyte cell lines: • Human HepG2 • Rat RL-34 Adipose tissue fragments from: • Human SAT and VAT • Rat SAT (inguinal) and VAT (epididymal) depots	Immortalised hepatocytes seeded on adipose tissue fragments embedded in a type I collagen gel (solidified at 37°C) in an inner dish with a permeable nitrocellulose membrane. Dish placed within a larger dish and medium added to both.	Study adipose tissue-liver interactions; may have relevance in studying non-alcoholic fatty liver disease.
Louis *et al*. 2017	Murine or human adipose	3T3-L1 and 3T3-F442A murine cell lines Commercial primary human white preadipocytes	Spheroids formed in HA hydrogel functionalised with adipose ECM (collagen types I and IV and fibronectin RGDS binding motif).	
Cheng *et al*. 2012	Human SAT	Human ADSCs isolated from abdominal SAT	Chitosan coated cell culture plates used to form ADSC spheroids.	Transplantation of ADSC spheroids in hindlimbs of nude mice.
Tsai *et al*. 2019	Human SAT	Human ADSCs isolated from SAT	Cells seeded in bespoke agarose microwell plate, created using PDMS mould of AggreWell™ plate. Spheroids cultured in gelatin-based hydrogel which was enzymatically crosslinked.	Injection of gelatin/mTG hydrogels in subcutaneous dorsum of ICR mice.

Publication	3D Model	Cell source	Description	Applications
Method: Microfluidic				
Kongsuphol *et al*. 2019	Inflamed human adipose tissue	Commercial human pre-adipocytes from SAT Peripheral blood mononuclear cells	Preadipocytes indirectly co-cultured with PBMCs in a perfusion-based microfluidic chip system. Cell compartments separated by a porous membrane.	Study of immune-metabolic interactions.
Hsiao *et al*. 2016	Human WAT	Commercial primary human ADSCs	Hydrogel microfibers fabricated by flowing ADSC and ECM proteins through a capillary tube, around which an encompassing shell of sodium alginate was formed.	
Loskill *et al*. 2017	WAT-on-a-chip	3T3-L1 fibroblasts	Pellets of 3T3-L1 cells formed in WAT chambers within a microfluidic device made from PDMS. An isoporous PET membrane, mimicking an endothelial barrier, segregated WAT chambers from the media channel; media was transported through the channel mimicking blood flow.	

1.11 Concluding remarks

Modelling adipose tissue *in vitro* presents challenges due to its structural and cellular complexity. Recent developments in 3D culture techniques have increased the range of tools available for adipose biology research. Refining existing *in vitro* models may reduce future reliance on animal-based studies, however there is still a lack of scalability which limits high-throughput studies. Standardising production workflows and introducing automation would overcome these limitations, creating a platform to investigate genes implicated in adipose tissue dysfunction. Developing depot-specific models that accurately represent both upper- and lower-body adipose tissue would enhance the relevance of these studies. This is particularly important for researching certain diseases that affect specific fat depots, such as partial lipodystrophy, where mechanisms are currently poorly understood.

1.12 Thesis aims

The main aims of this thesis were to:

1. Develop and characterise an automated high-throughput 3D adipose cell culture model to improve throughput and reproducibility of spheroid production. This would provide a physiologically relevant *in vitro* system for studying adipose biology and gene function.
2. Further develop the 3D adipocyte culture system by establishing spheroids derived from preadipocytes originating from different human adipose tissues to model depot-specific differences in function.
3. Employ the 3D adipose cell culture system to a mouse knock-out model of a human type 2 diabetes risk gene (*RREB1*) associated with altered adipose tissue function to study disease mechanisms.
4. Employ the 3D adipose cell culture system to a rare human monogenic disorder (familial partial lipodystrophy type 2) by creation of spheroids with and without the LMNA R482W mutation in abdominal and gluteofemoral preadipocytes.

2 Methods

2.1 Preparation of reagents for spheroid fabrication

2.1.1 Sterile oil preparation

Oil mixtures for spheroid fabrication were prepared as described previously (Graham, *et al*., 2019). Briefly, each oil stock was filtered (0.2 µm) and UV irradiated (30 minutes) prior to mixing. Biofabrication oil consisted of a 35:65 v:v mixture of undecane (Cat. U407) to silicone oil AR 20 (Cat. 10836), supplemented with 1.2 mM 1,2-diphytanoyl-*sn*-glycero-3-phosphocholine (DPhPC, Avanti Polar Lipids, Cat. 850356 C). The DPhPC lipid films, supplied dissolved in chloroform, were prepared by removing the solvent through evaporation under gentle air pressure, followed by vacuum drying for at least 2 hours. Alternatively, an evaporator system (TurboVap LV, Biotage) was used to remove the chloroform solvent within 10 minutes using nitrogen gas (5 psi). The resulting dried lipid films were stored at -20°C and used for spheroid fabrication within 6 months. Transfer oil comprised a 3:1 v:v mixture of hexadecane (Cat. 296317) and mineral oil (Cat. M3516), with all oil stocks purchased from Sigma-Aldrich.

2.1.2 Fmoc dipeptide solution preparation

Fmoc dipeptide solutions were prepared to strengthen the hydrogel used in spheroid production. 12 mg of fluorenyl-methyloxycarbonyl-isoleucine-glycine (Fmoc-IG, Bachem) and 16 mg of Fmoc-diphenylalanine (Fmoc-FF, Bachem) powders were weighed into glass vials. 1.5 mL of deionised water (diH2O) was added to each powder. 20 µL and 15 µL of 1 M sodium hydroxide was added to Fmoc-IG and Fmoc-FF, respectively, and stirred overnight for partial dissolution. Each dipeptide was then fully dissolved using at least three rounds of sonication (40 minutes, 40°C, 40 kHz) in an ultrasonic water bath (2.75 L S-Series, Fisherbrand™). The pH was adjusted to 8.5 for Fmoc-IG and 9.5 for Fmoc-FF using 0.1 M sodium hydroxide.

Solutions were then topped up to 3 mL with diH2O to achieve 10 mM stocks for each dipeptide, which were stored at room temperature before being added to the hydrogel.

2.1.3 Hydrogel-based matrix preparation

The hydrogel-based matrix solution was prepared following the method outlined by Graham *et al*. (2019), comprising 11.2 mg/mL ultra-low gelling temperature agarose (ULGTA, Sigma-Aldrich, A5030), 0.5 mM Fmoc-IG (pH 8.5), 0.5 mM Fmoc-FF (pH 9.5) and 15 µg/mL type I collagen (bovine origin, Gibco™, A1064401) in an 8:1:1 v:v ratio of DMEM, PBS and diH_2O. DMEM+GlutaMAX™ (Gibco™, 31966) was used for mouse spheroid production, while DMEM/F12 (Gibco™, 11320) supplemented with 15 mM HEPES (Gibco™, 15630080) was used for fabricating human spheroids. The hydrogel solution was prepared on the day of spheroid production and maintained at 37°C to preserve its fluid state until use. Prior to cell resuspension, the hydrogel was homogenised using sonication (5 minutes, 40^{o}C, 40 kHz) in an ultrasonic water bath.

2.2 Automation of spheroid fabrication and culture

2.2.1 Cellular droplet production

The fabrication of spheroids in 96-well plates was automated using a nanolitre liquid handler (Mosquito LV Genomics, SPT Labtech). The liquid handler consists of a two-position deck, housing both the source and destination plates (Greiner, 650161), and a bandolier spool of disposable micropipettes feeding the pipetting head. Cellular hydrogel (i.e. cells re-suspended in the hydrogel solution) was thoroughly re-suspended and immediately aliquoted into a well column on the source plate. Cellular droplets were generated by programming the Mosquito to aspirate cellular hydrogel solution from the source plate and dispense into biofabrication oil within destination plates (pre-prepared with 50 µL of oil per well). Dispensing was via positive

displacement pipetting and occurred column-by-column using the same tips unless changing between samples. The dispensing volume (nL) was set in the Mosquito software. Other parameters used were: aspirate speed 25 mm/s, dispense speed 5 mm/s, aspirate clear speed 6.3 mm/s, dispense clear speed 2.5 mm/s, aspirate clear distance 2 mm, dispense clear distance 1 mm.

Dispensed droplets of cell-hydrogel mixture were solidified in the oil by immediately incubating the destination plates at 4^{o}C (25 minutes). The solidified droplets were then transferred into cell repellent 96-well U-bottom plates (Greiner, 650970) using an automated liquid handling robot (Assist Plus, Integra Biosciences). The Assist Plus was used to aspirate the entire biofabrication oil into widebore tips and dispense into the upper phase of a two-phase column; this comprised 50 µL of transfer oil over 120 µL of preadipocyte growth medium. When triplicate samples were required, this process was twice repeated to obtain three cellular droplets per well. The 96-well plates were then briefly centrifuged (<30 seconds, 50 x *g*) to ensure complete transfer of droplets to medium. The upper oil layer was then aspirated and fresh growth medium added (final well volume 200 µL) using the Assist Plus. Finally, cellular droplets in growth medium were transferred to an incubator at 37^{o}C, 5% CO_2.

2.2.2 Automated liquid handling of spheroids

The Assist Plus liquid handling robot equipped with a VIAFLO II 8-channel pipette was used to automate all spheroid media exchanges. This typically involved two partial liquid handling steps to avoid disturbing the spheroids, with 1 minute delay steps to allow spheroids to settle. Liquid handling steps were as follows:

1. Removal of 120 µL of culture media from each well.
2. Addition of 120 µL of fresh pre-warmed media from an 8 or 12-column polypropylene reservoir.
3. Steps 1 and 2 repeated.

This resulted in 84% v/v fresh media added to each well. Liquid handling programs were designed in VIALAB software (version 2.1.1.0). The tips were programmed to enter at the edge of the wells (2.6 mm offset from centre) and the pipetting speeds set to 3 (out of 10) for aspiration and 6 (out of 10) for dispensing.

2.3 Assessment of spheroid viability and lipid content by high-content imaging

2.3.1 Viability assay

Spheroids were stained with 1 µM calcein-AM (CAM, Cayman Chemical, CAY14948) and 5 µM propidium iodide (PI, Sigma-Aldrich, Cat. P4170) in 200 µL of DMEM+GlutaMAX™ (mouse spheroids) or DMEM/F12 (human spheroids) for visualising live and dead cells, respectively. Following the addition of staining solution, samples were incubated in the dark (30 minutes, 37ºC, 5% CO_2). 100 µL of the staining solution was then removed, and samples were washed twice with 100 µL of fresh pre-warmed culture medium in preparation for fluorescence imaging; washing was performed either manually or using the Assist Plus.

Fluorescence z-stack micrographs of spheroids were obtained using a high-content imager (Cytation 1, BioTek). Maximum intensity projections from image stacks were analysed with Gen5 software (BioTek), following the method described by Graham *et al*. (2019). Cell viability was determined by automated quantification of live cell (CAM) and dead cell (PI) fluorescent signal areas. Dead spheroid controls were produced by incubating samples (37°C, 5% CO_2) with 0.1% saponin for 10 minutes prior to dye addition. Single-stain control samples were used to check for fluorescence spillover in the GFP and PI channels.

2.3.2 Lipid phenotyping assay

Spheroids were washed four times with 1 × PBS and then fixed for 1 hour in 4% w/v formaldehyde (Thermo Scientific, 28908) at room temperature in the dark. Afterwards, the spheroids were washed four times in PBS and stored at 4°C in the dark until staining. Fixed spheroids were fluorescently labelled for neutral lipid droplets and nuclei using 1 µM BODIPY 493/503 (Thermo Scientific, D3922) and 3.85 µM Hoechst 33342 (Thermo Scientific, H3570), respectively. Samples were incubated (1 hour, room temperature, in darkness) and then washed four times in PBS. All liquid handling steps were carried out with the Assist Plus.

The Cytation1 high-content imager was used to acquire fluorescence z-stack images of spheroids for lipid phenotyping. Adipocyte differentiation levels were assessed by measuring the lipid droplet (BODIPY 493/503) and nuclei (Hoechst 33342) fluorescent signal areas in Gen5 software (Graham, *et al*., 2019). Relative lipid signal (i.e. lipid signal area normalised to nuclei signal area) was determined for each well, with consistent analysis settings used for each experiment. A relative lipid signal value of 100% indicates a sample with an equal area of total lipid and nuclei signal. Wells with staining artefacts or containing missing/damaged samples were eliminated from the final images following manual inspection.

2.4 Spheroid size determination

Brightfield images of spheroids in 96-well plates were acquired using the Cytation1 high-content imager. On the day of biofabrication, cellular droplet sizes were measured by automated image analysis using Gen5 software. Manual size analysis of spheroids was performed in ImageJ. Volumes were calculated from diameters using the formula $V = {}^{4}/_{3}\pi r^{3}$, applying the assumption that the 3D cultures were spherical.

2.5 Human cell culture

2.5.1 Background

2.5.1.1 Generation of depot-specific preadipocyte lines

The Metabolic Research Group at the Oxford Centre for Diabetes Endocrinology and Metabolism (OCDEM) generated immortalised (hTERT/HPV16-E7) human preadipocyte cell lines, referred to as imAbdo (immortalised abdominal) and imGlut (immortalised gluteal) cells, by lentiviral transduction of primary preadipocytes (Todorčević, *et al*., 2017). These were derived from the abdominal and gluteal subcutaneous adipose tissue depots of a 50-year old healthy male (BMI: 24.4 kg/m^2) from the Oxford BioBank. The cell lines were differentiated into mature adipocytes *in vitro* and subsequently de-differentiated into preadipocytes to generate de-differentiated fat (DFAT) cells, as described by Loh *et al*. (2020), which were the cell lines used in **Chapter 4** for human adipose spheroid model development.

2.5.5.2 Generation of doxycycline-inducible cell lines for LMNA overexpression studies

Doxycycline (Dox)-inducible cell lines were generated by Dr Nellie Loh (OCDEM) by transduction of abdominal and gluteal DFAT cells (described in **2.5.1**) with a lentiviral vector (pCW57.1, gift from David Root, Addgene #41393), containing either EGFP (enhanced green fluorescent protein), wild-type (WT) LMNA or R482W-mutated LMNA cDNA. Puromycin (2 µg/mL) application was used to select for successfully transduced cells. The resulting Dox-inducible cell lines were used to investigate the impact of LMNA overexpression on depot-specific adipocytes in **Chapters 5 and 6**.

2.5.2 Maintenance of preadipocyte lines in 2D culture

Abdominal and gluteal DFAT cells were cultured in T175 flasks in DMEM/F12 containing 10% foetal bovine serum (FBS, Gibco™, Lot 2266780K), 1% penicillin-streptomycin mixture (Pen-Strep, Invitrogen™, 15140-122), 15 mM HEPES (Gibco™, 15630080), 2.5 mM L-Glutamine (Invitrogen™, 25030-024) and 0.25 ng/mL human fibroblast growth factor (hFGF, R&D Systems, 233-FB-025). During subculturing, growth media was changed every 2-3 days and the cells were passaged when 80-90% confluent.

Doxycycline-inducible cell lines (described in **2.5.5.2**) were cultured identically but grown in DMEM/F12 containing 10% Tetracycline-system approved FBS (Gibco™, Lot 2350730RP, Cat. A4736401) and 2 µg/mL puromycin (Gibco™, A1113803).

During subculturing, cells were rinsed with 5 mL of 1 × DPBS and detached from flasks by adding 3 mL of TrypLE™ Express (Gibco™, 12604-021) and returned to the incubator for 2-3 minutes (37^{o}C, 5% CO_2). Flasks were examined under a light microscope to check that cells had successfully detached. Cell suspensions were collected into 50 mL Falcon tubes and centrifuged (270 x *g*) for 5 minutes. Each cell pellet was re-suspended in growth media and 20 µL dispensed into each side of a Nexcelom cellometer disposable counting chamber for automated cell counting (Nexcelom Cellometer Auto T4). Cells were seeded into new T175 flasks containing 22 mL of fresh preadipocyte growth media and placed in the incubator.

2.5.3 Freezing cells

Cells were harvested from T175 flasks and cell pellets re-suspended in freezing solution containing 50% DMEM/F12, 45% FBS (either standard or Tetracycline-approved) and 5% dimethyl sulfoxide (DMSO, Sigma-Aldrich, D2650). 1 mL of cell suspension containing ~1 × 10^6 cells was added per cryovial (Simport Scientific, T301-1), which were stored at -80^{o}C overnight in a polystyrene rack. The cell stocks were then transferred on dry ice to a liquid nitrogen (LN_2) tank for long-term storage.

2.5.4 Thawing cells

Cryovials containing frozen cell lines were transferred on dry ice from LN_2 storage. Each cryovial was held in a 37ºC water bath and gently swirled for 30-60 seconds until minimal ice crystals remained. The cryovials were then sprayed with 70% ethanol, dried and transferred into a Class II Biological Safety Cabinet (BSC) to work aseptically. 1 mL of thawed cell suspension from each cryovial was added in a dropwise manner to 5 mL of pre-warmed growth media (see **2.5.2**) and then centrifuged (270 × *g*) for 5 minutes. The supernatant was discarded to remove DMSO and the cell pellet re-suspended in 10 mL of fresh media. Re-suspended cells were added to a T175 flask with 12 mL of additional growth media (22 mL/T175 flask) and transferred to an incubator.

2.6 Adipogenic differentiation

For differentiating human preadipocytes, 2×10^5 or 1×10^4 cells were seeded per well in CellBIND 6-well or 96-well plates (Corning), respectively, and allowed to grow to confluency. Preadipocytes were induced to differentiate for up to 14 days following a protocol from Todorčević *et al*. (2017), with minor modifications. Confluent cells were treated with DMEM/F12 containing 1% v/v Pen-Strep, 100 nM human insulin (Invitrogen™, 12585014), 1 µM dexamethasone (Sigma, D2915), 130 nM transferrin (Sigma, T8158), 10 nM triiodothyronine (T3, Sigma, T5516), 17 µM pantothenate (Sigma, P5710), 33 µM biotin (Sigma, B4639), 250 µM 3-isobutyl-1-methylxanthine (IBMX, Sigma, I7018) and 4 µM troglitazone (Sigma, T2573) for the first 4 days of differentiation. From day 4 onwards, IBMX and troglitazone were omitted from the adipogenic cocktail and an exogenous fatty acid mixture (80 µM) added. The fatty acid mixture consisted of oleate:palmitate:linoleate:α-linoleate (45:30:24:1%) bound to bovine serum albumin (BSA) at a 4:1 molar ratio.

2.7 Doxycycline-induction of EGFP and LMNA expression

2.7.1 Preparation of doxycycline stock solution

A 1 mg/mL solution was prepared by dissolving doxycycline hyclate powder (Sigma-Aldrich, D9891) in autoclaved diH_2O and sterile filtering (0.2 µm). From this solution, a 0.1 mg/mL working stock was created by diluting the 1 mg/mL solution 1:10 in diH_2O. Doxycycline working stock solutions were stored at -20^oC, protected from light. Once thawed, solutions were stored at 4^oC, protected from light, and used within 1 month.

2.7.2 Doxycycline treatment

Induction of EGFP, WT LMNA or R482W-mutated LMNA expression in the doxycycline-inducible cell lines (described in **2.5.5.2**) was achieved by adding doxycycline solution to growth or adipogenic culture media (final concentration of 0.1 µg/mL). For transgene induction in spheroids, doxycycline treatment was performed approximately 24 hours after cellular droplet production. Media was exchanged every 2-3 days for both 2D and 3D experiments with doxycycline added to the appropriate media on the day of use. Experiments were conducted in parallel for abdominal and gluteal samples, and all cells used were between passages 12 to 23.

2.8 RNA applications

2.8.1 RNA isolation from 2D cultures of preadipocytes

Cells in 6-well plates were washed once in 1 × PBS and harvested in a fume hood by adding 350 µL of RLT Lysis Buffer (Qiagen) supplemented with 1% β-mercaptoethanol. Each well surface was then scraped and the cell lysates transferred into RNase-free 1.5 mL Eppendorf tubes, which were stored at -80^{o}C until RNA isolation.

Total RNA was extracted from samples using a RNeasy Mini Kit (Qiagen, 74106) with on-column DNA digestion performed using a RNase-Free DNase Set (Qiagen, 79256), following the manufacturer's instructions. RNA was eluted in a final volume of 35 µL of RNase-free water. RNA concentration was assessed using a NanoDrop 1000 Spectrophotometer (Thermo Scientific). Purity of samples was determined using 260/280 and 260/230 ratios, where samples with a 260/280 > 1.8 were considered free from DNA and protein contamination, and samples with a 260/230 ratio > 1.8 were considered free from guanidine salt contamination (e.g. from the RLT lysis buffer). Any samples with low ratios were cleaned up and concentrated using a RNeasy MinElute Cleanup kit (Qiagen, 74204).

2.8.2 cDNA Synthesis

cDNA was synthesised from 500-1,000 ng of total RNA using a High-Capacity cDNA Reverse Transcription Kit (Applied Biosystems, 4368814), following the manufacturer's instructions. A thermal cycler (MJ Research, PTC-225) was used with the conditions shown in **Table 2.1**. Negative controls for use in downstream gene expression analysis were prepared using all reaction components except RNA template (no template control, NTC) or reverse transcriptase enzyme (RT minus control, RT-).

Table 2.1. Thermal cycler conditions for cDNA synthesis.

Step	Temp. (ºC)	Time (minutes)
Primer annealing	25	10
Reverse transcription	37	120
Enzyme inactivation	85	5

2.8.3 Single nucleotide polymorphism (SNP) genotyping

A TaqMan SNP Genotyping Assay (C__64676006_10) was used to discriminate between WT and mutant alleles for the *LMNA* R482W (rs57920071) variant. 3.8 µL of dilute cDNA (1:20 dilution in 10 mM Tris-HCl), 0.2 µL of TaqMan assay and 4 µL of Fast Master Mix (Kappa Biosystems) were loaded on a 384-well plate in duplicate and run on the Quantstudio 7 Flex (ABI) system, using parameters shown in **Table 2.2**.

Table 2.2. qPCR conditions for *LMNA* SNP genotyping.

Step	Temp. (ºC)	Time (mm:ss)	Number of cycles
Initial denaturation	95	3:00	1
Denaturation	95	0:08	40
Annealing/extension	60	0:30	

2.9 Histology of spheroids and adipose tissue samples

2.9.1 Automatic sample processing, wax embedding and sectioning

Spheroid and adipose tissue samples were processed for histology using an automatic benchtop tissue processor (Leica TP1020), with the program settings shown in **Table 2.3**. Prior to processing, spheroids were embedded in HistoGel™ (Thermo Scientific, HG-4000-012) discs using custom moulds and transferred to histological cassettes.

The processed samples were embedded in paraffin wax blocks using a Leica EG1150H embedding station, and cooled on a Leica EG1150C cold plate. 5 µm-sections were cut from the wax blocks using a Leica RM2235 microtome and floated on distilled water in a Solmedia flotation bath set to 40ºC. The sections were mounted onto SuperFrost™ Plus glass slides and allowed to dry at room temperature, after which they were baked in an oven overnight (60ºC) to adhere the tissue sections to the slides. The slides were stored at room temperature ready for staining.

Table 2.3. Automatic tissue processor conditions. IMS, industrial methylated spirit.

Solution	Time
70% IMS	1 hour
90% IMS	1 hour
100% IMS	1 hour
100% IMS	1 hour
100% IMS	1 hour
Xylene	1 hour
Xylene	1 hour
Xylene	1 hour
Paraffin wax (60ºC)	1 hour
Paraffin wax (60ºC)	1 hour

2.9.2 H&E staining

Haematoxylin and eosin (H&E) staining of spheroid and adipose tissue sections was performed by transferring slides between tanks containing xylene and ethanol solutions (**Table 2.4**). At the end of the procedure, H&E-stained slides were covered with a glass coverslip and mounted with dibutylphthalate polystyrene xylene (DPX), and imaged using a Nikon ECLIPSE Ci-S microscope.

Table 2.4. Haematoxylin and eosin (H&E) staining. All steps involving xylene were carried out in a fume hood. Haematoxylin (Sigma-Aldrich, 1.05175) and 1% eosin reagents were used.

Step	Reagent/Procedure	Time
Deparaffinisation	Xylene (tank 1)	3 minutes
	Xylene (tank 2)	3 minutes
	Xylene (tank 3)	3 minutes
Rehydration	100% ethanol (tank 1)	3 minutes
	100% ethanol (tank 2)	3 minutes
	90% ethanol (tank 3)	3 minutes
	70% ethanol tank (tank 1)	3 minutes
	Rinse under running tap water	5 minutes
Nuclear staining	Haematoxylin solution	5 minutes
	Rinse under running tap water	3 minutes
Differentiation	Dip in acid-alcohol three times	9 seconds total
	Rinse under running tap water	3 minutes
Cytoplasmic staining	Eosin solution	7 minutes
	Rinse under running tap water	1 minute
Dehydration	Dip in 70% ethanol three times (tank 2)	9 seconds
	100% ethanol (tank 4)	2 minutes
	100% ethanol (tank 5)	2 minutes
	100% ethanol (tank 6)	2 minutes
	Xylene (tank 4)	3 minutes
	Xylene (tank 5)	3 minutes
	Xylene (tank 6)	3 minutes

2.10 Statistical analysis

All data was analysed using GraphPad Prism (version 9.1.0), with test details described in the figure legends. Differences were considered statistically significant at $p < 0.05$.

3 Development of a high-throughput spheroid model of mouse white adipose tissue

3.1 Introduction

3.1.1 Background

My supervisor's research group (the Cox group) previously established an *in vitro* 3D cell model of mouse WAT (Graham, *et al*., 2019) to bridge the gap between simplistic 2D *in vitro* and complex *in vivo* models, in collaboration with OxSyBio Ltd (former synthetic tissue company). A novel 3D culture method, termed 'droplet-in-oil' spheroid fabrication (**Figure 3.1**), was developed for generation of monoculture adipose spheroids, using 3T3-L1 cells encapsulated in hydrogel droplets.

This method involves forming droplets by manually dispensing an aqueous cellular hydrogel in oil, which solidifies upon cooling due to the hydrogel's thermal properties. Dispensed droplet sizes were assessed using a stereomicroscope where variable droplet sizes were observed. The solidified droplets were then manually transferred to culture media, resulting in the aggregation of 3T3-L1 cells into spheroids. These were induced to adipogenic differentiation, with spheroids displaying active lipid metabolism and drug responsiveness (Graham, *et al*., 2019).

Whilst this method was useful as a proof-of-concept, the production aspect of this process was labour intensive and generated spheroids of variable sizes. Therefore, I sought to automate this technique to improve reproducibility, providing a route to high-throughput applications. I hypothesised that increasing the complexity of the model, through the introduction of other native adipose tissue cells, would enhance adipocyte differentiation resulting in large lipid droplet formation more representative of *in vivo*. This could be achieved by utilising immortalised cell lines in a co-culture system or isolating primary cells from adipose tissue.

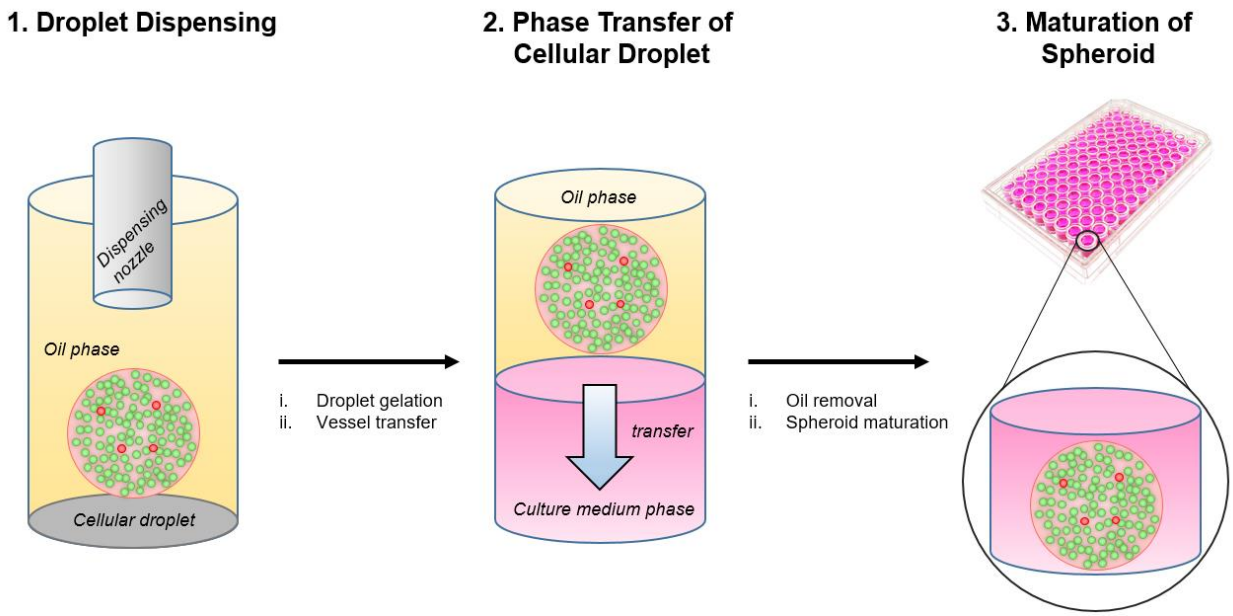


Figure 3.1. Steps for droplet-in-oil spheroid production. (**1**) Droplet dispensing: Droplets of cells suspended in a hydrogel-matrix are dispensed into an oil phase containing lipid ('biofabrication oil'). (**2**) Phase transfer of cellular droplet: Cellularised matrix droplets are solidified by standing at 4°C (25 min) and then transferred into a cell repellent 96-well plate containing 'transfer oil' layered above culture medium. After solidified droplets sink from oil to culture medium, the upper oil layer is removed. (**3**) Maturation of spheroid: Cellular droplets are cultured allowing spheroids to form. Figure adapted from Graham *et al*. (2019).

3.1.2 Chapter aims

The specific aims of this chapter were to:

- Further develop the adipose spheroid system developed by Graham *et al*. (2019), utilising high-throughput automation to increase reproducibility and its use at scale.
- Develop the model using adipose-derived mouse SVF cells, investigating the morphology and organisation of the spheroid and its functional metabolic characteristics.
- Apply the adipose spheroid system to a mechanistic study of a genetic determinant of adipose function, exploiting genes and mouse models under investigation within the Cox group. For example:
    - What is the basis of small adipocyte size in adipose tissue from haploinsufficient *Rreb1* (Ras-responsive element binding protein) mice; a gene linked to ectopic fat distribution and T2D in human association studies (Mahajan, *et al*., 2014) (Chu, *et al*., 2017).

3.2 Specific methods

3.2.1 Mouse stromal vascular fraction cell isolation and culture

SVF cells containing preadipocytes were isolated from subcutaneous inguinal white adipose tissue (iWAT) depots excised from 6-8 week old B6N male mice. Left and right iWAT depots were washed in 1 × Dulbecco's Phosphate-Buffered Saline (DPBS, calcium and magnesium free, Gibco™, 14190144) and cut into smaller pieces in sterile Hanks' Balanced Salt Solution (HBSS, Sigma-Aldrich, H8264), containing 0.08% w/v collagenase type 2 (Worthington Biochemical Corporation, LS004174) and 3% w/v bovine serum albumin (Sigma-Aldrich, A9418). The tissues were digested in a shaking water bath (37^{o}C, 120 rpm) for a minimum of 40 minutes, or until minimal visible clumps remained, and also hand shaken at 10 minute intervals. The solution was then centrifuged (3 min, 300 x *g*) to pellet SVF cells.

SVF cells were re-suspended in 10 mL of DMEM containing high glucose (25 mM), GlutaMAX™ and pyruvate (Gibco™, 31966) supplemented with 10% v/v FBS (Gibco™, 10500064) and 1% v/v Pen-Strep (10,000 U/mL, Gibco™, 15140-122) (hereafter referred to as 'growth medium' in this Chapter). The cell suspension was filtered into a 10 cm culture dish (Greiner, 664160) using a sterile 40 µm diameter pore nylon mesh (Falcon™, 352340). SVF cells were cultured at 37^{o}C in the presence of 5% CO_2. The growth medium was changed the day after isolation, and then every 2-3 days thereafter.

Upon reaching 80-90% confluency (usually within 72-96 hours), expanded SVF cells were harvested for spheroid fabrication by washing once in 1 × DPBS followed by dissociation with TrpLE express 1 × (Gibco™, 12605-010). Cells were counted using an automated cell counter (Countess II, Thermo Fisher), and re-suspended in hydrogel solution at a concentration of 4 × 10^7 live cells/mL. Cell viability was measured using trypan blue staining. The SVF cells were then used for automated spheroid production as described in **Chapter 2**.

3.2.2 Spheroid culture and adipogenic differentiation using automated liquid handling

Cellular droplets were cultured in growth media for two days during which the SVF-derived cells aggregated into spheroids. Two days after droplet production (designated day 0), preadipocyte spheroids were induced to undergo adipogenic differentiation using a protocol adapted from Merrick *et al*. (2019). In brief, growth medium was exchanged for DMEM-31966 containing 10% v/v FBS and 1% v/v Pen-Strep supplemented with 2.5 µM dexamethasone (D2915), 50 µM IBMX (I5879), 20 nM human insulin (I9278), 125 µM indomethacin (I7378) and 1 nM T3 (T6397) ('differentiation medium'; all differentiation reagents purchased from Sigma-Aldrich). After 4 days, the differentiation medium was replaced with an equivalent medium less dexamethasone, IBMX and indomethacin ('maintenance media' contained 20 nM insulin and 1 nM T3 adipogenic factors).

Spheroids were differentiated for up to 14 days with media exchanges carried out approximately every 48 hours, using an Assist Plus automated pipetting robot (described in **2.2.2**). Undifferentiated spheroids were cultured in growth media for the same period.

3.2.3 Measurement of glycerol, FFA and adiponectin concentrations in culture media

Spheroid media samples collected at 48-hour intervals during an adipogenic differentiation time-course were processed by the Clinical Biochemistry Department at the MRC Harwell Institute, using a Chemistry Analyser (AU680, Beckman Coulter) to quantify the release of glycerol and FFAs.

Adiponectin concentrations in culture medium were measured using an Adiponectin Mouse ELISA kit (Invitrogen™, KMP0041), following the manufacturer's instructions. Samples for adiponectin ELISA were diluted 1:20 with 1× ELISA Buffer provided in the ELISA kit. The absorbance of samples at 450 nm was measured using an Epoch Microplate Spectrophotometer (BioTek). Culture medium was stored at -80^{o}C until analysis.

3.2.4 Immunofluorescence staining of perivascular cells in spheroids

Fixed spheroids were permeabilised in 0.3% Triton X-100 for 15 minutes and then washed three times in 1 × PBS. Spheroids were incubated in blocking solution (1% BSA, 0.3 M Glycine, 0.2% Tween-20 in PBS) for 15 minutes. Primary anti-αSMA antibody (ab184675) diluted 1:100 in blocking solution was added and spheroids incubated at 37ºC in darkness overnight. The following day, spheroids were washed three times in PBS and cell nuclei counterstained using 1 µg/mL DAPI (in methanol) for 5 minutes. Finally, spheroids were washed twice in PBS before confocal imaging.

3.2.5 Plasma membrane staining

Spheroids were stained with 5 µg/mL wheat germ agglutinin (WGA, Alexa Fluor 594 conjugated, Thermo Scientific, W11262), which labels cell surface glycoproteins N-acetyl-D-glucosamine and N-acetylneuraminic acid. WGA was added to spheroids incubated at 37ºC 5% CO_2 for 10 minutes, after which samples were washed four times with PBS before being fixed (described in **2.3.2**).

3.2.6 Confocal and light sheet imaging

A Zeiss LSM700 confocal microscope was used for confocal fluorescence imaging of adipocyte spheroids. Spheroids were transferred in a low volume of PBS (typically 15-20 µL) to glass bottom dishes using wide bore tips, and the liquid surrounding the samples was removed before embedding spheroids in 1.5% w/v low gelling temperature agarose (A9045, Sigma-Aldrich). Alternatively, the spheroids were imaged in suspension following transfer to a µ-Slide (ibidi, 2018001).

For light sheet fluorescence microscopy (LSFM), adipocyte spheroids were transferred to V-shaped 1% agarose wells and after sinking to the bottom, imaged top down using a TCS SP8 DLS (digital light sheet). The samples were taken to the Central Laser Facility (Rutherford Appleton Laboratory, Harwell Campus, Oxford) for LSFM imaging, which was carried out by Dr Robert Lees.

3.2.7 Quantification of mouse adipocyte sizes

H&E-stained adipose tissue sections (prepared by the histology department at MRC Harwell) from subcutaneous iWAT and visceral perigondal white adipose tissue (gWAT) depots of *Rreb1*$^{+/+}$ and *Rreb1*$^{+/-}$ mice, were scanned at 20× magnification using a NanoZoomer Digital slide scanner (Hamamatsu). Random images from each tissue sample were exported at 10× magnification from the NDP.view2 software; the number of images exported was dependent on tissue size, up to a maximum of 15. Adipocyte area and number were quantified using ImageJ software with Adiposoft plug-in version 1.16 (Galarraga, *et al*., 2012). The following parameters were used: auto-mode was deselected to enable manual editing of adipocyte selection, the exclude on edges parameter was selected, and the minimum to maximum diameter was set to 5-100. Frequency distributions of adipocyte areas were calculated and expressed as a percentage of the total number of adipocytes counted. The results were plotted as histograms using a bin range of 0 to 20,000 μm^2 and a bin width of 250 μm^2 in **Figure 3.12**.

3.3 Results

3.3.1 Optimisation of mouse SVF spheroid production

To improve throughput and reproducibility of the culture system previously developed (Graham, *et al*., 2019), we selected the Mosquito LV Genomics system (SPT Labtech) to test spheroid production, a commercially available automated liquid handler capable of dispensing nanolitre volumes (25 nL - 1200 nL reported range). The capability of the robotic system to automate and miniaturise 'droplet-in-oil' spheroid production was first tested by setting the liquid handler to dispense different volumes of aqueous cellular hydrogel solution into oil.

Mouse SVF cells were selected for the specific variety of adipose progenitor cells to develop a model that better reflected the complexity of *in vivo* adipose tissue. To achieve sufficient quantities for spheroid production, SVF cells isolated from subcutaneous iWAT were initially cultured and expanded *in vitro* under 2D conditions. During expansion one or two media changes were carried out, during which non-adherent cells were naturally lost favouring the expansion of adherent cells.

On the day of spheroid fabrication, expanded SVF cells (hereafter referred to as preadipocytes) were harvested from 2D culture dishes and re-suspended in the aqueous hydrogel solution at a high cell density (4×10^7 cells/mL). If necessary, cells from multiple mice (three to four) were pooled to ensure adequate cell quantities for re-resuspension at the desired concentration.

Cellular droplets were successfully generated using the Mosquito instrument programmed to dispense nanolitre volumes (100-250 nL) of cell-hydrogel mixture into oil in U-bottom 96-well plates (**Figure 3.2**).

The sizes of dispensed droplets, once solidified and transferred to culture media, were determined by automatic image analysis of bright field micrographs obtained with a high-content imager (Cytation1, BioTek) (**Figure 3.2**). This enabled assessment of the instrument's dispensing parameters across the range of volume settings tested, from which it was established that the instrument overestimated the droplet sizes by approximately 12-23% (**Table 3.1**).

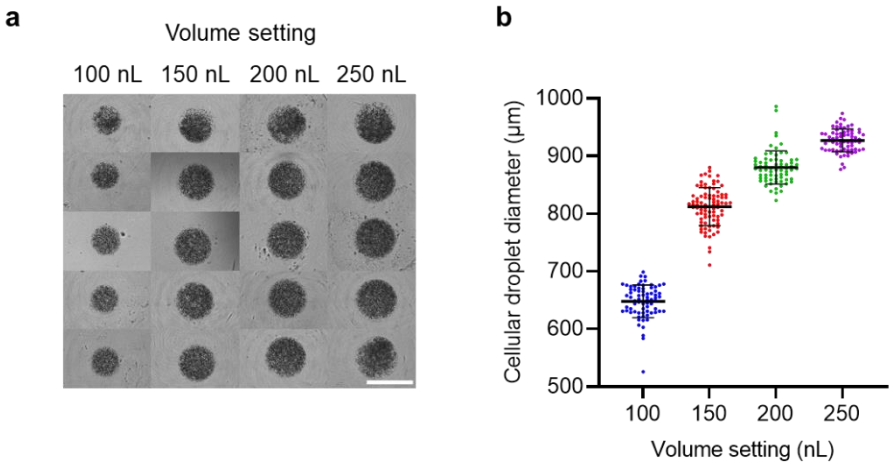


Figure 3.2. Cellular droplet sizes after automated dispensing. (**a**) Representative bright field micrographs of cellular droplets fabricated at 100 nL, 150 nL, 200 nL and 250 nL volumes set in the Mosquito software. Scale bar represents 1 mm. (**b**) Sizes of cellular droplets fabricated using the Mosquito instrument at 100, 150, 200 and 250 nL volume settings (from 8 96-well plates, 3 independent experiments). Cellular droplet diameters (*n* = 70-87 measurements per setting) were determined immediately after production by automated image analysis using a high-content imager (Cytation1, BioTek). Data are mean ± SD.

Table 3.1. Mosquito instrument dispensing qualities for volume settings. CV, coefficient of variation.

Volume setting (nL)	Target diameter (mm)	Dispensing inaccuracy (%)	CV (%)
100	0.576	+12.5	4.3
150	0.659	+23.2	4.0
200	0.726	+21.0	3.1
250	0.782	+18.6	2.1

Following dispensing an Assist Plus pipetting robot (Integra Biosciences) was used for the automated transfer of droplets from oil to media. Automated bright field imaging was undertaken during the first 48 hours of culturing, to monitor if spheroids would form. This showed the preadipocytes, which were initially homogenously distributed throughout the droplets, condensing to form homogenous-sized spheroids (**Figure 3.3**). The spheroid formation would typically occur within ~16 hours of transfer to growth media (**Figure 3.3c**).

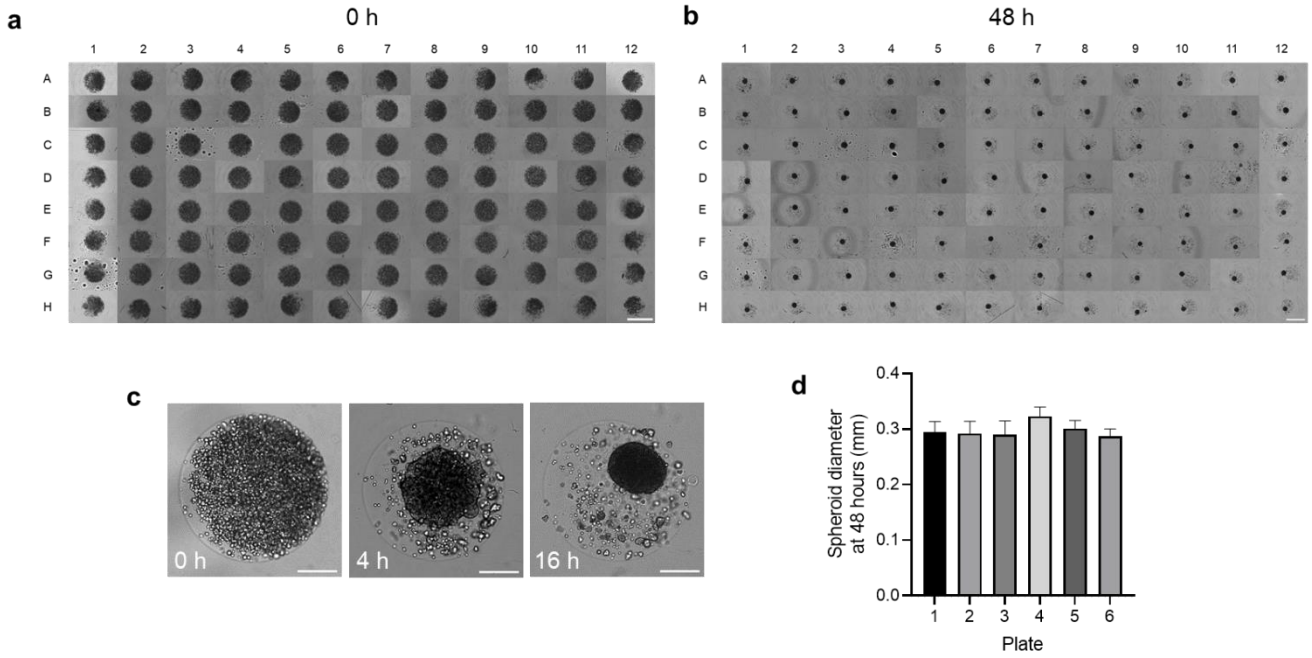


Figure 3.3. Reproducible spheroid formation in 96-well plates. (a and b) Image matrices of bright field micrographs of cellular droplets within 96-well plates, fabricated using the Mosquito (250 nL dispense setting). Images were acquired using a high-content imager immediately after droplet production (**a**) and 48 hours-post production (**b**) of the condensed spheroids. Scale bars represent 1 mm. (**c**) Representative bright field micrographs depicting spheroid formation (cell aggregation) in hydrogel droplet over the initial 16 hours of culturing (at 0, 4 and 16 hours). Scale bars represent 250 µm. (**d**) Sizes of condensed spheroids at 48 hours (*n* = 506 spheroids, from 6 plates, from 3 independent experiments). Data are mean ± SD.

Cellular droplets produced using a setting of 250 nL in the Mosquito software had an average diameter of 927 µm (SD 19.91 µm, *n* = 70) on the day of production. Cells within hydrogel droplets aggregated to form compact spheroids with an average diameter of 298 µm (SD 23 µm, *n* = 506) two days post-fabrication (**Figure 3.3d**). Of the volume settings tested, it was found that the 250 nL setting generated the most reproducible sized droplets (lowest CV, **Table 3.1**), which in turn gave the most consistent spheroid sizes 48 hours post-production.

The reproducibility of the automated spheroid production system was demonstrated by the consistency of spheroid sizes across multiple plates (**Figure 3.3d**).

3.3.2 Spheroid culturing and cell viabilities

High-throughput media changes for the spheroid cultures was enabled by using the automated Assist Plus liquid handling system. At the start of culturing, spheroids were embedded in hydrogel spheres. After 2 to 3 days, the majority of spheroids had dislodged from the droplets and were free-floating in the ULA plates (**Figure 3.4**). Whilst useful for providing an initial support scaffold for cellular aggregation, the hydrogel is likely remodelled by factors secreted by the SVF-derived cells, and was not needed for the long-term maintenance of spheroids.

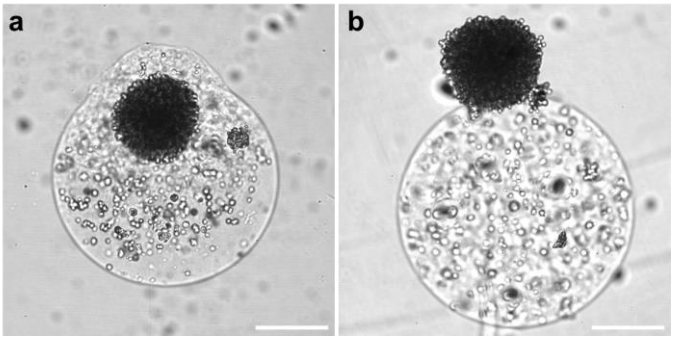


Figure 3.4. Representative bright field images of spheroids dislodging from hydrogel spheres. Spheroids were observed to dislodge from the hydrogel spheres during culturing. (**a**) Spheroid embedded in hydrogel droplet and (**b**) dislodged from droplet after two days. Scale bars represent 250 µm.

It was considered that larger sized spheroids, exceeding 200 µm in diameter, may display increased cell death at the core due to limited oxygen and nutrient availability. This is a common issue in larger 3D tissue models lacking a perfusion environment. Therefore, spheroids were generated at 100 nL, 150 nL, 200 nL and 250 nL dispensing settings to carry out a viability assay using the high-content imager (described in **2.3.1**). This assay had been validated and optimised prior to my project characterising the viability of 3T3-L1 spheroids.

Two days after droplet dispensing, spheroids were induced to undergo adipogenic differentiation (described in **3.2.2**), with cell viabilities measured on days 0 and 7. **Figure 3.5** shows that the SVF-derived spheroids had high cell viabilities at both time points, regardless of droplet production volume.

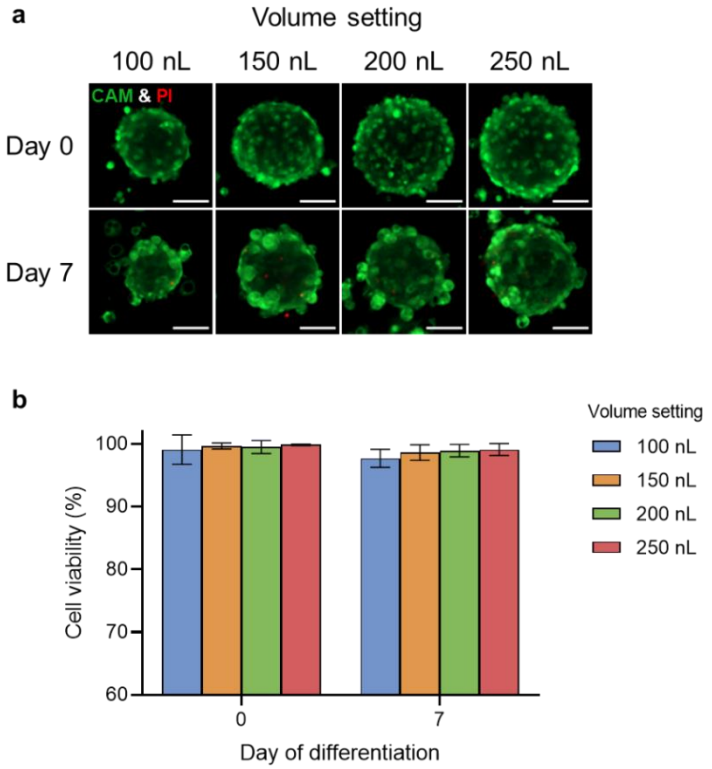


Figure 3.5. Cell viability assessment of spheroids generated using the Mosquito instrument at 100, 150, 200 and 250 nL dispense volumes. (**a**) Representative fluorescence micrographs of spheroids fabricated at volume settings (set in the Mosquito software), acquired using a high-content imager. Spheroids were stained for live cells (CAM, green) and dead cells (PI, red). Scale bars represent 100 µm. (**b**) Viability measurements of spheroids measured by high-content imaging on days 0 and 7 of adipogenic differentiation (n = 8-13 spheroids per volume setting). Data are mean ± SD.

Based on the assay results, the 250 nL setting was found to be optimal for reliably producing healthy spheroids with consistent formation, therefore this was selected as the setting for future experiments. Fabrication of smaller sized spheroids (100 nL setting) was ruled out due them being easily lost during liquid handling and prone to disaggregation.

3.3.3 Investigating cell types present within undifferentiated spheroids

Given that the spheroids were derived from SVF, which consists of a mixture of different cell types, I performed immunofluorescence staining to better understand the cellular composition using undifferentiated (day 0) spheroids (described in **3.2.4**). Confocal imaging detected cytoplasmic staining of alpha-smooth muscle actin (α-SMA) (**Figure 3.6**), indicating spheroids contained perivascular cells. CD34 was used as a marker for ASCs, however staining results are not presented due to high fluorescent background signal affecting image quality.

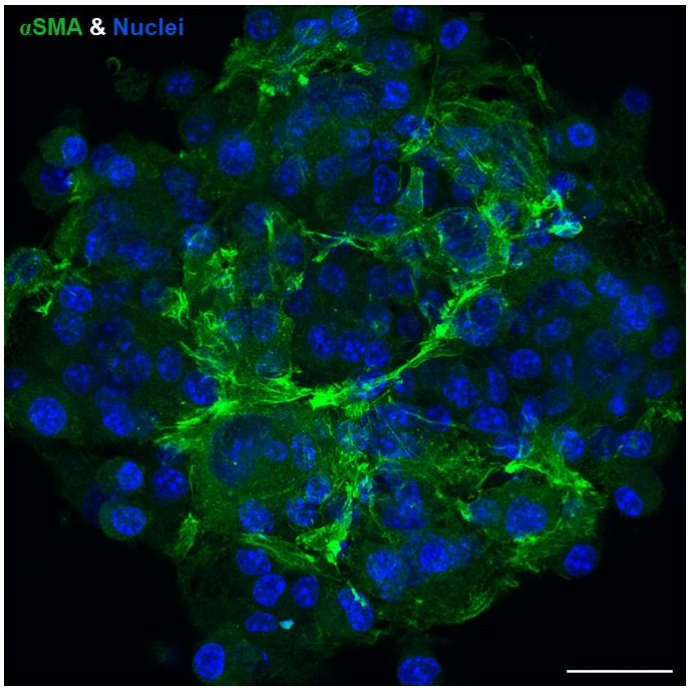


Figure 3.6. Immunofluorescence staining of undifferentiated SVF-derived spheroid. Confocal image (maximum intensity projection) of day 0 spheroid stained with anti-α-SMA antibody (green) and Hoechst 33342 (blue). Scale bar represents 25 µm.

3.3.4 Assessment of adipogenesis

To assess the ability of spheroids to undergo adipogenic differentiation, lipid droplet and nuclei staining with BODIPY 493/503 and Hoechst 33342, respectively, was performed on days 0, 7 and 14 of differentiation (**Figure 3.7**). Preadipocyte spheroids had successfully undergone adipogenesis, as evidenced by the formation of lipid droplets, with minimal change in spheroid sizes; whereas lipid droplets were absent in undifferentiated control spheroids with their size decreasing over the same period.

High-content imaging is a powerful tool using automated image acquisition and data analysis, enabling high-throughput phenotypic characterisation. This technique was used to assess the lipid phenotype (i.e. lipid fluorescence signal area normalised to nuclei signal area) of spheroid cultures during differentiation (described in **2.3.2**). The relative lipid signal remained low for undifferentiated samples throughout the 14 days, as expected (**Figure 3.7b**).

On day 7, differentiated samples had an average relative lipid signal of ~114% (SD 18.6%, n = 43), decreasing to ~92% on day 14 with greater variability (SD 34.2%, n = 9). The increased variability (increase in SD from day 7 to 14) in the lipid phenotype could be, in part, attributed to the reduced integrity of the adipocyte spheroids (i.e. increasing fragility with the progression of differentiation). The differentiated spheroids also became buoyant due to increased lipid content and samples were more easily lost at this stage during liquid handling. To mitigate this issue, I reduced the aspiration and dispensing speeds of the automated liquid handling robot in future experiments.

On day 7, differentiated adipose spheroids had a consistent morphology of lipid-laden cells in a central core surrounded by undifferentiated cells at the edges (**Figure 3.7a** and **Figure 3.8**); viability measurements at this time point indicated that these cells were not dead (**Figure 3.5**). This is consistent with the morphology observed on day 28 of differentiation by the Cox group in the 3T3-L1 adipose spheroid model; this could be due to adipocyte dedifferentiation or reorganisation/migration of undifferentiated cells to the outside. Interestingly, in my work using

SVF-derived cells, the opposite pattern of cell organisation was seen on day 14 compared to day 7, with the spheroid core lacking lipid droplets and differentiated cells located around the edges (**Figure 3.7a**).

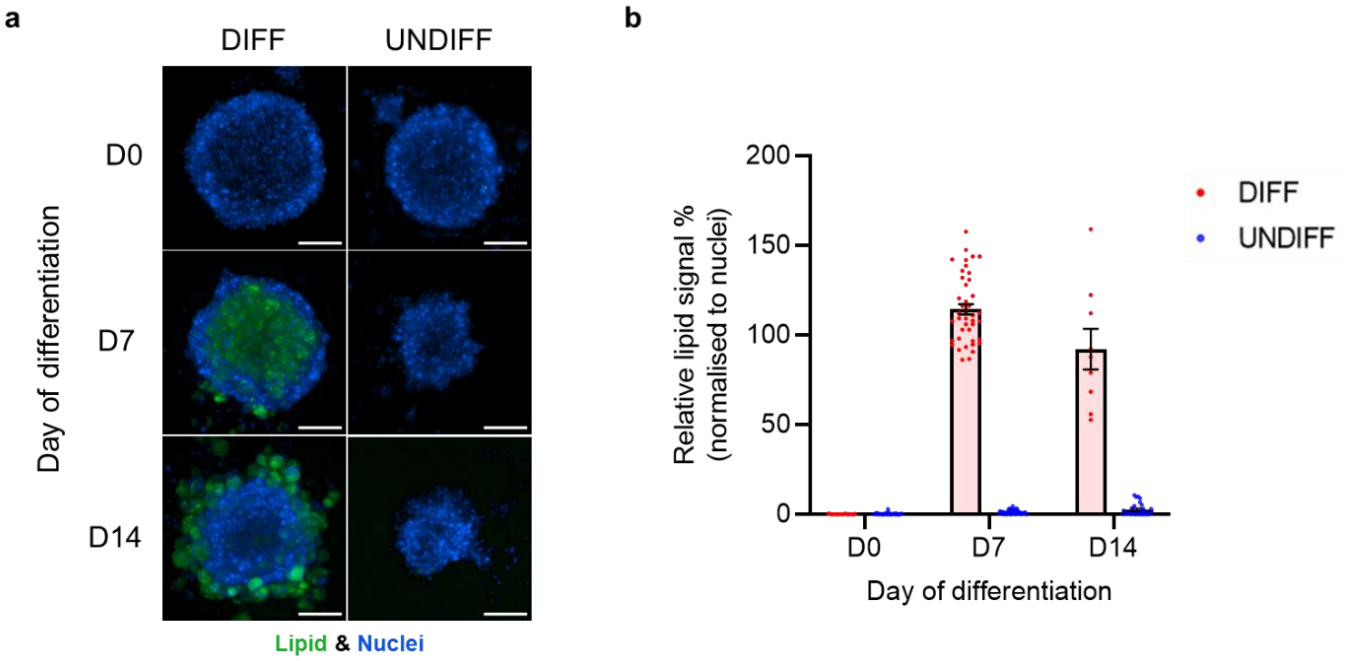


Figure 3.7. Lipid phenotyping of spheroids during adipogenesis. (a) Representative fluorescence micrographs of differentiated (DIFF) and undifferentiated (UNDIFF) spheroids on days 0, 7 and 14 of adipogenic differentiation acquired with the Cytation1 high-content imager. Spheroids were stained for lipid droplets (BODIPY 493/503, green) and nuclei (Hoechst 33342, blue). Scale bars represent 100 µm. (**b**) Quantification of lipid fluorescence signal area (normalised to nuclei signal area) measured by high-content imaging. *n* = 9-43 spheroid singlets per time point. Data are mean ± SEM.

I next utilised confocal and light sheet fluorescence microscopy to investigate lipid droplet morphologies of cells within spheroids fixed throughout differentiation. Demarcation of cells by staining plasma membranes (described in section **3.2.5**) revealed that spheroids contained multilocular adipocytes with heterogeneous lipid droplet sizes, ranging up to ~20 µm (**Figure 3.8**). Detailed assessment of the lipid droplet morphology of inner cells was limited due to the thickness of the sample which restricted light and/or dye penetration. Light sheet microscopy offers several advantages over confocal for high-resolution imaging of thick 3D samples, such as minimal photobleaching (Dyer, *et al*., 2022). This technique was therefore also used to image a set of spheroid samples differentiated under various conditions (**Figure 3.9**).

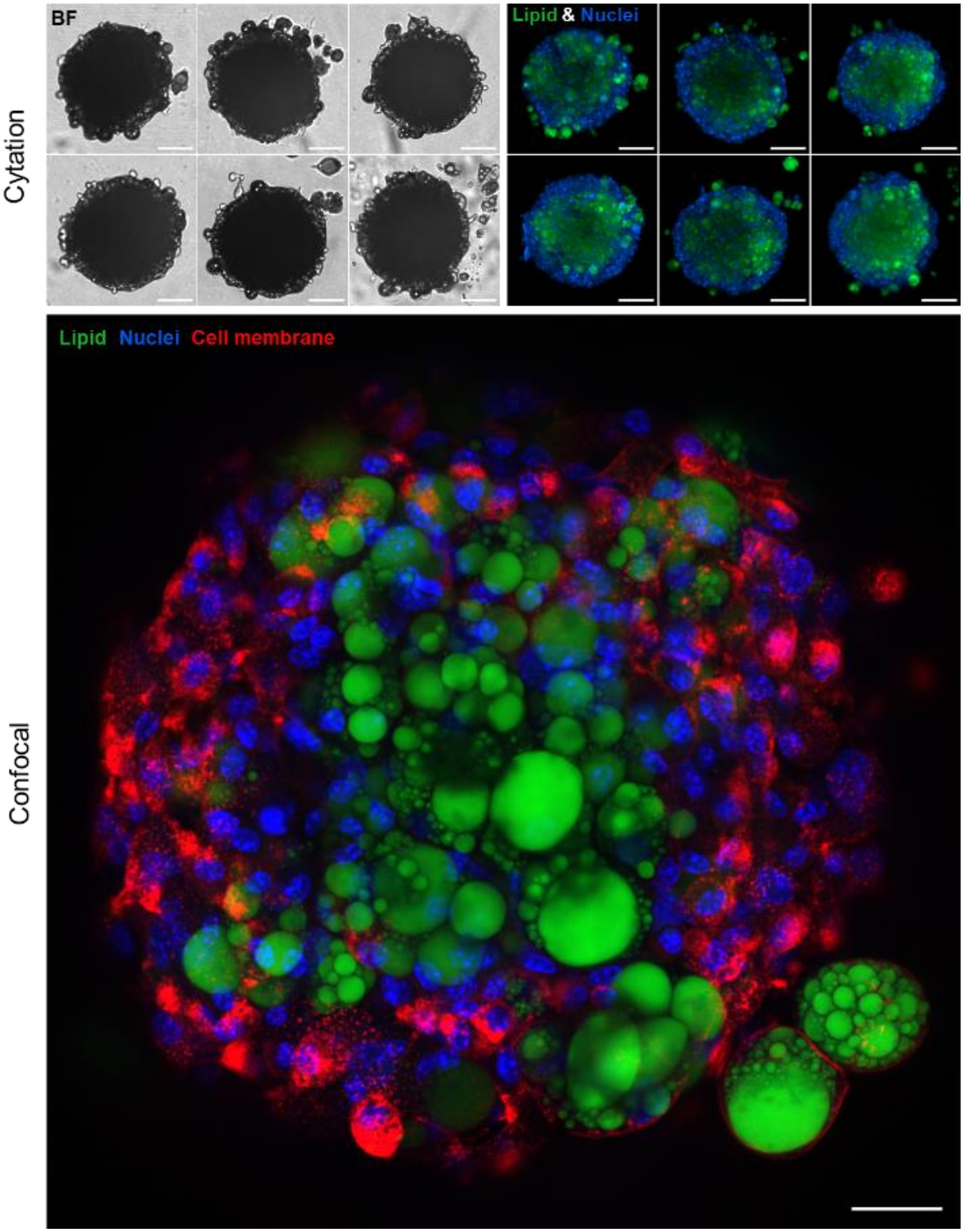


Figure 3.8. Spheroid lipid droplet morphologies on day 7 of differentiation. Upper images: Representative bright field and fluorescent micrographs of differentiated adipose spheroids on day 7, acquired with a high-content imager (Cytation1). Scale bars represent 100 µm. Lower image: Representative confocal image (maximum intensity projection) of a day 7 adipose spheroid. Staining was performed for lipid droplets (BODIPY 493/503, green), nuclei (Hoechst 33342, blue) and the cell membrane (Alexa Fluor 594 wheat germ agglutinin, red). Scale bar represent 25 µm.

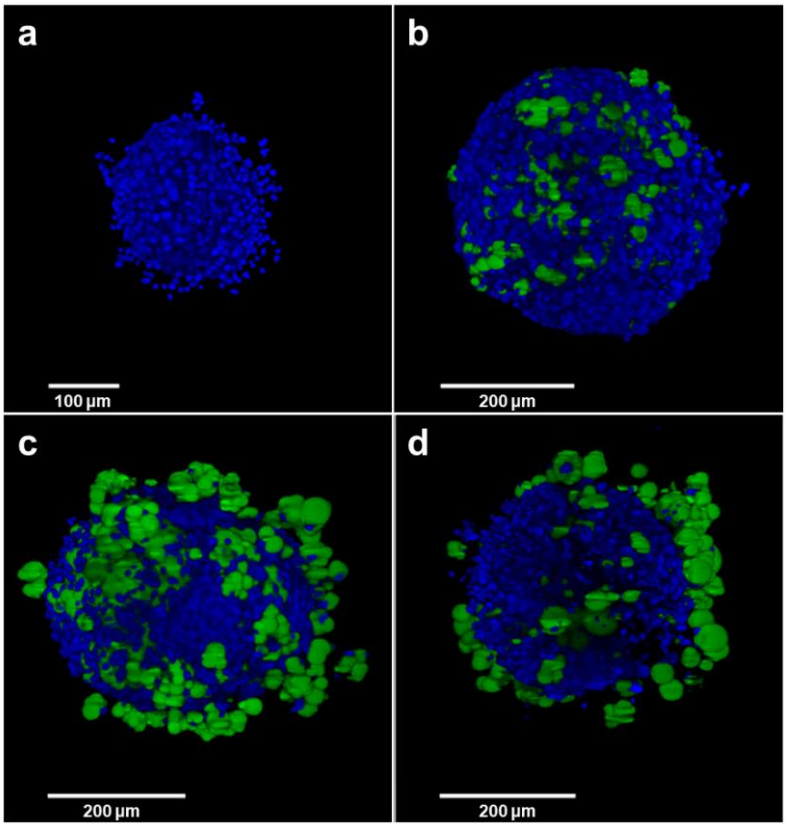


Figure 3.9. Light sheet fluorescence microscopy images (3D rendering) of fused spheroid triplicate models on day 14 of differentiation. Spheroids were cultured as triplicates (three per well) and treated under four different conditions: (**a**) undifferentiated (in preadipocyte growth media), (**b**) standard adipogenic cocktail (AC), (**c**) AC with high insulin (860 nM), or (**d**) AC without brown adipogenesis-promoting factors T3 (triiodothyronine) and indomethacin. Due to fusion of the spheroid triplicates, a single spheroid is shown for each condition. Spheroids were stained for lipid droplets (BODIPY 493/503, green) and nuclei (Hoechst 33342, blue). Light sheet imaging was performed by Dr Robert Lees at the Central Laser Facility. Scale bars are indicated in the images.

3.3.5 Secreted metabolite and adipokine concentrations

Media samples were collected during differentiation (standard adipogenic cocktail) to verify functional aspects of the adipose spheroids, by measuring the secreted metabolite and adipokine concentrations (described in section **3.2.3**). Spheroid triplicate samples (three spheroids per well) were used to increase the number of cells and concentration of secreted factors available for detection. During differentiation, the spheroid triplicates were often observed to fuse together to form one larger spheroid.

Concentrations of glycerol and FFAs in the media were measured to assess the rate of basal lipolysis (**Figure 3.10**). There was an increase in glycerol concentrations during differentiation (**Figure 3.10a**), but not in the levels of FFAs which had insufficient concentration levels for detection. This could be due to the FFAs from lipolysis being re-esterified to form TGs, whereas the lack of glycerol kinase expression in adipocytes prevents recycling of glycerol. Since insulin, which suppresses lipolysis and promotes lipogenesis, was included in the adipogenic differentiation media, these results were expected.

ELISAs were used to measure the concentrations of key adipocyte hormones, leptin and adiponectin. The concentration of secreted leptin from spheroids was minimal and effectively undetectable (data not shown), whereas adiponectin levels were determined to be 68.08 ng/mL (S.D. 8.76 ng/mL) and 45.29 ng/mL (S.D. 5.25 ng/mL) on days 7 and 10, respectively (**Figure 3.10b**). The low level of leptin secretion was consistent with the Cox group's previous findings for the 3T3-L1 adipose spheroids.

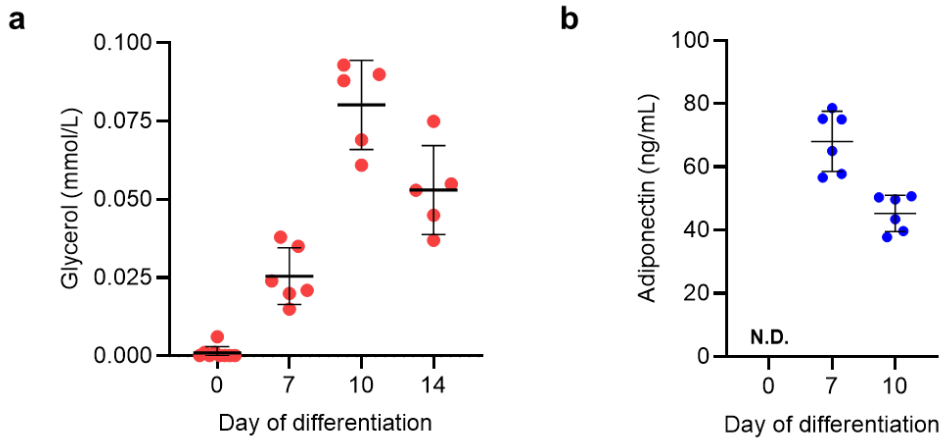


Figure 3.10. Quantification of glycerol (a) and adiponectin (b) in 48-hour conditioned media from differentiated adipose spheroids. *n* = 5-6 spheroid triplicates per time point. Data are mean ± SD. N.D.: not determined.

3.3.6 Investigating adipogenesis using global heterogeneous *Rreb1* knockout mice

Having established a process for automated adipocyte spheroid production, I aimed to apply it to study the T2D-associated gene *Rreb1* (Ras-responsive element binding protein 1). *Rreb1* encodes a zinc finger transcription factor linked to ectopic fat distribution and T2D in GWA studies and is expressed in several relevant tissues, including the pancreas, adipose tissue, and skeletal muscle (Mattis, *et al*., 2023). However, its role in metabolism and adipose tissue development remains unclear.

3.3.6.1 Quantification of adipocyte sizes in mouse WAT depots

To investigate the impact of *Rreb1* loss on adipose tissue development *in vivo* the Cox group, together with our collaborators (Gloyn and Krentz research groups), generated and characterised global heterozygous *Rreb1* knockout (*Rreb1*$^{+/-}$) mice. These mice displayed sex- and diet-dependent changes in adipose tissue mass and adipocyte size (Yu, *et al*., 2024). The Cox group previously found that male *Rreb1* haploinsufficient mice, fed on a regular RM3 chow diet (11% fat, 27% protein, 62% carbohydrates), displayed a higher frequency of smaller adipocytes in several adipose depots (**Figure 3.11**); this suggested a partial failure towards adipogenesis.

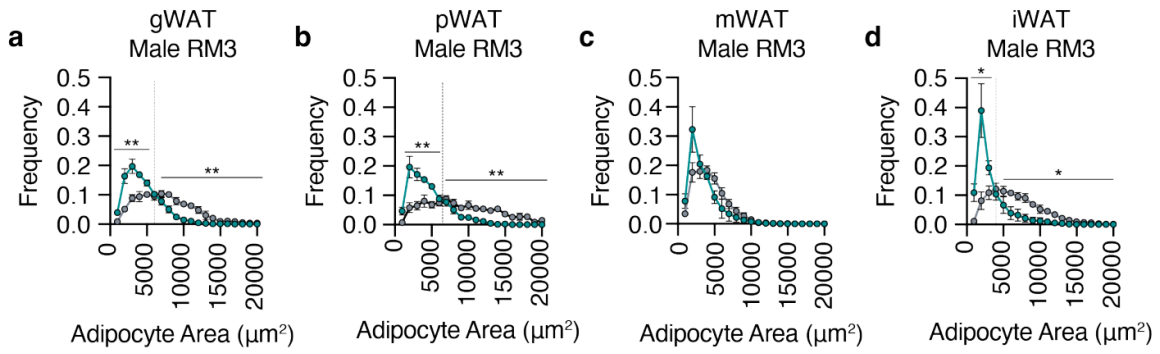


Figure 3.11. Male *Rreb1* haploinsufficient mice display depot-specific reductions in adipocyte size (unpublished data (Yu, *et al*., 2024) from the Cox group). a-d Quantification of adipocyte area (µm^2) within (**a**) gonadal visceral (gWAT), (**b**) perirenal (pWAT), (**c**) mesenteric (mWAT), and (**d**) inguinal subcutaneous (iWAT) fat depots from 38 week old male *Rreb1*$^{+/+}$ (grey symbols) and *Rreb1*$^{+/-}$ (green symbols) mice, fed on a standard RM3 diet. Dotted line denotes the interval where the dataset converges. (**a**) n = 3, 4; (**b**) n = 3, 4; (**c**) n = 3, 3; and (**d**) n = 3, 5 *Rreb1*$^{+/+}$ and *Rreb1*$^{+/-}$, respectively. Statistical analyses were performed by unpaired t test of the area under the curve (AUC) for adipocytes (**a**) 6,000 µm^2 or (**b**) 7,000 µm^2 , or (**c**) 4,000 µm^2 or (**d**) 4,000 µm^2. Data are shown as mean adipocyte frequency within each 1,000 µm^2 sized bin with standard error (SE). *p<0.0001.

To further investigate effects of *Rreb1* haploinsufficiency on adipocyte development, I quantified adipocyte sizes in histological sections of subcutaneous (iWAT) and visceral (gWAT) adipose tissue depots from *Rreb1* heterozygous mice fed on either a high-fat diet (HFD: 60% fat, 20% protein, 20% carbohydrates) or control low-fat diet (LFD: 10% fat, 20% protein, 70% carbohydrates) (**Figure 3.12**). Adiposoft software was used for semi-automatic quantification of adipocyte sizes (described in **3.2.7**).

In inguinal subcutaneous depots, female mice on a HFD had a higher proportion of small adipocytes (area < 4,500 μm^2) in *Rreb1* heterozygotes than in wild-type (WT) colony-mates (p=0.0064), however in these same mice the frequency of large adipocytes (area > 5,250 μm^2) was increased (p=0.0089) in WT animals (**Figure 3.12a**). Interestingly, these differences were not observed in male mice (**Figure 3.12b**), which were previously found to have more smaller subcutaneous adipocytes on the RM3 diet (**Figure 3.11d**). However, it should be noted that the ages of the mice fed a HFD/LFD (29 weeks old) differed to those examined on the RM3 diet (38 weeks old).

In perigonadal visceral depots, female mice on a HFD did not show any genotype differences in adipocyte cell areas (**Figure 3.12c**). In contrast, in male mice there were less smaller adipocytes in heterozygotes than WT (p<0.0001), and more larger adipocytes in heterozygotes than WT (p<0.0001) colony-mates (**Figure 3.12d**). Thus, male *Rreb1* heterozygotes on HFD had a greater number of larger visceral adipocytes than WT mice.

No genotype differences were found in mice on a LFD in either subcutaneous or visceral depots for both sexes (data not shown), and in general showed more smaller adipocytes than in mice fed a HFD. Together, this work indicates sexually dimorphic, depot- and diet-specific effects of *Rreb1* haploinsufficiency on adipocyte size. Male *Rreb1*$^{+/-}$ mice showed a metabolically unfavourable hypertrophic gondal response to HFD feeding, whereas female heterozygotes may retain more hyperplastic capacity. These findings gave impetus to further studies using the 3D spheroid model to investigate adipocyte lipid droplet formation during adipogenic differentiation.

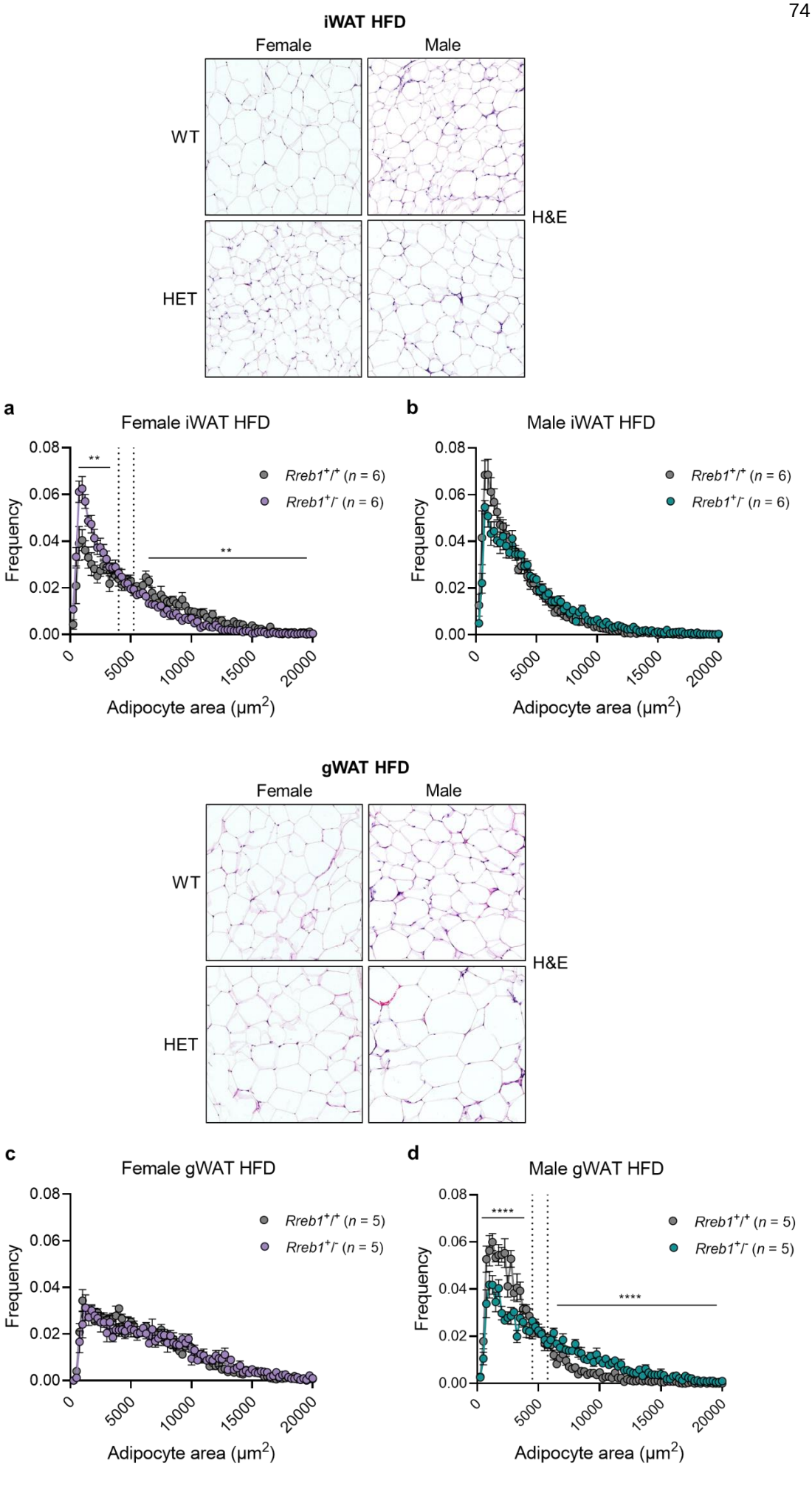

iWAT HFD
Female
Male
WT
HET
H&E
a
Female iWAT HFD
b
Male iWAT HFD
Frequency
Adipocyte area (μm2)
Rreb1+/+ (n = 6)
Rreb1+/- (n = 6)
**
gWAT HFD
c
Female gWAT HFD
d
Male gWAT HFD
Rreb1+/+ (n = 5)
Rreb1+/- (n = 5)
****

Figure 3.12. Relative frequency of adipocyte areas in *Rreb1* heterozygous knockout mice on a 60% high-fat diet (HFD) within 250 µm^2 bin divisions. Representative H&E-stained images of adipose tissue used for adipocyte area quantification are shown. (**a and b**) Adipocyte areas within **inguinal subcutaneous depots (iWAT)** from (**a**) female and (**b**) male mice. Wild-type (*n* = 6) and heterozygous (*n* = 6) mice were fed a HFD and data collected at 29 weeks of age. (**a**) Dotted lines denote the interval where the datasets converge. For adipocytes in bins < 4,500 µm the area under the curve (AUC) was larger in female heterozygotes (27.13% ± 7.91% (SE) more cell area) than wildtypes (*p*=0.0064, unpaired two tailed t-tests) and for adipocytes in bins > 5,250 µm the AUC was larger for female wild-types (37.27% ± 11.52% more cell area) (*p*=0.0089, unpaired two tailed t-tests). Overall, the AUC for all bins was not significantly different between the two genotypes (*p*=0.8182, Mann-Whitney two tailed test). (**b**) No differences between genotypes in males were observed for AUC in bins < or > than 4,500µm or for the entire dataset (*n* = 6 wild-type and 6 heterozygotes, *p*=0.2403, 0.1797, 0.7381 Mann-Whitney test). (**c and d**) Adipocyte areas within **perigonadal visceral depots (gWAT)** from (**c**) female and (**d**) male mice. Wild-type (*n* = 5) and heterozygous (*n* = 5) mice were fed a HFD and data collected at 29 weeks of age. (**c**) No differences between genotypes in females were observed for AUC in bins smaller or larger than 4,500 µm or for the entire dataset (*p*=0.1617, 0.1979 unpaired two tailed t tests and 0.4206 Mann-Whitney test). (**d**) Dotted lines denote the interval where the two datasets converge. For adipocytes in bins < 4,500 µm the AUC was larger in wild-types (33.5% ± 3.45% (SE) more cell area) than heterozygotes (*p*<0.0001, unpaired two tailed t-tests), and for adipocytes in bins larger than 5,750 µm the AUC was larger in heterozygotes (56.93% ± 5.44% more cell area) than wild-types (*p*<0.0001, unpaired two tailed t-tests). Overall, the AUC for all bins was also higher in heterozygotes (overall a difference of 1.19% ± 0.16% (SE) more cell area) than wild-types (*p*<0.0001 unpaired two tailed t test). Data are shown as mean adipocyte frequency within each 250 µm^2 sized bin with standard error. ***p*<0.01, *****p*<0.0001.

3.3.6.2 Characterisation of Rreb1 haploinsufficient spheroids

To test whether primary *Rreb1* haploinsufficient cells cultured in a 3D environment displayed defects in adipogenesis, SVF cells sourced from iWAT of male *Rreb1*$^{+/-}$ and WT mice were used for spheroid fabrication (*n* = 3 mice per genotype). The RM3 diet-fed mice were used, as it was from this cohort that the smaller adipocytes had been previously observed in iWAT (**Figure 3.11**).

Cellular droplet sizes were consistent between genotypes on the day of biofabrication (**Figure 3.13a**), further demonstrating the reproducibility of this system. Cells condensed within the hydrogel droplets forming uniform spheroids on day 0, with no size difference between genotypes (**Figure 3.13c**). On day 4 of differentiation *Rreb1* haploinsufficient spheroids were significantly smaller than WT spheroids (*p*<0.05), and continued to reduce in size through to day 7 (*p*<0.005), until adipogenesis was deemed complete (**Figure 3.13b, c**).

Lipid phenotyping by high-content imaging found that *Rreb1* haploinsufficient spheroids had lower lipid signal area compared to WT samples (**Figure 3.13d**), although this was not statistically significant (p=0.0697); possibly due to the number of biological replicates. Due to the difference in spheroid sizes between genotypes, normalisation of lipid signal to nuclei signal area was not undertaken. Confocal imaging also showed fewer and smaller sized lipid droplets in *Rreb1* haploinsufficient spheroids compared to WT samples on day 7 (**Figure 3.14**). These results demonstrate that the spheroid system replicated an *in vivo* phenotype (i.e. smaller sized adipocytes in iWAT of male *Rreb1*$^{+/-}$ mice on RM3 diet), most likely dependent on a partial failure in adipogenesis.

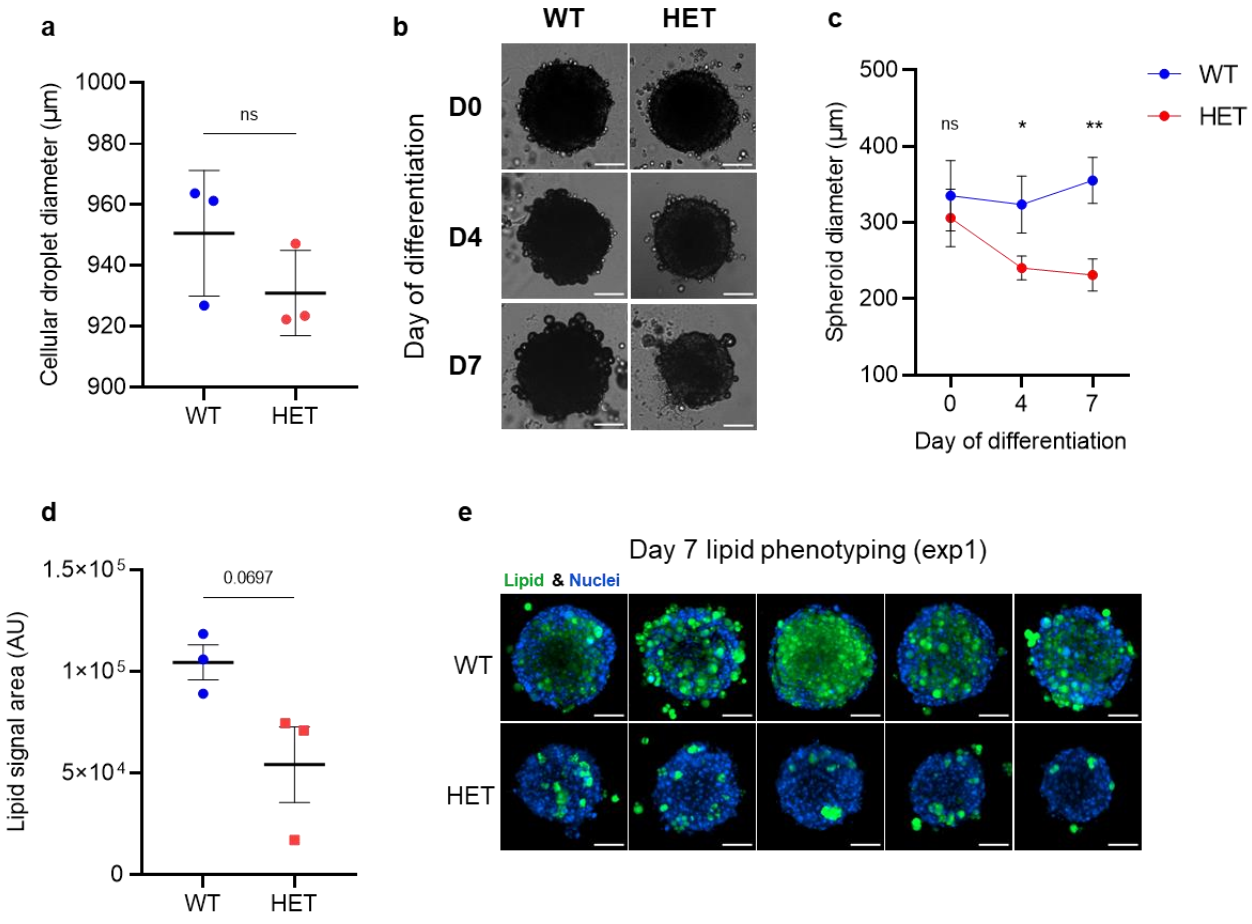


Figure 3.13. Characterisation of *Rreb1* haploinsufficient spheroids during adipogenesis. (**a**) Cellular droplet sizes on the day of biofabrication (day -2). (**b**) Representative bright field micrographs of *Rreb1* haploinsufficient and wildtype spheroids on days 0, 4 and 7 of differentiation. Scale bars represent 100 µm. (**c**) Spheroid sizes on days 0, 4 and 7 (from three independent experiments, with 14-35 spheroids each, n = 3 mice per genotype). (**d**) Lipid signal area quantified by high-content imaging in fluorescence micrographs, from independent three experiments for wildtype (n = 11-20) and *Rreb1* haploinsufficient (n = 20-28) spheroids on day 7 (n = 3 mice per genotype). Data are mean ± SEM. Statistical analyses were performed by unpaired t test (**a and d**) or two-way ANOVA (**c**). ns, non-significant; p*<0.05; p*<0.005. (**e**) Representative fluorescence micrographs of day 7 adipose spheroids (from experiment 1) recorded by high-content imaging. Scale bars represent 100 µm. Lipid droplets, BODIPY 493/503; nuclei, Hoechst 33342.

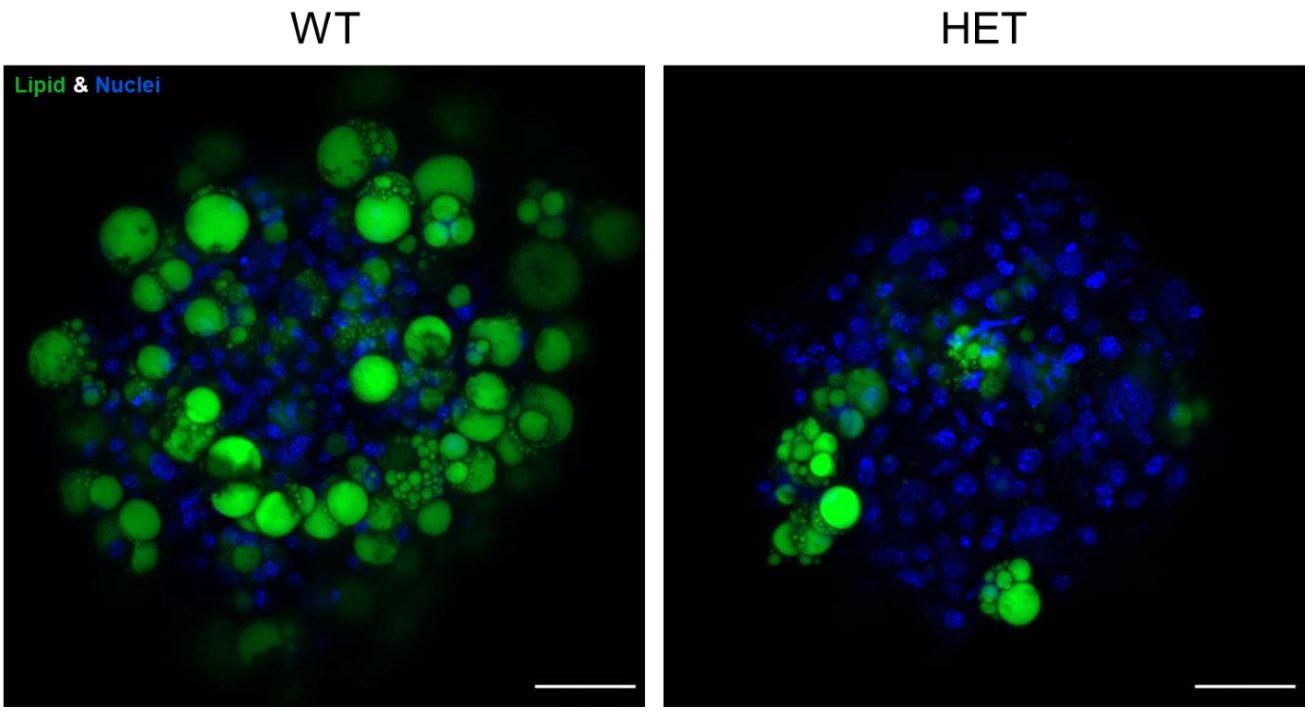


Figure 3.14. Confocal imaging of *Rreb1* haploinsufficient spheroids on day 7 of adipogenesis. Lipid droplets, BODIPY 493/503; nuclei, Hoechst 33342. Scale bars represent 50 µm.

3.4 Discussion

In this work, my aim was to develop our group's initial 'droplet-in-oil' spheroid production method for the high-throughput fabrication of mouse adipose spheroids, and test this in a mouse model with a whole-body adipose tissue phenotype. This was achieved utilising automated robotic liquid handlers and changing the cell source to primary preadipocytes, followed by testing the system in the *Rreb1* heterozygous KO model. The reproducible spheroid sizes and the expeditious generation of cellular droplets overcame several limitations of our group's previous manual method.

The 3T3-L1 cell line (previously used in the method) is a widely used preadipocyte model derived from mouse embryonic fibroblasts, and being immortalised can be used to generate large quantities of cells, enabling multiple rounds of experimentation. However, this cell line is not truly representative of *in vivo* tissue, consisting of a homogenous cell population. My choice to adopt the use of primary preadipocytes was due to the heterogeneous nature of SVF cells (which contain a variety of cell types), potentially better reflecting *in vivo* adipose tissue composition.

Due to my method requiring a high number of cells for re-suspension in the hydrogel, it was necessary to combine cells from several mice if fabricating multiple plates of spheroids. The use of freshly isolated as opposed to cultured SVF cells (which reduces heterogeneity) could further enhance the complexity of the model. Despite this, αSMA^{+} cells were still observed in the undifferentiated spheroids, indicating the presence of perivascular cells after *in vitro* expansion of SVF cells. The use of freshly isolated SVF could provide a source of immune cells, but this method would require sacrificing an even greater number of animals to obtain sufficient cell quantities.

It has been shown in several studies that a 3D culture environment promotes the formation of large or unilocular lipid droplets (Emont, *et al*., 2015) (Klingelhutz, *et al*., 2018). Assessment of lipid droplet morphology revealed that spheroids differentiated to day 7 contained

adipocytes with multilocular lipid droplets, notably larger than those typically found in 2D culture. As my focus was workflow automation, 2D control cells were not included.

Quantification of adipokines in culture media revealed that differentiated spheroids secreted adiponectin, but not leptin. Similar results for 3T3-L1 spheroids were previously observed by our group, who measured adipokine concentrations in cell lysates to determine whether reduced secretion was due to protein entrapment within the spheroid matrix. It was shown that the lysates contained higher levels of leptin and adiponectin compared to supernatant samples collected from intact spheroids. However, regardless of whether the spheroids were intact or lysed, 3D cultures exhibited lower adipokine concentrations compared to 2D. This suggests these proteins may either be trapped in the spheroid matrix or their production is naturally reduced in a 3D environment. Interestingly, low leptin release has also been observed in other 3D WAT models derived from both mouse (Wolff, *et al*., 2022) and human (Ioannidou, *et al*., 2022b) preadipocytes, indicating that 3D culture may limit or delay leptin production, although the mechanisms behind this are unclear.

The majority of 3D adipose culture models published to date are manually produced and/or low-throughput, with just a handful of large-scale automated models. A different method to ours, the hanging drop technique, was used by Klingelhutz *et al*. (2018), in the high-throughput generation of scaffold-free SVF spheroids, although this lacked automation. The scaffold-based approach utilised in my work, incorporating a hybrid hydrogel-matrix made from both natural and synthetic polymers, provided cells with an artificial ECM, promoting cellular aggregation. Inclusion of type I collagen in the hydrogel provides potential cell adhesion sites, facilitating cellular attachment and migration, while the Fmoc-dipeptides act to strengthen it (Graham, *et al*., 2019). Additional ECM factors found in native adipose tissue could be incorporated into the hydrogel to modify its properties, improve spheroid retention within droplets, and enhance similarity to the *in vivo* environment.

During this work, I generated spheroids using SVF from iWAT of *Rreb1* haploinsufficient mice, characterising samples during adipogenic differentiation. A reduction in spheroid size was observed, suggesting that *Rreb1* loss potentially increased cell death, and/or weakened cell-cell adhesion, resulting in disaggregation. Rreb1 is a multifunctional transcription factor involved in tissue architecture maintenance through regulation of cytoskeleton gene expression and adheren junction organisation (Morgani, *et al*., 2021), which may contribute to the reduced differentiation potential observed in cells with reduced *Rreb1* expression; cell-cell contacts are crucial for murine preadipocytes to undergo adipogenesis (Guo, *et al*., 2009).

Loss of *Rreb1* is also likely to reduce differentiation through a reduction in adipogenic gene expression. This is supported by our collaborators showing that silencing *RREB1* expression in human SGBS cells reduces their differentiation capacity and lowers the expression levels of *PPARG* and *CEBPA* (Yu, *et al*., 2024). Consistent with this data, my work also showed a reduced level of adipogenesis in the SVF-derived spheroids, supporting the importance of *Rreb1* in adipocyte development. These results clearly demonstrate the ability of the 3D culture system to capture phenotypic differences, highlighting its potential for mechanistic studies.

3.4.1 Summary

The focus of this work was to demonstrate that adipocyte spheroids could be fabricated at scale (96-well plate) with high-reproducibility. Building on our group's previous research, I developed a system that automates the generation, maintenance and characterisation of adipose spheroids, demonstrating that the process is compatible with primary preadipocytes. The system was validated for use in mechanistic studies using the murine *Rreb1* gene, but it can also be applied to investigate the effects of various genetic modifications on adipogenesis.

I anticipate that future work could focus on analysing the cellular composition of the adipose spheroids using techniques such as immunofluorescence staining and flow cytometry to identify specific cell types. This would support the classification of the model as an 'organoid' if multiple cell types are confirmed to be present. In addition to studying genetically modified preadipocytes, the system could be applied to cells of tissue-specific origin and incorporate other cell types, such as macrophages and endothelial cells, to study cell-cell communication under physiologically relevant conditions. It could also be adapted for high-throughput compound screening using a 384-well plate format.

4 Development of a human adipose tissue depot-specific 3D cell culture model

4.1 Introduction

4.1.1 Background

Following the closure of the Mammalian Genetics Unit at MRC Harwell, I moved to the Metabolic Research Group at OCDEM (University of Oxford) under new supervision. The equipment for spheroid production also moved with me so that the methodology described in **Chapter 3** could be applied to develop human adipose spheroids.

The Metabolic Research Group generated immortalised human preadipocyte cell lines derived from paired abdominal and gluteal adipose tissue biopsies from a male donor (Todorčević, *et al*., 2017). By differentiating these into mature adipocytes, isolating the lipid-rich cells and then dedifferentiating them, adipocyte precursor cells, termed dedifferentiated fat (DFAT) cells, were generated (Loh, *et al*., 2020). I selected these cells for my work as, due to their higher adipogenic potential, they served as a preferred model over primary and immortalised SVF cells to study human adipogenesis *in vitro*. The abdominal and gluteal DFAT cells have also been demonstrated to retain functional characteristics of their depot of origin (Todorčević, *et al*., 2017) (Loh, *et al*., 2020), such as endogenous fatty acid metabolism, providing a useful tool for investigating regional adipocyte biology.

While our group routinely cultures preadipocytes in standard 2D culture, transitioning to 3D could enhance adipocyte differentiation, leading to larger lipid droplets and other functional characteristics more representative of the *in vivo* situation in a tissue.

4.1.2 Chapter aims

The aim of this work was to trial the spheroid production system developed in the murine cells to model human WAT. Specifically, to:

- Optimise automated 'droplet-in-oil' dispensing to generate standardised and reproducible abdominal and gluteal adipose spheroids.
- Characterise undifferentiated and differentiated DFAT spheroids for:
    - Cell viability
    - Size during differentiation
    - Lipid droplet morphology
    - Adipokine secretion

4.2 Specific methods

4.2.1 2D cell plating and staining for lipid droplet imaging

For cell plating, coverslips were sterilised in 70% ethanol and allowed to air dry in a Class II BSC. Once the ethanol had evaporated, a single 12 mm diameter coverslip (VWR, 631-1577) was transferred into each well of a CellBIND 24-well plate using forceps. 500 µL of dilute collagen solution (10 µg/cm^2, Sigma, C4243), was pipetted on the coverslip of each well and incubated for 30 minutes, after which the wells were washed twice with sterile PBS. 1 mL of growth media containing 4 × 10^4 cells was added to each well. The cells were left undisturbed for ~15 minutes to promote even distribution, before being transferred to the incubator (37^{o}C, 5% CO_2).

For cell proliferation and differentiation, approximately 72 hours after plating, confluent preadipocytes were induced to undergo adipogenic differentiation in parallel with spheroid samples, following the protocol outlined in section **2.6**. On day 11 of differentiation, 2D cells were fixed in 4% PFA for 15 minutes in the dark at room temperature. The cells were then washed twice with PBS and stored at 4^{o}C until fluorescent staining.

For staining, 2D cells were incubated with 1 µM BODIPY 493/503 and 4 µM Hoechst 33342 in PBS, protected from light, for 20 minutes. After two washes with PBS, coverslips were mounted onto slides using VECTASHIELD Vibrance Antifade Mounting Medium (Vector Laboratories, H-1700). Images were captured at 60× magnification using an Olympus FluoView FV3000 confocal microscope, with assistance from Jason Tong (OCDEM), using the same imaging settings as those employed for spheroid imaging. For details on spheroid staining and imaging, refer to section **2.3.2**.

4.2.2 Lipid droplet segmentation and size analysis

For segmentation of lipid droplets, the deep-learning segmentation tool Cellpose (Stringer, *et al*., 2021) was used. The pre-trained ‘cyto’ model was selected and then fine-tuned using a ‘human-in-the-loop’ approach, to improve the accuracy of lipid droplet segmentation in the green channel. The object masks were exported to Fiji/ImageJ, with the diameters quantified using the BIOP (bioimaging and optics platform) plugin.

4.3 Results

4.3.1 Optimisation of human preadipocyte spheroid production

Abdominal and gluteal preadipocytes were re-suspended in the ULGTA-based hydrogel solution at three different densities (4×10^7 cells/mL, 2×10^7 cells/mL and 1×10^7 cells/mL), and cellular droplets fabricated at the 250 nL setting using the Mosquito (described in **2.2.1**). Bright field imaging of abdominal and gluteal cellular droplets, three days after production, showed that preadipocytes from both depots had condensed into spheroids at the 4×10^7 and 2×10^7 cells/mL densities (**Figure 4.1**). Poor spheroid formation was observed at the lowest cell density (1×10^7 cells/mL), with the majority of cells failing to condense and remaining embedded throughout the hydrogel droplet.

Viability was assessed via a live/dead cell assay (described in **2.3.1**). Spheroids fabricated at the highest density (4×10^7 cells/mL) were expectedly the largest in size and displayed the lowest cell viabilities (**Figure 4.1**). Abdominal preadipocyte spheroids had the lowest cell viabilities (~41%) and contained necrotic cores; whereas gluteal spheroids of equivalent sizes had higher cell viabilities (~94%), and contained a greater proportion of live cells within the spheroid centre. This suggests that abdominal-derived cells are more sensitive to hypoxia, have higher nutrient requirements, and/or accumulate more metabolic waste products, compared to gluteal cells. This corresponds to the previously reported increased metabolic activity of abdominal over femoral adipose tissue *in vivo* (McQuaid, *et al*., 2010a).

Figure 4.1 shows that abdominal spheroids fabricated at the medium cell density of 2×10^7 cells/mL had cell viabilities of ~75%, compared to gluteal spheroids which were highly viable (~99%). Despite having high cell viabilities (~100%), abdominal and gluteal cellular droplets fabricated at the lowest cell density were not suitable for spheroid fabrication, due to poor condensation and small spheroid formation.

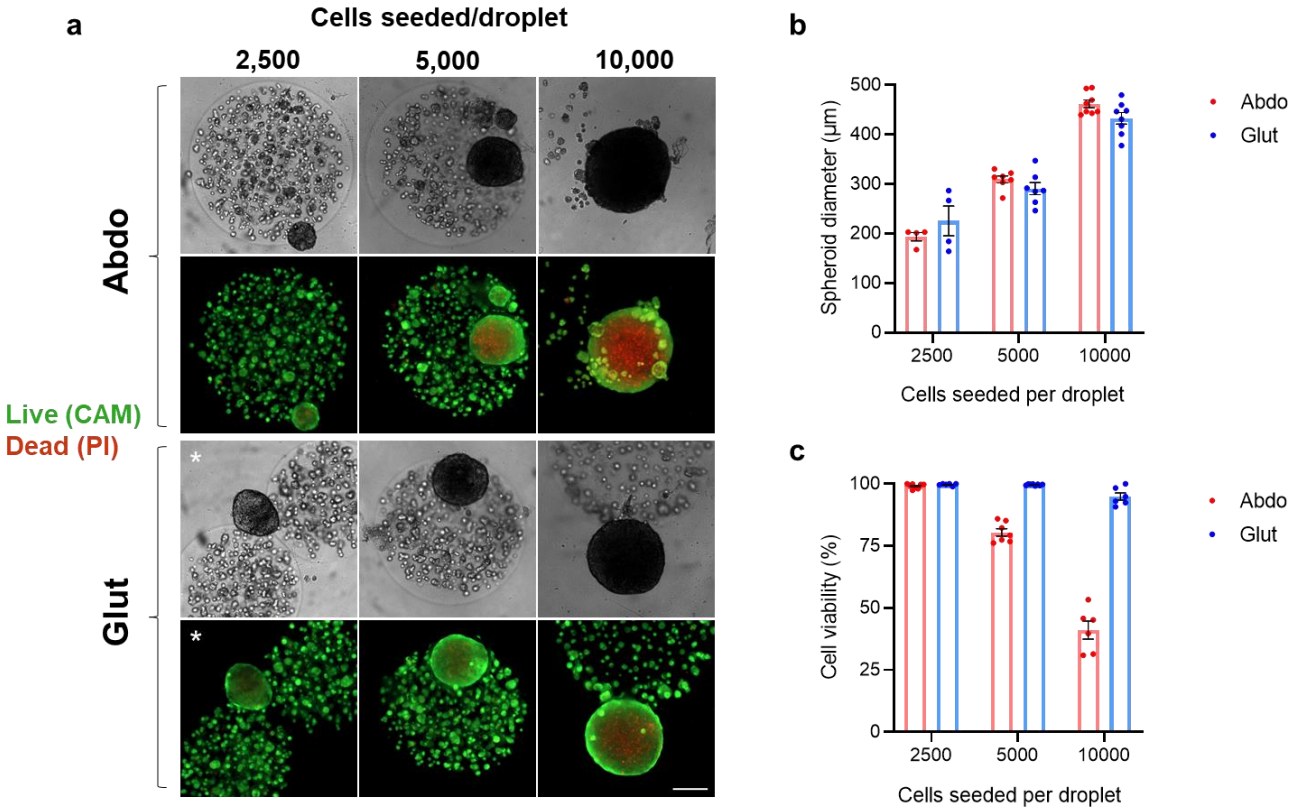


Figure 4.1. Optimisation of human abdominal and gluteal preadipocyte spheroid production. (**a**) Bright field and fluorescent micrographs of human abdominal (Abdo) and gluteal (Glut) preadipocyte spheroids, 3 days after cellular droplet fabrication. Droplets of cellular hydrogel were dispensed (250 nL volume setting) using the Mosquito LV Genomics (SPT Labtech). Prior to dispensing, preadipocytes were re-suspended in the hydrogel at 3 different cell densities: 1×10^7 cells/mL, 2×10^7 cells/mL and 4×10^7 cells/mL, which corresponds to ~2,500, ~5,000 and ~10,000 cells per droplet respectively. CAM, live cells (green); PI, dead cells (red). * Indicates a well where two cellular droplets inadvertently dispensed. Scale bar represents 200 µm. (**b**) Spheroid diameters measured manually from bright field images. (**c**) Cell viabilities determined by high-content imaging for each seeding density. *n* = 4-8 spheroids per condition. Data are mean ± SD.

Further experiments were required to identify the optimal conditions to achieve efficient spheroid formation whilst minimising cell death. Through multiple rounds of spheroid fabrication and viability assessment, I found that both abdominal and gluteal spheroids generated (using a density of 3×10^7 cells/mL and dispensed in the smaller volume of 100 nL) achieved this compromise; this gave good reproducibility in spheroid sizes and samples showing more than 88% cell viability two days post-production (**Figure 4.2**). Therefore, I chose these conditions for future experiments.

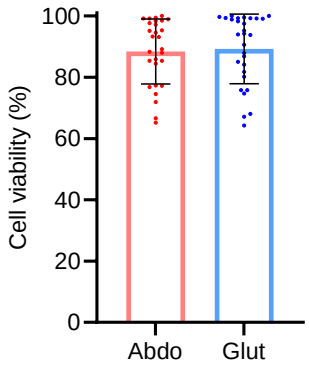


Figure 4.2. Viabilities of abdominal and gluteal preadipocyte 3D cultures two days post-production. Cells were harvested and re-suspended in the hydrogel at **3×10^7 cells/mL**, before dispensing cellular droplets at the **100 nL volume setting** using the Mosquito. After spheroids condensed within droplets, samples were stained with CAM and PI for viability assessment by high-content imaging. *n* = 28-29 spheroids (technical replicates) for each cell line, from 2 independent experiments (biological replicates). DMSO-treated spheroids were used as dead cell controls and were confirmed as such. Data are mean ± SD.

Under these conditions, the hypothetical number of cells seeded per droplet was 3,000, however given that I established the Mosquito overestimates dispensing volumes by ~18% (**Chapter 3**, **Table 3.1**), the actual number of cells likely corresponds to ~3,540. During condensation, a low number of cells remained embedded throughout the hydrogel droplet, forming smaller cell clusters surrounding the main spheroid, referred to as ‘satellite’ cells.

4.3.2 Characterisation of abdominal and gluteal DFAT spheroids during adipogenesis

Having optimised the spheroid production my next aim was to demonstrate successful differentiation of abdominal and gluteal preadipocyte spheroids, for which I used my group's standard adipogenic differentiation protocol (section **2.6**). Two days after droplet production, preadipocyte spheroids were induced to undergo adipogenesis by switching the growth media to differentiation media, using the Assist Plus pipetting robot. From day 4 of adipogenic differentiation, spheroids were treated with or without an exogenous FA mixture enriched in unsaturated FAs, which our lab terms 'OPLA' (Nagarajan, *et al*., 2022). OPLA consists of 45% oleic acid (OA), 30% palmitic acid (PA), 24% linoleic acid (LA) and 1% α-linolenic acid (ALA), designed to reflect the proportion of FAs found in human plasma (Hodson, *et al*., 2008).

Automated bright field imaging using the Cytation showed that abdominal and gluteal spheroids increased in size during differentiation (**Figure 4.3a**). The spheroids tended to remain embedded within the hydrogel droplets throughout culturing, unlike the SVF-derived spheroids in **Chapter 4**, which had a tendency to dislodge. Spheroid sizes were assessed by calculating the relative spheroid volume compared to day 0 (**Figure 4.3b**). On day 7, no significant difference was observed in relative spheroid volume between abdominal spheroids treated with or without FAs. However, by day 11, FA-treated abdominal spheroids showed a significantly greater increase in volume compared to untreated samples ($p<0.0001$). A similar pattern was observed for gluteal spheroids, with FA treatment also resulting in a significant larger increase in relative volume on day 11 ($p<0.0001$).

To confirm preadipocytes had undergone adipogenesis and to assess lipid droplet morphology, samples fixed on days 0 and 11 were fluorescently labelled for lipid droplets and nuclei. Confocal imaging showed spheroids from both depots had successfully differentiated by day 11 (**Figure 4.3c**). Spheroids differentiated without FAs contained cells with multilocular lipid droplets, while, in the FA-treated spheroids, there was a noticeable shift towards larger droplet sizes (although most cells remained multilocular). An unexpected finding was the

observation of regions devoid of cells (cavities) within the day 11 adipose spheroids (**Figure 4.3c**, arrows).

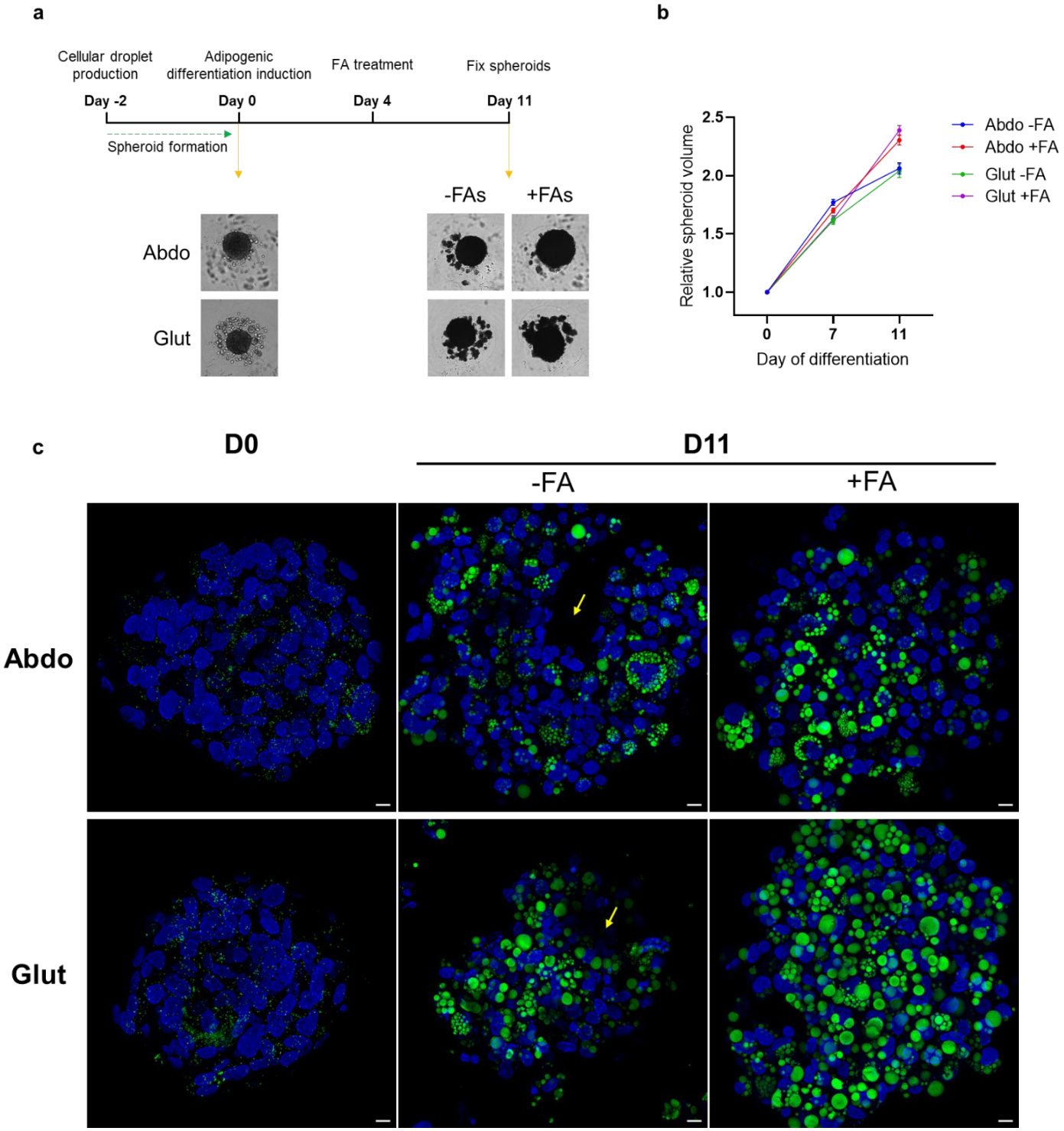


Figure 4.3. Differentiation of human abdominal and gluteal DFAT spheroids. **(a)** Schedule for preadipocyte spheroid formation within hydrogel droplets and adipogenic differentiation. Treatment either with a mixture of fatty acids (+FAs) or without (-FA) was from day 4 onwards. **(b)** Relative spheroid volumes during adipogenesis. *n* = 21-24 spheroids (technical replicates) for each condition, from 3 independent experiments (biological replicates). Data are mean ± SEM. **(c)** Representative confocal images of DFAT spheroids treated with or without fatty acids. Samples were fixed on days 0 and day 11 and stained for lipid droplets (BODIPY 493/503, green) and nuclei (Hoechst 33342, blue). Yellow arrows indicate cavities in spheroids where no cells were present. Scale bars represent 10 µm.

Further high-throughput characterisation of the DFAT spheroids, by high-content imaging, was undertaken to provide a quantitative measure of adipogenesis. The high-intensity lipid signal area (i.e. BODIPY signal area with greater than 30,000 intensity per pixel) was measured in day 11 spheroids, and normalised to the nuclei signal area, as described in section **2.3.2**. The high-intensity lipid signal was higher in gluteal compared to abdominal spheroids, irrespective of FA treatment (**Figure 4.4b**); the same pattern was observed after normalisation to nuclei signal (**Figure 4.4c**). These results were consistent with the confocal images, showing a higher level of differentiation per cell in gluteal samples. Despite gluteal spheroids containing nearly double the lipid content of abdominal spheroids at D11 (**Figure 4.4b, c**), there was no difference in relative spheroid volume between depots (**Figure 4.3b**). These results indicate a difference in how preadipocytes from these two depots expand in 3D culture.

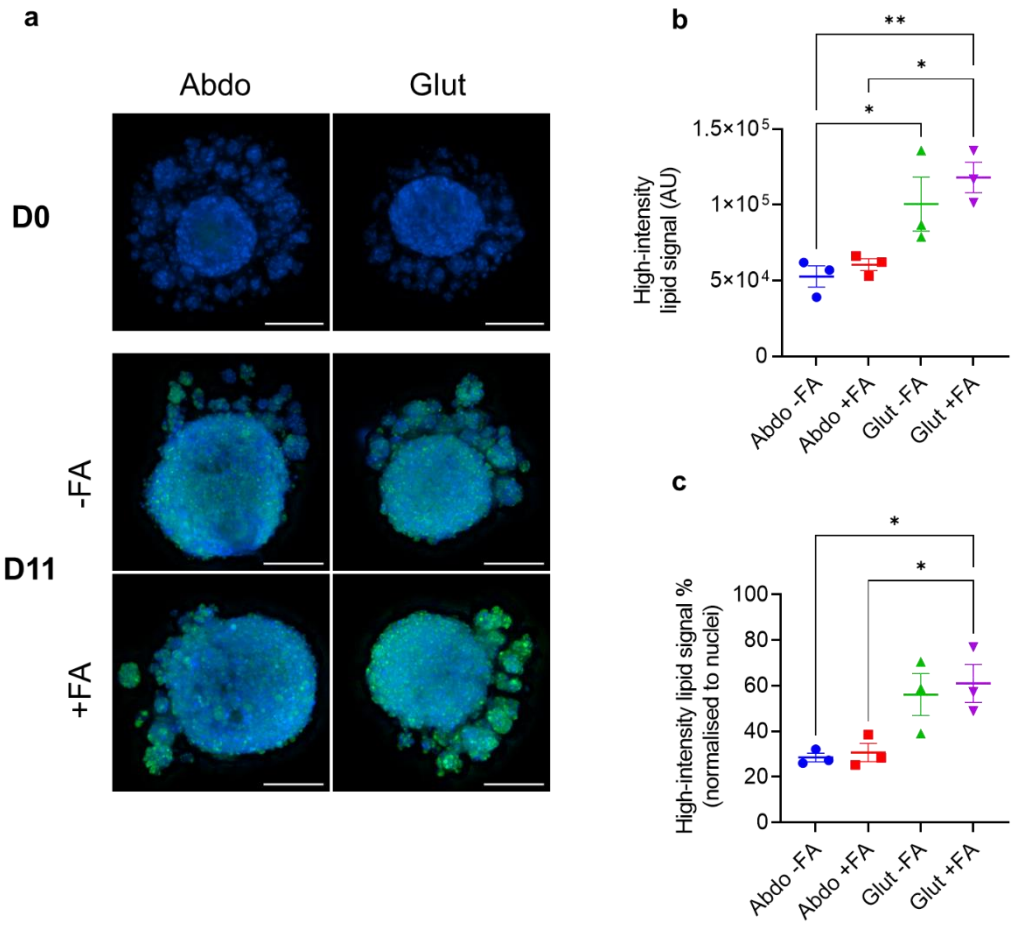


Figure 4.4. Lipid phenotyping of abdominal and gluteal DFAT spheroids. (**a**) Representative fluorescence micrographs of DFAT spheroids during differentiation, treated with (+FA) or without (-FA) fatty acids. Images were captured using a high-content imager. Scale bars represent 200 µm. (**b**) High-intensity lipid signal (signal with greater than 30,000 intensity per pixel) in spheroid samples (n = 8 spheroids per condition, from 3 independent experiments). (**c**) Normalised high-intensity lipid signal area for the same samples. Data are mean ± SD. Statistical analysis was by two-way ANOVA. *p<0.05, **p<0.01.

4.3.3 3D culture improves differentiation of abdominal and gluteal DFAT cells

It was hypothesised that 3D culture would enhance differentiation of adipocyte precursors. In order to evaluate this, I seeded cells in both 2D and 3D cultures which were induced to differentiate simultaneously for direct comparison. **Figure 4.5a** shows that abdominal preadipocytes, differentiated in the absence of exogenous FAs, exhibited poor differentiation in 2D culture by day 11. By contrast, a much improved level of differentiation was observed in 3D spheroid cultures (**Figure 4.5e-h**), with the formation of more numerous lipid droplets, which appeared larger. The most striking of these differences was in the abdominal spheroids without supplemental FA in the medium (**Figure 5e**) compared to 2D controls (**Figure 5a**).

Cellpose software was used to automatically segment lipid droplets and assess their sizes (described in **4.2.2**). There was no significant difference in the average lipid droplet size between 2D abdominal and gluteal cells (depot comparison), when cultured without FAs (**Figure 4.5i, j**). However, it should be noted that since the abdominal cells differentiated poorly, the number of lipid droplets was much lower in these samples. FA treatment significantly increased the lipid droplet size in 2D gluteal cells (p<0.0001), but not in abdominal, compared to non-FA treated cells for each depot.

Despite the improvement in differentiation in 3D culture (development of more numerous lipid droplets), this method did not significantly increase the lipid droplet size in abdominal spheroids. In contrast, gluteal spheroids showed a significant increase in lipid droplet size (p<0.0001) compared to 2D samples, with the FA-treated spheroids developing even larger lipid droplets (p<0.0001) (**Figure 4.5j**). Depot comparison also revealed significantly larger lipid droplets in the gluteal samples under both FA and non-FA conditions (p<0.0001). Overall, these results demonstrate that 3D culture improved the differentiation of DFAT preadipocytes from both depots, and increased accumulation of larger lipid droplets in gluteal over abdominal spheroids.

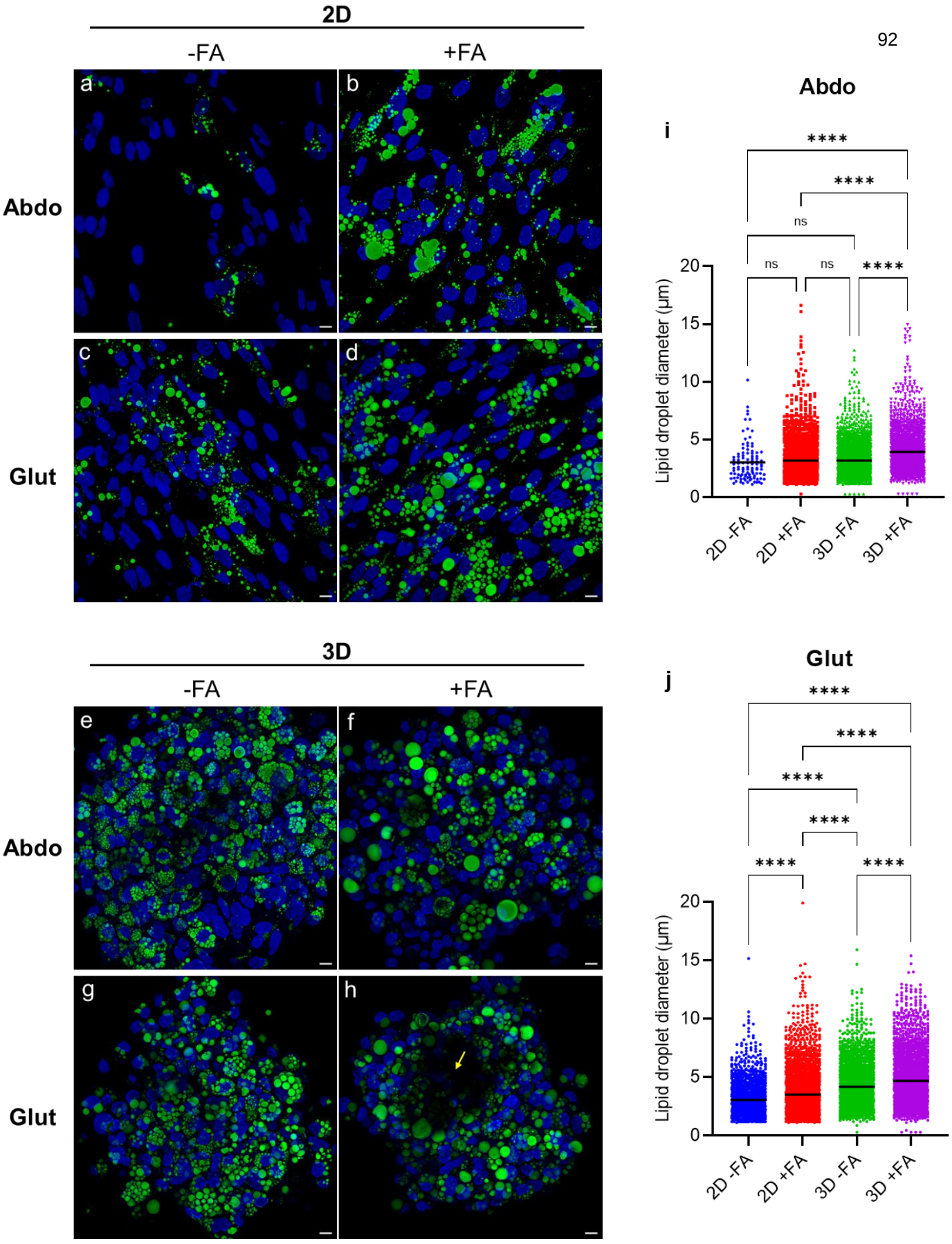


Figure 4.5. Quantification of lipid droplet sizes in 2D and 3D cultures on day 11. Representative confocal images of abdominal (**a, b, e, f**) and gluteal (**c, d, g, h**) DFAT cells differentiated in (**a-d**) 2D culture and (**e-h**) 3D culture. 2D and 3D cultures were stained for lipid droplets (BODIPY 459/503, green) and nuclei (Hoechst 33342, blue). Yellow arrow indicates cavity in spheroid where no cells were present. Scale bars represent 10 µm. Lipid droplet sizes quantified for abdominal (**i**) and gluteal (**j**) samples. Lines represent means. A total of 100 to 3,886 lipid droplets per condition were pooled and analysed from spheroids (n = 3 technical replicates) or from 2−3 images of 2D-cultured cells on one coverslip, except for the non-FA treated 2D condition where cells displayed poor differentiation and were analysed using only 2 images. Statistical analysis was performed by two-way ANOVA. ****p<0.0001.

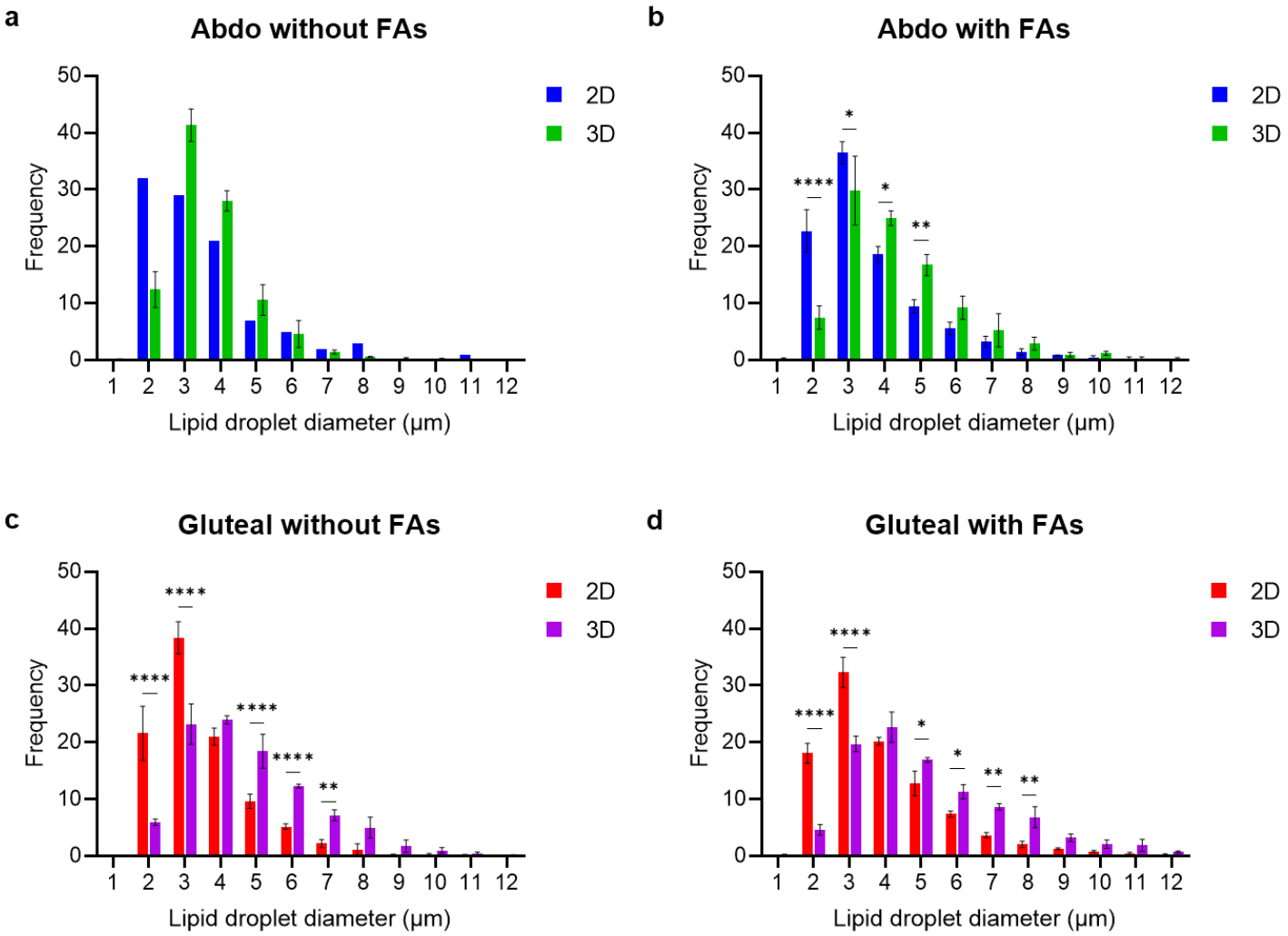


Figure 4.6. Relative frequencies of lipid droplet diameters in abdominal and gluteal DFAT cells differentiated in 2D and 3D culture conditions, with or without fatty acid treatment. Lipid droplet diameters were measured in abdominal (**a, b**) and gluteal (**c, d**) DFAT cells differentiated under both 2D and 3D culture conditions, with (**b, d**) or without (**a, c**) fatty acid (FA) exposure. Data are presented as mean lipid droplet diameter frequencies within 1 μm bin divisions, with SD. Statistical analysis was performed by two-way ANOVA. *p<0.05, **p<0.005, ****p<0.0001.

Several studies have demonstrated that formation of unilocular adipocytes in 3D culture can take in excess of two weeks (Klingelhutz, *et al*., 2018) (Hsiao, *et al*., 2015) (Ioannidou, *et al*., 2022b). Based on this, I differentiated the adipose spheroids to day 14, during which conditioned media samples were collected and analysed for secreted adipokines. Regardless of FA treatment, leptin concentrations in culture media, measured using ELISA, were practically undetectable (data not shown). This was consistent with my findings in the previous chapter for mouse SVF-derived spheroids, and results from other studies (Ioannidou, *et al*., 2022b) (Wolff, *et al*., 2022).

Although spheroids remained intact and, for the most part, partially embedded in the hydrogel droplets, they started to float to the liquid surface by day 14. This was most prevalent in the FA-fed gluteal samples, likely due to an increase in buoyancy as a result of the high levels of lipid accumulation. Therefore, at day 14, the spheroids were manually processed to avoid sample losses during automated liquid handling. As the focus was on automation and confocal imaging showed the spheroids to be highly differentiated, I reverted to day 11 as the differentiation endpoint.

The concentration of adiponectin secreted into culture media was also measured on day 11 (**Figure 4.7**), showing that spheroids produced adiponectin at levels similar to other reports (Liszewski, *et al*., 2024) (Wagner, *et al*., 2025). No differences in adiponectin secretion between depots or treatments was found.

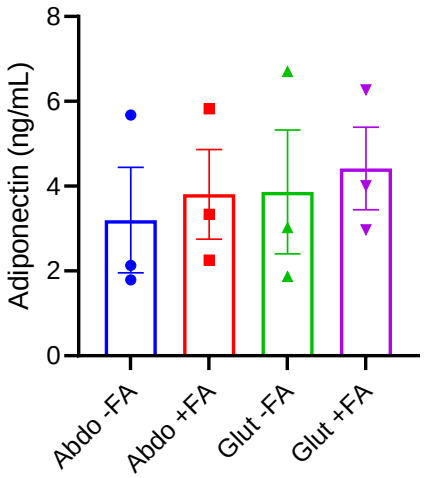


Figure 4.7. Adiponectin secretion in 48-hour conditioned media from abdominal and gluteal DFAT spheroids on day 11 of differentiation. Media samples were diluted 1:2 and ran by Amy Barrett (OCDEM) using a human adiponectin ELISA kit (Invitrogen™, KHP0041). Adiponectin was not detectable in media from day 0 undifferentiated spheroids. *n* = 3 independent experiments, with 4 spheroids per condition. Data are mean ± SEM.

4.3.4 Histological analysis of spheroids

To investigate the morphology of cells in the spheroid core, histological processing was undertaken on spheroids fixed on days 0 and 14 (as outlined in **2.9.1**). Spheroid sections were stained with H&E (described in **2.9.2**), with lipid droplets observed as empty spaces (vacuoles) within the eosin-stained cytoplasm due to dissolution of fat during histological processing. H&E staining of spheroids on day 14 showed that differentiation (presence of lipid droplet vacuoles) was more uniform across the gluteal adipose spheroids (**Figure 4.8**). In contrast, the central cells of abdominal spheroids appeared less well differentiated compared to those in the outer layer.

Consistent with the confocal imaging results, high magnification images revealed that the lipid droplets were larger in gluteal spheroids (**Figure 4.9**). The histology results also showed regions within the spheroids where cells were absent (**Figure 4.8**, and indicated by asterisks in **Figure 4.9**).

To test whether the cavities were due to necrosis, a viability assay was carried out on spheroids differentiated to day 11. **Figure 4.10** shows that spheroids were healthy and did not contain necrotic regions. Importantly, examination of the paraffin-embedded spheroid sections, used for the H&E staining, showed that the hydrogel could be seen surrounding the spheroid and also within the cavities (**Figure 4.10a**). This suggests that the cavities are due to the way the cells have condensed and arranged themselves within the hydrogel. These cavities may facilitate nutrient delivery and gas exchange to the centre of the spheroid. Necrosis was also ruled out based on the day 0 spheroids displaying high cell viabilities (**Figure 4.10b**), and cavities confirmed by H&E staining at this time point (**Figure 4.8**). Additionally, no morphological features indicative of necrosis (such as cell/nuclear swelling, loss of cell detail or cell debris) were observed in cells adjacent to the cavities.

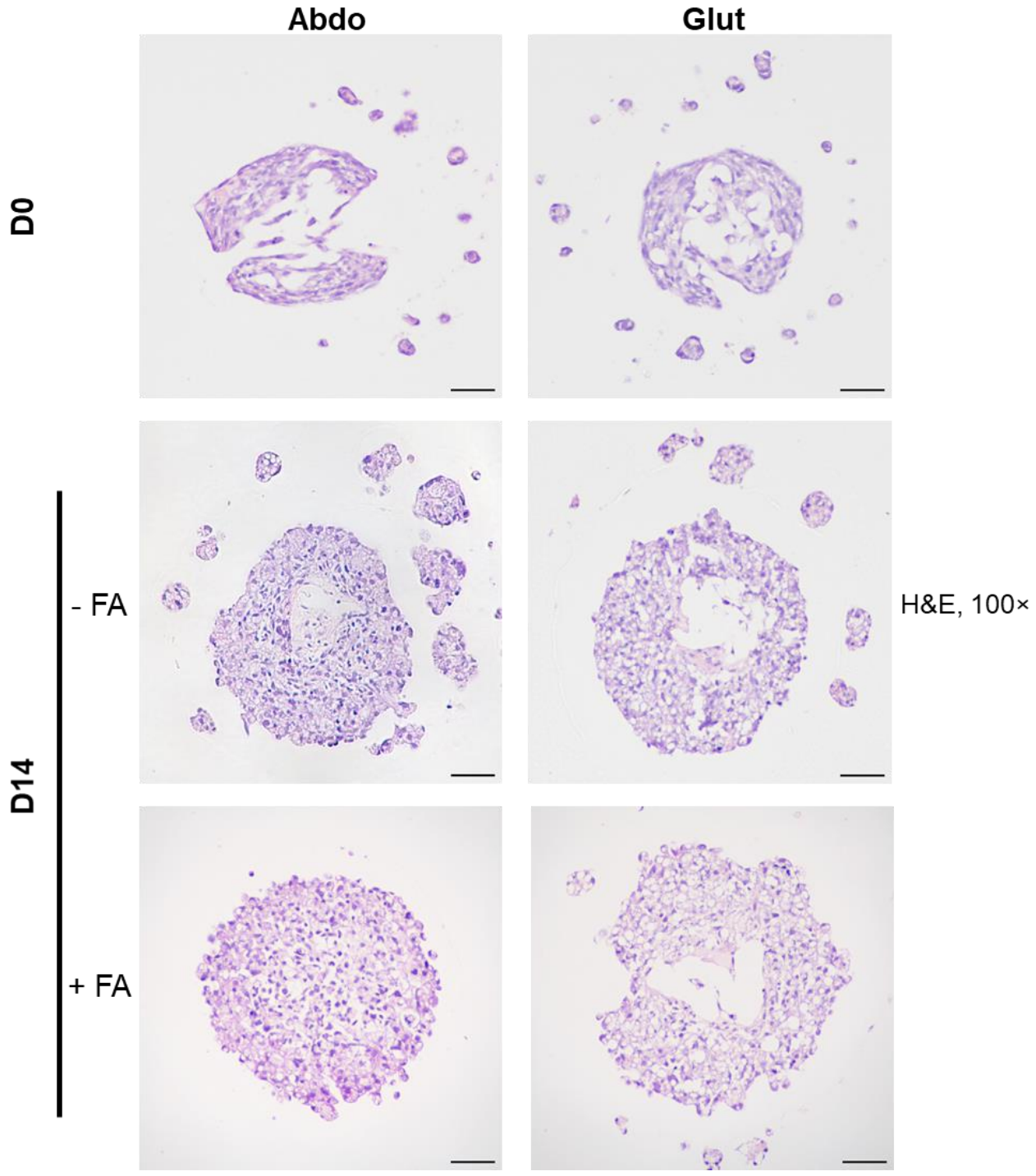


Figure 4.8. H&E staining of abdominal and gluteal DFAT spheroids during adipogenesis (days 0 and 14). Images taken at 100× magnification. Cavities were observed in some spheroids which, based on viability staining (see **Figure 4.10**), were ruled out as being due to necrosis. Scale bars represent 50 µm. Abbreviations: -FA, fatty acid-untreated; +FA, fatty acid-treated.

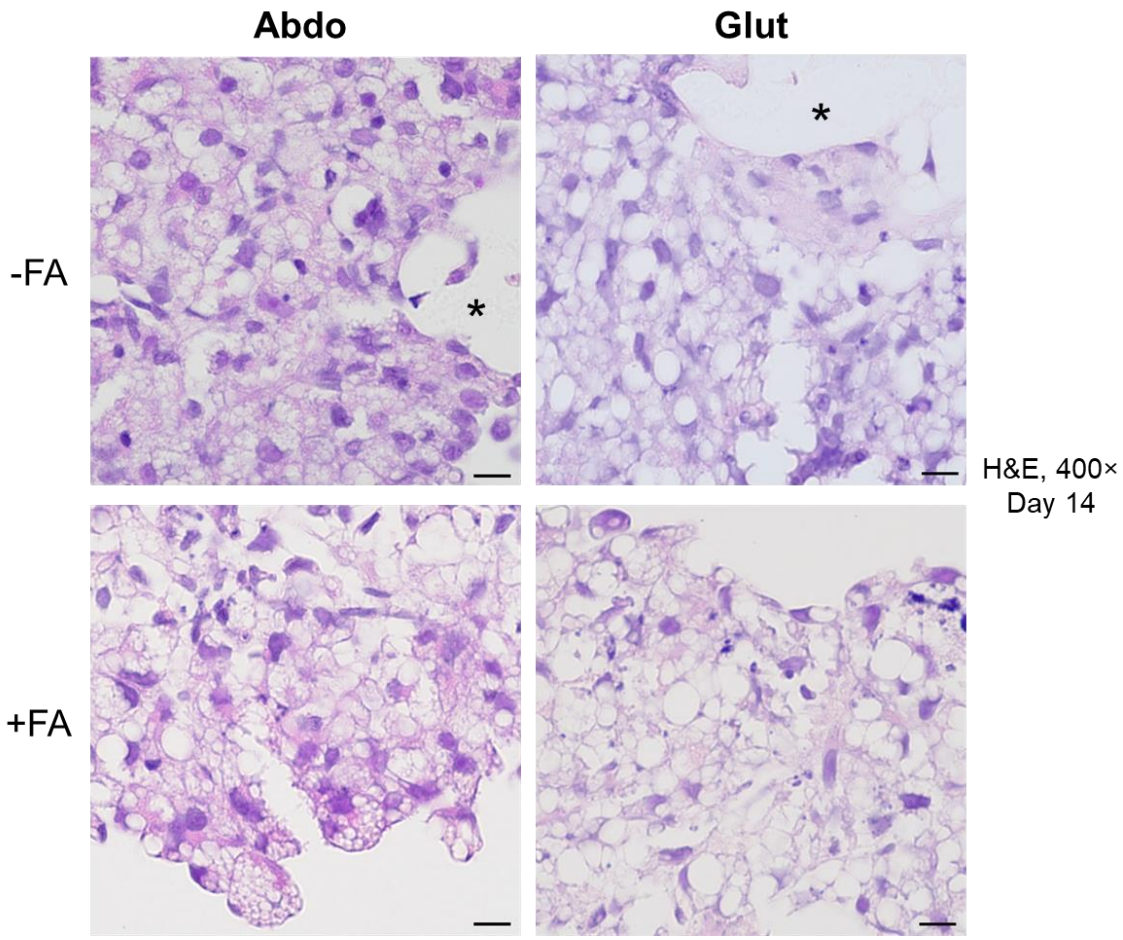


Figure 4.9. Higher magnification H&E images (400×) of abdominal and gluteal DFAT spheroids differentiated to day 14. Asterisks indicate cavities. Scale bars represent 10 µm. Abbreviations: -FA, fatty acid-untreated; +FA, fatty acid-treated.

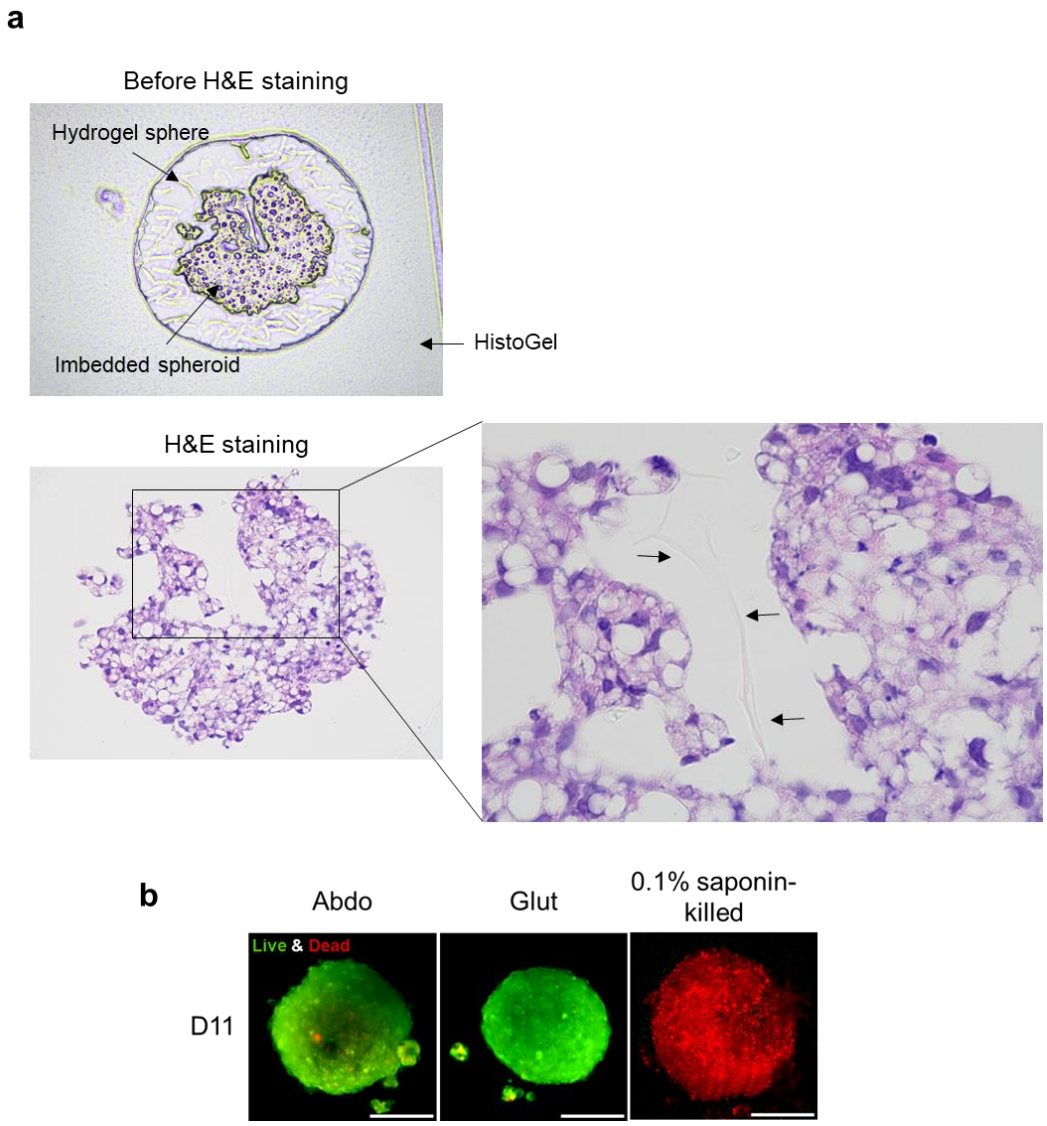


Figure 4.10. Differentiated adipose spheroids showed no strong evidence for necrosis. (**a**) Representative HistoGel™-embedded spheroid showing spheroid within the hydrogel droplet. Arrows indicate hydrogel within the spheroid cavity. (**b**) Representative fluorescent micrographs of spheroids stained with CAM and PI at day 11 of differentiation. Scale bars represent 200 µm.

4.4 Discussion

The aim of this work was to test whether the automated 3D adipose culture system developed in **Chapter 3** could be applied to human adipocytes and adapted to cells of tissue-specific origin. Despite the initial challenge with optimising conditions for abdominal spheroid production, I successfully developed a 3D adipose model, using depot-specific human preadipocytes, characterising the spheroid morphology and differentiation. This highlights the versatility of 'droplet-in-oil' spheroid production, and its potential use in the study of regional human adipocyte biology.

To the best of our knowledge, this work presents the first *in vitro* 3D adipose model using paired subcutaneous adipose cells derived from abdominal and gluteal regions. Investigating the differentiation of preadipocytes from these contrasting adipose depots, which represent upper- and lower-body fat, revealed distinct differences in lipid droplet size and morphology. Gluteal-derived spheroids accumulated larger lipid droplets compared to those from the abdominal region. These findings align with unpublished work from our lab, where similar differences in lipid droplet size between 2D-cultured abdominal and gluteal cell lines from a female donor (named MBdfat5 cells) were detected (i.e. larger droplet sizes in gluteal-derived adipocytes). Larger lipid droplet sizes in the gluteal depot have also been observed in *in vivo* tissue histology datasets, analysed by our lab, supporting that this is a real characteristic of *in vivo* adipose tissue and not just a feature of *in vitro* systems. Thus, these differences in the cell lines likely reflect an intrinsic depot-specific cellular 'memory' retained by gluteal adipocyte precursors, consistent with the known function of gluteofemoral adipose tissue as a 'metabolic sink' for FAs (Manolopoulos, *et al*., 2010). This depot is characterised by a reduced lipid turnover compared to abdominal adipose tissue (Karpe & Pinnick, 2015).

It is well-established that lipid droplet sizes are larger in 3D adipocyte cultures compared to 2D (Klingelhutz, *et al*., 2018) (Shen, *et al*., 2021) (Dariolli, *et al*., 2025), and the results obtained using my system reflect this. This difference was most apparent when differentiating

preadipocytes without the addition of FAs. Many protocols for adipogenic differentiation do not include exogenous FAs, despite their physiological relevance (Gamwell, *et al*., 2023).

Treating adipose spheroids with defined mixtures of FAs may be used to model weight gain, dietary macronutrient composition and adipocyte dysfunction, supporting research into obesity and related metabolic disorders. For example, Ioannidou *et al*. (2022b) used a plant-derived FA mixture (soybean oil emulsion) to simulate over-nutrition in their 3D adipose model, resulting in adipocyte hypertrophy and increased secretion of the pro-inflammatory adipokines interleukin-6 (IL-6) and macrophage chemoattractant protein-1 (MCP1). Similarly, Shen *et al*. (2021) induced adipocyte hypertrophy in spheroids using a mixture of OA and PA.

Interestingly, adipocyte precursors differentiated using our group's standard protocol (exogenous FA-free) showed the greatest improvement when cultured in 3D, compared to poor differentiation under 2D conditions; this difference was most striking for abdominal adipocyte precursors. This suggests that intrinsic DNL is more enhanced than lipid uptake in a 3D environment. This is supported by lipidomic analysis performed by Shen *et al*. (2021), whose data indicates that the formation of intracellular TGs in adipocyte spheroids occur predominately through DNL. Furthermore, the lipid profiles of 3D-cultured adipocytes may more closely resemble those of *in vivo* tissue, as demonstrated in SVF-derived organoids (Taylor, *et al*., 2020).

Consistent with results from other 3D adipose models, the largest lipid droplet size I found in gluteal spheroids was ~20 µm by day 11 of differentiation. Although these sizes are smaller than those observed *in vivo*, they represent a significant improvement compared to conventional 2D culture models. Further research is needed to understand the exact mechanisms as to why adipogenesis is enhanced in 3D culture systems, but it may be related to increased cell-cell interactions, ECM production, adipogenic gene expression and mitochondrial respiration (Shen, *et al*., 2021) (Endo, *et al*., 2023). To confirm adipogenesis in the model, expression of PLIN1 could be used as a downstream effector readout of PPARG. Measuring increased PLIN1 mRNA or protein expression would therefore indicate active

PPARγ signalling and progression toward a differentiated adipocyte phenotype. This is particularly relevant when preadipocytes are differentiated with FAs in the media, as it would help distinguish bona fide adipogenic differentiation from lipid droplet expansion driven solely by FA uptake. Assessing the proportion of PLIN1 coated lipid droplets would act as an additional method of verification.

During this work, histological analysis of spheroids was undertaken, revealing areas devoid of cells (cavities); these appear to be pockets of trapped solidified hydrogel around which the cells have condensed. This feature of my model may prove advantageous by creating channels and allowing inner cells to access media and therefore nutrients, thereby reducing necrotic events. Furthermore, the majority of spheroids fabricated at the selected conditions remained embedded in their hydrogel spheres, which partially immobilised them.

4.4.1 Summary

Overall, my data supports that I have developed a viable and robust 3D spheroid model for studying depot-specific human adipogenesis, with improved differentiation over conventional 2D models. This has the potential to be used to investigate differences in human regional adipocyte biology for a given gene or biological process, within a physiologically relevant 3D culture system. Introduction of other cell types, such as vascular or immune cells, would further improve the model's relevance to *in vivo* tissue. This would depend on the research goal and may require optimisation of the media composition to support the viability of different cell types, allowing simultaneous adipogenesis and angiogenesis (for instance, if incorporating endothelial cells).

I will use this model in the next results chapter as part of my investigation into a partial lipodystrophy-causing mutation on regional adipocyte biology.

5 Investigation of a familial partial lipodystrophy type 2 mutation on regional human adipose biology

5.1 Introduction

5.1.1 The *LMNA* gene and laminopathies

The *LMNA* gene encodes for lamin A/C (hereafter referred to as lamin A), a type V intermediate filament protein that forms part of the nuclear lamina; this a fibrous protein network located beneath the inner nuclear membrane that provides structural and mechanical support to the nucleus. Lamin A undergoes polymerisation at the nuclear periphery where it is mainly localised. It is also found in the nucleoplasm (Dittmer & Misteli, 2011). In addition to supporting nuclear architecture, lamin A interacts with chromatin, both directly and indirectly, and is involved in various nuclear activities including transcription, chromosome positioning, proliferation and DNA replication (Dechat, *et al*., 2008).

Mutations in the *LMNA* gene are the cause of a group of clinically diverse diseases called 'laminopathies', that manifest as either tissue-specific or multi-systemic diseases (Zhang, *et al*., 2013). Genetic instability and abnormal nuclear morphology are common attributes of the wide range of laminopathies. In these diseases, tissues of mesenchymal origin, such as muscle, adipose and bone, are disproportionately affected (Malashicheva & Perepelina, 2021). One such laminopathy is FPLD2 (described in section **1.6.1**) which affects upper- and lower-body adipose tissue to differing severities.

As discussed in **Chapter 1**, regional adiposity, be it in the abdominal or gluteofemoral region, is associated with opposite metabolic outcomes. Increased fat storage in the upper-body is metabolically detrimental, whereas accumulation of fat in the lower-body gluteofemoral region may confer metabolically protective effects (Karpe & Pinnick, 2015). In people affected by FPLD2, there is a loss of subcutaneous adipose tissue predominately in the gluteofemoral region; the abdominal region can also be affected but this is often more variable between

patients and dominated by a proportional increase in intra-abdominal (visceral) fat. Therefore, gaining insight into mechanisms driving selective adipose tissue loss (particularly in the gluteofemoral region) would improve understanding of adipose biology, and could contribute towards future treatments of lipodystrophy syndromes.

5.1.2 Chapter hypothesis

- The LMNA R482W mutation causes FPLD2 by exerting effects in adipose precursor cells which impair depot-specific adipogenesis.

5.1.3 Chapter aims

In this chapter, I will investigate the effect of the FPLD2-causing LMNA R482W mutation on regional human adipocyte biology. This will combine human *in vivo* work, the use of *in vitro* models including LMNA R482W mutant preadipocytes evaluated in conventional 2D culture and, finally, application to a 3D spheroid model.

The specific aims of my work were to:

- Assess regional adipose tissue function in FPLD2 patients carrying the LMNA R482W mutation by measuring *in vivo* leptin secretion from abdominal and femoral subcutaneous adipose tissue depots.
- Investigate adipose tissue structure in patients with FPLD2 using histological analyses.
- Use depot-specific *in vitro* cell models to investigate the effect of LMNA R482W expression on preadipocyte proliferation and nuclear morphology.
- Use both 2D and 3D cell culture systems to explore the effect of the LMNA R482W mutation on depot-specific preadipocyte differentiation.

5.2 Specific methods

5.2.1 Human leptin ELISA

Leptin concentrations in arterial and venous plasma samples from FPLD2 and control subjects were measured using a human leptin ELISA kit (Invitrogen™, KAC2281), following the manufacturer's instructions. The plasma samples were diluted 1:100 in standard diluent buffer and ran in duplicate. Absorbance readings were measured at 450 nm using a FLUOstar Omega microplate reader (BMG LabTech) and used to generate a standard curve, allowing interpolation of the curve and calculation of leptin concentrations.

5.2.2 Histological processing of human subcutaneous adipose tissue biopsies

Core needle biopsies (~20 mg) of human subcutaneous abdominal (5 cm lateral to the umbilicus) and femoral (front of the mid 1/3 thigh) adipose tissue were collected from FPLD2 and control patients; the samples obtained were a 20 mm (length) by 1.5 mm (diameter) core. The biopsies were obtained by Professor Fredrik Karpe with assistance from the research nursing staff of the Clinical Research Unit (CRU) at OCDEM. The tissue samples were first washed in sterile PBS to remove blood, then fixed in either 4% paraformaldehyde (PFA) or 10% formalin overnight. The fixed tissues were then placed in histological cassettes, processed, wax embedded and sectioned for histology (described in section **2.9.1**).

5.2.3 Picrosirius red staining for detection of collagen fibres

Histological sections of human adipose tissue biopsies and cell spheroids were stained using haematoxylin and picrosirius red (PSR) solutions (Abcam, ab246832) to detect nuclei and collagen fibres, respectively (**Table 5.1**). After staining, the sections were covered with glass coverslips and mounted with DPX, then imaged with a Nikon ECLIPSE Ci-S microscope.

Table 5.1. Haematoxylin and picrosirius red staining of human adipose tissue and spheroid sections. All stages involving xylene were carried out in a fume hood. * 12 minute staining with haematoxylin as picrosirius red causes nuclear destaining.

Step	Reagent/Procedure	Time
Deparaffinisation	Xylene (tank 1)	3 minutes
	Xylene (tank 2)	3 minutes
	Xylene (tank 3)	3 minutes
Rehydration	100% ethanol (tank 1)	3 minutes
	100% ethanol (tank 2)	3 minutes
	100% ethanol (tank 3)	3 minutes
	90% ethanol tank	3 minutes
	Rinse under running tap water	5 minutes
Nuclear staining	Haematoxylin solution	12 minutes *
	Rinse under running tap water	10 minutes
Collagen staining	Picrosirius red solution	1 hour
	Rinse in acidified water (5 mL of acetic acid per litre of water)	
Dehydration	100% ethanol (tank 4)	3 minutes
	100% ethanol (tank 5)	3 minutes
	100% ethanol (tank 6)	3 minutes
	Xylene (tank 4)	
	Xylene (tank 5)	

5.2.4 Quantitative polymerase chain reaction (qPCR)

qPCR was used to assess relative gene expression in 2D cell culture samples. cDNA samples were first synthesised from total RNA (described in **2.8.2**). For qPCR preparation, a cDNA pool was created by mixing 2 µL of each experimental sample, which was then serially diluted (1:10, 1:20, 1:40, 1:80, 1:160, 1:320) in 10 mM Trizma® hydrochloride (Tris-HCl, pH 8.0). Each cDNA sample was then diluted 1:40 in 10 mM Tris-HCl for qPCR.

3.6 µL of each dilute cDNA sample was loaded onto a 384-well qPCR plate, in triplicate. 0.4 µL of TaqMan assay and 4 µL of Fast Master Mix (Kappa Biosystems) were mixed and added to each well, giving a final volume of 8 µL. The TaqMan assays used are shown in **Table 5.2**. The plates were sealed and briefly centrifuged. A Quantstudio 7 Flex (ABI) machine was used for qPCR, with the amplification parameters shown in **Table 5.3**.

Relative transcript expression was calculated using the ΔΔCt relative quantification method (Pfaffl, 2001). The ΔCt values of target genes were normalised to the ΔCt of housekeeper transcript 18S (Neville, *et al*., 2011).

Table 5.2. TaqMan assay probes used for qPCR.

Target gene	Assay number
LMNA	Hs00153462_m1
18S	Hs99999901_s1

Table 5.3. Thermal cycling conditions for TaqMan Fast qPCR.

Step	Temp. (°C)	Time (mm:ss)	Number of cycles
Initial denaturation	95	3:00	1
Denaturation	95	0:03	40
Annealing/extension	60	0:20	

5.2.5 Doxycycline dose response curves

Doxycycline (Dox)-inducible cell lines (described in **2.5.5.2**) were seeded at 2 × 10^5 cells per well in 6-well plates (Corning, CellBIND) and cultured for 24 hours. Cells then received fresh growth media containing Dox at a range of concentrations (0, 0.05, 0.1, 0.5 and 1 µg/mL). After a further 48 hours, cells were transferred to a fume hood and harvested for RNA isolation as described in section **2.8.1**.

5.2.6 High-content imaging for quantification of adipogenesis levels in 2D cultures

For quantifying adipogenesis levels in 2D cultures, the Dox-inducible cell lines were seeded in 96-well plates and induced to differentiate (described in **2.6**). Cells were fixed with 4% PFA (15 minutes) on days 0, 7 and 14 of differentiation and stained with HCS LipidTOX™ Red neutral lipid stain (1:200 dilution, Invitrogen™, Cat No. H34476) and Hoechst 33342 (1 µg/mL, Thermo Scientific, 62249) in 1 × PBS for 30 minutes in the dark (40 µL/well). After staining, cells were washed three times with 1 × PBS (with calcium and magnesium, Gibco™, 14040174) and imaged at 4× magnification using the Cytation1 high-content imager.

Fluorescent micrographs from a montage (6 × 4) were stitched together using Gen5 software to create an image for each well in a 96-well plate. This image was subjected to a pre-processing step to remove excessive background signal using consistent settings. Images were cropped by fitting a central circular plug (3500 µm × 3500 µm). The processed images were then analysed using the 'cellular analysis' function in the software, with stained lipid droplets identified in the propidium iodide (PI) channel using a pixel intensity threshold determined from the negative (unstained) control samples. Adipogenesis was quantified by measuring the total area of lipid droplet signal (LipidTOX™ stained regions) in each image. Nuclei detection in the DAPI channel, for measurement of nuclei signal area, was used for normalisation of lipid signal area, when required. Manual inspection of images enabled exclusion of wells containing artefacts or damaged cells.

5.2.7 Measurement of intracellular triglyceride content

On day 9 of differentiation, Dox-inducible cell lines in 6-well plates were washed twice in PBS and 150 µL of 1% NP-40 lysis buffer (**Table 5.4**) added. Cells were left for 5 minutes at room temperature and then homogenised by scraping. Cell lysates were collected into clean 1.5 mL Eppendorf tubes and stored at -80ºC until further processing.

Samples were thawed on ice and briefly sonicated (5 second pulses for 15 seconds at 40 kHz), before collecting 22 µL of the lysate for determining protein concentration using a DC (detergent compatible) Protein Assay kit (BioRad), following the manufacturer's protocol. The remaining sample was heated at 95°C for 30 minutes. Samples were then vortexed and centrifuged at 12,000 x *g* at 4°C for 10 minutes. Triglyceride concentrations in supernatants were determined on an AU480 Chemistry Analyser (Beckman Coulter), using a triglyceride assay kit (ILab, 0018255640), and normalised to protein content for each sample.

Table 5.4. 1% NP-40 lysis buffer composition. Abbreviations: Tris-HCl, Trizma® hydrochloride; dH2O, distilled water.

Reagent	Volume for 50 mL
5 M NaCl	1.5 mL
10% NP-40	5 mL
1 M Tris-HCl (pH 8.0)	2.5 mL
dH2O	41 mL

5.2.8 Proliferation experiments

Proliferation rates of the Dox-inducible cell lines were quantified by counting the number of stained nuclei using high-content imaging. Cells were plated at a low density (1×10^3) in CellBIND 96-well plates (Corning) in 200 µL of preadipocyte growth medium (see **2.5.2**) and cultured for ~19 hours before commencing the proliferation experiment. Cells were fixed at two time points with 4% PFA (15 minutes) and nuclei stained with 1 µg/mL Hoechst 33342 (30 minutes), following which the total number of nuclei were counted by whole-well fluorescent imaging using the Cytation1. Gen5 software was used for automatic segmentation and counting of cell nuclei. The cell doubling time, *Td*, was calculated using the formula $Td=(t2-t1)\times[\log(2)\div\log(q2\div q1)]$, where t = time point (days) and q = cell number.

5.2.9 Differential nuclear staining assay

A differential nuclear staining (DNS) assay for quantification of viable cells was performed as described by Lema *et al*. (2011). For the experiment, 1 x 10^3 cells were seeded per well in 200 µL of growth media (see **2.5.2**) and treated with or without 0.1 µg/mL Dox after 19 hours. 48 hours after Dox treatment, cells were treated with Hoechst 33342 and PI (1 µg/mL each) and incubated for 1 hour; no cell washing was performed. The stained cells were then imaged using the Cytation1 at 20× magnification and fluorescent images analysed in Gen5 software, where dead cells were identified as PI-positive nuclei and live cells as Hoechst-positive nuclei.

5.2.10 EdU assay

Dox-inducible cell lines were treated with 10 mM EdU (5-ethynyl-2'-deoxyuridine) for 2 hours then immediately fixed with 4% PFA (15 minutes). To determine the percentage of cells in S-phase, a Click-iT Plus EdU Alexa Fluor 594 Imaging Kit (Invitrogen™, C10639) was used, following the manufacturer's instructions. Images of cells at 20× magnification were captured using the Cytation1 high-content imager, and Gen5 software used to count the total number of Hoechst-positive nuclei and the number of EdU-positive (S-phase) nuclei.

5.2.11 High-throughput assessment of preadipocyte nuclear morphology

Fluorescent images of Dox-inducible cell lines stained with Hoechst 33342 were acquired at 20× magnification using the Cytation1. 25 images were obtained per well. The fluorescence images were analysed using CellProlifer software (version 4.2.5) to assess nuclear morphology parameters, including the form factor (or roundness) and solidity (ratio of the net area of an object to the area of the convex envelope of the object). A circularity value of 1 indicates a perfect circle, whereas values approaching 0 have increasing elongated shapes. A solidity score of 1 signifies a solid object, whereas objects with values less than 1 have irregular boundaries or contain holes.

5.2.12 Lipid droplet staining of spheroids

Fixed spheroids were stained using LipidTOX™ (1:200 dilution) and 4 μM Hoechst 33342 in PBS for 2 hours. Spheroids were washed four times in PBS using the Assist Plus robot and stored at 4^{o}C until confocal imaging. For imaging, spheroids were immobilised by embedding in agarose as previously described (see **3.2.6**).

5.3 Results

5.3.1 Examination of FPLD2 patients

5.3.1.1 Depot-specific leptin release

The MRG group previously conducted an *in vivo* human physiological study in five patients with diagnosed FPLD2 (*LMNA* p.R482W mutation) and five controls (without FPLD2 and matched for sex and BMI) to assess TG extraction across specific adipose depots (data unpublished). Plasma samples were obtained from veins draining the abdominal and femoral (thigh) adipose depots, as well as an arterialised plasma sample, using the using the arterio-venous (A-V) difference technique (McQuaid, *et al*., 2010b); this enables quantification of depot-specific metabolite flux.

Using these samples, I aimed to extend the original analysis and assess regional differences in leptin secretion; leptin levels are typically reduced in FPLD2 patients, as a consequence of reduced adiposity. However, as there was insufficient sample remaining for 3 controls I selected new age- and BMI- matched control samples from a larger sample set (subject characteristics are listed in **Table 5.5**).

Plasma leptin concentrations were measured by ELISA (described in **5.2.1**). Arterialised leptin concentrations were found to be significantly lower in FPLD2 patients compared to control subjects (**Figure 5.1a**). There was significantly lower leptin release (veno-arterial (V-A) difference) from both abdominal and femoral adipose tissue depots in FPLD2 patients compared to control subjects (**Figure 5.1b, c**). However, the release of low but detectable levels of leptin indicated the presence of some functional adipocytes in these depots. The *in vivo* study had already demonstrated a small but significant extraction of plasma TGs indicating some presence of LPL, the origin of which should have been adipose tissue.

Table 5.5. Clinical parameters of FPLD2 (*LMNA* p.R482W) and control subjects from *in vivo* physiological study (unpublished data, MRG group). Data are mean ± SEM.

	LMNA	Control
Males / Females	2 / 3	2 / 3
Age (y)	50.6 ± 3.4	48.8 ± 3.9
BMI (kg/m^2)	27.7 ± 1.7	27.0 ± 1.5

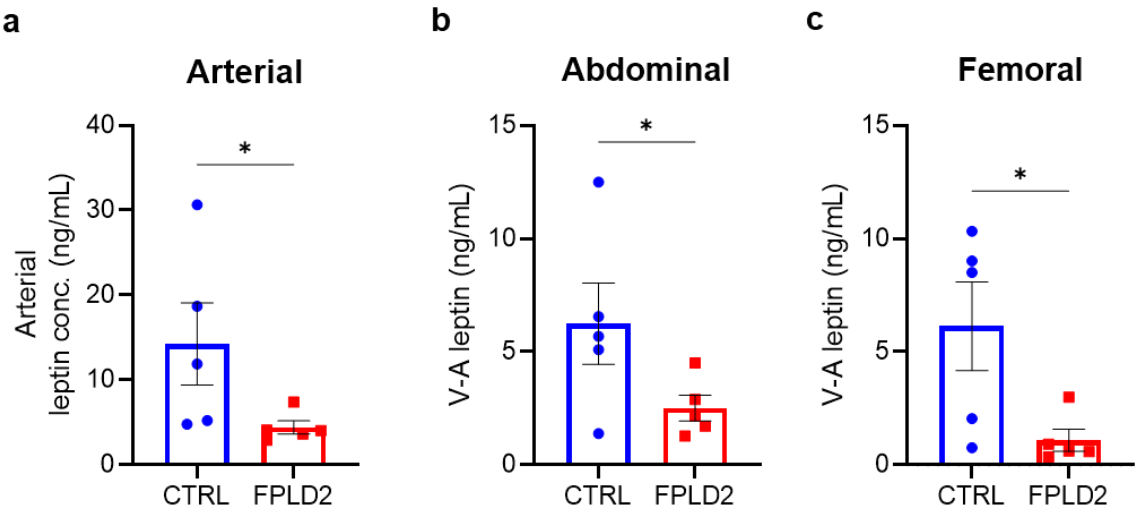


Figure 5.1. Depot-specific release of leptin in FPLD2 patients. (**a**) Arterial plasma leptin concentrations in control (CTRL; *n* = 5) and FPLD2 (*n* = 5) patients determined by ELISA. These values were used to calculate the veno-arterial (V-A) difference across upper-body abdominal (**b**) and lower-body femoral (**c**) subcutaneous adipose tissue depots. Venous effluent was sampled via cannulation of the superficial epigastric vein (abdominal depot) and the saphenous vein (femoral depot). Data presented as mean ± SEM. Statistical comparisons were made using unpaired one-tailed Student's t-test or Mann-Whitney test, depending on the normality of the data distribution; **p*<0.05.

5.3.1.2 Body composition by DXA

A father and son diagnosed with FPLD2 (*LMNA* p.R482W mutation) visited OCDEM for clinical assessment. Upon clinical examination the son appeared more lipodystrophic compared to the father, exhibiting greater loss of lower-body adipose tissue. Dual-energy X-ray absorptiometry (DXA) enables assessment of body composition and is the 'gold standard' for assessing body fat percentage. To quantitatively assess body fat parameters, DXA measurements from the FPLD2 patients were compared to 462 healthy control subjects (BMI < 25) from the Oxford BioBank (**Table 5.6**). The average leg fat percentage in the control group was 20.6% (95% confidence interval [CI], 20.1 - 21.0). Supporting the clinical observation of greater disease severity in the son, this subject's leg fat percentage fell below the lower 95% CI, whereas the father's value was above the upper 95% CI.

The fat mass ratio (FMR), defined as trunk fat percentage divided by leg fat percentage, has been proposed as a potential biomarker for partial lipodystrophy (Agrawal, *et al*., 2024). In this study, FMR thresholds of 1.2 and 1.7 were considered as the cut-off points for FPLD in females and males, respectively. Both FPLD2 subjects had high FMR values above the upper 95% CI of controls, reflective of their abnormal fat distribution (**Table 5.6**). However, their FMRs remained below the 1.7 threshold proposed by Agrawal *et al*. (2024), highlighting the limitations of using DXA-based measurements alone to identify FPLD2.

Table 5.6. Clinical parameters and DXA measurements of two FPLD2 subjects (*LMNA* p.R482W) compared with control subjects from the Oxford Biobank. Control subject data are presented as means with 95% confidence intervals. The fat mass ratio (FMR), which is the ratio of trunk fat percentage to leg fat percentage, is shown in the rightmost column.

	Age (y)	**BMI (kg/m^2)**	**Tissue total, % fat**	**Tissue legs, % fat**	**Tissue trunk, % fat**	**FMR**
FPLD2 donor 1	45	24.4	31.9	24.5	38.9	1.59
FPLD2 donor 2	18	21.5	20.8	15.3	24.0	1.57
Controls (*n* = 462)	44.6 (44.3 - 44.9)	23.1 (22.9 - 23.2)	22.8 (22.3 - 23.3)	20.6 (20.1 - 21.0)	25.0 (24.5 - 25.8)	1.22 (1.2 - 1.3)

5.3.1.3 Histological assessment of FPLD2 subcutaneous adipose tissue

To assess adipose tissue architecture in FPLD2, subcutaneous adipose tissue biopsies were taken from the abdominal and femoral sites of the father and son, and processed for histology (described in **5.2.2**). In subcutaneous WAT depots, adipocytes are organised into lobules separated by sheets of collagen-rich septa (Robino, *et al*., 2024). H&E staining (described in **2.9.2**) of abdominal and femoral WAT biopsies from the father showed normal adipocyte morphology and size in both depots, compared to that of a healthy donor (**Figure 5.2**). It was necessary to present the abdominal samples as fluorescent images due to the H&E staining results being much fainter for this depot.

In contrast, the son's femoral subcutaneous adipose tissue biopsy had smaller fat lobules and thicker connective tissue septa, indicating fibrosis (**Figure 5.2b**). Accumulation of non-adipocyte cells, reminiscent of 'crown-like' structures, were visible around some adipocytes, which suggested inflammation. Unfortunately, the abdominal biopsy could not be assessed histologically due to unsuccessful fixation and/or processing of the sample (fragmented cell membranes were observed in H&E staining).

The degree of fibrosis levels was assessed using picrosirius red (PSR) staining (described in **5.2.3**) (**Figure 5.3**). The son's femoral biopsy had intense PSR staining indicating increased collagen deposition, in addition to areas of adipocyte 'trapping' (i.e. adipocytes surrounded by thick ECM), as shown in the higher magnification images in **Figure 5.3b**. Of note, the father's femoral biopsy did not show any similar signs of fibrosis. Therefore, these results suggest that there was increased fibrosis in the femoral adipose tissue of the subject with the more severe lipodystrophy phenotype.

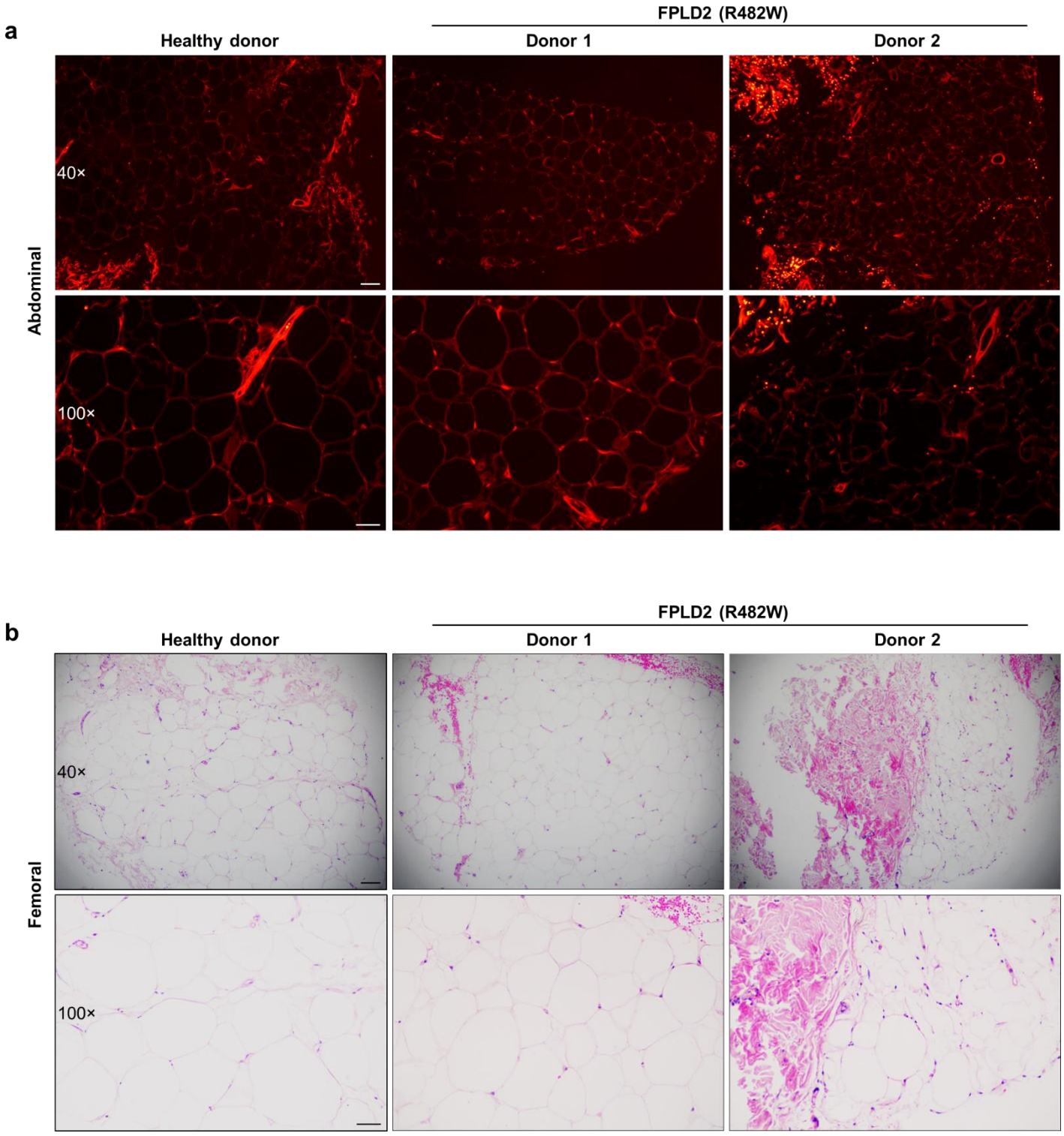


Figure 5.2. Histological assessment of subcutaneous abdominal and femoral adipose tissue from FPLD2 subjects. H&E staining was undertaken for (**a**) subcutaneous abdominal (upper panel, using the fluorescent channel because the bright field image was too weakly stained) and (**b**) subcutaneous femoral (lower panel) adipose tissue biopsies from two related FPLD2 subjects, a father (donor 1) and son (donor 2), carrying the LMNA R482W mutation. Comparison to sample from a healthy donor is shown in the left images. The scale bar is 100 µm at 40× magnification, and 50 µm at 100× magnification.

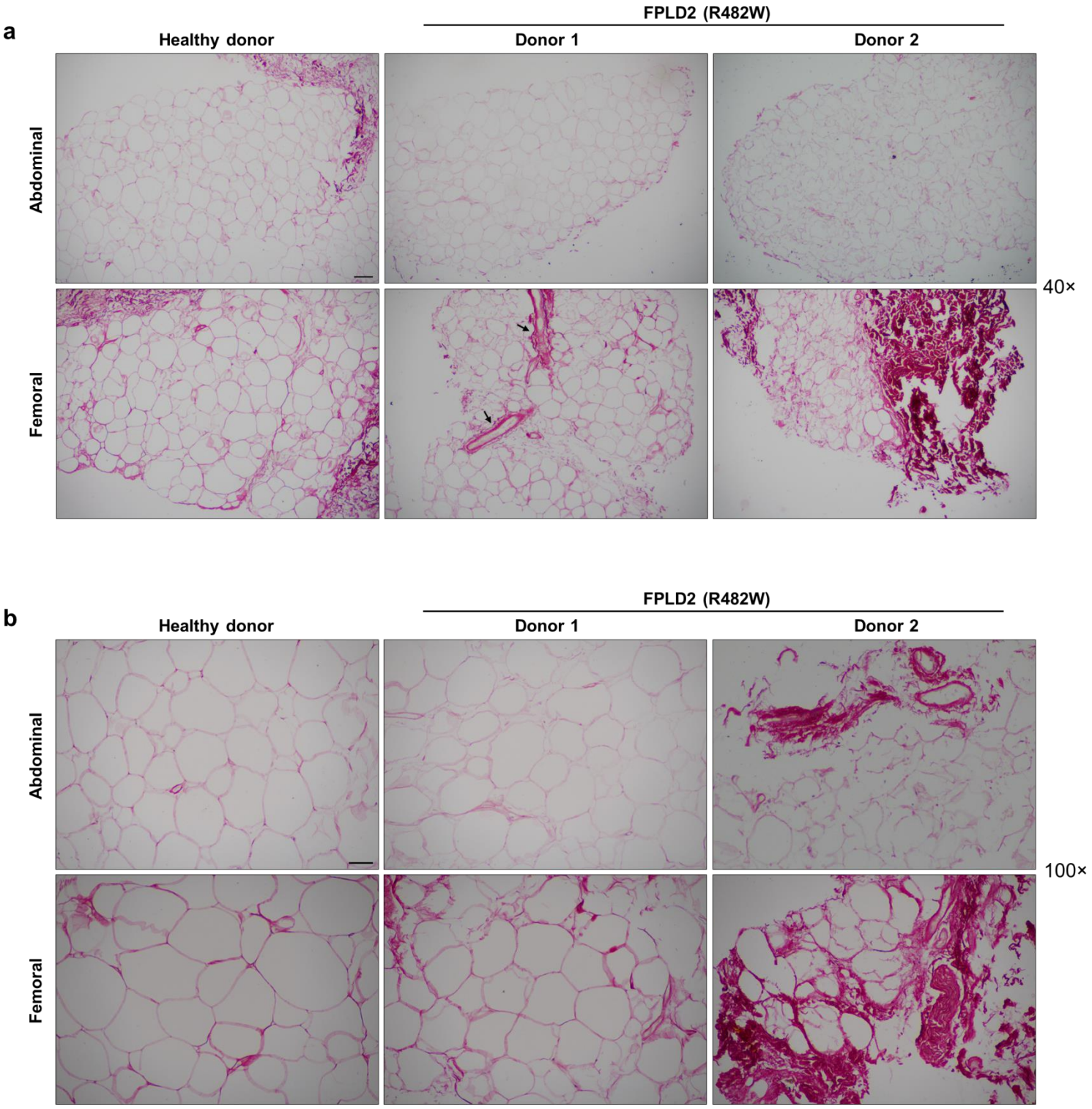


Figure 5.3. Picrosirius red staining images of subcutaneous abdominal and femoral adipose tissue from FPLD2 subjects. Images taken at **(a)** 40× and **(b)** 100× magnification. Arrows in FPLD2 donor 1's femoral sample indicate blood vessels. Comparison to sample from a healthy donor is shown in the left images. The scale bar is 100 µm at 40× magnification, and 50 µm at 100× magnification.

5.3.4 Endogenous *LMNA* expression during differentiation of abdominal and gluteal DFAT cells

The studies from the FPLD2 patients indicated the presence of at least some functional adipose tissue in both abdominal and gluteofemoral depots. Therefore, to further explore the effects of the LMNA mutation on depot-specific adipose expandability and function, I moved to an *in vitro* cell system.

I selected abdominal and gluteal preadipocyte cell lines that (over)expressed either enhanced green fluorescent protein (EGFP), wild-type (WT) LMNA or R482W-mutated LMNA under a Dox-inducible promoter (hereafter referred to as EGFP, LMNA-WT and LMNA-R482W cells). These cell lines were generated by Dr Nellie Loh, as briefly described in section **2.5.5.2**, but had not been evaluated prior to the start of my project. For ease, I aimed to initially characterise the cell lines under 2D culture conditions to assess the effects of LMNA R482W expression on human adipocyte biology, before progressing to 3D culture experiments.

Abdominal and gluteal EGFP cells, to be used as controls, were differentiated into adipocytes (described in **2.6**) to assess the levels of endogenous *LMNA* mRNA expression during proliferation and adipogenic differentiation. Whilst *LMNA* expression assessed by qPCR (described in **5.2.4**) did not differ between EGFP cells from either depot, expression levels changed significantly over time (p<0.0001) (**Figure 5.4**). *LMNA* expression was highest in proliferating preadipocytes the day after seeding (day -2), which decreased in post-confluent cells before adipogenic differentiation was induced (on day 0). Levels of *LMNA* expression further reduced during early adipocyte differentiation (days 2-4), and from day 7 (Abdo) and day 10 (Glut) onwards recovered to levels seen at day 0.

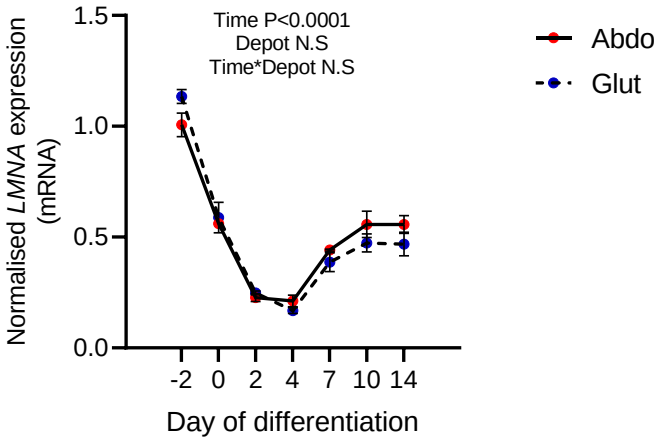


Figure 5.4. Endogenous *LMNA* mRNA expression in abdominal and gluteal EGFP cells. qPCR analysis of *LMNA* mRNA expression in abdominal and gluteal EGFP cells during proliferation (day -2) and a 14 day differentiation time course (days 0-14) (*n* = 3 independent experiments). *LMNA* expression normalised to *18s*. Data presented as mean ± SEM. Statistical significance was assessed by two-way ANOVA with Bonferroni correction for multiple testing. N.S; non-significant.

5.3.5 Induction of *LMNA* expression in preadipocytes

To determine the optimal dose of Dox to induce LMNA overexpression in the cell lines, preadipocytes were treated with a range of Dox concentrations for approximately 48 hours and RNA harvested (described in **5.2.5**).

qPCR analysis (described in **5.2.4**) showed that, in gluteal preadipocytes, increasing the Dox concentration caused *LMNA* mRNA expression to increase linearly in the LMNA-WT and LMNA-R482W cells, with both cell lines showing similar levels of *LMNA* expression upon induction (**Figure 5.5a**). Likewise, in abdominal preadipocytes, increasing the Dox concentration caused *LMNA* mRNA expression in the LMNA-WT cells to increase in a linear fashion, as opposed to LMNA-R482W cells which showed lower *LMNA* expression, plateauing at 0.5 µg/mL Dox. As expected, *LMNA* expression was unaffected by increasing the Dox concentration in the EGFP control cells, however, a concentration dependent increase in green fluorescent signal was observed in these cells (**Figure 5.5b**). Based on these results, I selected a Dox concentration of 0.1 µg/mL in order to overexpress WT and mutant LMNA to similar levels in each preadipocyte cell line and to achieve a 2-3 fold induction above endogenous LMNA expression.

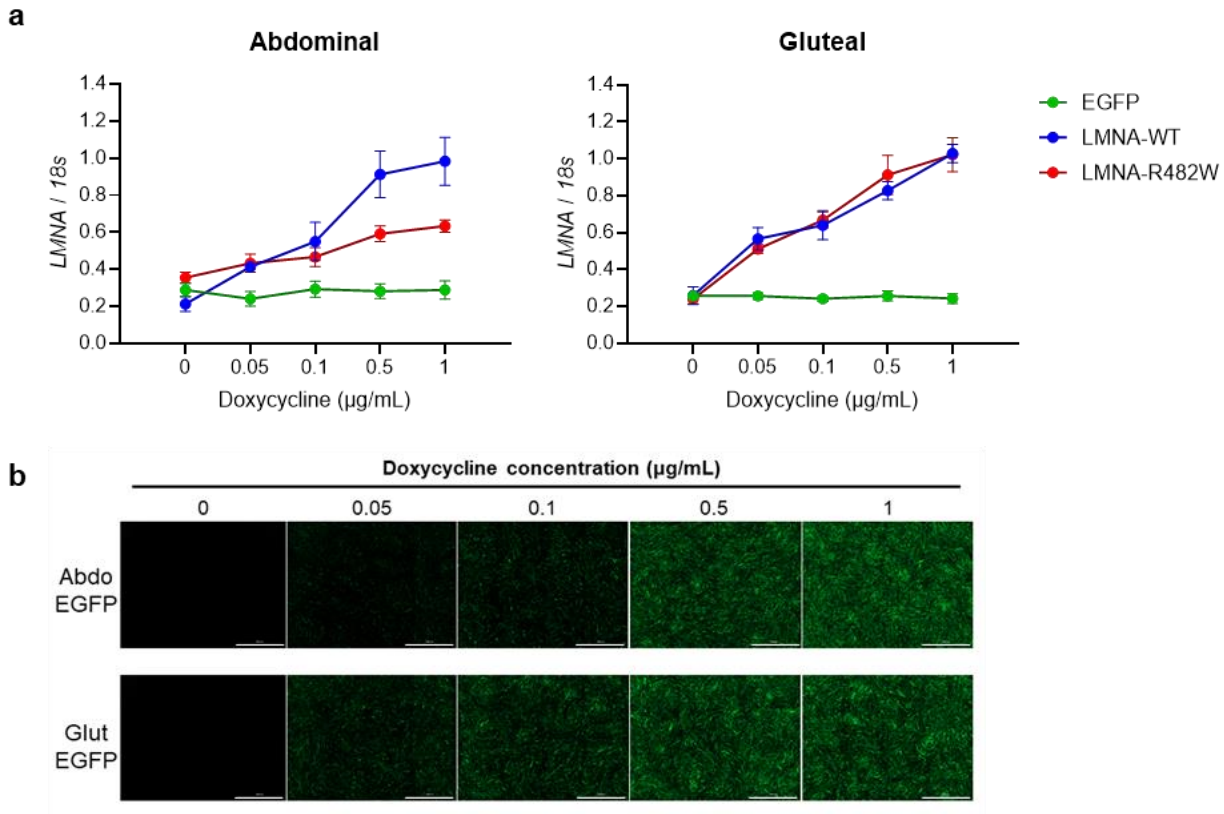


Figure 5.5. Doxycycline dose response curves of abdominal and gluteal Dox-inducible cell lines. (**a**) *LMNA* mRNA expression (normalised to *18S*) in EGFP, LMNA-WT and LMNA-R482W cell lines (*n* = 3 independent experiments). Data presented as mean ± SEM. (**b**) Representative fluorescence micrographs of abdominal and gluteal EGFP cells treated with different doses of doxycycline for 48 hours. Scale bars represent 1000 µm.

5.3.6 Expression of LMNA R482W reduced adipogenesis in both abdominal and gluteal adipocytes *in vitro*

High-content imaging was next used to investigate the effect of R482W-mutated LMNA expression on adipogenesis in fixed 2D cultures (described in **5.2.6**) (**Figure 5.6**). Abdominal and gluteal Dox-inducible preadipocytes were seeded in 96-well plates and treated with or without Dox to overexpress LMNA R482W, prior to adipogenic induction, and differentiated for up to 14 days, with cells fixed on days 0, 7 and 14 for lipid quantification.

Figure 5.6 shows that, on day 7 of differentiation, significantly lower lipid signal area was detected in Dox-untreated abdominal and gluteal LMNA-R482W cell lines compared to EGFP control cells ($p<0.05$). However, the addition of Dox to the LMNA-R482W cells did not result in a further reduction in lipid signal area, which suggested basal transgene expression (leakiness) in the Dox-untreated cells.

To examine if lamin A R482W was expressed in the Dox-untreated samples, cell lysates were collected for Western blotting. The commercial anti-lamin A/C R482W antibody (Novus Biologicals, 5H8-B4) gave inconsistent results and in one experiment detected endogenous lamin A protein in all sample lanes (data not shown). Other members of our research group have also experienced similar issues with the commercial antibody binding non-specifically. I therefore used cDNA from preadipocytes to carry out a SNP genotyping assay to discriminate between WT and mutant alleles.

Leaky LMNA R482W expression was confirmed by SNP genotyping (described in **2.8.3**), with mutant T allele expression detected in Dox-untreated LMNA-R482W preadipocytes from both depots (**Figure 5.7**). This was despite the use of Tetracycline-free FBS in these experiments. Mutant T allele expression was not detected using cDNA from control samples (DFAT EGFP cells and an alternative human preadipocyte cell line derived from a different donor).

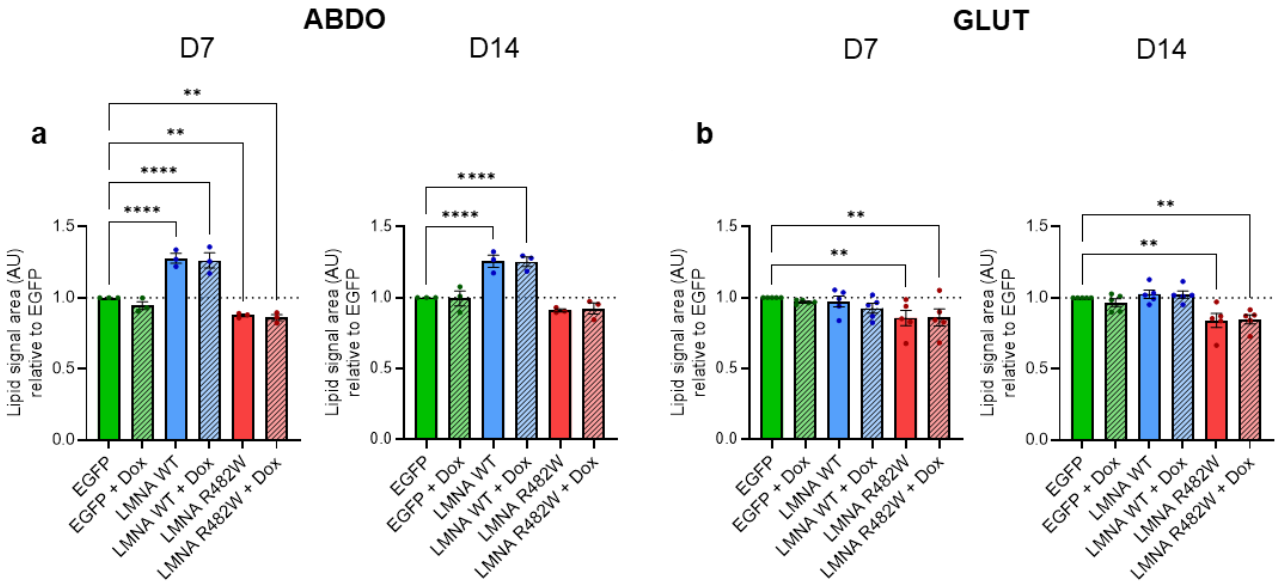


Figure 5.6. Effect of WT and R482W *LMNA* overexpression on adipogenesis in abdominal and gluteal Dox-inducible cells. Lipid fluorescence signal areas measured for differentiated cells fixed on days 7 and 14 of differentiation for abdominal (**a**) (*n* = 3 independent experiments) and gluteal (**b**) (*n* = 5 independent experiments) cells. Preadipocytes were differentiated in the presence of 0.1 µg/mL doxycycline (shaded bars) or left doxycycline-untreated (solid bars) (*n* = 8-16 replicates/treatment). Results are shown relative to lipid signal areas measured for doxycycline-untreated EGFP control cells within each experiment. Data are presented as mean ± SEM. Statistical significance was assessed by two-way ANOVA with Dunnett's multiple comparison test; ***p*<0.005, *****p*<0.0001.

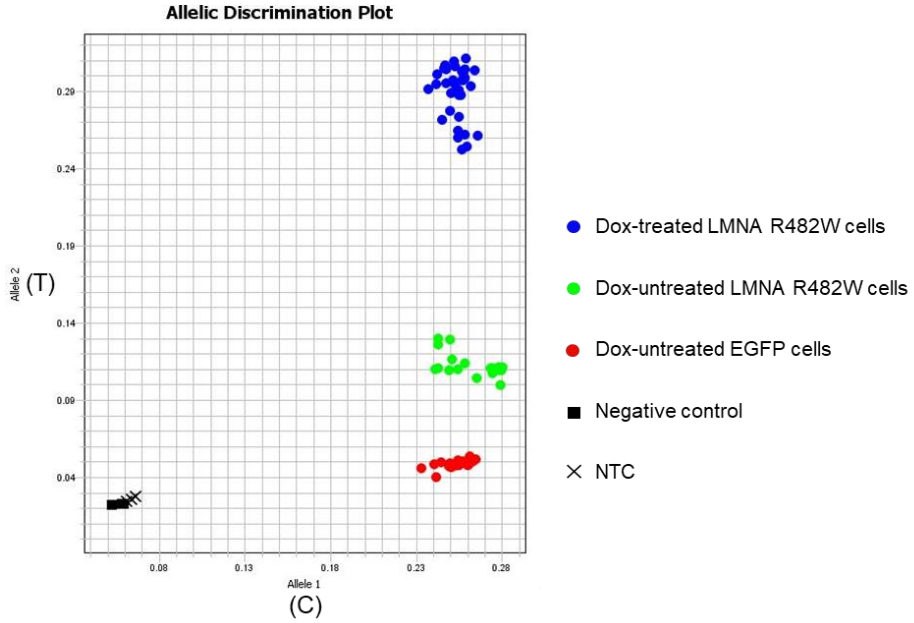


Figure 5.7. Single nucleotide polymorphism (SNP) genotyping of Dox-inducible cell lines showing leaky LMNA R482W expression. Allelic expression analysis of *LMNA* in *in vitro* cultured abdominal and gluteal preadipocytes on day 0 of differentiation (*n* = 3 independent experiments). Expression of C (wild-type [WT], x-axis) and T (mutant, y-axis) alleles were assessed by qPCR using a TaqMan SNP Genotyping Assay, C__64676006_10 (rs57920071). Three distinct clusters are shown representing the cell lines' genotypes: homozygous WT cells (C/C, red cluster) and heterozygous mutant cells (C/T, green *and* blue clusters). Each data point represents one well (technical replicate) in qPCR, with three wells ran per sample. Dox, doxycycline; NTC, no-template control.

Interestingly, in abdominal-derived cells, high-content imaging revealed that adipocyte differentiation was significantly higher in the LMNA-WT cells compared to EGFP control cells on day 7 of differentiation (p<0.0001) (**Figure 5.6**). On day 14 of differentiation, only gluteal LMNA-R482W cells displayed lower lipid signal area compared to control cells (p<0.005), while abdominal LMNA-R482W and EGFP cells had differentiated comparably. The lipid signal areas remained significantly higher in differentiated abdominal LMNA-WT cell lines than in control cells on day 14 (p<0.0001). Interestingly, the higher differentiation capacity of the abdominal LMNA-WT cells occurred irrespective of Dox treatment, possibly due to leakiness of the Tet-On inducible expression system.

Taken together, these results suggest that LMNA R482W expression reduced differentiation of gluteal preadipocytes, which was present during both early and late time points of adipogenesis. In contrast, in abdominal cells, a reduction in lipid signal area was only observed on day 7 which lost significance by day 14. These data also suggest that WT LMNA overexpression promoted adipogenesis in abdominal, but not gluteal, preadipocytes.

5.3.7 Validation of high-content imaging for quantifying adipogenesis in 2D culture

The use of high-content imaging for quantifying adipogenesis may underestimate the actual lipid content of cells, as it analyses 2D images of spherical lipid droplets, and is therefore not a direct measure of intracellular TG concentration. Therefore, validation experiments were performed using EGFP cells differentiated for 9 days with varying concentrations of an exogenous FA mixture, for high-content imaging, and parallel biochemical measurement of intracellular TG content (described in **5.2.7**). Positive correlations were found between cellular TG concentration with both the raw (**Figure 5.8b**) and normalised (**Figure 5.8c**) lipid signal areas, confirming the validity of the imaging-based method for quantifying adipogenesis.

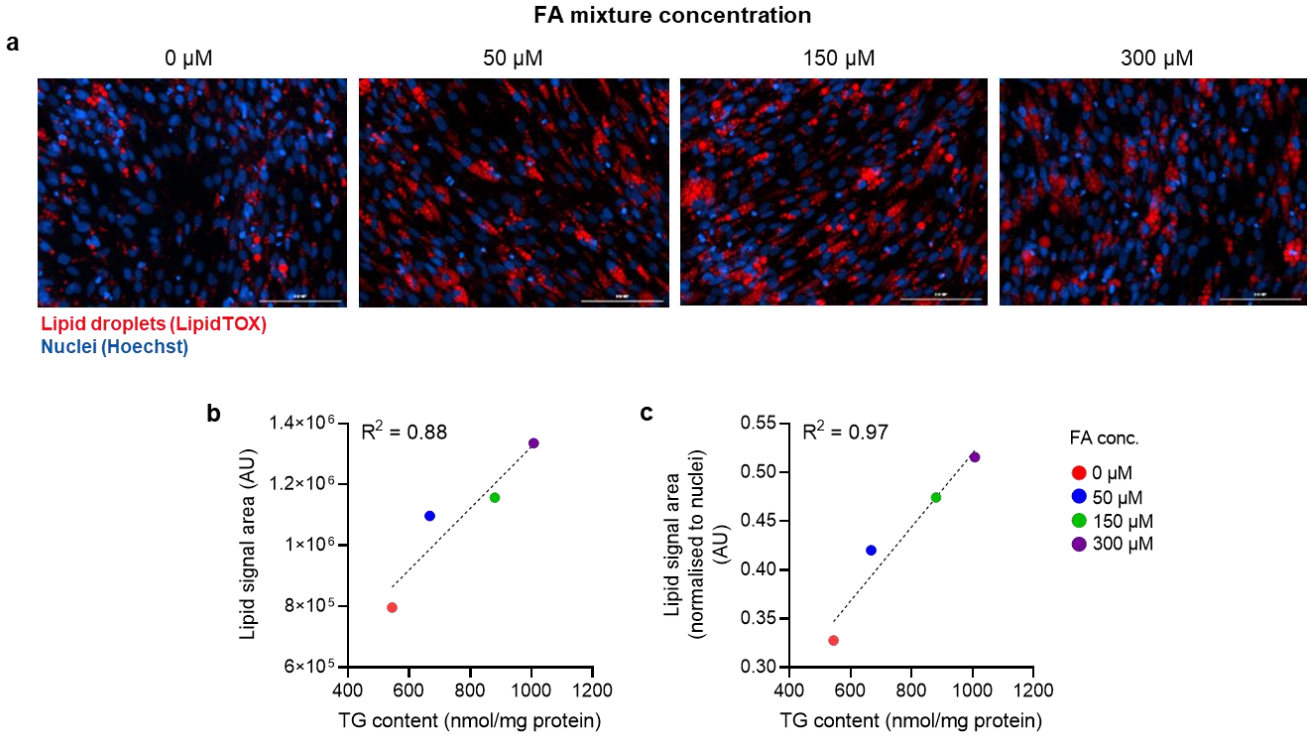


Figure 5.8. Validation of *in vitro* adipogenesis assay. (**a**) Representative fluorescence micrographs of gluteal EGFP cells on day 9 of differentiation (20× magnification) treated with different concentrations of an exogenous fatty acid (FA) mixture (n = 3-8 wells/treatment). Scale bars represent 100 µm. (**b**) Relationship between total lipid signal area and intracellular triglyceride (TG) content (normalised to protein content) of cells differentiated in parallel in the presence of 0 µM, 50 µM, 150 µM or 300 µM of an exogenous FA mixture. (**c**) Relationship between total lipid signal area (normalised to nuclei) and TG content. The R-squared values from the correlation analysis (performed in GraphPad Prism) are displayed in the graphs.

5.3.8 *LMNA* overexpression reduced abdominal but not gluteal preadipocyte proliferation *in vitro*

Overexpression of LMNA has been demonstrated to affect cell proliferation (Piekarowicz, *et al*., 2017), and there is evidence that A-type lamins play important roles in cell cycle regulation (Andrés & González, 2009). Therefore, to investigate the effect of WT and R482W-mutated LMNA overexpression on preadipocyte growth, proliferation experiments were conducted. Abdominal and gluteal preadipocytes seeded at a low density were cultured with or without Dox for 48 hours for calculation of cell doubling times as described in section **5.2.8**.

Dox, used at 1 µg/mL, has been reported to significantly alter proliferation in various human cell lines, with milder effects still observed at 0.1 µg/mL in some cell lines (Ahler, *et al*., 2013). However, both abdominal and gluteal EGFP preadipocytes showed no difference in their cell doubling times whether treated or untreated with 0.1 µg/mL Dox for 48 hours (**Figure 5.9**). In gluteal preadipocytes, WT or mutant LMNA overexpression did not affect cell doubling times compared to Dox-untreated EGFP cells.

In contrast, in abdominal preadipocytes, Dox-induced WT (p<0.0001) and R482W-mutated (p=0.076) LMNA overexpression increased cell doubling times compared to EGFP control cells. Abdominal cells with Dox-induced WT LMNA overexpression were the slowest at proliferating with a mean doubling time of ~29.4 hours compared with controls. This effect was slightly increased when cells were treated with a higher concentration of Dox (0.5 µg/mL), extending the mean doubling time to ~31.0 hours (**Figure 5.10**); this supports a dose-dependent effect of WT LMNA expression on proliferation. Interestingly, abdominal LMNA-WT cells without Dox treatment also exhibited slower proliferation compared to EGFP controls (**Figure 5.9** and **Figure 5.10**). As this is directionally consistent with the effects of WT LMNA overexpression on proliferation, these results provide further evidence for leaky transgene expression in the cell lines and corroborate the SNP genotyping results (**Figure 5.7**).

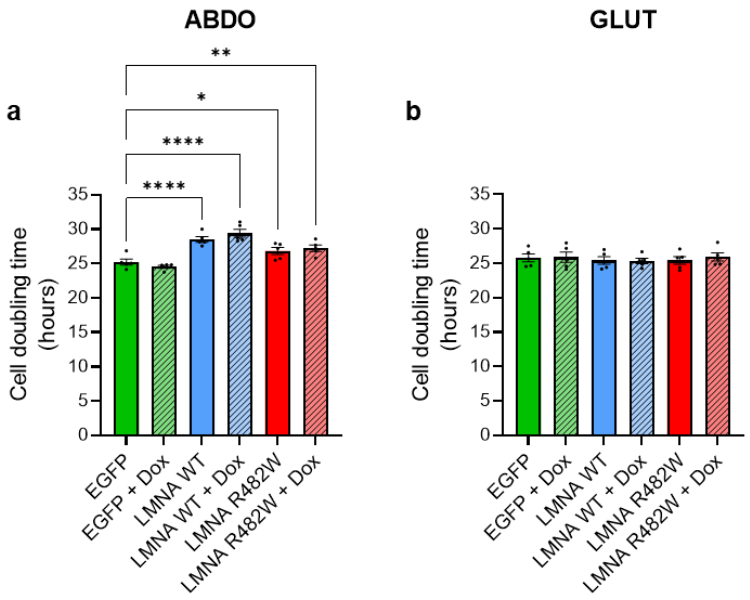


Figure 5.9. Effect of WT and R482W LMNA overexpression on proliferation of abdominal and gluteal Dox-inducible preadipocytes. Cell doubling times for abdominal (**a**) and gluteal (**b**) preadipocytes treated with 0.1 µg/mL doxycycline (shaded bars) or without doxycycline (solid bars) for 48 hours (*n* = 5 independent experiments, *n* = 8-16 replicates each). Data are presented as mean ± SEM. Statistical significance was assessed by two-way ANOVA with Dunnett's multiple comparison test; **p*<0.05, ***p*<0.01, *****p*<00001.

Apparent changes in proliferation based on cell counts may actually reflect altered cell death rates rather than true differences in proliferation. Therefore, to assess cell viability, cultured cells were stained with propidium iodide and Hoechst for a differential nuclear staining (DNS) assay (Lema, *et al*., 2011) (described in **5.2.9**). Quantification of cell death (percentage of viable cells of total cell number) showed that Dox treatment did not induce cell death, nor did LMNA overexpression, in the preadipocyte cell lines (**Figure 5.11**).

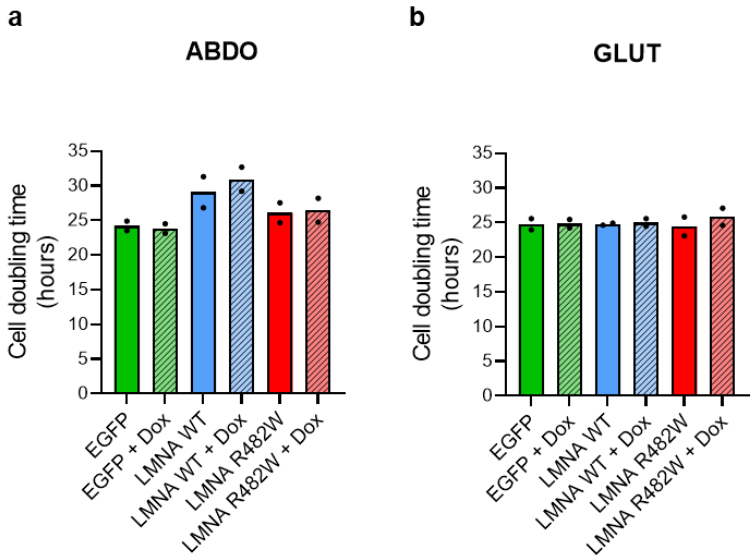


Figure 5.10. Cell doubling times of abdominal (a) and gluteal (b) preadipocytes after 48 hour doxycycline treatment at higher dosage (0.5 µg/mL). *n* = 2 independent experiments, *n* = 8 replicates each.

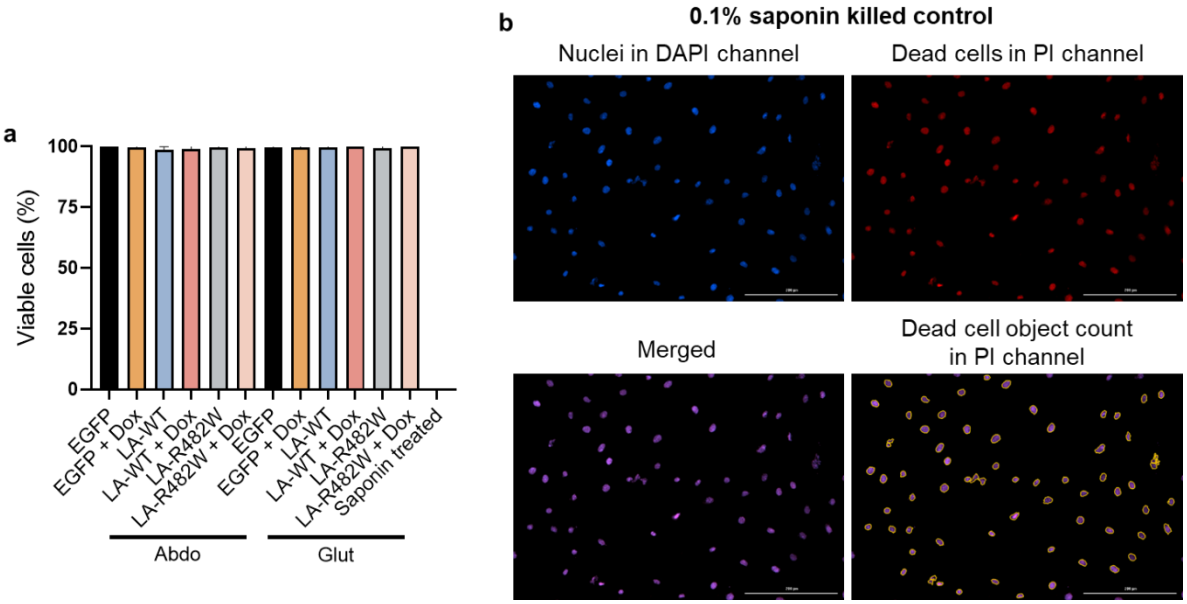


Figure 5.11. Differential nuclear staining assay on preadipocytes. Preadipocytes undergoing proliferation were treated with Hoechst and propidium iodide (PI) for detection of all nuclei or dead cells, respectively, to calculate the number of viable cells after 48 hour doxycycline treatment (at 0.1 µg/mL concentration). Cells were incubated with dyes for 1 hour prior to imaging. (**a**) Percentage of live cells determined by high-content imaging after treatment. *n* = 5-8 replicates each. Data are mean SD. (**b**) Fluorescent micrographs showing dead cell control well (treated with 0.1% saponin to permeabilise cells). The number of dead cell objects (PI-positive nuclei) and live cell objects (Hoechst-positive nuclei) were counted in Gen5 software. Scale bars represent 200 µm.

The retinoblastoma (Rb) protein regulates cell cycle progression by controlling the G1 to S phase transition. Given that endogenous lamin A has been previously shown to regulate the stability of Rb protein (Johnson, *et al*., 2004), and to investigate whether the effects on proliferation seen in abdominal cells could be linked to entry into S-phase, I treated the Dox-inducible cell lines with EdU reagent pre- and post- differentiation induction (**Figure 5.12**) (described in **5.2.10**).

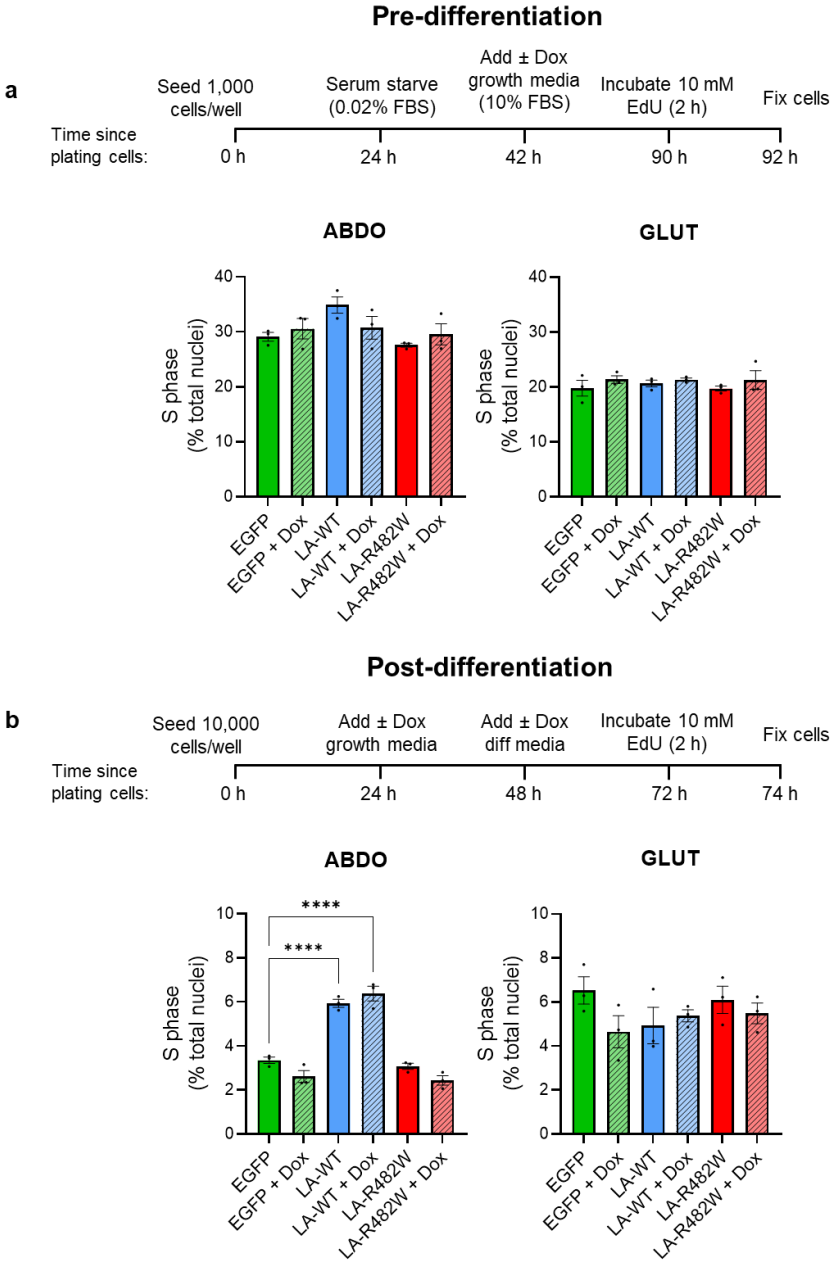


Figure 5.12. Quantification of abdominal and gluteal preadipocytes in S-phase of the cell cycle. EdU labelling was performed on preadipocytes, treated with doxycycline (shaded bars) or without doxycycline (solid bars), pre- (**a**) and post-differentiation (**b**) induction (n = 3 wells/group). Cell nuclei positive for EdU were quantified by high-content imaging. Data are presented as mean ± SEM. Statistical significance was assessed by two-way ANOVA with Dunnett's multiple comparison test; ****p<0.0001.

EdU is a thymidine analogue that is incorporated into newly synthesised DNA during S-phase of the cell cycle and so can be used to identify and quantify proliferating cells. No significant differences in S-phase cells were found before adipogenic induction in preadipocytes from either depot (**Figure 5.12a**). However, a higher proportion of S-phase cells was detected for abdominal Dox-treated and untreated LMNA-WT cells approximately 24 hours after induction compared to control cells (**Figure 5.12b**).

Taken together, these results indicate that WT and R482W LMNA overexpression reduced the proliferation rate of dividing preadipocytes in the abdominal, but not gluteal depot, yet there was no change in the proportion of abdominal cells in S-phase or in their viability. Conversely, the abdominal LMNA-WT cells showed an increased proportion of S-phase cells after the first 24 hours of differentiation indicating a higher rate of proliferation. Indeed, high-content fluorescent imaging confirmed higher numbers of cells (nuclei) in differentiated abdominal LMNA-WT cultures (data not shown).

5.3.9 Overexpression of LMNA R482W increased nuclear shape defects in gluteal preadipocytes more than in abdominal preadipocytes

Primary skin fibroblasts from FPLD2 patients with the LMNA R482W mutation have been shown to have abnormally shaped nuclei in a subset of cells (Vigouroux, *et al*., 2001). Ectopic expression of LMNA R482W and other LMNA mutants have also been shown to cause nuclear deformities in different cell types, for example in endothelial cells (Bidault, *et al*., 2013) and HEK 293 cells (Piekarowicz, *et al*., 2017). Indeed, nuclear shape irregularities, such as protrusions of the nuclear envelope (blebs), are considered a hallmark of LMNA-related disorders. To investigate the effect of R482W-mutated LMNA overexpression on nuclear morphology in preadipocytes, I conducted a high-throughput image analysis of Dox-treated and untreated cells using CellProfiler (**Figure 5.13**) (described in **5.2.11**).

In proliferating preadipocytes from either depot, no differences in nuclear roundness or solidity were seen in EGFP cells, with or without Dox induction, ruling out an independent effect of Dox treatment on nuclear morphology (**Figure 5.13a, b, c, d**). In gluteal preadipocytes, Dox-treated LMNA-R482W cells showed a significant reduction in nuclear roundness (p<0.0001) and solidity (p<0.0001) compared to EGFP control cells (**Figure 5.13b, d**). This differed from overexpression of WT LMNA where nuclei were more rounded (p<0.0001) (**Figure 5.13b**).

Less pronounced effects of the LMNA mutation were seen in abdominal preadipocytes with reduced nuclear solidity (p=0.0011), but no effect on nuclear roundness (**Figure 5.13a, c**). Interestingly, abdominal LMNA-WT cells untreated with Dox exhibited lower nuclear roundness compared to control cells which was restored to control levels upon Dox treatment (**Figure 5.13a**).

There are various types of nuclear shape abnormalities such as nuclear blebs, nuclear envelope invaginations and micronuclei (Janssen, *et al*., 2022). Nuclear blebbing was observed as the main reason for the greater reduction in solidity values in gluteal mutant cells. To quantify the proportion of irregular nuclei, I calculated the percentage with a nuclear irregularity index (NII, defined as 1 – solidity) greater than 0.05, using the threshold established by Stephens *et al*. (2018). This threshold was applied in this analysis, as nuclei with the most irregular shapes, including those with significant blebbing, exceeded this value (**Figure 5.13e**). Nearly 14% of nuclei in gluteal cells induced to overexpress LMNA R482W displayed NII values > 0.05, compared to only ~4% in EGFP control cells. In contrast, in the abdominal samples, ~5% of LMNA-R482W cells were above this threshold, which was similar to Dox-treated LMNA-WT cells, compared to ~3% in control cells (**Figure 5.13f, g**).

To test whether increasing the expression of LMNA R482W would worsen nuclear morphology defects, preadipocytes were treated with a higher Dox concentration (0.5 µg/mL) (**Figure 5.14**). During these experiments, I found that nuclear solidity in gluteal LMNA-R482W cells was further reduced and the percentage of nuclei with NII > 0.05 increased to ~22% (**Figure 5.14d**), predominately as a result of increased frequency and severity of nuclear blebs, as shown in **Figure 5.14e**. In abdominal LMNA-R482W cells, whilst the higher Dox treatment also increased the percentage of cells with NII above 0.05 to ~10%, the effect was less than in gluteal samples and the severity of nuclear deformities was less pronounced.

When imaging experiments were repeated using 0.1 µg/mL Dox for induction, but nuclear morphology analysed in growth-arrested confluent preadipocytes, the effect of LMNA R482W overexpression on lowering nuclear roundness in gluteal cells was not replicated (**Figure 5.15b**). This suggests that increased nuclear abnormalities occur during proliferation. In contrast, the effect of WT LMNA overexpression on increasing nuclear roundness in gluteal cells was still observed in confluent samples.

Altogether, these results indicate that increased nuclear shape abnormalities occur in gluteal preadipocytes over abdominal cells during proliferation upon induction of LMNA R482W overexpression.

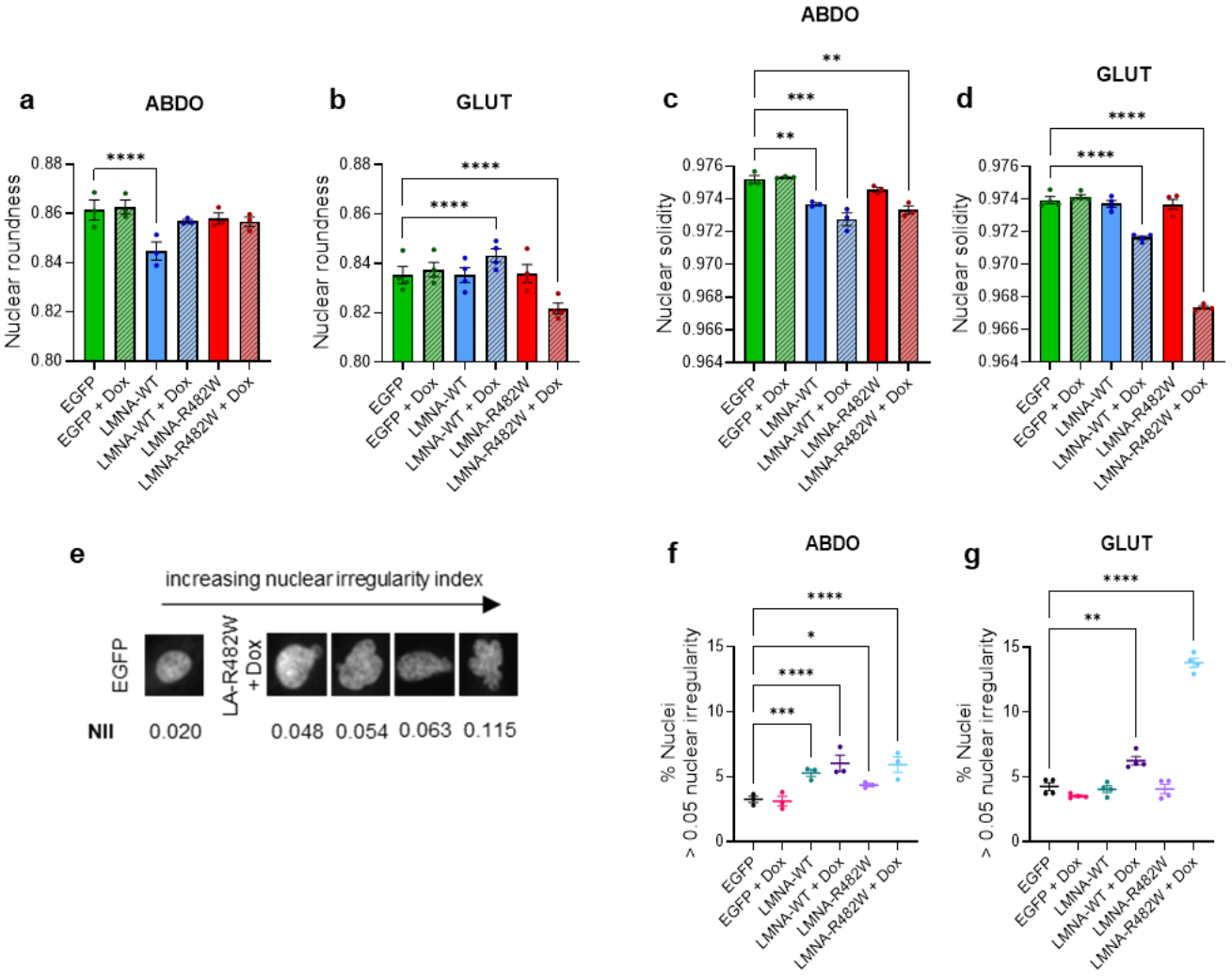
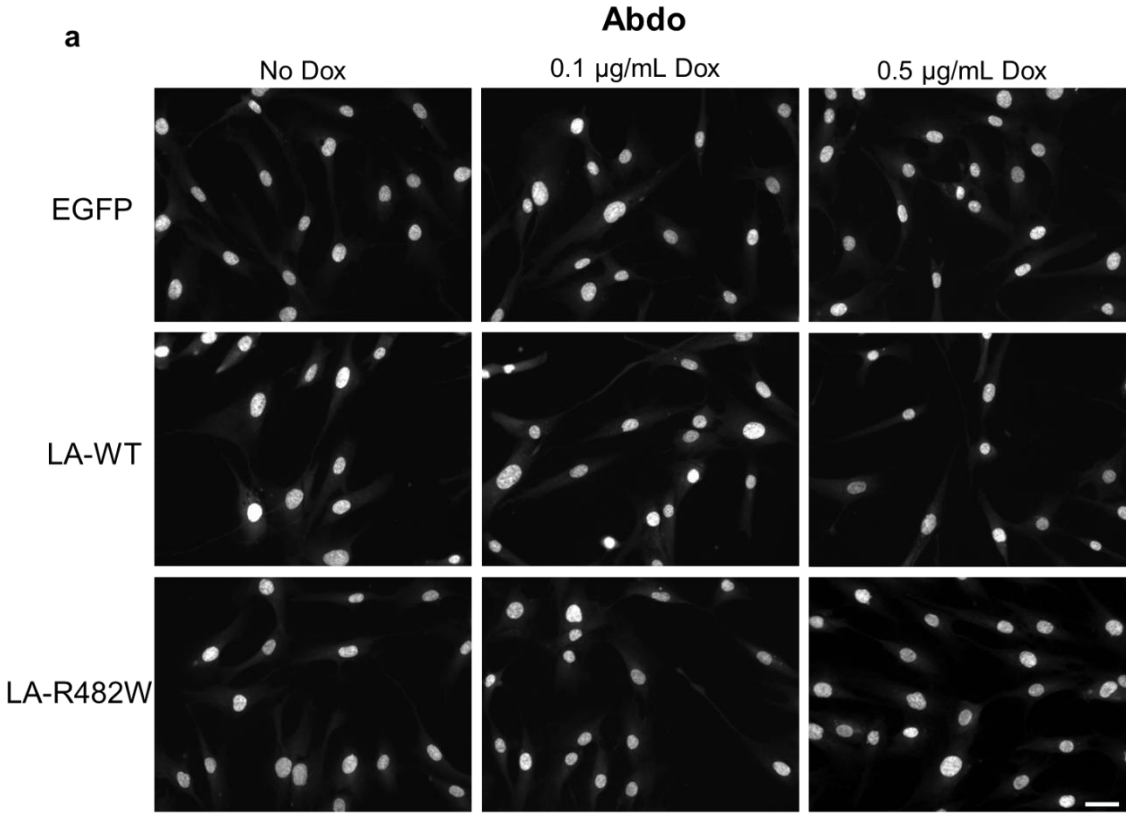
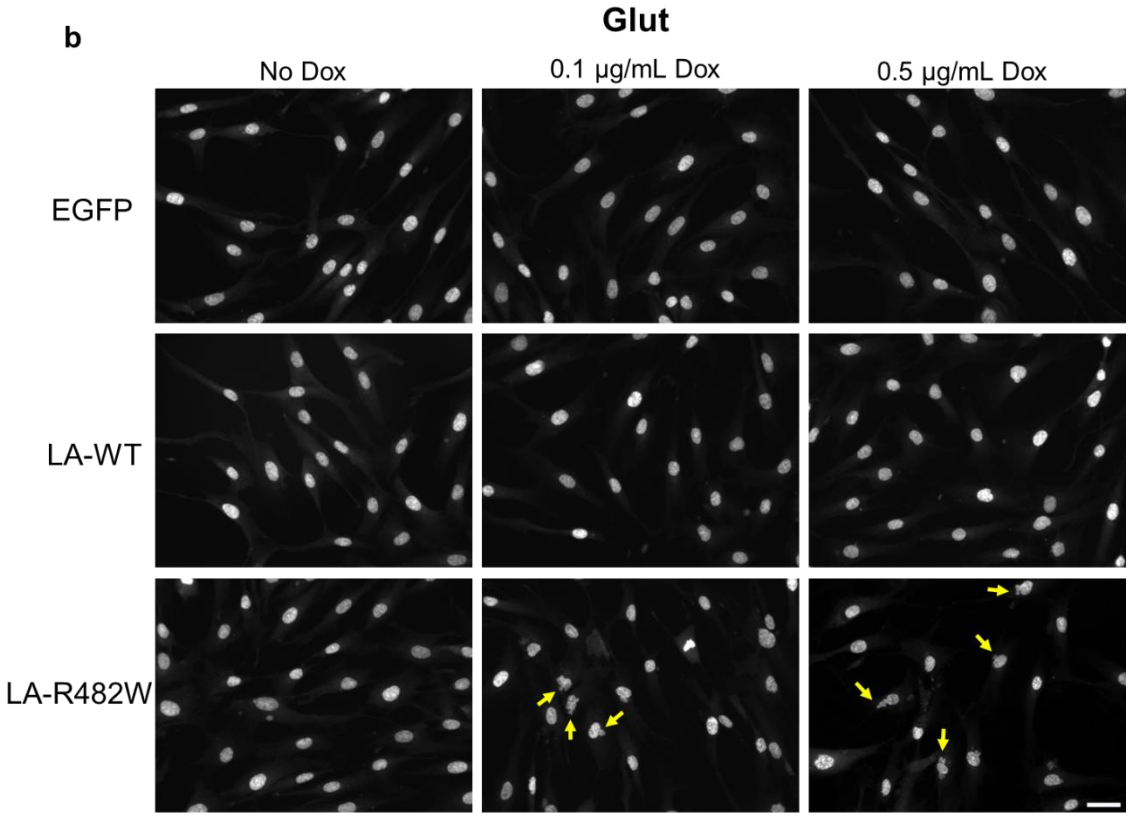
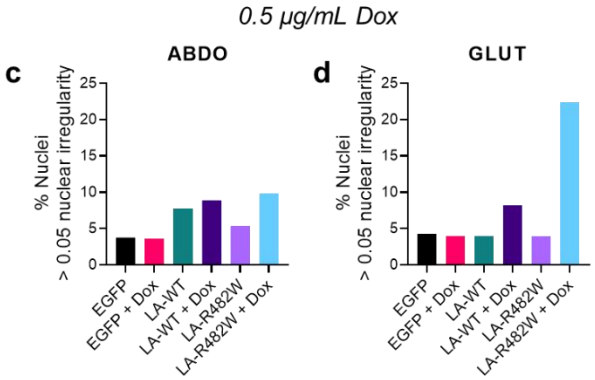


Figure 5.13. Effect of WT and R482W LMNA overexpression on nuclear morphology in abdominal and gluteal preadipocytes during proliferation. (**a**) Nuclear morphology analysis of *in vitro* cultured preadipocytes from abdominal (n = 3 independent experiments) and gluteal (n = 4 independent experiments) depots after 48 hour doxycycline (Dox) treatment. Each data point represents the mean nuclear roundness (**a** and **b**) and solidity (**c** and **d**) of 2,020-3,557 nuclei (abdominal cells, **a** and **c**) or 2,194-3,901 nuclei (gluteal cells, **b** and **d**) from each experiment. (**e**) Representative fluorescence micrographs of Hoechst-stained nuclei in gluteal-derived preadipocytes with increasing nuclear irregularity index (NII, 1 – solidity) values, showing increased nuclear shape deformities from left to right. Percentage of misshapen nuclei with NII above 0.05 for abdominal (**f**) and gluteal (**g**) cells. All data are presented as mean ± SEM. Statistical significance was assessed by two-way ANOVA with Dunnett's multiple comparison test; *p<0.05, **p<0.005, ***p<0.001, ****p<00001.


a
Abdo
No Dox
0.1 µg/mL Dox
0.5 µg/mL Dox
EGFP
LA-WT
LA-R482W


b
Glut
No Dox
0.1 µg/mL Dox
0.5 µg/mL Dox
EGFP
LA-WT
LA-R482W


0.5 µg/mL Dox
c
ABDO
% Nuclei > 0.05 nuclear irregularity
0
5
10
15
20
25
EGFP
EGFP + Dox
LA-WT
LA-WT + Dox
LA-R482W
LA-R482W + Dox
d
GLUT
% Nuclei > 0.05 nuclear irregularity
0
5
10
15
20
25
EGFP
EGFP + Dox
LA-WT
LA-WT + Dox
LA-R482W
LA-R482W + Dox

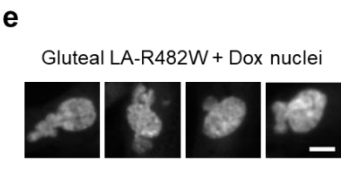

e
Gluteal LA-R482W + Dox nuclei

Figure 5.14. Higher doxycycline treatment exacerbated the nuclear morphology defects in gluteal preadipocytes overexpressing LMNA R482W. Representative fluorescent micrographs of Hoechst-stained nuclei in Dox-inducible abdominal (**a**) and gluteal (**b**) preadipocytes treated with 0, 0.1 or 0.5 µg/mL doxycycline for 48 hours. Images were acquired by high-content imaging at 20× magnification. The yellow arrows indicate nuclear blebs in doxycycline-treated gluteal mutant preadipocytes overexpressing LMNA R482W. Scale bars represent 40 µm. Percentage of misshapen nuclei with nuclear irregularity index (NII) above 0.05 for abdominal (**c**) and gluteal (**d**) cells (*n* = 1 experiment, 1,928-3,869 nuclei analysed per condition). (**e**) Zoomed-in images of blebbed nuclei in gluteal LMNA-R482W cells treated with 0.5 µg/mL doxycycline. Scale bar represents 10 µm.

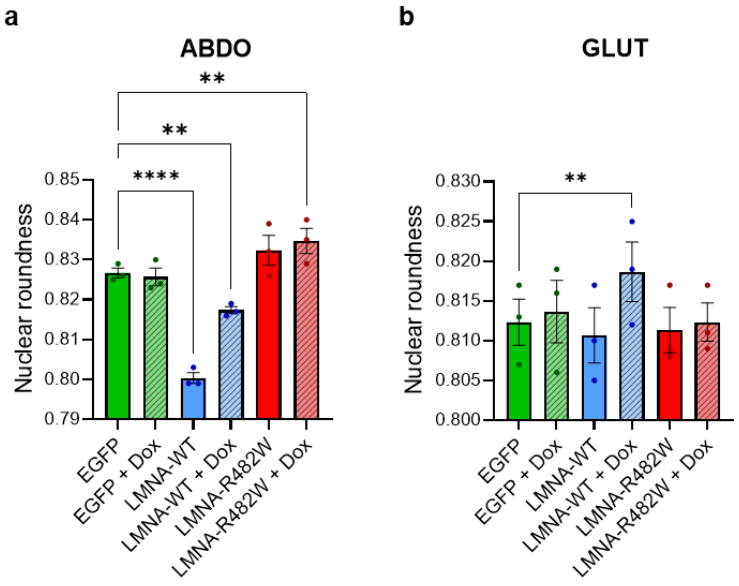


Figure 5.15. Effect of WT and R482W LMNA overexpression on nuclear roundness in confluent abdominal and gluteal preadipocytes. Nuclear roundness in growth-arrested confluent preadipocytes for abdominal (**a**) and gluteal (**b**) preadipocytes treated with 0.1 µg/mL doxycycline (shaded bars) or without doxycycline (solid bars) for 24 hours (*n* = 3 independent experiments, >4,000 nuclei analysed per group). Data are presented as mean ± SEM. Statistical significance was assessed by two-way ANOVA with Dunnett's multiple comparison test; ***p*<0.01, *****p*<0.0001.

5.3.10 Characterisation of LMNA R482W mutant spheroids

Having characterised LMNA mutant cells under 2D culture conditions, I then progressed to 3D culturing, this being more reflective of physiological conditions. The Dox-inducible cell lines were initially expanded in 2D culture and harvested for spheroid fabrication by mixing with the ULGTA-based hydrogel. Automated liquid handlers were used to generate and culture abdominal and gluteal preadipocyte spheroids as described in section **2.2.1**.

After allowing cells to condense within hydrogel droplets for 24 hours, spheroids were treated with Dox to overexpress EGFP, WT LMNA or R482W-mutated LMNA. After a further 24 hours, preadipocyte spheroids were then induced to undergo adipogenic differentiation, either with or without exogenous FAs, for up to 14 days and fixed for analysis. The visualisation of EGFP signal at the start and end of the differentiation period in control spheroids, as shown using fluorescent imaging (**Figure 5.16**), was indicative of their viability.

During differentiation, spheroids made from each Dox-inducible cell line expanded in size as cells proliferated following adipogenesis induction (**Figure 5.17**). At day 14, abdominal LMNA-WT spheroids were significantly larger than EGFP control spheroids ($p<0.0001$), with an average diameter of 688 ± 47 µm compared to 527 ± 30 µm (n = 16 spheroids each) for the FA-treated samples; this was consistent with their increased proliferation capacity observed during differentiation in 2D culture. Gluteal LMNA-R482W spheroids were significantly smaller than both LMNA-WT ($p=0.0012$) and EGFP ($p<0.0001$) spheroids for the FA-treated samples on day 14. Interestingly, the addition of FAs during differentiation did not significantly change the overall size of the spheroids for any of the cell lines.

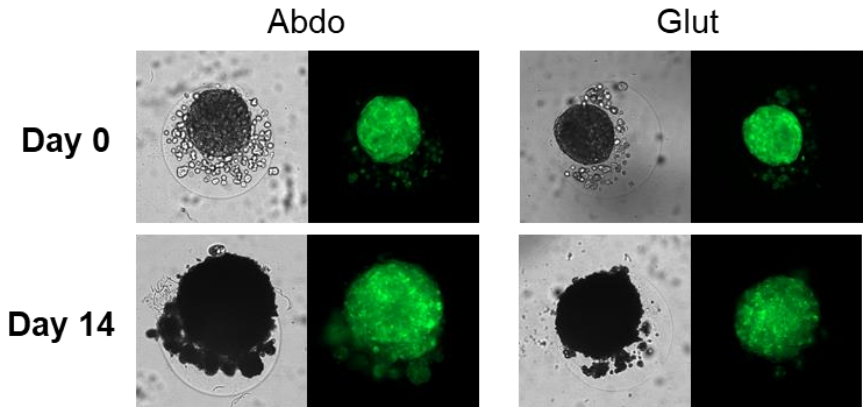


Figure 5.16. Representative bright field and fluorescent micrographs of abdominal and gluteal EGFP spheroids on days 0 and 14 of differentiation. Spheroids were induced to express EGFP by adding 0.1 µg/mL doxycycline to the culture media.

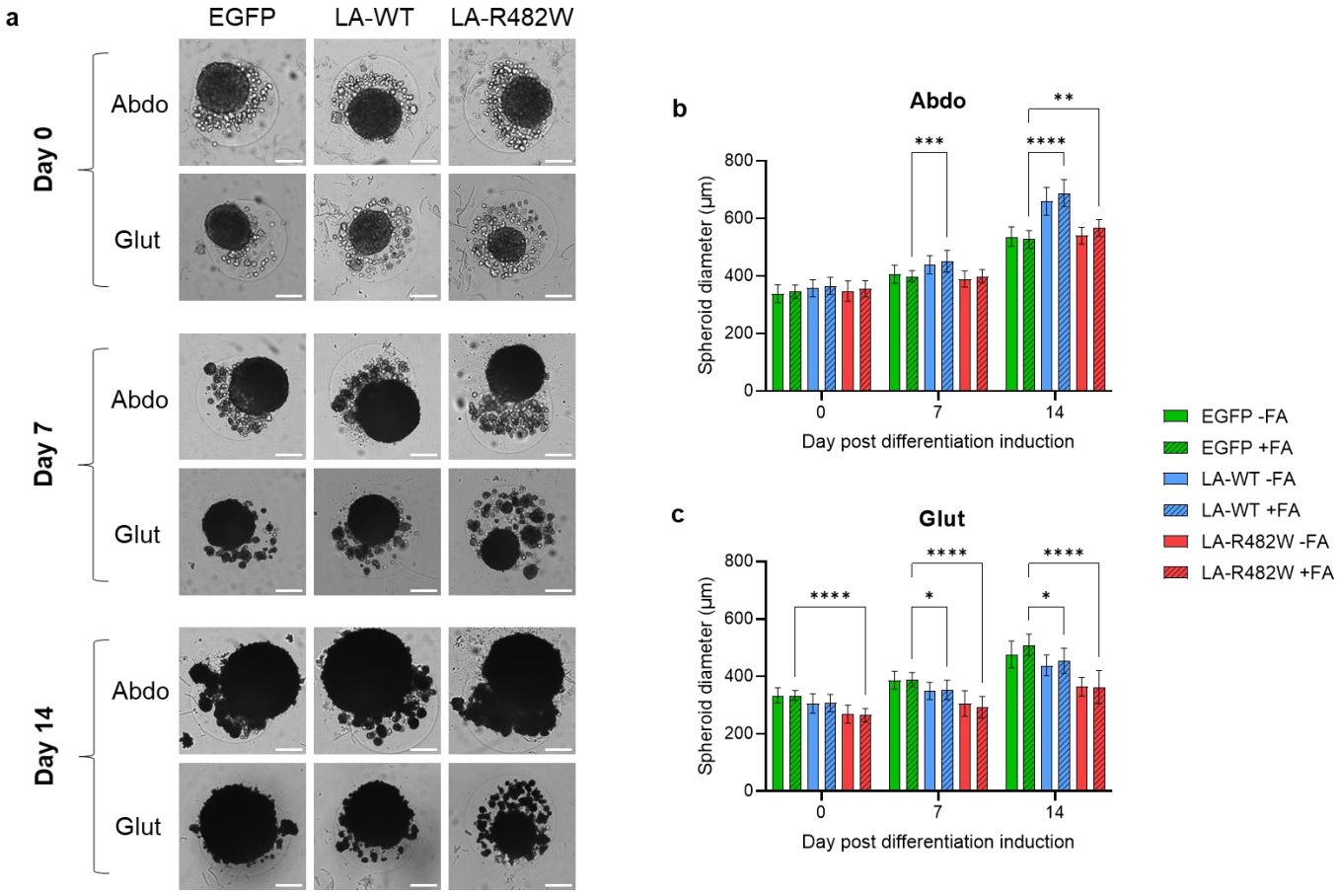


Figure 5.17. Sizes of LMNA R482W mutant spheroids during *in vitro* differentiation. (**a**) Representative bright field micrographs of fatty acid-untreated (-FA) abdominal (Abdo) and gluteal (Glut) adipose spheroids, made from Dox-inducible cell lines overexpressing EGFP, LMNA-WT or LMNA-R482W. Scale bars represent 200 µm. Sizes of abdominal (**b**) and gluteal (**c**) spheroids on days 0, 7 and 14 of differentiation, with (+FA) or without (-FA) fatty acid treatment. *n* = 12-16 spheroids/condition. Data are presented as mean ± SD. Statistical significance was assessed by two-way ANOVA with Bonferroni correction for multiple testing; **p*<0.05, ***p*<0.005, ****p*<0.001, *****p*<00001. Only statistically signficant comparisons between FA-treated EGFP spheroids and other FA-treated groups are shown.

Spheroids fixed on day 12 or 14 of differentiation were fluorescently labelled for lipid droplets and nuclei to assess adipogenesis. BODIPY 493/503 staining could not be used to quantify adipogenesis via high-content imaging due to emission spectra overlap with EGFP expression in the control spheroids. Therefore, the LipidTOX™ Red neutral lipid stain was tested as an alternative fluorescent dye for lipid droplets (described in **5.2.12**). However, fluorescence images obtained with the Cytation revealed that the dye predominately stained peripheral cells (data not shown), suggesting either limited dye penetration with the adopted staining protocol or the presence of undifferentiated cells in the spheroid centre.

As my previous work in 2D culture involved differentiating cells with exogenous FAs added, confocal imaging was only performed for the FA-treated samples to assess the lipid droplet morphologies of peripheral cells in greater detail. As shown in **Figure 5.18**, confocal imaging confirmed the presence of multilocular lipid droplets in all spheroids, demonstrating successful differentiation across the cell lines. Thus, whilst gluteal LMNA mutant spheroids were clearly capable of differentiation, their overall sizes were smaller than controls (**Figure 5.17**) suggesting impaired proliferation during differentiation.

It should be noted that the gluteal LMNA-R482W spheroids displayed varying levels of differentiation efficiency across the three experiments. A lower differentiation efficiency was visually observed compared to EGFP spheroids in one experiment, whereas in others the differentiation appeared similar. The cause of this variability remains unclear but may be attributed to technical factors or biological variability.

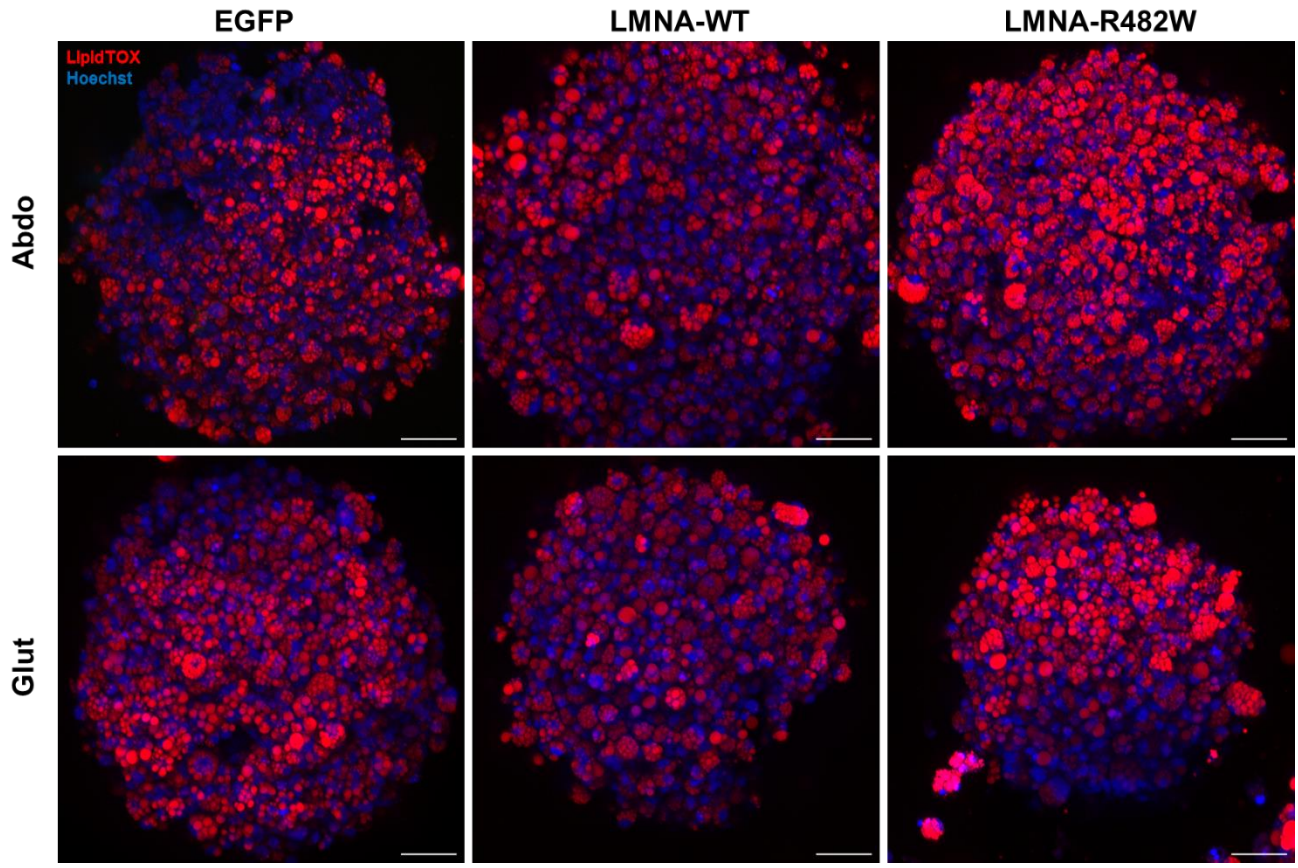


Figure 5.18. Confocal imaging of lipid droplets in LMNA spheroids at day 12 of differentiation. Images are maximum intensity projections of fatty acid-treated (+FA) spheroids after 12 days of adipogenic differentiation (from experiment 3). Spheroids were stained for lipid droplets (LipidTOX™ neutral lipid stain, red) and nuclei (Hoechst 33342, blue). Identical brightness and contrast settings were applied to all images in Fiji/Image J. Scale bars represent 50 µm.

As it was not possible to visualise the morphology of the central cells by confocal, the FA-treated spheroids next underwent histological processing. H&E staining showed larger sized lipid droplets in gluteal EGFP spheroids than in abdominal at day 14 (**Figure 5.19**), as seen in the previous chapter when optimising the human spheroid model. Cavities were also frequently observed across all conditions, likely resulting from cellular organisation in the hydrogel, consistent with my observations detailed in **Chapter 4**.

Without quantifying the lipid droplet sizes, and based purely on visual observations, there were few notable differences between LMNA-R482W and EGFP control spheroids for both depots. The only notable difference was in abdominal LMNA-WT spheroids, which appeared to have larger lipid droplets than controls (**Figure 5.19b**).

Due to the previous observation of increased fibrosis in one of the FPLD2 patients' tissue samples, I next performed PSR staining on the spheroid sections (described in **5.2.3**). This showed all spheroids (regardless of treatment) stained positively for PSR, indicating the presence of a collagen-rich matrix (**Figure 5.20**). The ULGTA-based hydrogel did not stain strongly for collagen but the areas surrounding cells did, indicating this was endogenous collagen produced by adipose cells and not exogenous collagen that was initially added to the hydrogel at a low concentration.

Interestingly, abdominal LMNA-R482W spheroids displayed a higher frequency of dense collagen fibres with more intense staining compared to the other spheroids, suggesting a trend towards increased collagen deposition. **Figure 5.20a** shows a large bundle of these fibres trapped in the centre of a LMNA-R482W spheroid, with a higher magnification displayed in **Figure 5.20b**.

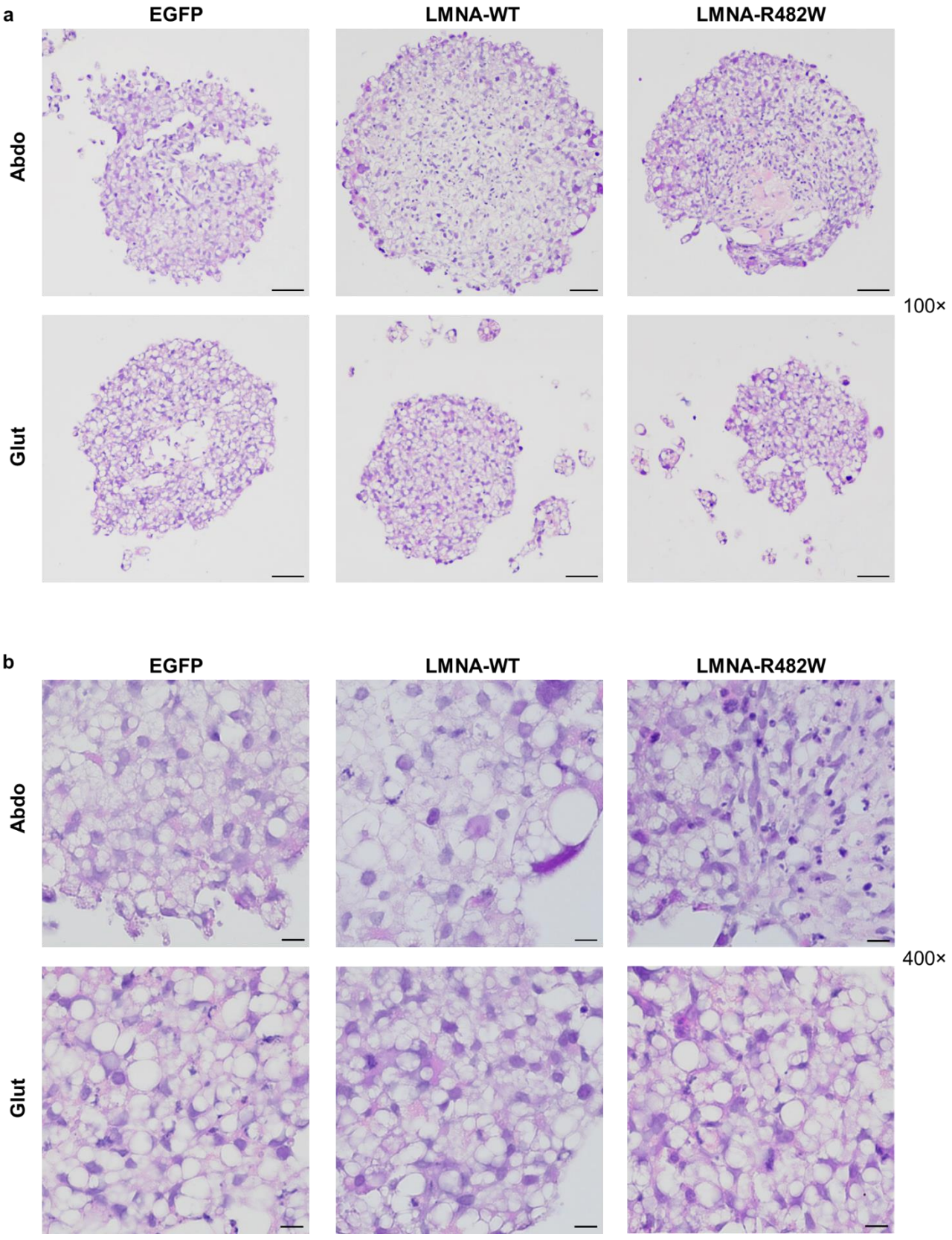


Figure 5.19. H&E staining of LMNA-R482W spheroids. Representative images of H&E-stained sections of EGFP, LMNA-WT and LMNA-R482W spheroids after 14 days of differentiation at (**a**) 100× and (**b**) 400× magnification. The scale bars are 50 µm at 100× magnification (upper panel), and 10 µm at 400× magnification (lower panel).

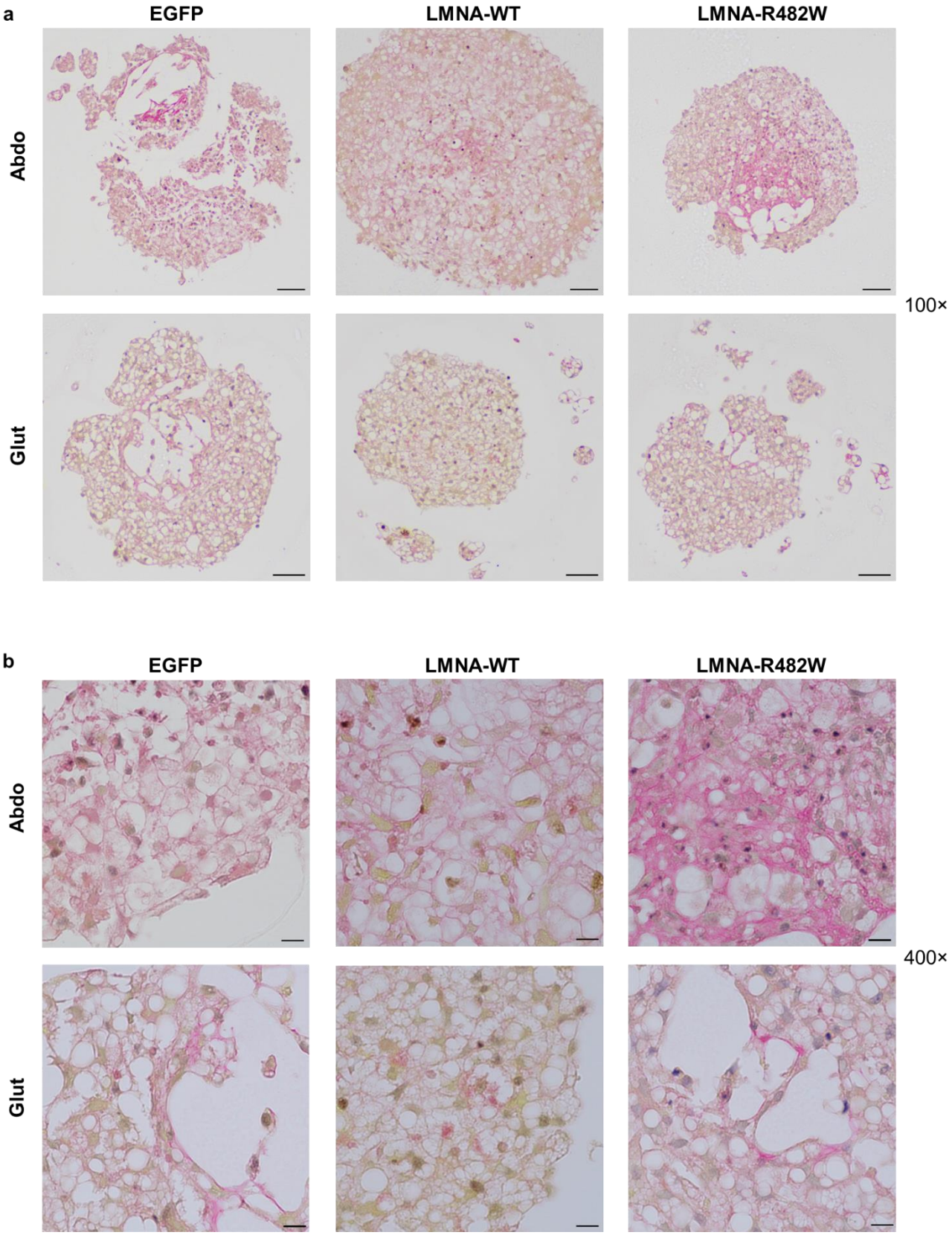


Figure 5.20. Collagen staining of LMNA-R482W spheroids. Representative images of picrosirius red-stained sections of EGFP, LMNA-WT and LMNA-R482W spheroids after 14 days of differentiation at (**a**) 100× and (**b**) 400× magnification. Arrows indicate collagen fibres in the abdominal LMNA mutant spheroid. The scale bars are 50 µm at 100× magnification (upper panel), and 10 µm at 400× magnification (lower panel).

5.4 Discussion

In this chapter, a combined approach involving measurement of plasma leptin levels, histology and *in vitro* cell models were used to investigate the effects of FPLD2 on regional adipocyte biology. Leptin release from abdominal and femoral adipose depots in FPLD2 patients revealed that the femoral depot, typically considered the most lipodystrophic, retained some capacity for leptin production. This finding prompted a structural analysis of subcutaneous adipose tissue, which revealed the presence of unilocular adipocytes in both sites. However, differences were found between the two FPLD2 patients, including evidence of increased collagen accumulation (fibrosis) in the femoral adipose tissue of the subject with a more pronounced phenotype. To further explore these depot-specific effects, I utilised *in vitro* cellular models (over)expressing the lipodystrophy-associated LMNA R482W mutation and found distinct effects on abdominal and gluteal preadipocyte proliferation, adipogenic differentiation and nuclear morphology. Cells were differentiated under both 2D and 3D culture conditions, with potentially increased collagen accumulation observed in abdominal LMNA mutant spheroids. Each aspect of the *in vitro* work carried out is discussed in further detail below.

5.4.1 Adipogenesis

The presence of mature adipocytes in the FPLD2 patients' adipose tissue suggested that the adipocyte precursors were, at some stage, able to differentiate. Indeed, adipose tissue generally develops normally in FPLD2 subjects with the reduction being gradual during puberty (Wojtanik, *et al*., 2009) (Fiorenza, *et al*., 2011). Assessment of lipid accumulation in abdominal and gluteal preadipocytes differentiated *in vitro* revealed that adipogenesis was not inhibited *per se*. However, quantitative assessment of lipid accumulation in a classic 2D culture system showed there was a small, albeit significant reduction in adipogenesis level during differentiation (at day 7 and 14) in gluteal cells. Thus, whilst cells from both depots underwent

adipogenesis, a more pronounced effect on reduced lipid accumulation was only observed in gluteal cells throughout differentiation. With neither adipose depot being spared in FPLD2 (abdominal tissue is affected but the greater fat loss typically occurs from the gluteofemoral tissue), this suggests the cellular construct is faithfully reflecting the FPLD2 patient phenotypes.

An unexpected result was that LMNA-R482W cells from both depots displayed reduced adipogenesis, irrespective of Dox treatment. This was hypothesised to be due to a low level of LMNA R482W expression (leakiness) from the Dox-inducible promoter (pCW57.1 vector). Indeed, mutant T allele expression was confirmed as 'leaky' by SNP genotyping. Previous studies have shown that the LMNA R482W exerts a dominant-negative effect on adipogenesis, with expression of mutant lamin A interfering with WT protein activity. This was demonstrated in a study by Oldenburg *et al.* (2014) who expressed LMNA R482W in human ASC cultures, isolated and pooled from the gluteofemoral depots of three female subjects. Within this study, GFP-tagged LMNA R482W expression inhibited adipocyte differentiation, as assessed by Oil-Red-O staining, and reduced expression of several adipogenic genes.

Further work from this group (Briand, *et al*., 2018a) suggests that one mechanism by which lamin A R482W inhibits differentiation involves interference with recruitment of the polycomb repressive complex 2 (PRC2). This is a large chromatin-modifying complex that regulates gene expression by catalysing the trimethylation of histone H3 at lysine 27 (H3K27me3), a modification that is associated with gene repression (Margueron & Reinberg, 2011). The PRC2 contributes to formation of heterochromatin (the condensed transcriptionally inactive form of chromatin), making it an important epigenetic regulator. Divoux *et al*. (2018) demonstrated differences in chromatin accessibility between abdominal and gluteal adipose depot-derived preadipocytes. Given this, along with the normal function of lamin A in the regulation of chromatin structure, one effect of the R482W mutation could be to cause different epigenetic alterations in a cell type-specific manner.

The move to an *in vitro* 3D culture system was used to provide a more physiologically relevant environment for cells to differentiate. Since differentiation efficiency was not assessed quantitatively for 3D cultures, comparison of lipid accumulation was limited to visual assessment. The confocal microscopy and histology results showed that LMNA mutant spheroids clearly exhibited good levels of differentiation, despite their smaller overall sizes for the gluteal depot. Higher levels of differentiation may have occurred due to the enhanced adipogenesis promoted by this method (previously demonstrated in **Chapter 4**), as well as the provision of exogenous FAs, which may have masked the relatively mild phenotype observed in 2D culture. Overexpression of WT LMNA appeared to increase the lipid droplet sizes in spheroids, although this was not quantified during my work. This could be further investigated to identify potential effects on lipid droplet morphology caused by either WT or mutated LMNA overexpression.

5.4.2 Nuclear morphology

Overexpression of LMNA R482W in proliferating gluteal preadipocytes led to increased nuclear shape abnormalities, the most prominent being nuclear blebbing, compared to abdominal preadipocytes. These findings are in line with results reported by Vigouroux *et al*. (2001), who showed that nuclear shape abnormalities were only present in a small percentage (~5-13%) of skin fibroblasts from two LMNA R482W patients. High-throughput image analysis of nuclear morphology revealed more pronounced effects on nuclear solidity in gluteal samples than in abdominal cells. A nuclear irregularity index of 0.05 was selected to define more highly misshapen nuclei, however it should be noted that this cut-off is not specific to blebbed nuclei. Future work could further quantify this by co-staining cells for lamin B1 and DNA as lamin B1 is reported to be absent from nuclear blebs (Janssen, *et al*., 2022).

It is unknown whether nuclear blebbing is a cause or a consequence of mutations in lamin A (Deolal & Mishra, 2021). Nuclear shape abnormalities likely result in a weakened nuclear envelope which could result in membrane rupturing, DNA damage and, ultimately, cell death ('structural' hypothesis) (Osmanagic-Myers & Foisner, 2019). Nuclear blebs are associated with changes to chromatin structure, for example an enrichment of euchromatin in nuclear blebs has been reported (Stephens, *et al*., 2018). Whether these nuclear shape deformities result in altered chromatin organisation and/or gene expression in cells from one adipose tissue depot but not another is an interesting question for future study. The use of cell models derived from other regions where fat tissue storage is maintained or even increased, such as neck adipose tissue, could provide further valuable insights into why patients with partial lipodystrophy can experience adipose tissue expansion in some depots, whilst having a reduction in others.

5.4.3 Proliferation

The nuclear lamina (NL) is a dynamic structure and must undergo disassembly and reassembly during mitosis for allowing sister chromatids to segregate (Heald & McKeon, 1990). My work showed that endogenous *LMNA* transcript levels in the DFAT cells changed during adipogenesis, first decreasing after differentiation induction and then increasing. This initial reduction in LMNA expression might correspond to breakdown of the NL as preadipocytes undergo several rounds of cell division (mitotic clonal expansion, MCE) following adipogenic induction. Indeed, MCE has been reported to occur during the first 48 hours of adipogenic differentiation of human ASCs, in a manner analogous to that of the well-studied murine 3T3-L1 cell model (Marquez, *et al*., 2017).

Different effects of LMNA overexpression on preadipocyte growth were also observed during this work, depending on depot. In abdominal preadipocytes, overexpression of WT LMNA decreased cell proliferation, consistent with results for other cell types (Ivorra, *et al*., 2006)

(Piekarowicz, *et al*., 2017). Similarly, (over)expression of LMNA R482W reduced proliferation of adipocyte precursors. In contrast, gluteal cells overexpressing WT or mutant LMNA showed no difference in their proliferation rates before differentiation induction. Interestingly, these cells come from the tissue that diminishes most in FPLD2, and the proliferation results suggest this is not due to the cessation of progenitor cell proliferation.

After adipogenic induction, abdominal LMNA-WT cells showed increased proliferation and notably demonstrated the highest adipogenic capacity. In 3D culture, where cell growth was not limited by well surface area, abdominal LMNA-WT spheroids expanded the most in size during differentiation. It may be relevant that lamin A is known to be overexpressed in several types of cancer (Dong, *et al*., 2021).

Together, these results suggest that lamin A has distinct effects on the proliferation of abdominal and gluteal preadipocytes, which may contribute to differences in adipose tissue expansion. Indeed, lamin A is known to affect cell cycle progression and has been shown to play a role in protecting the G1-S phase regulator, Rb protein, from proteasomal degradation (Johnson, *et al*., 2004). Additionally, Araújo-Vilar *et al*. (2009) previously compared the expression levels of several genes by qPCR in abdominal and thigh subcutaneous adipose tissue from FPLD2 (n = 7) and control (n = 10) subjects. Their results showed reduced expression of several genes involved in cell cycle regulation (*RB1*, *CCND3 and CCND1*), as well as adipogenic genes (*LPL*, *FTO*, *PPARG2* and *GLUT4*), in the thigh adipose tissue of FPLD2 patients. Significant reductions in the mRNA levels of *RB1*, *CCND3*, *PPARG2* and *LPL* mRNA were only observed in thigh samples from FPLD2 patients, with no significant differences for the same genes in abdominal tissue.

5.4.4 ECM environment

Adipose tissue fibrosis, a key pathological event in obesity, has been suggested as one mechanism underlying adipocyte dysfunction in lipodystrophy syndromes (Chun, 2012). Reduced ECM degradation or increased ECM production (Wernstedt Asterholm, *et al*., 2014) could contribute to an increase in adipose tissue fibrosis, limiting the ability of adipocyte precursors to expand via hyperplasia and favouring hypertrophy (Sakers, *et al*., 2022).

Obtaining subcutaneous adipose tissue biopsies from the femoral region of FPLD2 patients (LMNA R482W) for histological analysis was a novel aspect of this work. This approach revealed variability in collagen deposition between two related subjects (father and son). The presence of some large adipocytes trapped in fibrotic tissue in the son's leg fat suggests that the preadipocytes must have once been made into large functional cells. Histological assessment of *in vitro* adipose spheroids also showed collagen fibres appeared more prominent in the abdominal LMNA mutant spheroids. Further investigation into ECM assembly and maintenance may verify whether fibrosis is a component of the disease, particularly in patients with more severe forms of lipodystrophy.

A previous study investigating cervical (neck) subcutaneous adipose tissue from FPLD2 patients (Bérériat, *et al*., 2011) reported smaller sized adipocytes with increased fibrosis in individuals with the R482W mutation. In a study of patients with the same LMNA mutation (Araújo-Vilar, *et al*., 2012), unexpectedly larger adipocytes, as well as increased macrophage infiltration, were observed in lipomas suggesting increased inflammation. To the best of our knowledge, this is the first report of histological analysis of femoral subcutaneous WAT from FPLD2 patients carrying the LMNA R482W mutation. This may be due to the challenges of procuring adipose tissue from patients who have minimal fat in this region. This is compounded by the difficulty in recruiting volunteers with the same mutation, given the rarity of the disease.

5.4.5 Limitations

The following limitations of this work should be recognised. Firstly, the use of DFAT cells which were originally generated by our lab to provide cells with a higher adipogenic potential. These cells had previously undergone one round of adipocyte differentiation, selection and dedifferentiation back into preadipocytes, therefore the DFAT cells are potentially primed to undergo adipogenesis, which could mask effects of the LMNA mutation on cell commitment to the adipocyte lineage. Adipocytes are derived from multipotent MSCs, which give rise to several other cell types, including osteoblasts, chondrocytes and myocytes. There is some evidence that the LMNA R482W mutation may reprogram mesenchymal precursor cells to adopt a myogenic lineage (Oldenburg, *et al*., 2014), and causal to the muscular hypertrophy of patients.

FPLD2 is a complex, heterogeneous disease with patients displaying phenotypes ranging from mild to severe. This variation was evident in the father and son, from whom biopsies were taken, with each showing differing severities of the disease. Whilst the son showed a more apparent phenotype, the father did not have any classic lipodystrophy features in terms of body fat distribution or identified by adipose tissue histology; therefore he was a phenotypically non-penetrate case. The factors affecting FPLD2 penetrance remain unclear, but epigenetic influences have been suggested (Díaz-López, *et al*., 2024).

Since adipose tissue loss typically starts around puberty, replicating this effect *in vitro* using adipocytes differentiated over a short time frame is limited, as it cannot fully reflect the complex development of *in vivo* tissue. It would be interesting to study the effect of the LMNA mutation in adipocytes cultured long term (>14 days), although there are certain challenges associated with long-term culturing of adipocytes in 2D culture (such as cell detachment due to high lipid content). Furthermore, the donor characteristics of the cells used in this work may also represent a limitation. The DFAT cells were derived from a 50-year-old male donor (Todorčević, *et al*., 2017), whereas FPLD2 typically manifests around puberty and is more severe in females (Garg, 2000). Therefore, both the donor age and sex may have influenced

the outcome of these results. Given the above, with this condition being more clearly observed in women (affecting the estrogen-dependent gynoid/femoral fat depot), it is also possible that some aspect of hormone signalling such as estrogen is involved, which is not currently studied.

In order to make the adipogenic cocktail more 'physiological', a FA mixture (reflecting dietary fat) was provided during adipocyte differentiation. However, it should be noted that the provision of FAs could have masked any potential effects of the LMNA mutation on adipocyte DNL. Other adipose tissue-resident cell types were absent from the *in vitro* system. Bidault *et al*. (2013) have shown that the R482W substitution not only affects adipocyte function, but also endothelial cells, providing a potential link to the cardiovascular issues that patients may develop.

5.4.6 Summary

In summary, this work explored effects of the LMNA R482W mutation on human adipocytes from two adipose depots variably affected in FPLD2.

Low levels of leptin release from *in vivo* femoral adipose tissue indicated a low number of functional adipocytes, the presence of which was demonstrated by histological assessment of adipose biopsies. A distinct defect in adipogenesis was ruled out due to the ability of abdominal and gluteal LMNA mutant cells differentiating *in vitro*, along with the observation of adipocytes with 'normal' morphology in the FPLD2 patients' adipose tissue. This raises the question as to whether the disease mechanism occurs via other pathways, such as altered regulation of preadipocyte expansion (e.g. during MCE) or ECM remodelling.

The *in vitro* FPLD2 cellular models provide a useful tool for further investigation into the pathophysiology of partial lipodystrophy, which will be used in the next chapter for investigating transcriptomic changes in LMNA R482W mutant cells.

6 RNA-sequencing analysis of LMNA R482W adipose cells

6.1 Introduction

The nuclear lamina (NL) has a complex relationship with transcriptional control. In this chapter, I will describe data on transcriptional regulation in regional human preadipocyte cell lines in which the FPLD2-causing LMNA R482W mutation has been introduced. Therefore, it is first relevant to give a background on the NL in relation to transcriptional control and human disease.

6.1.1 The role of lamins in regulating transcription: lamina-associated domains

As discussed in **Chapter 5**, the NL is a complex protein network, composed primarily of A-type (lamin A and C) and B-type (lamin B) filaments, that provides both mechanical and gene regulatory functions by supporting nuclear architecture and organising the genome. The NL influences gene expression by forming molecular contacts with DNA at large genomic regions called 'lamina-associated domains' (LADs) (van Steensel & Belmont, 2017) (**Figure 6.1**). LADs are generally heterochromatic regions characterised by a low gene density, high repeat content and an enrichment for repressive histone marks (such as H3K9me2/3 and H3K27me3) (Dechat, *et al*., 2009) (Rullens & Kind, 2021) (Alagna, *et al*., 2023). Due to these features, most genes within LADs have low levels of expression or are repressed. In mammals, LADs form a large proportion of the genome (30-50%), with between 1,100 and 1,400 having been identified across multiple cell types (van Steensel & Belmont, 2017) (Kind, *et al*., 2013) (Alagna, *et al*., 2023).

The bacterial enzyme, DNA adenine methyltransferase (Dam), has been traditionally used for LAD identification as it methylates adenine resides in 5'-GATC-3' sequences (van Steensel & Belmont, 2017) (Briand & Collas, 2020). In this method, Dam is fused to lamin B1 or lamin A and used to identify genomic regions that are in close contact with the NL. This relies on the

absence of adenine methylation in eukaryotic cells, meaning methylation by Dam acts as a unique tag identified by sequencing to map NL-genome interactions (DamID-seq).

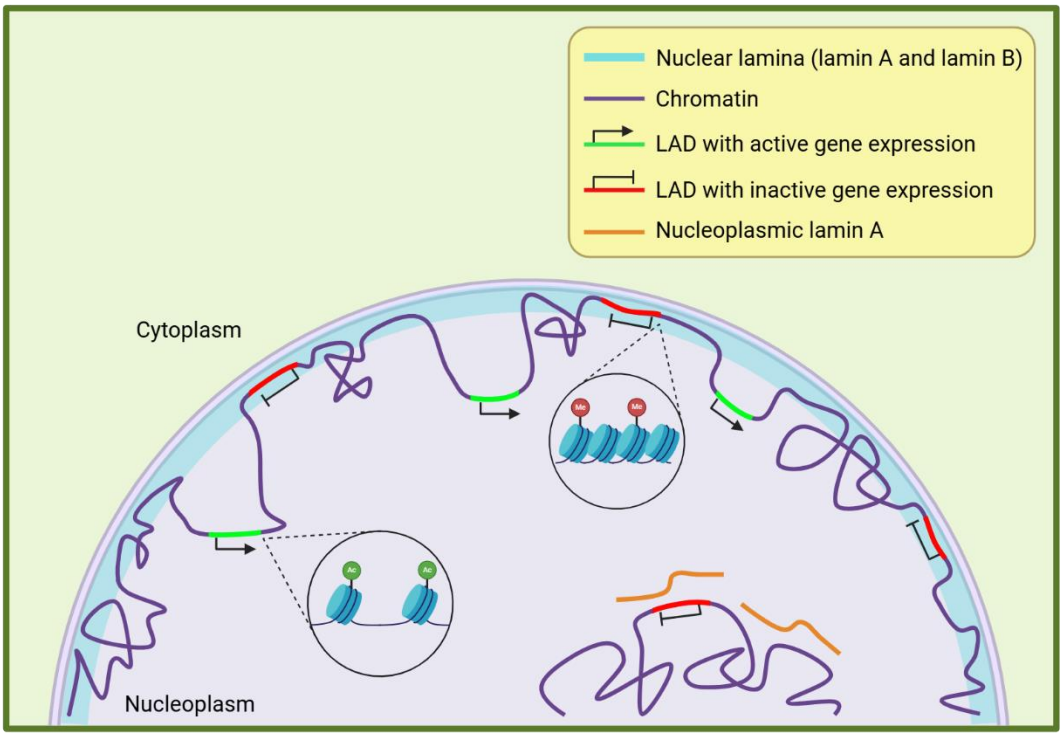


Figure 6.1. Lamina-associated domain (LAD)-mediated gene regulation. The nuclear lamina interacts with heterochromatin, at the nuclear periphery, to form a repressive environment for transcription; these DNA regions are enriched in histone methylation (Me) marks. In contrast, LADs with active gene expression are characterised by histone acetylation (Ac) marks. Nucleoplasmic lamin A also forms LADs within the nuclear interior. Figure created using BioRender and adapted from (Malashicheva & Perepelina, 2021).

Both A- and B-type lamins interact with DNA and show overlap in LADs, but also display unique characteristics (Briand & Collas, 2020). Lamin B1 is located mainly at the nuclear periphery where it polymerises to form the NL, whereas lamin A exists as both a polymer within the NL and as a soluble fraction in the nucleoplasm (Kolb, *et al*., 2011) (Gesson, *et al*., 2016). This suggests that the distinct lamin A LADs may arise from DNA interactions within the nucleoplasm. In fact, lamin A binds to both heterochromatin and euchromatin in the nuclear interior, with the latter relying on lamina-associated polypeptide 2 alpha (LAP2α) (Gesson, *et al*., 2016), a nucleoplasmic protein that mediates lamin A solubility (Naetar, *et al*., 2021). Together, lamin A and LAP2α regulate Rb/E2F signalling, essential for cell transition from G1 to S phase (Dorner, *et al*., 2006).

LADs that are conserved across different cell types are known as constitutive LADs (cLADs), whereas LADs that are variable are referred to as facultative LADs (fLADs) (or genomic variable LADs, vLADs) (Nazer, 2022) (Madsen-Østerbye, *et al*., 2022) (Bellanger, *et al*., 2022). This has led to the hypothesis that cLADs, which make up about 15% of the mammalian genome, may help anchor interphase chromosomes to the nuclear periphery (Meuleman, *et al*., 2013) (van Steensel & Belmont, 2017). Conversely, fLADs are hypothesised to aid cell type-specific gene expression and influence cell fate decisions (Chavan, *et al*., 2024) (Nazer, 2022).

LADs are not static but show dynamic reorganisation between nuclear compartments during cellular processes, which affects gene expression. For example, in myogenic and neurogenic differentiation, 5-15% of genes are repositioned away from the nuclear periphery toward the interior (Alagna, *et al*., 2023). Here they are more likely to be transcribed, while another 5-10% relocate to the nuclear periphery, a gene repressive environment.

However, while LAD repositioning generally alters gene expression, this is not always the case. For example, in adipocyte precursor cells differentiated *in vitro*, Madsen-Østerbye *et al*. (2022) did not find a strong correlation between vLAD movement and changes in early adipogenic gene expression during the first 72 hours of differentiation. Certain genes with important functions for adipocytes, such as fatty acid synthesis and steroid metabolism, lost their association with lamin following differentiation induction. In contrast, genes with more irrelevant non-adipogenic functions, such as neuron differentiation and cardiac function, were sequestered or maintained at the NL. However, owing to the pre-committed state of ASCs, the authors noted that many of the adipogenic genes were already positioned externally to LADs in undifferentiated cells. An important observation was the genes with non-adipogenic functions were confined within LADs, and therefore suppressed, following differentiation induction.

6.1.2 Chromatin alterations in laminopathies

As discussed in **Chapter 5**, mutations in the *LMNA* gene cause multiple tissue-specific or multi-systemic diseases known as laminopathies, which predominately affect mesoderm tissues. *LMNA* is ubiquitously expressed in most differentiated cell types; therefore, a crucial question is how over 350 distinct mutations result in such varied phenotypes (Dittmer & Misteli, 2011). Despite the varied symptoms, common hallmarks such as nuclear morphology and chromatin organisation defects are observed across different cell types. Initial evidence suggesting lamin proteins play a role in chromatin organisation was observed in fibroblasts and hepatocytes from *Lmna* null mice, which showed a discontinuous layer of heterochromatin at the nuclear periphery (Sullivan, *et al*., 1999).

Hutchinson-Gilford progeria syndrome (HGPS) is one of the most severe forms of laminopathy characterised by an accelerated aging phenotype, including lipodystrophy, bone abnormalities and premature cardiovascular disease (Goldman, *et al*., 2004). The condition involves abnormal production of a truncated dominant negative form of lamin A called ‘progerin’, which causes significant changes in chromatin organisation (McCord, *et al*., 2013). Progerin synthesis is typically due to a silent point mutation (G608G) within exon 11 of the *LMNA* gene (Eriksson, *et al*., 2003). This mutation introduces a cryptic splice site resulting in the removal of a 50-amino acid segment at the C-terminal end of pre-lamin A (the immature, precursor form of lamin A). Consequently, progerin remains permanently farnesylated and anchored to the inner nuclear membrane, leading to nuclear blebbing, which can be reduced by treatment with farnesyltransferase inhibitors (FTIs) (Capell, *et al*., 2005).

In addition to irregular nuclear morphology, progerin-expressing cells display a wide range of nuclear functional abnormalities, including a notable loss of heterochromatin (Goldman, *et al*., 2004), accumulation of DNA double-strand breaks (Liu, *et al*., 2006) and telomere shortening (Decker, *et al*., 2009); these alterations drive transcriptional dysregulation (Csoka, *et al*., 2004). Rescue of heterochromatin defects in HGPS fibroblasts *in vitro* is possible with compounds that modulate chromatin structure (Columbaro, *et al*., 2005). Interestingly,

progerin accumulates at low levels during aging in healthy tissue (McClintock, *et al*., 2007), and is suggested to be a natural part of the aging process (Ashapkin, *et al*., 2019).

Several other mutations in the *LMNA* gene alter chromatin organisation in various cell types. For instance, human iPSC-derived cardiomyocytes with *LMNA* T10I and *R541C* mutations, linked to generalised lipodystrophy-associated progeroid syndrome (GLPS) and dilated cardiomyopathy (DCM), respectively, demonstrated a loss of peripheral chromatin (Shah, *et al*., 2021). These chromatin abnormalities were specific to cardiomyocytes and not observed in iPSC-derived hepatocytes or adipocytes (Shah, *et al*., 2021), highlighting the cell type-specific effects of different *LMNA* point mutations.

In patients with *LMNA*-related lipodystrophy (e.g. FPLD2), there is evidence of changes in heterochromatin organisation. Chromatin abnormalities in nuclei of skin fibroblasts (Capanni, *et al*., 2003) and adipocytes (Araújo-Vilar, *et al*., 2009) from FPLD2 patients, carrying the R482L and R482W mutations, respectively, were observed in ultrastructural experiments. Both studies noted a similar loss of peripheral heterochromatin with non-continuous NL observed in FPLD2 cells. Araújo-Vilar *et al*. (2009) also observed a thickening of the NL in some adipocyte nuclei from thigh and abdominal adipose tissue.

3D modelling of genome structure in FPLD2 and control patient fibroblasts, using the computational tool Chrom3D (Paulsen, *et al*., 2017), has revealed further insight into the consequences of lamin A R482W expression. This study showed that the R482W mutation reconfigures global chromatin organisation, creating new LADs specific to FPLD2 fibroblasts in the nuclear interior. Further research by the same group indicates that epigenetic deregulation is an important feature underlying FPLD2 pathophysiology (discussed further in **section 6.1.4**).

Therefore, multiple studies support that *LMNA* mutations disrupt chromatin structure, likely affecting LAD formation and causing improper activation or silencing of essential genes during development of a given cell type. This model is known as the 'gene expression' or 'epigenome' hypothesis (**Figure 6.2**). The 'structural' hypothesis, an alternative model, states that NL structure is weakened by mutant lamin incorporation, resulting in cell death (Osmanagic-Myers & Foisner, 2019). Both models can co-exist.

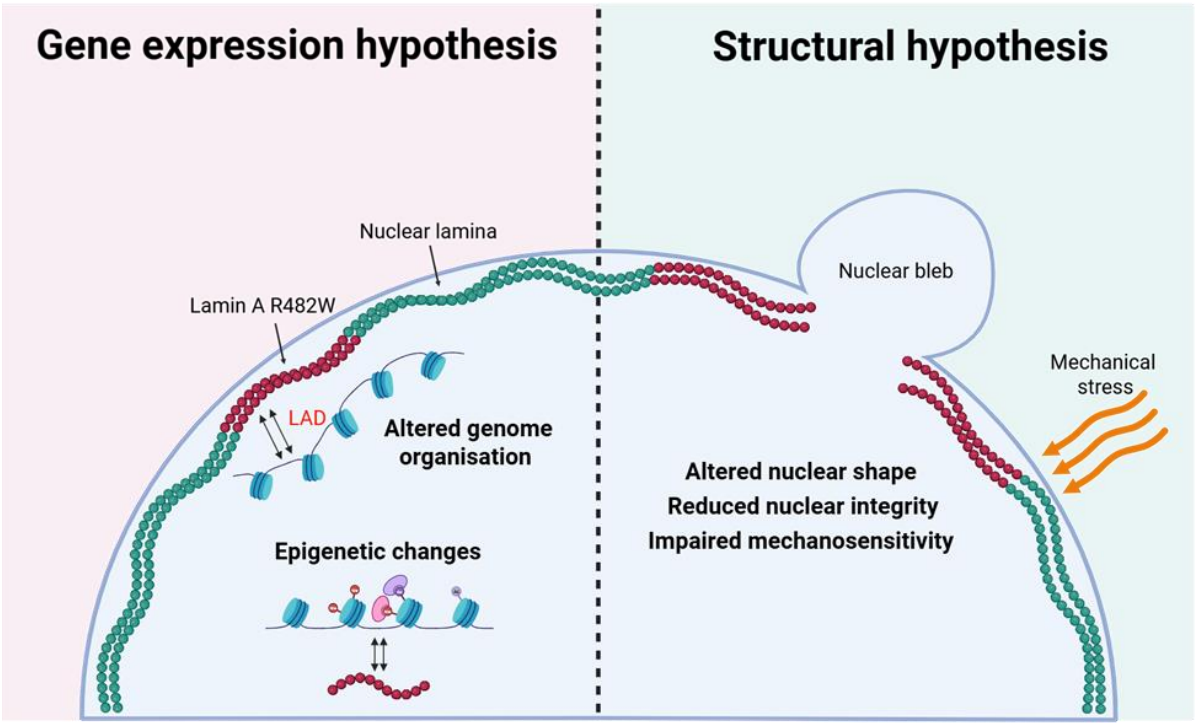


Figure 6.2. The two main models of laminopathies. According to the 'gene expression' (also known as the 'epigenome') hypothesis, mutant lamin A expression causes changes to global genome organisation. Heterochromatic lamina-associated domains (LADs) may be lost or gained, resulting in transcriptional dysregulation. Genes may also be switched 'on or 'off' by epigenetic changes (e.g. DNA methylation and other histone modifications), due to altered recruitment of chromatin-modifying factors. In the 'structural' hypothesis, mutant lamin A weakens the nuclear lamina meshwork causing loss of structural integrity and reduces the cell's ability to withstand mechanical stress. This causes nuclear shape defects, such as blebbing (commonly seen across multiple laminopathies). Nuclear shape defects may also be associated with altered chromatin structure and gene expression, linking the two hypotheses. Figure created using BioRender.

6.1.3 Transcription factors

6.1.3.1 Sterol-regulatory element binding protein

In addition to regulating chromatin structure, lamin A also regulates gene expression by either binding directly to DNA or interacting with transcription factors (TFs). Among the various TFs that lamin A is known to interact with, Sterol-regulatory element binding protein (SREBP1) has been proposed as a key interactor affected in FPLD2. Initial evidence for the regulation of SREBP1 by lamin A came from *in vitro* binding experiments showing that lamin A and SREBP1 proteins interact, with the R482W mutation shown to weaken this interaction (Lloyd, *et al*., 2002).

Another study demonstrated that pre-lamin A, but not mature lamin A, was bound to SREBP1 at the nuclear periphery in FPLD2 fibroblasts and in mouse 3T3-L1 preadipocytes induced to accumulate pre-lamin A using FTIs (Capanni, *et al*., 2005). It was found that the LMNA R482W mutation increased retention of SREBP1 away from the nuclear interior, theoretically reducing its DNA binding and transcriptional activity.

Vadrot *et al*. (2015) later investigated the interaction of lamin A R482W with SREBP1 using different human cellular models, demonstrating that lamin A, SREBP1 and its DNA responsive elements form ternary complexes *in vitro*. They found that in gluteofemoral-derived ASCs induced to overexpress GFP-labelled LMNA R482W, the number of LMNA-SREBP1 nuclear interactions reduced, coinciding with an upregulation of SREBP1 target genes. Conversely, overexpression of GFP-labelled WT LMNA led to a downregulation of SREBP1 targets. In line with this, the endogenous lamin A-SREBP1 interactions decreased in fibroblasts from two FPLD2 patients, accompanied by upregulated SREBP1 target gene expression.

The authors suggest that WT lamin A normally inhibits SREBP1 activity through direct binding activity. However, the R482W mutation impairs this, disrupting the interaction between endogenous lamin A and SREBP1. As a result, SREBP1 target genes (that would typically be silenced) become activated, contributing to deregulation of SREBP1 activity; SREBP1

functions as both a transcriptional activator and repressor. While these results differ in some aspects from those reported by Capanni *et al*. (2005), possibly due to the different cell models used, both studies point towards SREBP1 function being altered by the R482W mutation.

6.1.3.2 Specific protein 1

Another TF, Sp1 (specific protein 1), has been shown to interact with accumulated pre-lamin A in human MSCs, thereby reducing their adipogenic differentiation (Ruiz de Eguino, *et al*., 2012). After performing RNA-sequencing (RNA-seq) of hMSCs forced to accumulate pre-lamin A, the authors identified an enrichment of genes with Sp1 binding sites in their promoter regions. Many of the dysregulated genes identified by RNA-seq were associated with ECM and lipid metabolism pathways. Pre-lamin A and Sp1 proteins co-localised in differentiated adipocytes, resulting in reduced Sp1 transcriptional activity. Sp1-specific inhibitor treatment revealed that timing modulated its effect on differentiation, with earlier inhibition (day 10) proving more detrimental to lipid accumulation than at later stages (day 19).

However, it is debatable whether pre-lamin A accumulates in FPLD2 and is part of the disease mechanism. Whilst supported in several studies, this was challenged by Tu *et al*. (2016) as neither the *CAAX* motif (required for the farnesylation of pre-lamin A), or the ZMPSTE24 cleavage site (required for proteolytic maturation of lamin A), are in close proximity to the R482 residue. Intriguingly, the authors found no evidence of pre-lamin A accumulation in the FPLD2 fibroblasts that they examined (Tu, *et al*., 2016).

6.1.4 Epigenetic regulators

Lamin A also interacts with epigenetic regulators including methyltransferases and histone deacetylates (HDACs), which regulate chromatin structure and accessibility.

Research by the Collas group has provided key evidence for lamin A interactions with the polycomb repressive complex 2 (PRC2), a crucial chromatin-modifying complex, being altered by lamin A R482W. As discussed in **Chapter 5**, Briand *et al*. (2018a) suggest a dominant-negative mechanism whereby cells expressing LMNA R482W are impaired in recruiting or binding the PRC2 to its target genes. This is based on work by the same group (Oldenburg, *et al*., 2017) showing that an anti-adipogenic microRNA (miR-335) is upregulated in cultured human preadipocytes expressing the mutation, as well as in FPLD2 patient fibroblasts.

miR-335 and its host gene, the mesoderm-specific transcript (*MEST*) (also known as paternally expressed *gene* 1 (*PEG1*)), have been implicated in adipogenesis; in human adipocytes the *MEST* gene is a negative regulator of adipogenesis (Karbiener, *et al*., 2015). Interestingly, the *MEST/MIR335* locus is situated between two previously identified LMNA LADs (Rønningen, *et al*., 2015) (Oldenburg, *et al*., 2017).

Chromatin immunoprecipitation followed by sequencing (ChIP-seq) experiments showed a low-level interaction of the *MEST* gene with lamin A in human ASCs (Oldenburg, *et al*., 2017). Further ChIP experiments within the same study revealed epigenetic changes in ASCs expressing LMNA R482W, with increased acetylation and decreased methylation at H3K27. The authors propose that decreased H3K27me3 levels were due to deregulated PRC2 targeting to the *MIR335* locus, and that this results in the increased H3K27 acetylation and a looping of chromatin structure onto enhancer elements at the *MEST/MIR335* locus, resulting in upregulation of miR-335 expression.

Lamin A interacts with polycomb group (PcG) proteins, including PRC1 (polycomb repressive complex 1) and PRC2 (Cesarini, *et al*., 2015). Interestingly, our own research group has previously shown that a gluteal depot-specific long non-coding RNA (lncRNA), *HOTAIR* (*HOX* transcript antisense RNA), interacts with PRC2 and regulates regional adipocyte development (Kuo, *et al*., 2022). Such adipose depot-specific factors (*HOTAIR* is lowly expressed in abdominal adipose tissue) that differentially interact with PRC2 may be of potential interest for further research into the depot-specific effects of LMNA mutations.

6.1.5 Regulation of transcription by LMNA R482W: a complex and incomplete picture

The regulation of gene expression by lamin A and its pathogenic variants, including R482W, is complex and likely involves several mechanisms dependent upon the cellular context. To date, only a few studies have examined the transcriptomic effects of LMNA R482W expression in human preadipocytes isolated from the gluteofemoral depot (Vadrot, *et al*., 2015) (discussed in **6.1.3.1**) and FPLD2 patient-derived iPSCs (Briand, *et al*., 2018b).

The authors of the iPSC study performed RNA-seq of mutant and gene-edited WT isogenic control iPSCs during the first four days of mesodermal induction. They found that a network of PRC2 target genes was dysregulated in the mutant iPSCs, suggesting that lamin A R482W disrupts both transcriptional and epigenetic regulation during early stages of mesodermal development.

Given the selective adipose tissue loss in FPLD2 patients, it is important to investigate how this mutation influences adipocyte development and function in a depot-specific manner. Bulk RNA-seq provides a robust, unbiased technique for characterising transcriptome-wide changes in the abdominal and gluteal LMNA mutant preadipocytes used in my work. This Chapter will therefore focus on the ‘gene expression’ hypothesis. This may offer novel insights into the molecular mechanisms underlying adipocyte dysfunction in FPLD2.

6.1.6 Chapter hypothesis

- The LMNA R482W mutation causes adipose depot-specific effects in FPLD2 by differentially altering gene expression in differentiating abdominal and gluteal preadipocytes.

6.1.7 Chapter aims

In this chapter, I aimed to investigate the transcriptional effects of (over)expressing LMNA R482W in abdominal and gluteal preadipocytes differentiated *in vitro*. The overall aim was to gain a mechanistic understanding of the tissue-specific and shared effects of the mutation using RNA-seq.

The specific aims of this work, in order, were to:

1. At each time point of differentiation, identify differentially expressed genes (DEGs) that are specific to LMNA-R482W mutant cells compared to control and LMNA-WT cells.
2. Identify distinct DEGs for each depot, including those that are mutant-specific or show opposite expression patterns relative to LMNA-WT cells (divergent).
3. At each time point, compare the distinct mutant DEGs between abdominal and gluteal adipose cells to identify depot-specific or shared transcripts, and perform pathway enrichment analysis to gain a mechanistic understanding of the mutation's effects.
4. For each depot, compare DEGs across differentiation time points to identify a core subset of conserved, mutant-specific transcripts independent of differentiation status, and perform pathway enrichment analysis.

Contributions: Daniel Phillips provided invaluable help during all stages of RNA-seq data analysis, including raw data processing and differential gene expression analysis (described in section **6.2.3**).

6.2 Specific methods

6.2.1 RNA sample quality control

RNA isolated from cultured preadipocytes during an adipogenesis time course were quality checked prior to RNA-seq. Sample concentrations and purity were assessed using a NanoDrop 1000 Spectrophotometer (Thermo Scientific) and the RNA integrity number (RIN) values were determined using a TapeStation 4150 system (Agilent). For RNA-seq experiments, 96-well plates were loaded with 2.2 µg of high quality RNA (260/280 2.05-2.19 and RIN > 9.0) and then sealed. Samples were transported on dry ice to Azenta (Leipzig, Germany) for library preparation and RNA-seq.

6.2.2 EGFP PCR

Following cDNA synthesis of selected RNA samples (described in **Chapter 2**, section **2.8.2**), cDNA was diluted 1:10 in 10 mM Tris-HCl and used as a template in polymerase chain reaction (PCR) with EGFP primers (PCR components are shown in **Table 6.1**). Thermocycling conditions used are shown in **Table 6.2**. The PCR products were then loaded onto a 1% agarose gel containing ethidium bromide and ran at 90 V for 30 minutes. A 1 kb DNA ladder (Meridian Bioscience HyperLadder) was loaded into the first and last lanes. DNA bands were visualised using a BioRad ChemiDoc instrument running Image Lab software.

Table 6.1. PCR component volumes.

Component	Volume (µL)
Diluted cDNA	2
REDTaq ReadyMix PCR Reaction Mix	10
Forward EGFP primer	1
Reverse EGFP primer	1
ddH_2O	6

Table 6.2. Thermocycling conditions for EGFP PCR.

Step	Temp. (°C)	Time	Number of cycles
Initial denaturation	95	3 min	1
Denaturation	95	30 sec	40
Annealing	56	30 sec	
Extension	72	45 sec	
Final extension	72	6 min	1

6.2.3 RNA-seq data analysis

Daniel Phillips performed quality control and pre-processing steps of the raw data files (FASTQ) received from Azenta. Following gene- and isoform-level quantification using Salmon (Patro, *et al*., 2017), files were imported into RStudio (version 2024.04.2+764) using the tximport package (Soneson, *et al*., 2015). Raw count data were used to calculate counts per million (CPM) and $\log_2$(CPM) using the limma package (Ritchie, *et al*., 2015). Low expression transcripts were filtered out using the edgeR package (Robinson, *et al*., 2010), followed by sample normalisation using the trimmed means of M values (TMM) method (Robinson & Oshlack, 2010).

Multi-dimensionality scaling (MDS) plots were used to visualise broad variation between samples. Daniel Phillips also performed differential gene expression analysis (DGE) using limma. Genes were considered to be differentially expressed if the false discovery rate (FDR) was < 0.05 and $\log_2$FC (fold change) > 0.5 or < 0.5, corresponding to an approximate 1.41 fold-change in gene expression. UpSet plots were generated using the ComplexUpset package (Krassowski, 2020) to visualise unique and shared DEGs between groups.

6.2.4 Functional enrichment analysis

I undertook functional enrichment analysis of DEGs using the g:GOST function (g:SCS threshold 0.05) on the g:Profiler webpage (Kolberg, *et al*., 2023). The following data sources were selected: Gene Ontology (GO), KEGG (Kyoto Encyclopedia of Genes and Genomes), Reactome and WikiPathways (WP). Transcription factor-binding site and microRNA (miRNA)-target interaction analyses of DEGs were performed using TRANSFAC (TRANScription FACtor database) and miRTarBase data sources. Lists of enriched GO terms exceeding 30 were summarised using the online tool REVIGO (version 1.8.1) (Supek, *et al*., 2011), which uses a clustering algorithm to reduce GO terms based on semantic similarity (cut-off 0.7).

6.3 Results

2D cultures of abdominal and gluteal EGFP, LMNA-WT and LMNA-R482W preadipocytes were set up and differentiated into mature adipocytes (described in **Chapter 2**, section **2.6**). Cells were harvested at three time points to investigate transcriptional changes occurring across differentiation; the selected time points were day 0 (confluent preadipocytes before differentiation induction), day 7 (differentiating cells) and day 14 (mature adipocytes). RNA extractions were performed (described in **Chapter 2**, section **2.8.1**), and the sample quality confirmed (described in **6.2.1**), prior to submitting 144 samples for bulk RNA-seq.

6.3.1 Quality control of the RNA-seq dataset

Similarities between samples were visualised using a MDS plot, showing tight clustering of biological replicates in the first two-dimensions (**Figure 6.3a**). This plot projects high-dimensional data, such as counts for each gene in the transcriptome, onto a two-dimensional space while accurately maintaining relative distances between data points (Hill, *et al*., 2017).

Figure 6.3a shows that samples could be distinguished by differentiation time point (D0, D7, D14) and depot (abdominal or gluteal), with these factors explaining most of the variability. Specifically, the scree plot shows that dimension 1 explained 52% of the variance (**Figure 6.3c**) and was strongly influenced by time point. Dimension 2 explained 16% of the variation and was influenced by depot. Dimension 3 explained 6% of the variance, although the factors influencing this were less clear. Dimension 4 explained 4% of the variance and appeared to show an influence of cell line in the MDS plot in **Figure 6.3b**, observed at days 7 and 14 in the abdominal depot and at day 14 in gluteal. Labelling samples according to Dox treatment revealed no distinct patterns, indicating Dox did not have a strong effect on gene expression.

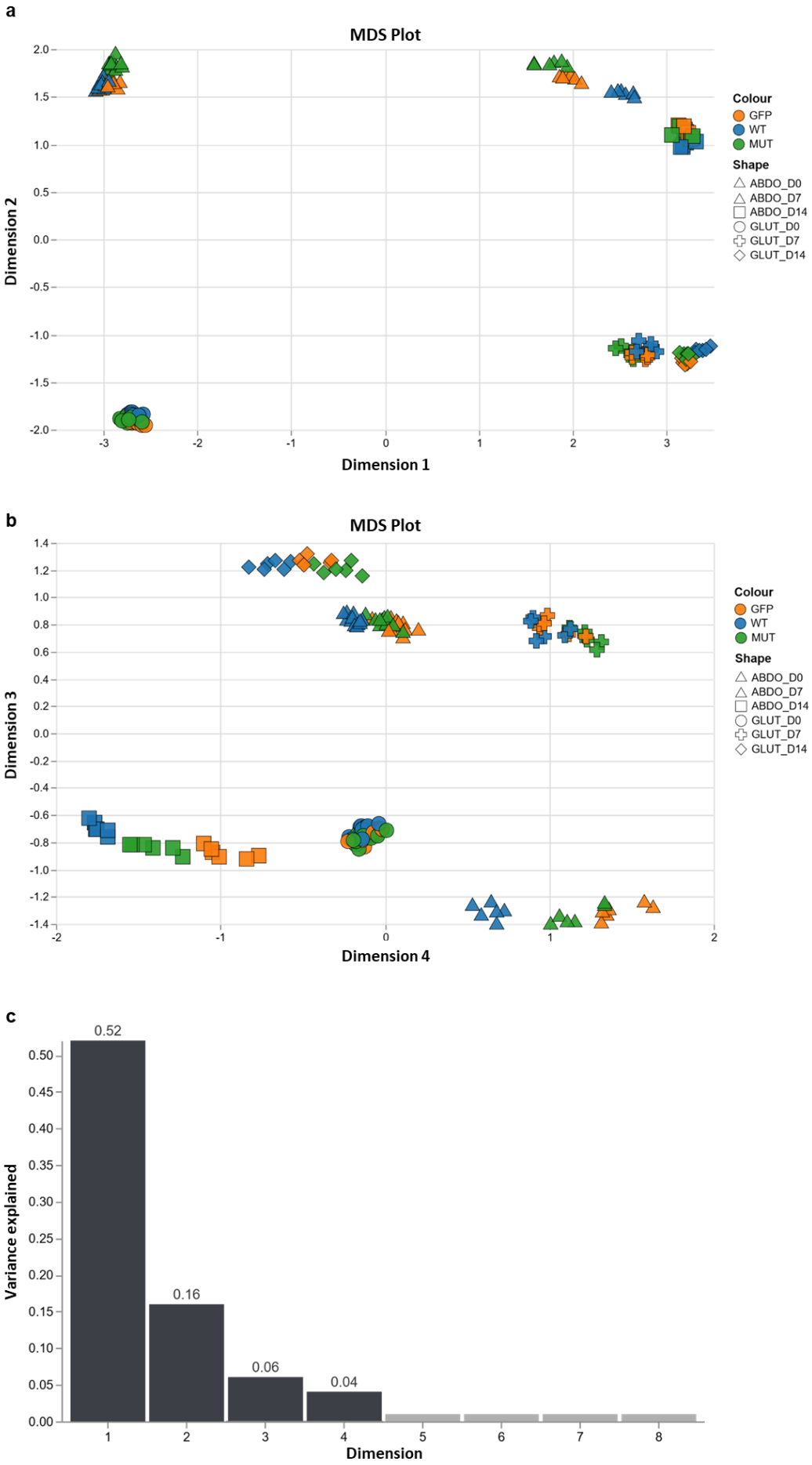


Figure 6.3. Multi-dimensional scaling (MDS) plots of RNA-seq dataset. MDS plots of dimensions 1 vs. 2 (**a**) and dimension 3 vs. 4 (**b**). Points represent individual samples coloured by cell line and shaped by depot and day. (**c**) Scree plot showing variance explained by each dimension.

Transgene leakiness in the Dox-inducible cell lines was previously observed (**Chapter 5**, **Figure 5.7**). To investigate this further, independent verification of sample transgene expression was carried out using qPCR analysis, on a selection of samples submitted for RNA-sequencing. cDNA was synthesised from the RNA samples and used as a template in PCR with EGFP-specific primers (described in **6.2.2**). **Figure 6.4a** shows the PCR products (~700 bp) in all EGFP sample lanes, demonstrating leakiness in the Dox-untreated cells. Additionally, a SNP genotyping assay (described in **Chapter 2**, section **2.8.3**) was undertaken, showing leakiness in LMNA-R482W cells at day 7 of differentiation (**Figure 6.4b**); this was previously observed in day 0 samples.

In order to evaluate whether Dox affected transcription, an initial comparison was made between EGFP cells treated with or without Dox for each depot. Dox treatment elicited a negligible transcriptional response, with fewer than five DEGs detected in the abdominal cells and only one DEG in gluteal cells across adipogenesis (data not shown). These results indicate that Dox, at the applied concentration of 0.1 µg/mL, had minimal off-target transcriptional effects in the human preadipocyte lines.

Based on this, and that Dox treatment had limited, if any, additional effect on adipogenesis or preadipocyte proliferation in the preceding chapter, replicates for Dox-treated and Dox-untreated cells were pooled in the RNA-seq analysis. This resulted in 12 biological replicates per cell line for the day 0 samples (abdominal or gluteal Dox-untreated + Dox-treated EGFP, LMNA-WT or LMNA-R482W cells), and 6 biological replicates per cell line for day 7 and 14 samples (abdominal or gluteal Dox-untreated + Dox-treated EGFP, LMNA-WT or LMNA-R482W cells); this enabled us to better examine tissue differences in gene expression.

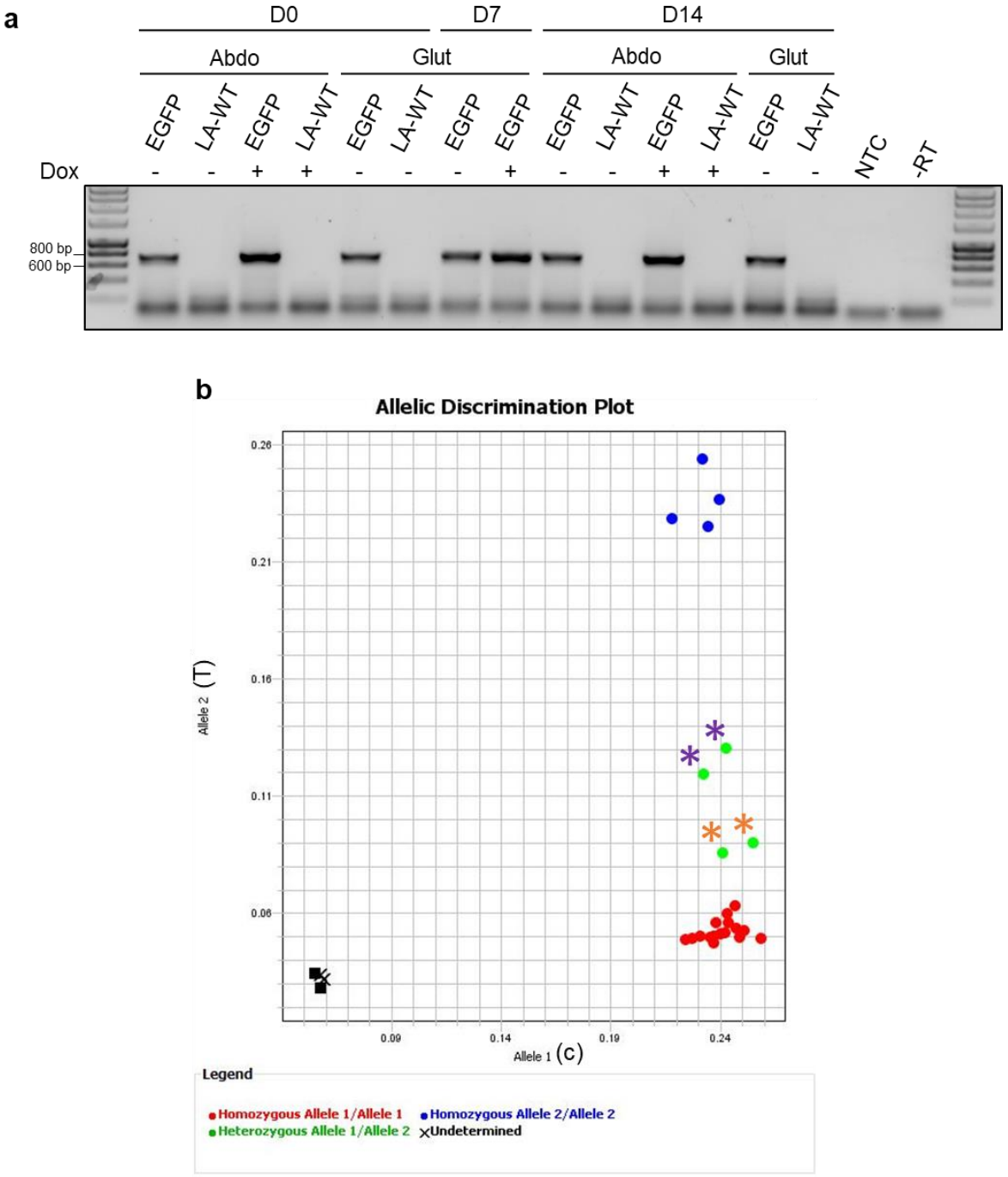


Figure 6.4. Sample verification and genotyping. (**a**) Agarose gel electrophoresis image showing DNA genotyping with EGFP primers. Amplification of ~700 bp bands were in all EGFP sample lanes. NTC, no template control; -RT, no-reverse transcriptase control. (**b**) Allelic discrimination plot from SNP genotyping qPCR for samples, from day 7 of differentiation. Expression of C (wild-type [WT], x-axis) and T (mutant, y-axis) alleles were assessed using a TaqMan SNP Genotyping Assay, C__64676006_10 (rs57920071). Each data point represents one well (technical replicate) in qPCR, with two wells ran per sample. Purple asterisks indicate Dox-untreated abdominal LMNA-R482W samples; orange asterisks indicate Dox-untreated gluteal LMNA-R482W samples. bp, base-pairs.

Following sample QC steps, normalised expression values (log_2CPM) for each transcript were calculated (described in **6.2.3**). As part of data QC, I examined the expression levels of depot-specific marker genes in all samples, which displayed the expected patterns. For example, higher expression of *HOXA6* (homeobox A6), an abdominal depot-specific transcription factor (Pinnick, *et al*., 2014), was observed in all abdominal samples compared to gluteal (**Figure 6.5a**), while higher expression of gluteal-specific *HOTAIR* was found in gluteal samples (**Figure 6.5b**). This confirms the depot-of-origin 'memory' of these cell lines. Several adipogenic marker genes were also examined (*PPARG*, *CEBPA*, *SLC2A4* and *PNPLA2*), which showed an increase in expression level across time (**Figure 6.6**), indicating the cells were committed to the adipocyte lineage.

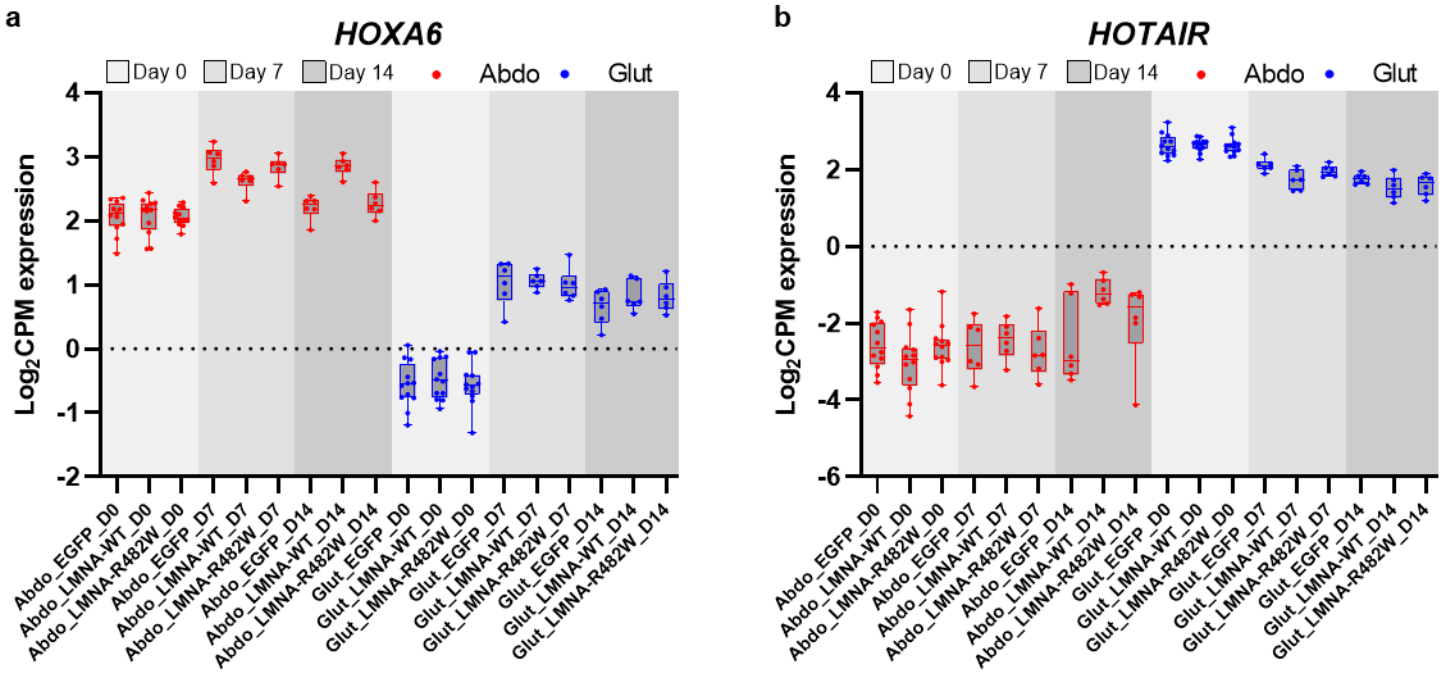


Figure 6.5. Depot-specific marker gene expression in abdominal and gluteal preadipocytes during differentiation. Log_2 counts per million (CPM) of depot-specific marker genes: (**a**) *HOXA6* and (**b**) *HOTAIR* on day 0 (n = 12), day 7 (n = 6) and day 14 (n = 6) of adipogenic differentiation.

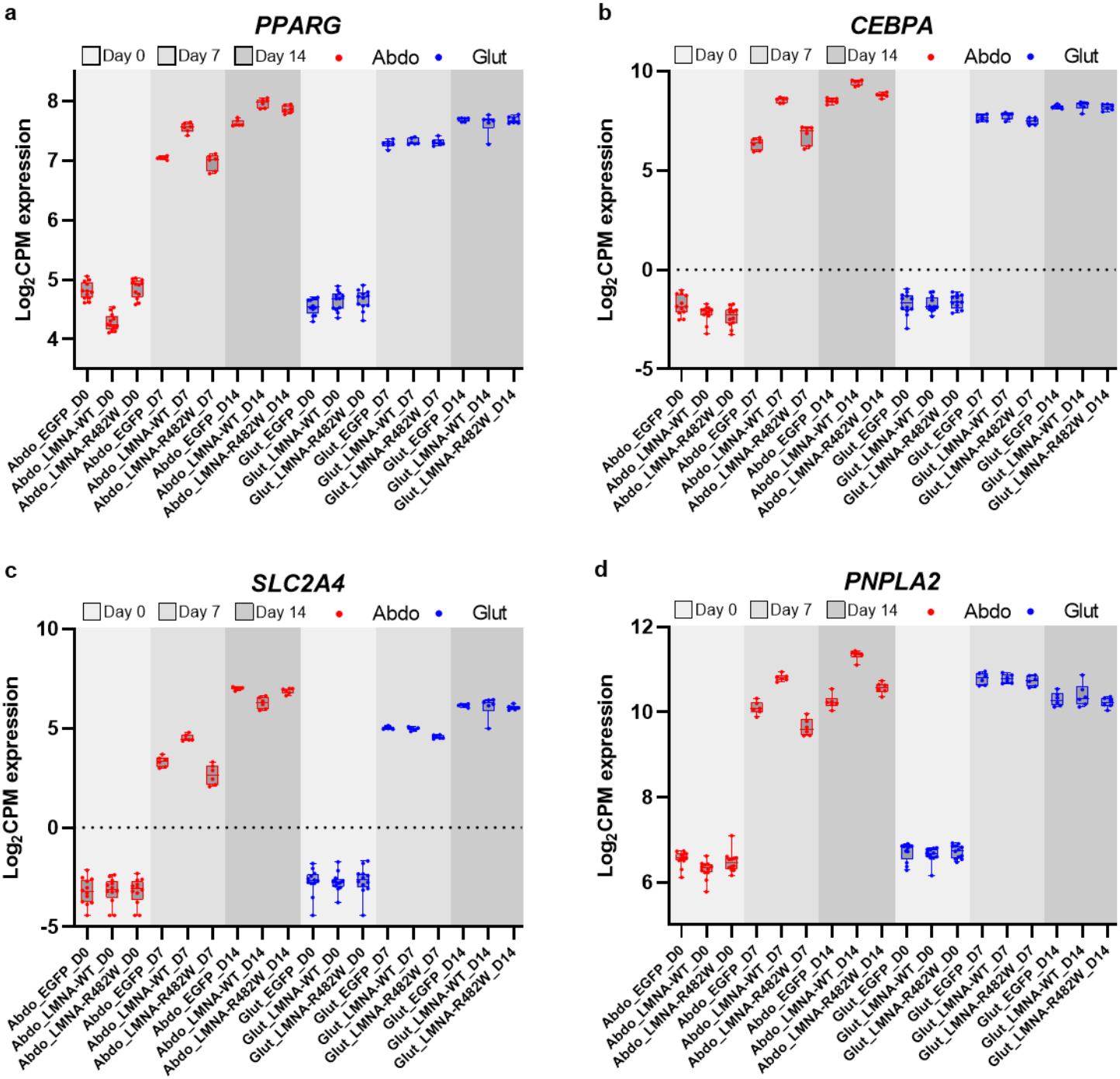


Figure 6.6. Adipogenic marker gene expression in abdominal and gluteal preadipocytes during differentiation. Log_2 counts per million (CPM) of adipogenic marker genes: (**a**) *PPARG* (**b**) *CEBPA* (**c**) *SLC2A4* (*GLUT4*) and (**d**) *PNPLA2* (*ATGL*) on day 0 (n = 12), day 7 (n = 6) and day 14 (n = 6) of adipogenic differentiation.

6.3.2 Abdominal cells show greater transcriptomic changes in response to LMNA R482W expression than gluteal cells

At day 0 of differentiation, a total of 2,276 DEGs were identified in abdominal LMNA-R482W cells compared to EGFP control cells, including 954 upregulated and 1,322 downregulated genes (**Figure 6.7a**). In contrast, gluteal LMNA-R482W cells showed a more limited transcriptomic response, with 257 DEGs identified (83 upregulated, 174 downregulated) (**Figure 6.7b**).

By day 7 of differentiation, 2,113 DEGs were detected in abdominal LMNA-R482W cells (892 upregulated, 1,221 downregulated) compared to controls (**Figure 6.7a**). In contrast, at the same time point, gluteal LMNA-R482W cells showed 326 DEGs (102 upregulated, 224 downregulated) (**Figure 6.7b**).

At day 14 of differentiation, abdominal LMNA mutant adipocytes showed 2,661 DEGs relative to controls (1,246 upregulated, 1,415 downregulated) (**Figure 6.7a**). In comparison, gluteal LMNA mutant adipocytes continued to display fewer transcriptomic changes, with only 99 DEGs identified (35 upregulated, 64 downregulated) (**Figure 6.7b**).

Overall, gluteal LMNA mutant cells were unique in displaying approximately double the number of downregulated genes than upregulated at each time point, which could reflect a gain of repressive LAD environments. Abdominal LMNA-R482W cells consistently showed more extensive transcriptomic changes than gluteal mutant cells across all stages of differentiation; a similar pattern was observed in LMNA-WT cells (**Figure 6.7**). These findings indicate that LMNA (over)expression (WT or mutant) had a stronger impact on gene expression in the abdominal-derived preadipocytes during differentiation *in vitro*.

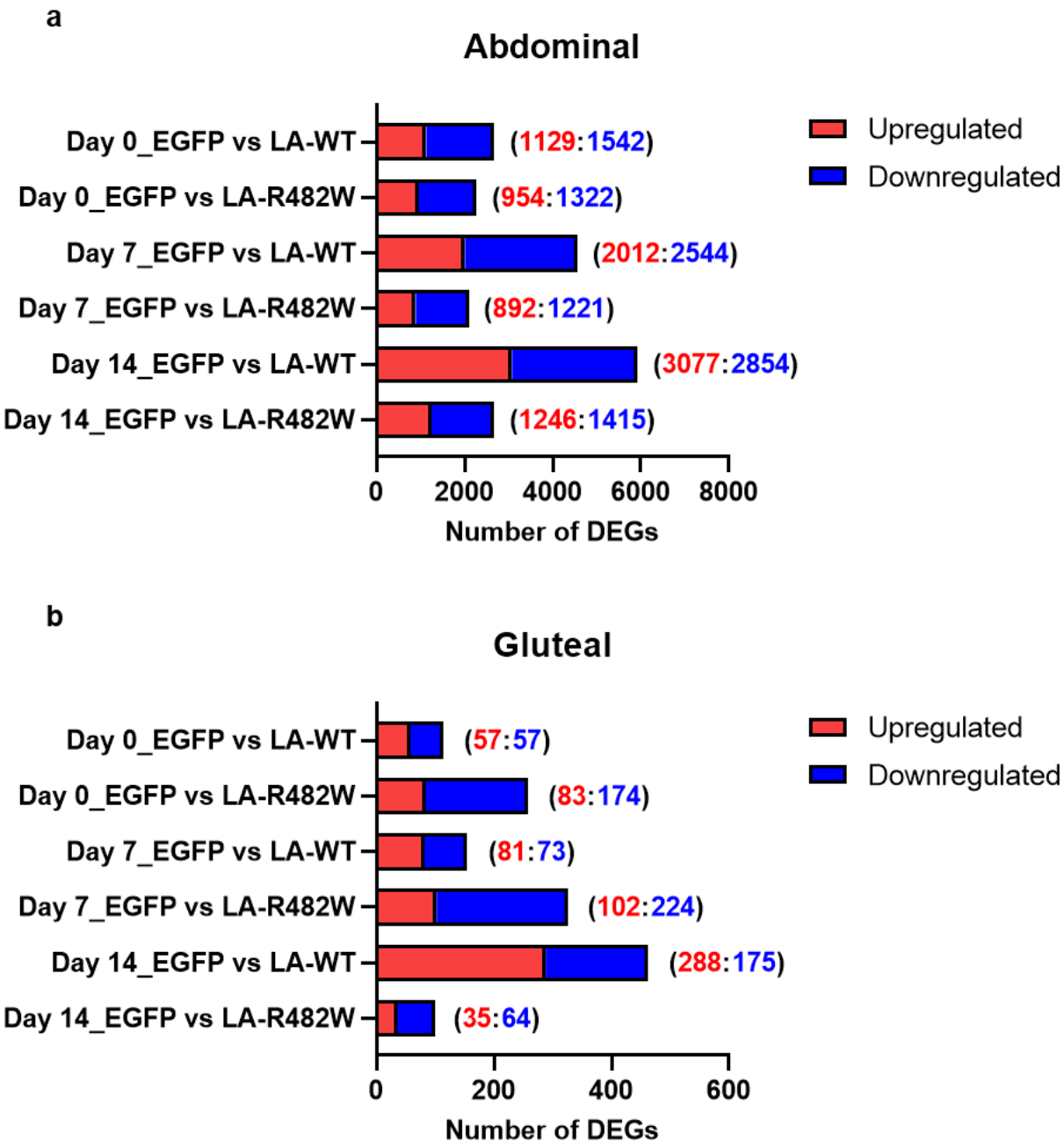


Figure 6.7. Total number of significant differentially expressed genes (DEGs) in LMNA-R482W mutant and LMNA-WT cells versus controls during adipogenic differentiation. Significant (FDR < 0.05) DEGs that were upregulated (log2FC > 0.5) or downregulated (log2FC < 0.5) in (a) abdominal and (b) gluteal LMNA-R482W or LMNA-WT cells versus EGFP control cells, on days 0, 7 and 14 of differentiation. The number of upregulated (red) and downregulated (blue) genes are referenced in brackets.

6.3.3 Identification of abdominal and gluteal distinct mutant DEGs

Following DEG identification, we next aimed to determine which transcripts were uniquely altered in the LMNA mutant cells from each depot. While these mutant-specific DEGs were the primary focus, we also identified DEGs that were shared with LMNA-WT cells but showed expression in the opposite direction, as these divergent transcripts could provide insight into distinct regulatory effects of mutant versus WT LMNA. UpSet plots capturing expression directionality and DEG overlap were generated by Daniel Phillips to visualise these relationships (**Figure 6.8**).

The most significant upregulated or downregulated DEGs distinct to LMNA-R482W cells on days 0-14 are shown in **Tables 6.3-8**.

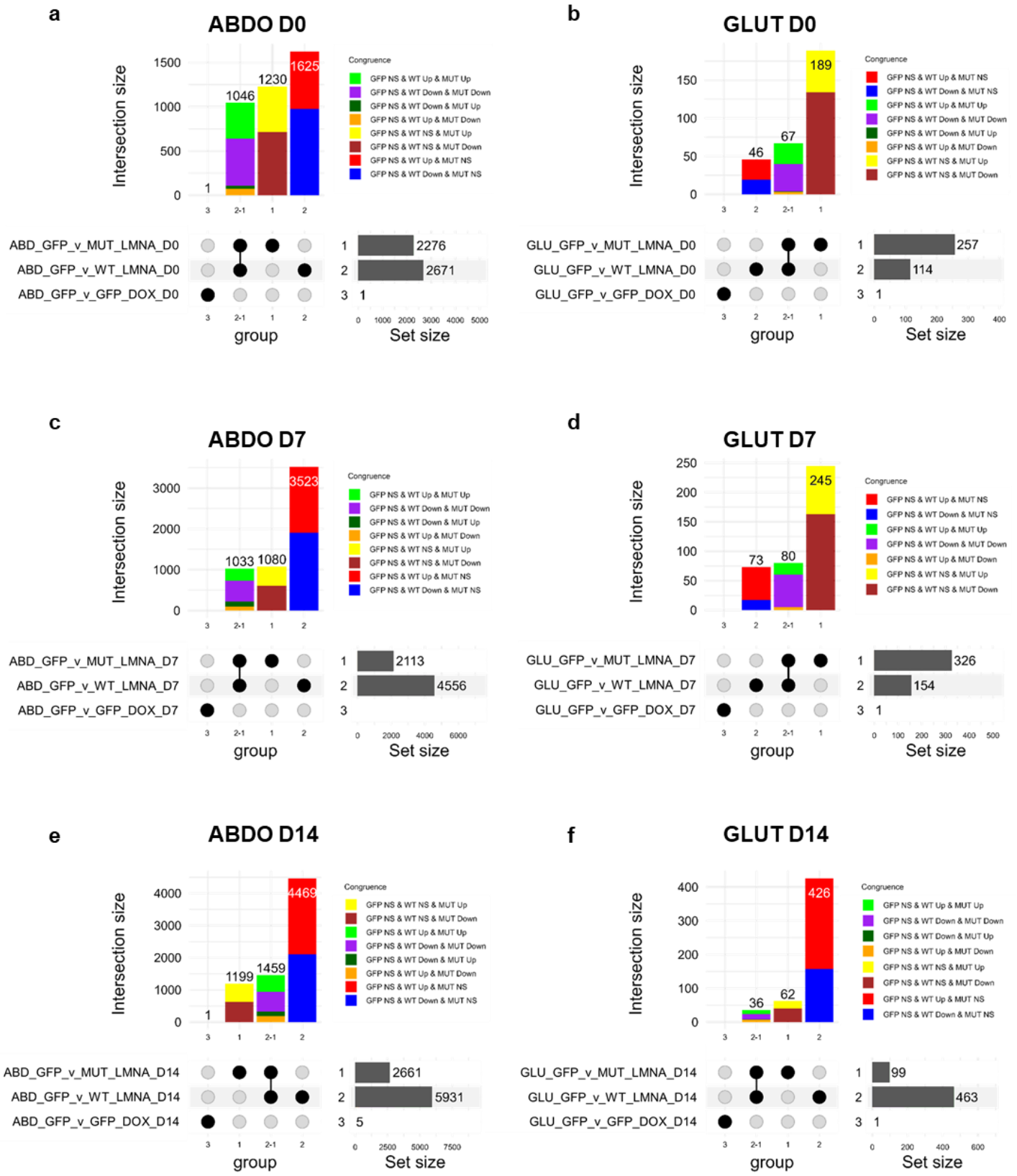


Figure 6.8. UpSet plots showing the number of unique or shared DEGs between sets. Comparisons between abdominal (**a, c, e**) and gluteal (**b, d, f**) DEG sets are shown, with each plot representing a different time point of differentiation (day 0, 7 and 14). Horizontal bars indicate the total number of DEGs in each set (set size). Vertical bars represent the size of each intersection, capturing either shared DEGs (genes found in two sets, indicated by connected black dots) or unique DEGs (genes found only in a single set, indicated by an unconnected black dot). Colours indicate expression direction congruency among intersecting sets.

Table 6.3. Top distinct DEGs in abdominal LMNA-R482W cells at day 0 of differentiation. LMNA-R482W DEGs were identified relative to EGFP cells ($log_2FC \pm 0.5$, FDR < 0.05). Common DEGs (sharing the same direction of expression) in LMNA-WT vs. EGFP were filtered out. Genes differentially expressed in both LMNA-R482W and LMNA-WT but in opposite directions are indicated in the rightmost column; all others are marked as nonDE. A total of **1,336 distinct DEGs** were identified; only the top 10 up- and downregulated genes (by significance) are shown. FC, fold change; nonDE, non-differentially expressed.

Gene symbol	Description	Log_2FC	Adjusted *p*-value	Status in LMNA-WT
Upregulated in LMNA-R482W cells (vs. EGFP)				
CPXM1	Carboxypeptidase X, M14 Family Member 1	2.628	1.46E-43	nonDE
FMNL2	Formin Like 2	1.144	1.98E-41	nonDE
PEG10	Paternally Expressed 10	1.504	4.60E-41	nonDE
AIM2	Absent In Melanoma 2	1.188	1.90E-36	nonDE
KIAA1217	Sickle Tail Protein Homolog	1.058	2.39E-36	nonDE
TMOD2	Tropomodulin 2	1.011	5.15E-35	nonDE
MELTF	Melanotransferrin	1.397	5.63E-35	nonDE
RPN1	Ribophorin I	0.7181	6.27E-35	nonDE
TBC1D23	TBC1 Domain Family Member 23	1.031	1.64E-34	nonDE
CCND2	Cyclin D2	0.8898	1.74E-34	nonDE
Downregulated in LMNA-R482W cells (vs. EGFP)				
SLC24A3	Solute Carrier Family 24 Member 3	-1.322	1.36E-40	nonDE
LHFPL6	Lipoma HMGIC Fusion Partner-Like Tetraspan Subfamily Member 6	-0.7454	2.30E-39	nonDE
STMP1	Short Transmembrane Mitochondrial Protein 1	-0.7827	3.02E-38	nonDE
SERPINE2	Serpin Family E Member 2	-1.267	1.77E-36	nonDE
BPGM	Bisphosphoglycerate Mutase	-0.787	3.37E-34	nonDE
USO1	General Vesicular Transport Factor p115	-0.522	7.54E-34	nonDE
ITGB3	Integrin Subunit Beta 3	-1.221	2.01E-32	nonDE
PDE4DIP	Phosphodiesterase 4D Interacting Protein	-0.7743	6.19E-32	nonDE
B3GNT9	UDP-GlcNAc:BetaGal Beta-1,3-N-Acetylglucosaminyltransferase 9	-0.6179	5.53E-31	nonDE
SEC24D	SEC24 Homolog D, COPII Coat Complex Component	-0.5437	3.71E-30	nonDE

Table 6.4. Top distinct DEGs in gluteal LMNA-R482W cells at day 0 of differentiation. LMNA-R482W DEGs were identified relative to EGFP cells ($log_2FC \pm 0.5$, FDR < 0.05). Common DEGs (sharing the same direction of expression) in LMNA-WT vs. EGFP were filtered out. Genes differentially expressed in both LMNA-R482W and LMNA-WT but in opposite directions are indicated in the rightmost column; all others are marked as nonDE. A total of **193 distinct DEGs** were identified; only the top 10 up- and downregulated genes (by significance) are shown. FC, fold change; nonDE, non-differentially expressed.

Gene symbol	Description	Log_2FC	Adjusted *p*-value	Status in LMNA-WT
Upregulated in LMNA-R482W cells (vs. EGFP)				
SERPINB2	Serpin Family B Member 2	1.064	2.25E-16	nonDE
PRAG1	PEAK1 Related, Kinase-Activating Pseudokinase 1	0.5344	3.31E-11	nonDE
WNT16	Wnt Family Member 16	0.7262	1.26E-10	nonDE
NTM	Neurotrimin	0.5393	7.13E-10	nonDE
KRT34	Keratin 34	0.6693	8.22E-10	nonDE
KRT14	Keratin 14	0.7532	1.08E-09	**down in WT**
CAMK2N1	Calcium/Calmodulin Dependent Protein Kinase II Inhibitor 1	0.5184	4.05E-09	nonDE
EPHA5	Ephrin Type-A Receptor 5	2.646	9.17E-09	nonDE
GDNF	Glial Cell Line-Derived Neurotrophic Factor	0.5449	2.82E-08	nonDE
MAMDC2	MAM Domain Containing 2	0.5473	1.05E-07	nonDE
Downregulated in LMNA-R482W cells (vs. EGFP)				
MXRA5	Matrix Remodeling Associated 5	-2.08	2.36E-27	nonDE
TP53I11	Tumor Protein P53 Inducible Protein 11	-1.461	1.16E-18	nonDE
MEG3	Maternally Expressed 3	-1.085	3.61E-17	nonDE
GAS1	Growth Arrest Specific 1	-0.8338	8.21E-17	nonDE
WNT2	Wnt Family Member 2	-0.6526	4.97E-13	nonDE
FBLN2	Fibulin-2	-0.659	6.03E-11	nonDE
IGFBP3	Insulin-like Growth Factor-Binding Protein 3	-0.5627	8.15E-11	nonDE
CD40	Cluster of Differentiation 40	-1.987	9.23E-11	nonDE
PTGFRN	Prostaglandin F2 Receptor Inhibitor	-0.6536	1.12E-10	nonDE
ACKR3	Atypical Chemokine Receptor 3	-2.294	6.88E-10	nonDE

Table 6.5. Top distinct DEGs in abdominal LMNA-R482W cells at day 7 of differentiation. LMNA-R482W DEGs were identified relative to EGFP cells ($log_2FC \pm 0.5$, FDR < 0.05). Common DEGs (sharing the same direction of expression) in LMNA-WT vs. EGFP were filtered out. Genes differentially expressed in both LMNA-R482W and LMNA-WT but in opposite directions are indicated in the rightmost column; all others are marked as nonDE. A total of **1,296 distinct DEGs** were identified; only the top 10 up- and downregulated genes (by significance) are shown. FC, fold change; nonDE, non-differentially expressed.

Gene symbol	Description	Log_2FC	Adjusted *p*-value	Status in LMNA-WT
Upregulated in LMNA-R482W cells (vs. EGFP)				
COL13A1	Collagen Type XIII Alpha 1 Chain	3.008	1.38E-43	nonDE
CRIP2	Cysteine Rich Protein 2	1.917	3.05E-31	nonDE
NNMT	Nicotinamide N-Methyltransferase	1.108	2.20E-29	nonDE
BNC1	Basonuclin Zinc Finger Protein 1	1.614	3.81E-28	nonDE
P4HA2	Prolyl 4-Hydroxylase Subunit Alpha 2	0.826	1.94E-27	**down in WT**
KLF3-AS1	Krüppel-Like Factor 3 Antisense RNA 1	1.53	2.54E-26	nonDE
BOC	BOC Cell Adhesion Associated, Oncogene Regulated	1.516	4.45E-25	**down in WT**
SLC66A1L	Solute Carrier Family 66 Member 1	0.6804	1.03E-24	nonDE
EMID1	Emilin And Multimerin Domain-Containing Protein 1	2.011	4.51E-24	**down in WT**
LRRC56	Leucine Rich Repeat Containing 56	1.549	1.90E-23	**down in WT**
Downregulated in LMNA-R482W cells (vs. EGFP)				
TRARG1	Trafficking Regulator Of GLUT4 1	-1.36	2.57E-34	nonDE
PDGFC	Platelet Derived Growth Factor C	-1.149	1.11E-30	nonDE
UCP2	Uncoupling Protein 2	-1.476	1.94E-27	**up in WT**
MYORG	Myogenesis Regulating Glycosidase	-0.8203	3.56E-27	nonDE
NPR1	Natriuretic Peptide Receptor 1	-1.439	1.04E-25	nonDE
SYNPO	Synaptopodin	-1.189	1.20E-25	nonDE
CCDC69	Coiled-Coil Domain Containing 69	-1.136	2.43E-25	nonDE
ENC1	Ectodermal-Neural Cortex 1	-1.206	3.28E-25	nonDE
RHEB	Ras Homolog, MTORC1 Binding	-0.6767	4.45E-25	nonDE
AOC3	Amine Oxidase Copper Containing 3	-0.9792	6.16E-25	nonDE

Table 6.6. Top distinct DEGs in gluteal LMNA-R482W cells at day 7 of differentiation. LMNA-R482W DEGs were identified relative to EGFP cells ($log_2FC \pm 0.5$, FDR < 0.05). Common DEGs (sharing the same direction of expression) in LMNA-WT vs. EGFP were filtered out. Genes differentially expressed in both LMNA-R482W and LMNA-WT but in opposite directions are indicated in the rightmost column; all others are marked as nonDE. A total of **250 distinct DEGs** were identified; only the top 10 up- and downregulated genes (by significance) are shown. FC, fold change; nonDE, non-differentially expressed.

Gene symbol	Description	Log_2FC	Adjusted *p*-value	Status in LMNA-WT
Upregulated in LMNA-R482W cells (vs. EGFP)				
CLDN11	Claudin 11	0.5874	5.05E-10	nonDE
NUDT11	Nudix Hydrolase 11	0.6976	5.05E-10	nonDE
SFRP1	Secreted Frizzled-Related Protein 1	0.5585	6.80E-06	nonDE
LINC01426	Long Intergenic Non-Protein Coding RNA 1426	0.541	1.25E-05	nonDE
ENSG00000290549		0.645	5.1E-05	nonDE
DKK1	Dickkopf-1	1.036	1.71E-04	nonDE
ADAMTSL1	A Disintegrin and Metalloproteinase with Thrombospondin Motif Like 1	0.5726	2.63E-04	nonDE
WNT5B	Wnt Family Member 5B	0.5694	3.07E-04	nonDE
IL33	Interleukin 33	0.6386	3.98E-04	nonDE
PROB1	Proline Rich Basic Protein 1	0.5029	4.49E-04	nonDE
Downregulated in LMNA-R482W cells (vs. EGFP)				
SLC12A7	Solute Carrier Family 12 Member 7	-2.108	2.28E-12	nonDE
SLC22A3	Solute Carrier Family 22 Member 3	-1.456	2.28E-12	nonDE
PCK1	Phosphoenolpyruvate Carboxykinase 1	-0.906	1.77E-11	nonDE
ZNF831	Zinc Finger Protein 831	-1.225	1.26E-10	nonDE
PMEPA1	Prostate Transmembrane Androgen Inducible Protein 1	-1.452	2.43E-10	nonDE
H2BC21	H2B Clustered Histone 21	-0.5217	1.79E-09	nonDE
ACKR3	Atypical Chemokine Receptor 3	-2.637	2.60E-09	nonDE
SELP	Selectin P	-1.005	6.53E-09	nonDE
LAIR1	Leukocyte Associated Immunoglobulin Like Receptor 1	-0.7047	1.07E-08	nonDE
CYP4B1	Cytochrome P450 4B1	-0.7661	1.19E-08	nonDE

Table 6.7. Top distinct DEGs in abdominal LMNA-R482W cells at day 14 of differentiation. LMNA-R482W DEGs were identified relative to EGFP cells ($log_2FC \pm 0.5$, FDR < 0.05). Common DEGs (sharing the same direction of expression) in LMNA-WT vs. EGFP were filtered out. Genes differentially expressed in both LMNA-R482W and LMNA-WT but in opposite directions are indicated in the rightmost column; all others are marked as nonDE. A total of **1,532 distinct DEGs** were identified; only the top 10 up- and downregulated genes (by significance) are shown. FC, fold change; nonDE, non-differentially expressed.

Gene symbol	Description	Log_2FC	Adjusted *p*-value	Status in LMNA-WT
Upregulated in LMNA-R482W cells (vs. EGFP)				
SRRM3	Serine/Arginine Repetitive Matrix 3	3.124	2.01E-46	nonDE
REEP6	Receptor Accessory Protein 6	1.502	1.67E-42	nonDE
CEND1	Cell Cycle Exit And Neuronal Differentiation 1	2.868	1.54E-37	**down in WT**
TNMD	Tenomodulin	1.822	1.58E-37	**down in WT**
MCCC1	Methylcrotonyl-CoA Carboxylase Subunit 1	1.018	5.37E-35	nonDE
ENSG00000290242		2.093	1.16E-33	nonDE
COX7A1	Cytochrome C Oxidase Subunit 7A1	1.309	8.44E-33	nonDE
HMCES	5-Hydroxymethylcytosine Binding, ES Cell Specific	1.006	3.36E-31	nonDE
AMOT	Angiomotin	2.987	3.34E-30	nonDE
ENSG00000290586		1.575	5.27E-30	nonDE
Downregulated in LMNA-R482W cells (vs. EGFP)				
ANTXR2	ANTXR cell adhesion molecule 2	-1.006	5.31E-32	nonDE
CES1	Carboxylesterase 1	-1.711	6.25E-32	**up in WT**
USO1	General Vesicular Transport Factor p115	-0.6994	2.98E-31	nonDE
PAPSS1	3'-Phosphoadenosine 5'-Phosphosulfate Synthase 1	-0.9641	2.98E-31	nonDE
ATMIN	ATM Interactor	-0.7795	7.04E-30	nonDE
STMP1	Short Transmembrane Mitochondrial Protein 1	-0.8296	1.92E-29	nonDE
VPS4A	Vacuolar Protein Sorting 4 Homolog A	-0.6371	4.99E-29	nonDE
SEC24D	SEC24 Homolog D, COPII Coat Complex Component	-0.8173	4.31E-28	nonDE
PAXIP1	PAX Interacting Protein 1	-0.8676	4.57E-27	nonDE
RPL13	Ribosomal Protein L13	-0.6553	5.52E-27	nonDE

Table 6.8. Top distinct DEGs in gluteal LMNA-R482W cells at day 14 of differentiation. LMNA-R482W DEGs were identified relative to EGFP cells ($log_2FC \pm 0.5$, FDR < 0.05). Common DEGs (sharing the same direction of expression) in LMNA-WT vs. EGFP were filtered out. Genes differentially expressed in both LMNA-R482W and LMNA-WT but in opposite directions are indicated in the rightmost column; all others are marked as nonDE. A total of **70 distinct DEGs** were identified; only the top 10 up- and downregulated genes (by significance) are shown. FC, fold change; nonDE, non-differentially expressed.

Gene symbol	Description	Log_2FC *p* value	Adjusted *p*-value	Status in LMNA-WT
Upregulated in LMNA-R482W cells (vs. EGFP)				
SATB1	Special AT-Rich Sequence Binding Protein 1	0.5256	2.74E-05	nonDE
FOXG1	Forkhead Box G1	3.068	1.97E-04	nonDE
CD34	Cluster of differentiation 34	0.6868	2.04E-04	nonDE
DKK2	Dickkopf-2	0.9436	2.33E-04	nonDE
OLFML1	Olfactomedin Like 1	1.463	8.99E-04	nonDE
MAP9	Microtubule Associated Protein 9	0.6895	1.13E-03	nonDE
PLPP2	Phospholipid Phosphatase 2	2.157	4.74E-03	nonDE
LRRN3	Leucine Rich Repeat Neuronal 3	0.5762	6.83E-03	nonDE
ADAMTS9	ADAM Metallopeptidase With Thrombospondin Type 1 Motif 9	1.04	7.53E-03	nonDE
ZFPM2-AS1	Zinc Finger Protein, FOG Family Member 2 Antisense RNA 1	1.498	7.53E-03	nonDE
Downregulated in LMNA-R482W cells (vs. EGFP)				
EBF3	Early B Cell Factor 3	-1.529	8.53E-16	nonDE
CDIP1	Cell Death Inducing P53 Target 1	-0.6354	2.34E-07	nonDE
SLC12A7	Solute Carrier Family 12 Member 7	-1.205	1.71E-06	**up in WT**
KIAA1671	Uncharacterized Protein KIAA1671	-1.739	3.10E-06	nonDE
H3C10	H3 Clustered Histone 10	-0.5151	4.22E-05	nonDE
H4C8	H4 Clustered Histone 8	-0.5627	8.65E-05	nonDE
HCN2	Hyperpolarization Activated Cyclic Nucleotide Gated Potassium And Sodium Channel 2	-0.7334	1.12E-04	nonDE
PMEPA1	Prostate Transmembrane Protein, Androgen Induced 1	-1.027	1.25E-04	nonDE
SAA1	Serum Amyloid A1	-0.5629	1.32E-04	**up in WT**
RNF212	Ring Finger Protein 212	-1.222	2.33E-04	nonDE

6.3.4 Pathway enrichment analysis

To identify pathways uniquely affected by LMNA R482W expression, the distinct mutant DEGs identified from UpSet plots were analysed using over-representation analysis (ORA) with gProlifer2 (described in **6.2.3** and **6.2.4**). To maximise biological insight, pathway enrichment analysis was performed using multiple databases, including Gene Ontology (GO), Kyoto Encyclopedia of Genes and Genomes (KEGG), WikiPathways (WP), Reactome, TRANScription FACtor database (TRANSFAC) and miRTarBase.

6.3.4.1 Depot comparisons in preadipocytes at day 0 of differentiation

At day 0, comparison of the distinct abdominal and gluteal mutant DEGs identified 1,299 genes specific to the abdominal cells and 156 genes specific to gluteal cells; an overlap of 37 genes was observed between tissues (**Figure 6.9**). Each gene set (abdominal-specific, gluteal-specific or shared) was analysed separately using gProfiler to identify enriched pathways. If shared genes displayed divergent expression between depots, they were included in the tissue-specific analysis.

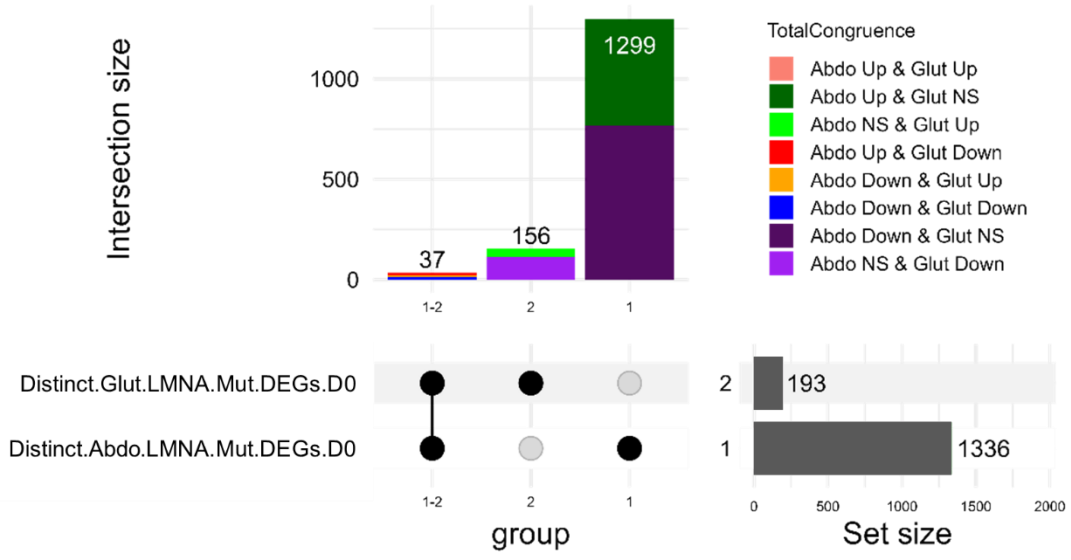


Figure 6.9. Comparison of day 0 abdominal and gluteal distinct LMNA mutant DEGs. The UpSet plot shows the number of unique or shared DEGs between gene sets. Colours indicate expression direction congruency among intersecting sets.

Day 0 abdominal DEGs

The day 0 abdominal-specific genes were enriched for a wide range of GO biological process (GO:BP) terms (174 results). Given the high number of enriched terms, REVIGO was used to reduce redundancy and produce a more interpretable list of representative terms (18 results) (described in **6.2.4**). These are presented in **Table 6.9** and included processes such as 'multicellular organism development', 'extracellular matrix organization', and 'apoptotic process'. Notably, several of the most highly upregulated genes within this set have previously been associated with regulating adipogenesis, including *CPXM1* (Kim, *et al*., 2016), *PEG10* (Hishida, *et al*., 2007) and *AIM2* (Gong, *et al*., 2019) (**Table 6.3**).

KEGG analysis revealed significant enrichment of several signalling pathways, including tumour necrosis factor (TNF), mitogen-activated protein kinase (MAPK) and phosphatidylinositol 3-kinase (PI3K)-Akt signalling pathways (**Table 6.9**). Among the top upregulated genes was *CCND2*, which is regulated by PI3K-Akt signalling (Maddika, *et al*., 2008). Metabolic pathways such as 'fatty acid metabolism' and 'biosynthesis of unsaturated fatty acid' were also significantly enriched. These pathways included genes encoding members of the ELOVL (elongation of very long-chain fatty acids) family (*ELOVL2*, *ELOVL4* and *ELOVL6*), enzymes responsible for fatty acid elongation and synthesis of important structural and signalling lipid molecules such as sphingolipids and ceramides (Wang, *et al*., 2023).

Day 0 gluteal DEGs

The day 0 gluteal-specific genes were enriched for 73 GO:BP terms, which were simplified to 11 terms using REVIGO. The resulting terms are shown in **Table 6.10** and included processes shared with abdominal preadipocytes, such as 'multicellular organism development' and 'cell communication'. Pathways uniquely enriched in gluteal cells were also identified, including 'regulation of locomotion', 'cell junction', 'glucose homeostasis' and 'regulation of growth'.

Within the 'glucose homeostasis' pathway, notable transcripts that were downregulated and involved in insulin signalling were *INSR* (insulin receptor) and *FOXO1* (forkhead box type O1). FOXO1 acts downstream of insulin signalling and has been shown to play a regulatory role in adipocyte development. Previous studies have shown conflicting results on the role of FOXO1 in adipogenesis, with both pro- (Nakae, *et al*., 2003) and anti-adipogenic effects reported (Munekata & Sakamoto, 2009) (Zou, *et al*., 2014). Importantly, sustained inhibition of FOXO1 in preadipocytes, using either specific antagonist (Zou, *et al*., 2014) or small interfering RNA (siRNA) (Munekata & Sakamoto, 2009), was shown to inhibit differentiation.

Among the top DEGs were several others involved in Wnt signalling (e.g. *WNT16*, *WNT2*), a key pathway regulating adipocyte differentiation (Christodoulides, *et al*., 2009). Other DEGs related to Wnt signalling were *WNT11*, *KREMEN1* and *ROR2*. Several ECM-related genes were also among the top DEGs (e.g. *MAMDC2, MXRA5* and *FBLN2*), with *MXRA5* identified as the most significantly downregulated (**Table 6.4**).

Pathway analysis of the 37 genes shared between depots showed these were enriched for 'animal organ morphogenesis' (padj 0.024450) and 'tissue morphogenesis' (padj 0.029737) terms.

Table 6.9. Enriched terms for distinct abdominal LMNA-R482W DEGs at day 0. GO:BP terms were reduced using REVIGO.

Source	Term name	Term ID	Adjusted *p*-value
GO:BP	**multicellular organism development**	GO:0007275	6.30E-20
	developmental process	GO:0032502	1.20E-19
	cell communication	GO:0007154	6.55E-12
	response to stimulus	GO:0050896	1.70E-11
	cell adhesion	GO:0007155	8.91E-07
	extracellular matrix organization	GO:0030198	2.69E-06
	cell death	GO:0008219	9.96E-06
	apoptotic process	GO:0006915	1.53E-05
	localization	GO:0051179	0.000141
	cell motility	GO:0048870	0.000264
	muscle structure development	GO:0061061	0.000723
	cell-cell adhesion	GO:0098609	0.003272
	regulation of membrane potential	GO:0042391	0.005671
	cell population proliferation	GO:0008283	0.009064
	homeostatic process	GO:0042592	0.011483
	locomotion	GO:0040011	0.013457
	protein phosphorylation	GO:0006468	0.015478
	response to mechanical stimulus	GO:0009612	0.018411
	energy homeostasis	GO:0097009	0.033005
	organic cation transport	GO:0015695	0.045522
KEGG	**TNF signaling pathway**	KEGG:04668	0.000291
	Alcoholic liver disease	KEGG:04936	0.002524
	MAPK signaling pathway	KEGG:04010	0.004077
	PI3K-Akt signaling pathway	KEGG:04151	0.008998
	Fatty acid metabolism	KEGG:01212	0.010828
	Pathways in cancer	KEGG:05200	0.013004
	Biosynthesis of unsaturated fatty acids	KEGG:01040	0.031054
	Graft-versus-host disease	KEGG:05332	0.043899
	AGE-RAGE signaling pathway in diabetic complications	KEGG:04933	0.045994

Table 6.10. Enriched GO:BP terms for distinct gluteal LMNA-R482W DEGs at day 0. Terms were reduced using REVIGO.

Term name	Term ID	Adjusted *p*-value
cell communication	GO:0007154	7.67E-08
cellular response to stimulus	GO:0051716	1.85E-05
regulation of locomotion	GO:0040012	0.000343
anatomical structure development	GO:0048856	0.000386
cell junction organization	GO:0034330	0.000510
multicellular organismal process	GO:0032501	0.000968
cellular response to chemical stimulus	GO:0070887	0.002728
developmental process	GO:0032502	0.002812
glucose homeostasis	GO:0042593	0.003395
regulation of growth	GO:0040008	0.011295
growth	GO:0040007	0.046967

6.3.4.2 Depot comparisons at day 7 of differentiation

At day 7 of differentiation, 1,261 DEGs were specific to abdominal cells and 215 DEGs specific to gluteal cells, with 35 genes shared between depots (**Figure 6.10**).

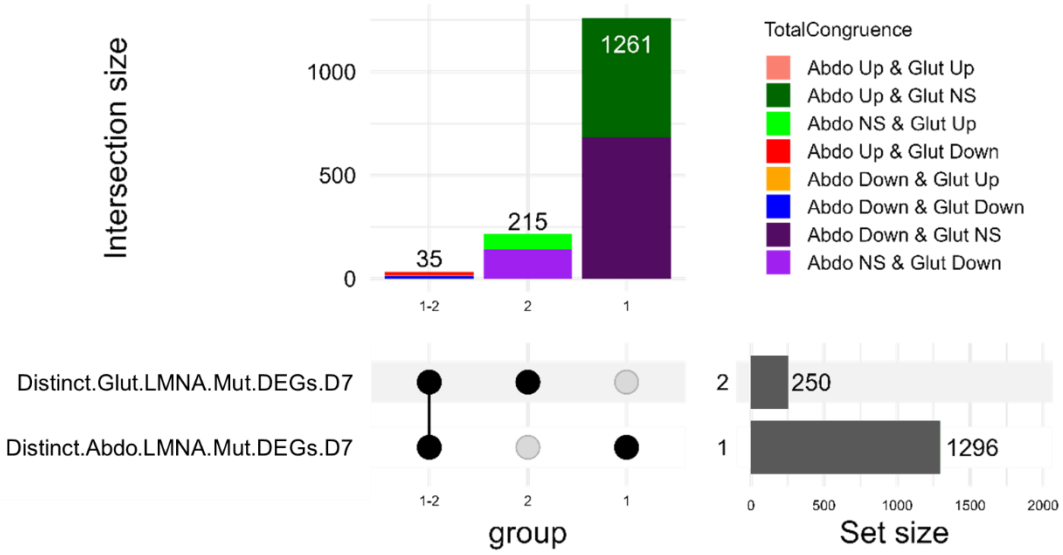


Figure 6.10. Comparison of day 7 abdominal and gluteal distinct LMNA mutant DEGs. The UpSet plot shows the number of unique or shared DEGs between gene sets. Colours indicate expression direction congruency among intersecting sets.

Day 7 abdominal DEGs

Pathway analysis of the D7 abdominal-specific DEGs detected a total of 133 GO:BP terms, which were simplified using REVIGO. The reduced GO terms included ‘cell adhesion’, ‘extracellular matrix organization’, ‘muscle structure development’ and ‘cell population proliferation’ (**Table 6.11**).

Notable enriched pathways from KEGG analysis included ‘biosynthesis of unsaturated fatty acids’ and ‘fatty acid metabolism’ (**Table 6.11**). Reactome analysis further revealed enrichment of pathways related to lipid metabolism (e.g. ‘metabolism of lipids’ and ‘fatty acid metabolism’), as well as several terms associated with ECM organisation and collagen production (e.g. ‘collagen biosynthesis and modifying enzymes’, ‘assembly of collagen fibrils and other multimeric structures’ and ‘elastic fibre formation’). *COL13A1* was the most

significantly upregulated gene (**Table 6.5**), with several other collagen genes (e.g. *COL3A1*, *COL5A1*, *COL8A2*, *COL9A2*, *COL21A1*) also upregulated. *P4HA2* was another significantly upregulated gene, which encodes a subunit of prolyl 4-hydroxylase, a key enzyme involved in collagen synthesis (Myllyharju, 2008). In addition, several other genes encoding lysyl oxidases (*LOX*, *LOXL1*, *LOXL2*, *LOXL4*) showed increased expression in abdominal mutant cells; these enzymes catalyse crosslinking of collagen and elastin fibres (Pastel, *et al*., 2018). Meanwhile, the most downregulated gene identified was *TRARG1*, which regulates glucose uptake into adipocytes.

Remarkably, these results also showed an enrichment for miRNA-335 targets from miRTarBase (**Table 6.11**), a database of experimentally validated microRNA binding sites. As previously discussed in section **6.1.4**, Oldenburg *et al*. (2017) showed LMNA-R482W cells overexpress miRNA-335, which was associated with epigenetic changes and anti-adipogenic effects. This prompted a look-up of the miRNA-335's host gene (*MEST*) at each time point, which was downregulated in abdominal preadipocytes (data not shown).

Day 7 gluteal DEGs

The D7 gluteal-specific genes were enriched for 22 GO:BP terms, which were not reduced (**Table 6.12**). The most significantly enriched GO:BP term was 'response to lipid', which contained a variety of genes involved in lipid uptake and metabolism. Specifically, *LPL* and *PCK1* (phosphoenolpyruvate carboxykinase 1) transcripts were downregulated, whereas *CES1* (carboxylesterase 1) expression was upregulated. LPL acts as the main 'gatekeeper' for FA entry into adipose tissue, whilst PCK1 plays a role in glyceroneogenesis and FA re-esterification. CES1 is involved in FA and cholesterol metabolism in adipose tissue. Interestingly, mice with targeted deletion of *PCK1* in iWAT exhibit varying degrees of adipose tissue loss, with some developing lipodystrophy (Olswang, *et al*., 2002).

Aside from these genes, several DEGs involved in Wnt signalling were either upregulated (*SFRP1*, *DKK1*, *DKK3*, *WNT5B*, *LRRK2*) or downregulated (*WNT9A*, *KREMEN1*). Reactome analysis revealed enrichment of 'Negative regulation of TCF-dependent signaling by WNT ligand antagonists', while 'BMP2 WNT4 FOXO1 pathway in primary endometrial stromal cell differentiation' was found using WikiPathways (**Table 6.12**). No enriched terms were identified for the 35 overlapping DEGs between depots.

Table 6.11. Enriched terms for distinct abdominal LMNA-R482W DEGs at day 7. GO:BP terms were reduced using REVIGO.

Source	Term name	Term ID	Adjusted *p*-value
GO:BP	**developmental process**	GO:0032502	1.11E-17
	multicellular organismal process	GO:0032501	7.71E-16
	response to stimulus	GO:0050896	8.68E-15
	cell communication	GO:0007154	2.26E-10
	cell adhesion	GO:0007155	2.49E-08
	cell migration	GO:0016477	1.03E-05
	extracellular matrix organization	GO:0030198	4.31E-05
	muscle structure development	GO:0061061	0.000501
	cell motility	GO:0048870	0.000971
	locomotion	GO:0040011	0.001092
	organic hydroxy compound metabolic process	GO:1901615	0.003392
	growth	GO:0040007	0.008104
	cell population proliferation	GO:0008283	0.011022
	cardiac muscle hypertrophy	GO:0003300	0.013620
	response to organic cyclic compound	GO:0014070	0.018717
	regulation of cell adhesion	GO:0030155	0.035100
	transport	GO:0006810	0.043209
	cell-substrate adhesion	GO:0031589	0.048376
KEGG	**Biosynthesis of unsaturated fatty acids**	KEGG:01040	0.027084
	AGE-RAGE signaling pathway in diabetic complications	KEGG:04933	0.037879
	Glycosaminoglycan biosynthesis - keratan sulfate	KEGG:00533	0.042589
	Fatty acid metabolism	KEGG:01212	0.043173
Reactome	**Extracellular matrix organization**	REAC:R-HSA-1474244	0.000009
	Collagen formation	REAC:R-HSA-1474290	0.000045
	Metabolism of lipids	REAC:R-HSA-556833	0.000538
	Collagen biosynthesis and modifying enzymes	REAC:R-HSA-1650814	0.002989
	Assembly of collagen fibrils and other multimeric structures	REAC:R-HSA-2022090	0.004233
	Fatty acid metabolism	REAC:R-HSA-8978868	0.012452
	Collagen chain trimerization	REAC:R-HSA-8948216	0.030651
	Elastic fibre formation	REAC:R-HSA-1566948	0.030651
	NADE modulates death signalling	REAC:R-HSA-205025	0.049635
MIRNA	**hsa-miR-335-5p**	MIRNA:hsa-miR-335-5p	0.000700

Table 6.12. Enriched terms for distinct gluteal LMNA-R482W DEGs at day 7.

Source	Term name	Term ID	Adjusted *p*-value
GO:BP	**response to lipid**	GO:0033993	0.000268
	positive regulation of multicellular organismal process	GO:0051240	0.000813
	regulation of multicellular organismal process	GO:0051239	0.001209
	positive regulation of macrophage activation	GO:0043032	0.002053
	negative regulation of multicellular organismal process	GO:0051241	0.004745
	system development	GO:0048731	0.006318
	nervous system development	GO:0007399	0.010089
	cellular response to lipid	GO:0071396	0.012787
	positive regulation of response to stimulus	GO:0048584	0.016823
	positive regulation of inflammatory response	GO:0050729	0.017953
	multicellular organismal process	GO:0032501	0.023946
	regulation of response to stimulus	GO:0048583	0.027087
	multicellular organism development	GO:0007275	0.028371
	heart induction	GO:0003129	0.032397
	regulation of synaptic transmission, glutamatergic	GO:0051966	0.036065
	positive regulation of cell communication	GO:0010647	0.036076
	positive regulation of signaling	GO:0023056	0.036454
	regulation of signaling	GO:0023051	0.038255
	anatomical structure development	GO:0048856	0.040009
	regulation of cell communication	GO:0010646	0.040288
	cellular response to chemical stimulus	GO:0070887	0.040378
	regulation of heart morphogenesis	GO:2000826	0.048342
Reactome	**Negative regulation of TCF-dependent signaling by WNT ligand antagonists**	REAC:R-HSA-3772470	0.002635
WP	**BMP2 WNT4 FOXO1 pathway in primary endometrial stromal cell differentiation**	WP:WP3876	0.039479

6.3.4.3 Depot comparisons at day 14 of differentiation

At day 14 of differentiation, 1,519 DEGs were specific to abdominal cells and 57 DEGs specific to gluteal cells, with only 13 genes shared (**Figure 6.11**).

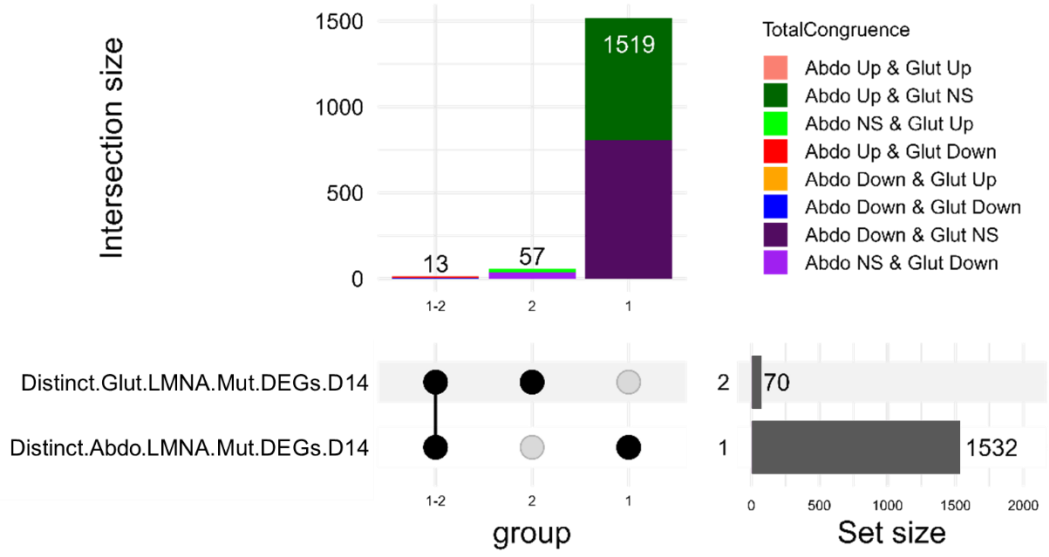


Figure 6.11. Comparison of day 14 abdominal and gluteal distinct LMNA mutant DEGs. The UpSet plot shows the number of unique or shared DEGs between gene sets. Colours indicate expression direction congruency among intersecting sets.

Day 14 abdominal DEGs

The D14 abdominal-specific genes were enriched for 123 GO:BP terms, which were simplified to 20 terms using REVIGO (**Table 6.13**). Notably, among these terms was 'fat cell differentiation' containing the lamin A interactor, *SREBF1*. A look-up of *SREBF1* expression levels at D14 showed this gene was upregulated in abdominal mutant adipocytes and downregulated in LMNA-WT adipocytes. In contrast, *SREBF1* expression in gluteal mutant preadipocytes was unaltered during adipogenesis.

Further analysis using KEGG revealed that 'glycolysis / gluconeogenesis' and 'fatty acid degradation' terms were significantly enriched (**Table 6.13**). TRANSFAC (a database of transcription factor binding sites) identified that the abdominal mutant DEGs were enriched for

numerous TF binding sites, including ZF5, Kaiso, E2F-4 and Sp1, of which ZF5 was the most significant (**Table 6.14**). As discussed in section **6.1.3.2**, Ruiz de Eguino *et al*. (2012) reported that Sp1 interacted with pre-lamin A in hMSCs, which impaired adipogenesis and altered ECM gene expression. This suggests that the LMNA R482W mutation causes dysregulation of various TFs in abdominal cells, which may explain the increased transcriptional changes compared to gluteal.

Table 6.13. Enriched terms for distinct abdominal LMNA-R482W DEGs at day 14. GO:BP terms were reduced using REVIGO.

Source	Term name	Term ID	Adjusted *p*-value
GO:BP	**developmental process**	GO:0032502	2.31E-17
	multicellular organismal process	GO:0032501	3.52E-12
	cell communication	GO:0007154	1.30E-10
	response to stimulus	GO:0050896	1.24E-09
	biological regulation	GO:0065007	2.69E-08
	homeostatic process	GO:0042592	0.000172
	cell surface receptor signaling pathway	GO:0007166	0.000329
	cell adhesion	GO:0007155	0.001397
	cell junction organization	GO:0034330	0.003382
	heart contraction	GO:0060047	0.003749
	alcohol metabolic process	GO:0006066	0.004751
	cellular response to external stimulus	GO:0071496	0.005996
	olefinic compound metabolic process	GO:0120254	0.009786
	secretion by cell	GO:0032940	0.010684
	cell migration	GO:0016477	0.013194
	cell-cell adhesion	GO:0098609	0.025375
	antigen processing and presentation of endogenous peptide antigen	GO:0002483	0.027960
	regulation of actin filament-based movement	GO:1903115	0.031677
	cell motility	GO:0048870	0.032406
	fat cell differentiation	GO:0045444	0.042438
KEGG	**Glycolysis / Gluconeogenesis**	KEGG:00010	0.000771
	Fatty acid degradation	KEGG:00071	0.003513
	Calcium signaling pathway	KEGG:04020	0.003876
	Rap1 signaling pathway	KEGG:04015	0.013787
	Phagosome	KEGG:04145	0.017957
	Metabolic pathways	KEGG:01100	0.020641
	Carbon metabolism	KEGG:01200	0.049926

Table 6.14. Top enriched transcription factor-binding motifs for distinct abdominal LMNA-R482W DEGs at day 14.

Term name	Term ID	Adjusted *p*-value
Factor: ZF5; motif: NRNGNGCGCGCWN; match class: 1	TF:M00333_1	1.06E-08
Factor: Kaiso; motif: GCMGGGRGCRGS; match class: 1	TF:M03876_1	7.85E-08
Factor: AP2; motif: GCCYGSGGSN	TF:M08867	1.48E-07
Factor: RERE; motif: CNGCNSCNNGSRCRGSGSS; match class: 1	TF:M13129_1	1.61E-07
Factor: E2F4; motif: YCCCGCCNCNNSSNNSNN; match class: 1	TF:M12599_1	5.26E-07

Day 14 gluteal DEGs

In gluteal mutant adipocytes, several DEGs encoding core histone proteins (*H4C8*, *H2AC25*, *H2AC13*, *H2BC17*, *H3C10*) were significantly downregulated at D14 in the 'structural constituent of chromatin' (GO:MF) and 'nucleosome' (GO:BP) enriched terms (**Table 6.15**).

The most significantly upregulated gene was *SATB1* (special AT-rich binding protein 1) (**Table 6.8**), encoding a cell-type-specific 'genome organiser' (Alvarez, *et al*., 2000). SATB1 binds to A-T rich sequences (called matrix-attachment regions (MARs)) that interact with the nuclear matrix, including lamin B1, to organise chromatin looping. These results are relevant given that lamin A binds directly to histone proteins, and its wider role in shaping chromatin structure.

Among the downregulated genes, *EBF3* (early B cell factor 3) was identified as the most significant (**Table 6.8**). This gene belongs to the EBF family of TFs, which are basic helix-loop-helix transcription factors, shown to play an important role in murine adipogenesis. Both *Ebf1* and *Ebf2* are essential for 3T3-L1 cell differentiation (Jimenez, *et al*., 2007), and mice with *Ebf1* deletion develop lipodystrophy (Fretz, *et al*., 2010). Whole-exome sequencing recently identified a novel truncating variant in *EBF2* in a human subject with partial lipodystrophy (Foss-Freitas, *et al*., 2024). The role of EBF3 in human adipose tissue development is less well characterised. Although widely used as a selective marker of murine brown adipocytes, *EBF3* expression in humans is observed in both brown and white adipose depots (Wu, *et al*.,

2012), with one study (Jespersen, *et al*., 2013) reporting a slight increase in levels in brown adipocytes. A look-up of *EBF3* in the RNA-seq dataset showed its expression levels were significantly higher in abdominal compared to gluteal cells, suggesting a potential depot-specific function, and its expression decreased during adipogenesis for both depots.

Table 6.15. Enriched terms for distinct gluteal LMNA-R482W DEGs at day 14. Abbreviations: HDACs, histone deacetylases; HCMV, human cytomegalovirus; HAT, histone acetyltransferases; RMTs, Arm/Rmt methyltransferases.

Source	Term name	Term ID	Adjusted *p*-value
GO:MF	**structural constituent of chromatin**	GO:0030527	0.003510
GO:CC	**nucleosome**	GO:0000786	0.005363
KEGG	**Neutrophil extracellular trap formation**	KEGG:04613	0.001115
	Systemic lupus erythematosus	KEGG:05322	0.002740
	Alcoholism	KEGG:05034	0.014269
Reactome	**HDACs deacetylate histones**	REAC:R-HSA-3214815	0.001500
	Amyloid fiber formation	REAC:R-HSA-977225	0.003247
	HCMV Late Events	REAC:R-HSA-9610379	0.003704
	HCMV Early Events	REAC:R-HSA-9609690	0.008785
	HATs acetylate histones	REAC:R-HSA-3214847	0.010834
	RMTs methylate histone arginines	REAC:R-HSA-3214858	0.017491
	HCMV Infection	REAC:R-HSA-9609646	0.019268

6.3.5 Comparison of distinct mutant DEGs conserved across adipogenesis

As part of a separate analysis, we also compared the distinct mutant DEGs across days 0, 7 and 14 of differentiation to identify transcripts intrinsic to LMNA-R482W cells that were conserved over time. This revealed a core set of 130 genes conserved across adipogenesis in abdominal mutant cells (**Figure 6.12a**), while a core set of 6 genes (*SLC12A7*, *ACKR3*, *LAPTM5*, *ROR2*, *TP53I11*, *ELOVL2*) were found in gluteal mutant cells (**Figure 6.12b**).

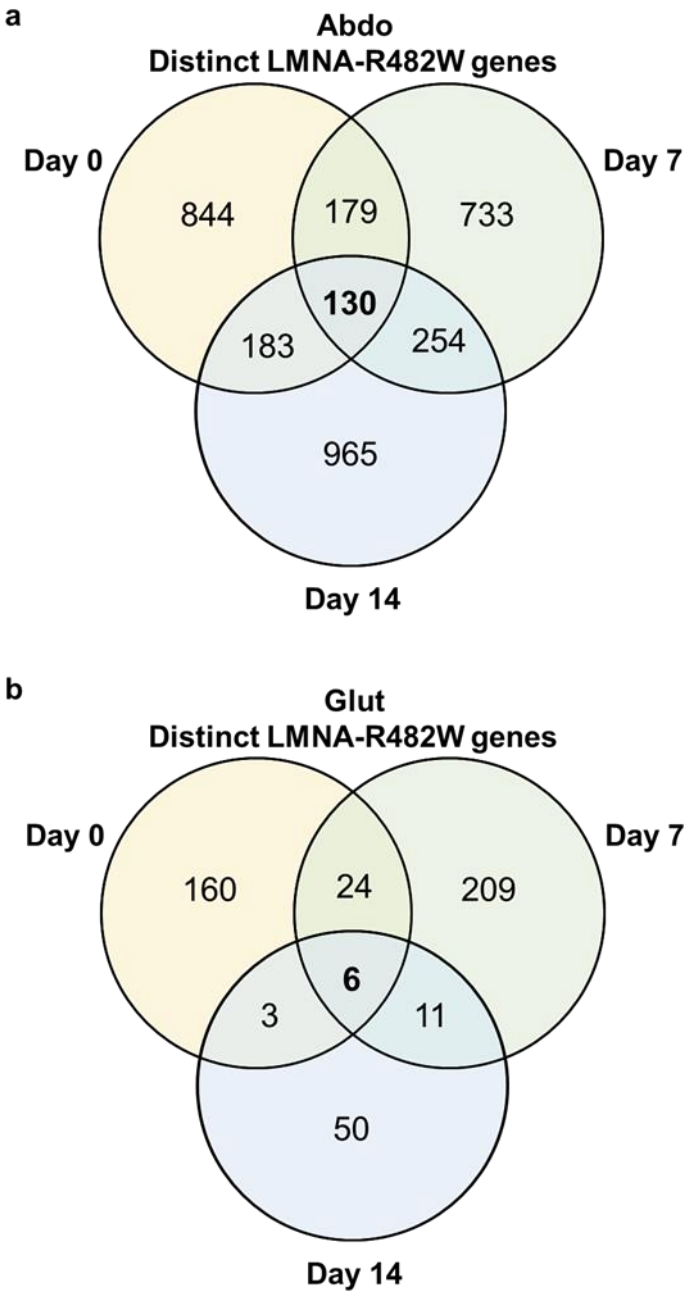


Figure 6.12. Comparison of day 0, 7 and 14 distinct LMNA mutant DEGs to find intersecting genes conserved across adipogenesis. Venn diagrams for abdominal (**a**) and gluteal (**b**) cells.

6.3.5.1 Abdominal mutant DEGs conserved during adipogenesis were linked to collagen, apoptosis and included a PRC1 component

Among the 130 conserved DEGs in abdominal mutant cells, several collagen-related genes were identified. Of these, *CPXM1*, *LOX* and *P4HA1* (all involved in collagen synthesis) were consistently upregulated, whilst *MMP15* (matrix metalloproteinase 15) (involved in ECM degradation) was consistently downregulated.

Another prominent upregulated gene was *PHC3*, encoding a component of the histone-modifying enzyme, PRC1 (Gao, *et al*., 2012). Both PRC2 and PRC1 contribute to chromatin compaction and gene silencing but unlike the PRC2, which has methyltransferase activity, PRC1 catalyses ubiquitination of histone H2A at lysine 119 (H2AK119ub1) (Margueron & Reinberg, 2011) (Simon & Kingston, 2009). PRC1 contributes to *HOX* gene repression (Eskeland, *et al*., 2010), which is interesting given the distinct expression profiles of these genes in subcutaneous abdominal and gluteal adipose tissue, as shown by our group (Pinnick, *et al*., 2014) and others (Karastergiou, *et al*., 2013) (Passaro, *et al*., 2017).

Pathway analysis of the core abdominal mutant genes showed that these were enriched for apoptosis-related pathways (**Table 6.16**), containing several downregulated caspase genes (*CASP2*, *CASP3* and *CASP6*). In particular, caspase-2 has a role that extends beyond apoptosis, including cell cycle regulation, DNA repair, metabolism and aging (Zhang, *et al*., 2007). Mice deficient in *casp2* were reported to show reduced visceral fat depot expansion, but not impaired preadipocyte differentiation (Kim, *et al*., 2018). TRANSFAC analysis revealed that the conserved DEGs were enriched for E2F and ZF5 binding motifs (**Table 6.16**).

Table 6.16. Enriched terms for abdominal LMNA-R482W DEGs conserved during adipogenesis.

Source	Term name	Term ID	Adjusted *p*-value
Reactome	**NADE modulates death signalling**	REAC:R-HSA-205025	0.001282
WP	**Apoptosis modulation by HSP70**	WP:WP384	0.000319
TF	**Factor: E2F-4; motif: SNGGGCGGGAANN**	TF:M09894	0.020698
	Factor: ZF5; motif: GSGCGCGR; match class: 1	TF:M00716_1	0.024401
	Factor: ZF5; motif: NRNGNGCGCGCWN; match class: 1	TF:M00333_1	0.028957
	Factor: E2F-4; motif: SNGGGCGGGAANN; match class: 1	TF:M09894_1	0.037415
	Factor: E2F-1; motif: NNNSSCGCSAANN	TF:M07250	0.041871

6.3.5.2 Gluteal mutant DEGs conserved during adipogenesis

In gluteal mutant cells, the 6 core genes identified were consistently downregulated but this number was too low to detect any enriched pathways. However, it did include two genes with roles in lipid metabolic processes (*ELOLV2* and *ACKR3*) and Wnt signalling (*ROR2*).

6.3.6 Effects on PRC2

Based on the evidence for altered PRC2 function in FPLD2, genes encoding the subunits of this complex were also examined; the subunit EZH2 is responsible for methyltransferase activity of PRC2.

EZH2 expression was significantly downregulated (FDR < 0.05, $\log_2$FC ± 0.5) in abdominal LMNA-R482W cells throughout adipogenesis, but not in gluteal (**Figure 6.13**). In contrast, in abdominal LMNA-WT cells, *EZH2* expression was upregulated at D7.

Further inspection of PRC2 target genes showed that several of these also had altered expression in the LMNA-R482W cells, particularly in abdominal. For example, PRC2 target genes were either upregulated (e.g. *GATA2*, *TBX3*) or downregulated (e.g. *EPAS1*, *TFAP2A*) in abdominal preadipocytes. Several of these genes have established roles in adipogenesis; for example, GATA2 is an anti-adipogenic transcription factor (Tong, *et al*., 2000), while TFAP2A is involved in lipid droplet biogenesis (Scott, *et al*., 2018). *GATA2* and *MSX1* also showed altered expression in gluteal preadipocytes. Further analysis to understand relationships and networks of interacting genes is ongoing in collaboration with Daniel Phillips.

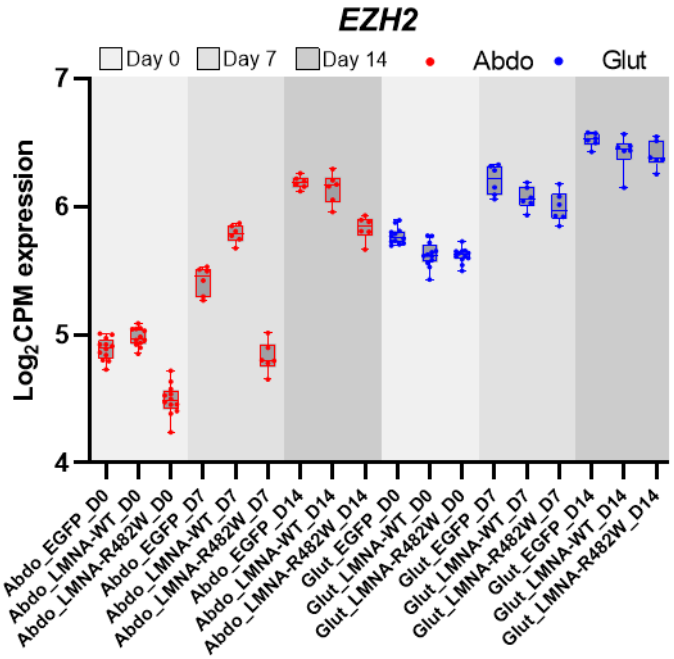


Figure 6.13. *EZH2* expression in abdominal and gluteal cells during differentiation. $\log_2$ counts per million (CPM) of *EZH2* expression on day 0 (*n* = 12), day 7 (*n* = 6) and day 14 (*n* = 6) of adipogenic differentiation.

6.3.7 Verification of mutant DEG selection process

To identify distinct mutant DEGs, both mutant and WT cells were initially compared to EGFP control cells. However, this approach may have resulted in the loss or dilution of certain signals due to statistical filtering during the DEG selection process. Therefore, an additional analysis was performed to directly compare gene expression between WT and mutant cells, serving as an internal control and validation of the original distinct mutant DEGs. These DEGs were then intersected with the previously defined set of distinct mutant DEGs (**Figure 6.14**). Genes present in both sets were considered high-confidence mutant-associated genes, reflecting robust detection across independent analyses. Given the pronounced phenotype in FPLD2 patients' gluteal tissue, I will focus on overlapping genes in this depot.

At day 0, a subset of 42 overlapping DEGs in gluteal cells were identified (**Figure 6.14a**). The downregulated genes included *MXRA5* (previously mentioned) (**Figure 6.15a**), as well as four core mutant DEGs (*ROR2*, *ACKR3*, *TP53I11*, *ELOVL2*) identified in the original analysis. Additional notable downregulated genes included *RARRES2*, which encodes chemerin, a multifunctional adipokine involved in adipogenesis, angiogenesis and inflammation (Helfer & Wu, 2018), and *G0S2* (G0/G1 switch gene 2), a known inhibitor of ATGL (Yang, *et al*., 2010).

At day 7, a total of 63 overlapping DEGs were identified (**Figure 14b**). Among these, *LPL* was the most significantly downregulated transcript in LMNA mutant cells relative to WT (**Figure 6.15b**), followed by *PCK1* (both previously discussed); these are vital for regulating lipid metabolism in adipose tissue. Again, several core mutant DEGs (*ACKR3*, *ROR2*, *SLC12A7*, *TP53I11*) were identified.

By day 14, a total of 42 genes were identified (**Figure 14c**), including *EBF3* (previously discussed) and *DKK2*, which can act as a stimulator or inhibitor of Wnt signalling (Christodoulides, *et al*., 2006). Again, core LMNA mutant DEGs were detected within this set (*ACKR3*, *ROR2*, *LAPTM5*, *ELOVL2*). Together, these results provide further evidence supporting these genes as functional candidates for the FPLD2 phenotype.

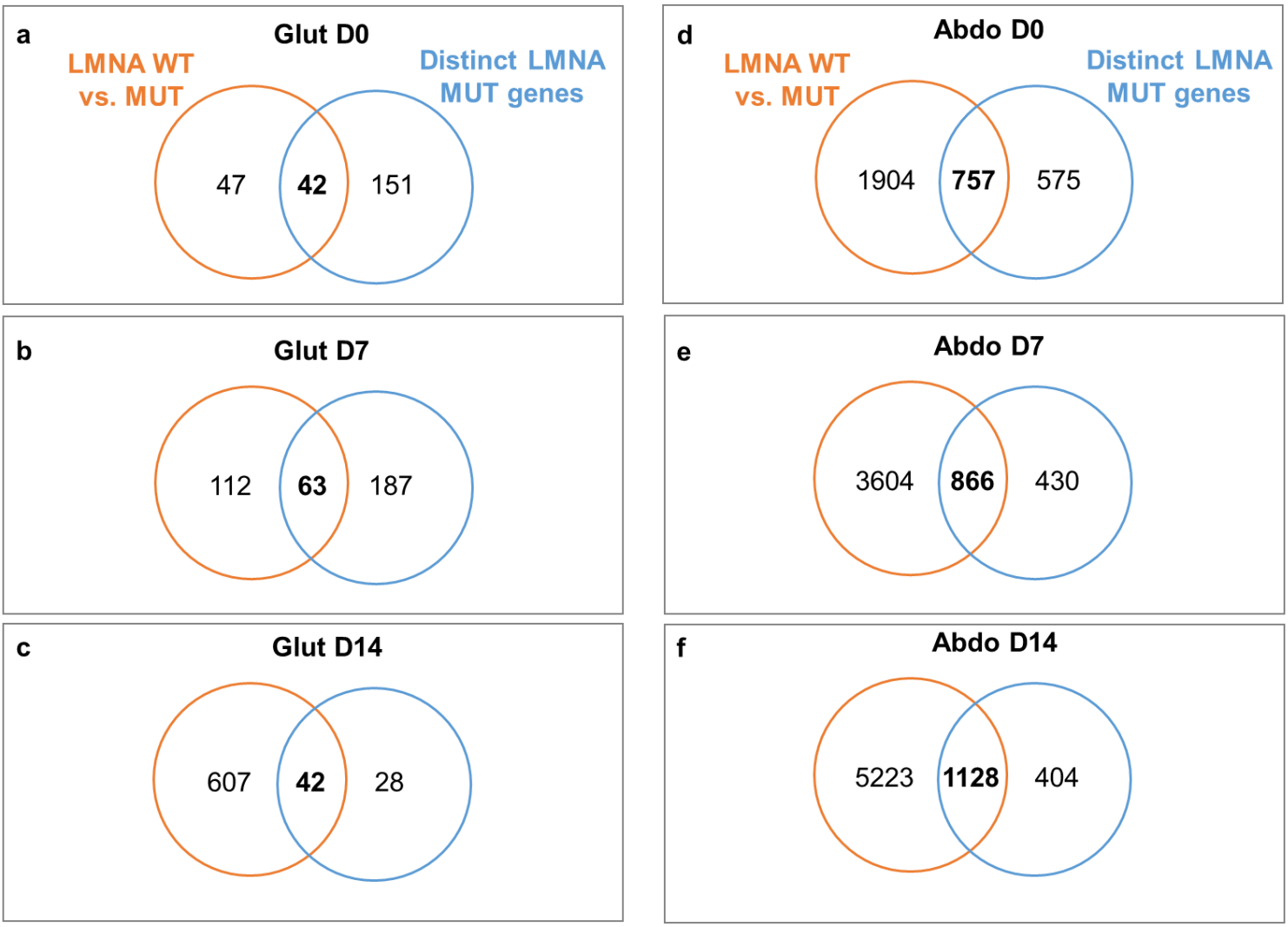
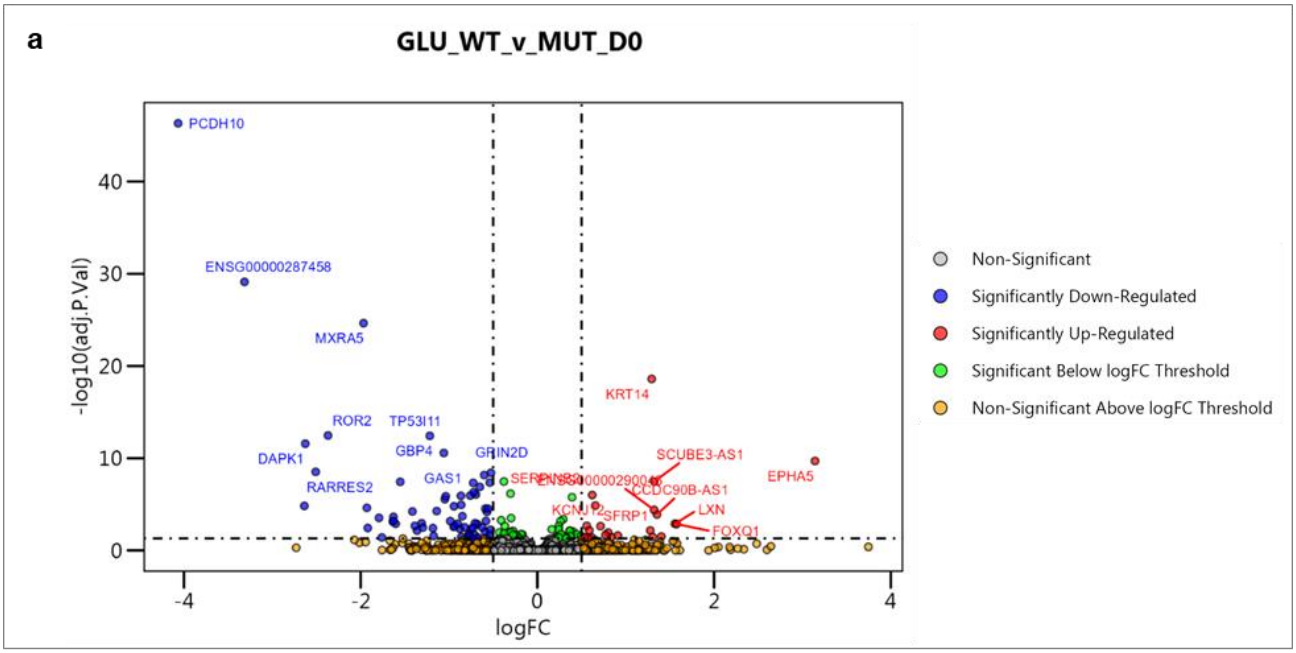
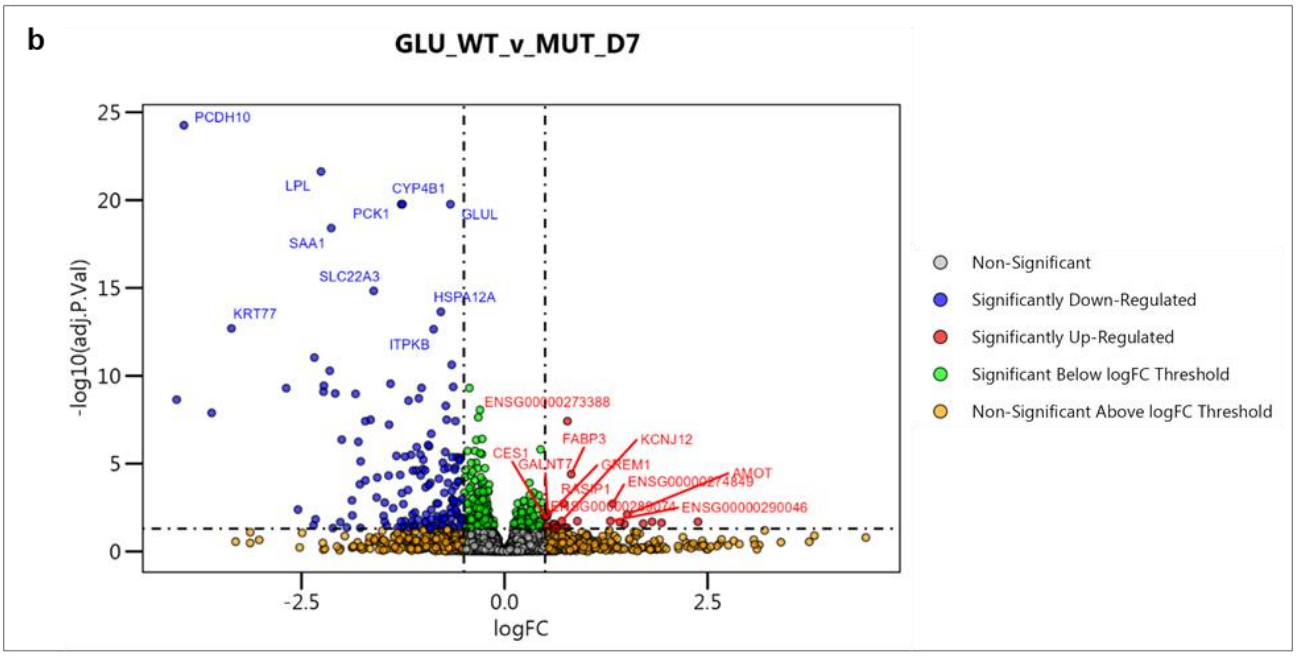


Figure 6.14. Number of overlapping DEGs dysregulated by LMNA R482W from independent analyses. Overlapping genes between distinct LMNA mutant DEG sets (blue circles) and LMNA-WT vs. LMNA-R482W comparisons (orange circles) were identified as validation of the original DEG selection process. Comparisons are at day 0 (**a**), day 7 (**b**) and day 14 (**c**) for gluteal cells; day 0 (**d**), day 7 (**e**) and day 14 (**f**) for abdominal.


a
GLU_WT_v_MUT_D0
PCDH10
ENSG00000287458
MXRA5
KRT14
ROR2
TP53I11
GBP4
GRIN2D
DAPK1
GAS1
RARRES2
SCUBE3-AS1
EPHA5
CCDC90B-AS1
LXN
FOXQ1
-log10(adj.P.Val)
logFC
Non-Significant
Significantly Down-Regulated
Significantly Up-Regulated
Significant Below logFC Threshold
Non-Significant Above logFC Threshold


b
GLU_WT_v_MUT_D7
PCDH10
LPL
CYP4B1
PCK1
GLUL
SAA1
SLC22A3
HSPA12A
KRT77
ITPKB
ENSG00000273388
FABP3
KCNJ12
CES1
GALNT7
GREM1
AMOT
ENSG00000274849
ENSG00000290046
-log10(adj.P.Val)
logFC
Non-Significant
Significantly Down-Regulated
Significantly Up-Regulated
Significant Below logFC Threshold
Non-Significant Above logFC Threshold

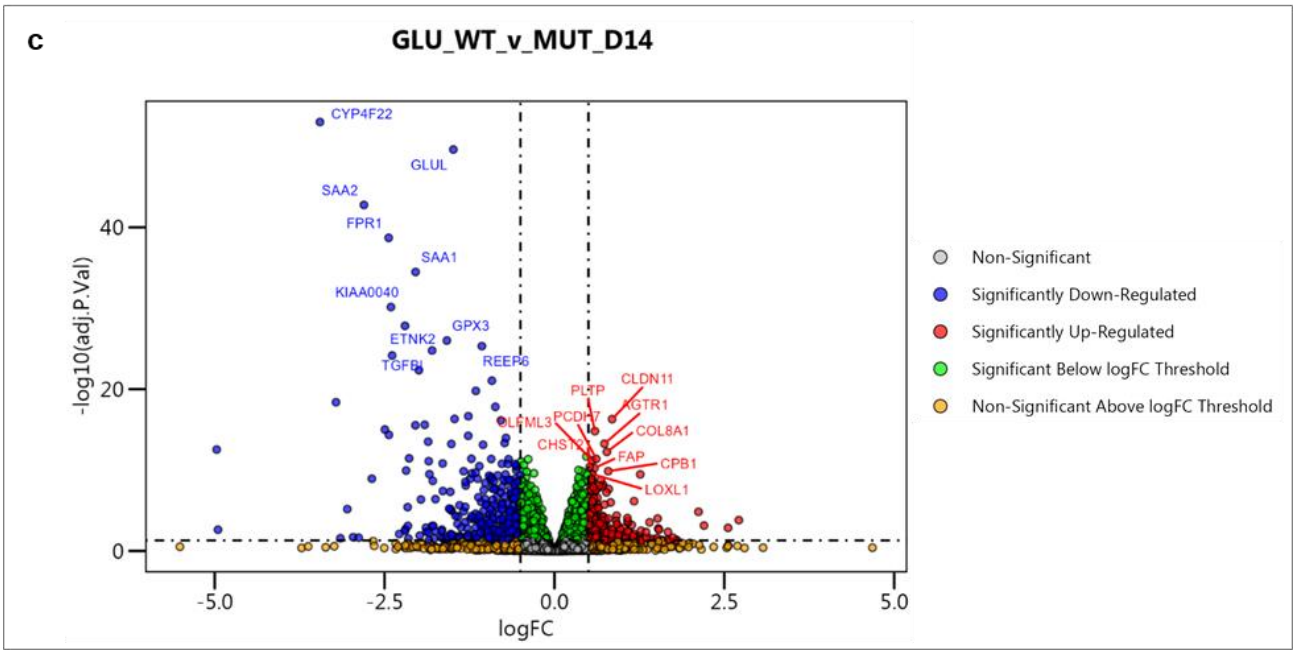

c
GLU_WT_v_MUT_D14
CYP4F22
GLUL
SAA2
FPR1
SAA1
KIAA0040
GPX3
ETNK2
TGFBI
REEP6
PLTP
CLDN11
AGTR1
PCDH7
COL8A1
FAP
CPB1
LOXL1
-log10(adj.P.Val)
logFC
Non-Significant
Significantly Down-Regulated
Significantly Up-Regulated
Significant Below logFC Threshold
Non-Significant Above logFC Threshold

Figure 6.15. Volcano plots showing differentially expressed genes between LMNA-WT and LMNA-R482W cells. DEGs identified at (**a**) day 0, (**b**) day 7, and (**c**) day 14 of differentiation. Log_2 fold change (logFC) is presented on the x-axis, and -log10(adjusted p-value) is presented on the y-axis. Horizontal dotted lines indicate adjusted p-value cut-off (0.05), and vertical dotted lines indicate logFC cut-off of 0.5 or -0.5. Genes that were significantly downregulated or upregulated at each time point are shown in blue or red, respectively. The top 10 most upregulated and downregulated genes are annotated. Genes with significant expression changes and below the logFC threshold are shown in green. Genes with non-significant expression changes and above the logFC threshold are shown in orange. Genes with non-significant expression changes and below the logFC threshold are shown in grey. Day 0 samples were analysed with $n = 12$, and day 7 and 14 samples analysed with $n = 6$, from combined Dox-treated and Dox-untreated replicates.

6.4 Discussion

Based on the 'classical' FPLD2 phenotype, it was hypothesised that the LMNA R482W mutation would cause different transcriptomic changes in depot-specific adipose cells, possibly explaining adipose tissue loss predominately affecting the lower-body. Bulk RNA-seq experiments of abdominal and gluteal mutant preadipocytes during adipogenesis revealed distinct effects on gene expression, with wider changes observed in abdominal cells, possibly driven by a higher number of TFs being affected by the mutation in this depot. Pathway analysis revealed enrichment of broad developmental and cell communication processes in both depots, while also identifying distinct pathways uniquely enriched in each. These results are discussed further below, with emphasis on key genes that may contribute to the FPLD2 phenotype.

6.4.1 Abdominal LMNA-R482W cells showed a striking upregulation of collagen-related genes

In differentiating abdominal cells at D7, several genes involved in collagen synthesis were upregulated, as well as genes encoding lysyl oxidase (LOX) and LOX like (LOXL) enzymes. These enzymes catalyse oxidisation of lysine and hydroxylysine residues, which is essential for the formation of collagen fibrils and thus fibrosis (Pastel, *et al*., 2018). These results indicate that LMNA-R482W adipocytes have increased collagen production, and are consistent with the previously observed increase in collagen fibres detected in spheroids in **Chapter 5**.

As previously mentioned, fibrosis in adipose tissue is closely associated with inflammation and insulin resistance in lipodystrophy and obesity – contrasting conditions that nevertheless share key pathological features. Two independent studies (Le Dour, *et al*., 2017a) (Bérériat, *et al*., 2011) have reported fibrotic changes in cervical subcutaneous adipose tissue from FPLD2 patients carrying the LMNA R482W mutation. Le Dour *et al*. (2017a) also observed increased

fibrosis in iWAT of transgenic mice overexpressing the lamin A R482Q variant compared to non-transgenic controls. Interestingly, these changes occurred without animals developing regional lipoatrophy, suggesting that early ECM alterations precede adipose tissue loss.

The composition of adipose tissue ECM varies between depots, playing a critical role in regulating cellular functions such as adipogenic potential and tissue expandability. For example, our group has previously investigated the role of COMP (cartilage oligomeric matrix protein), an ECM protein more highly expressed in gluteal than abdominal subcutaneous adipose tissue which exerts pro-adipogenic effects (Denton, *et al*., 2018). Collagen genes also show depot- and cell-type-specific expression patterns; collagen VI is more highly expressed in SAT than VAT, and shows higher expression in SVF than mature adipocytes (Jääskeläinen, *et al*., 2023). Consequently, the distinct ECM environment and cellular composition of each depot may contribute to the tissue-specific effects and variable disease severity associated with the LMNA R482W mutation. Based on histological evidence from previous studies, along with the findings presented here, excess ECM deposition likely represents one of the mechanisms involved in FPLD2 pathophysiology.

6.4.2 Altered ZF5 gene targets in abdominal LMNA mutant cells

Abdominal mutant DEGs showed enrichment for ZF5 binding sites. ZF5 is a Krüppel-like transcription factor which acts as a repressor of the fragile X-related (*FMR1*) gene (Orlov, *et al*., 2007), which was previously linked to lamin A function. Oldenburg *et al*. (2014) reported that lamin A interacts with FXFR1P (encoded by *FMR1*). Expression of lamin A R482W disrupted this interaction, leading to elevated FXFR1P levels in human ASCs. The authors carried out overexpression experiments to test the functional impact of FXFR1P on adipogenesis, which inhibited adipogenic differentiation and induced the expression of myogenic genes. Consistent with these findings, higher levels of FXFR1P were detected in FPLD2 patient fibroblasts.

In my results, enrichment for ZF5 binding motifs among the abdominal mutant DEGs may therefore represent a novel link between lamin A R482W and increased FXFR1P expression levels. In other words, lamin A R482W may also interfere with ZF5 transcriptional activity, leading to de-repression of *FMR1* and other target genes. This transcriptional dysregulation could reprogram adipocyte precursors toward a myogenic fate, contributing to the muscular hypertrophy commonly observed in FPLD2 patients, originally proposed by Oldenburg *et al*. (2014).

However, look-up of *FMR1* and myogenin (*MYOG*) within the abdominal gene set, transcripts previously reported as upregulated by Oldenburg *et al*. (2014), revealed no significant changes in their expression. Interestingly, several other genes associated with myogenesis were found to be dysregulated. These included *TBX5*, *SOX9*, *SHOX2*, *DES*, *SIX4*, which were upregulated, and *MYORG1*, *MYOM1*, *MLIP*, which were downregulated. These genes not only mapped to GO terms associated with muscle development and cardiac hypertrophy, but also showed enrichment for ZF5 binding motifs, supporting a regulatory role for ZF5 in their transcription. One of the downregulated DEGs, *MLIP* (muscular LMNA interacting protein), plays a critical role in protecting the heart against stress (Cattin, *et al*., 2015) and is of potential interest given the high prevalence of cardiomyopathy in FPLD2 patients (Vantyghem, *et al*., 2004). The lack of binding motif enrichment for ZF5 among gluteal LMNA mutant DEGs, suggests that alternative mechanisms may be driving gene expression changes in cells from this depot.

6.4.3 Altered Wnt gene expression in gluteal LMNA-R482W cells

Wnt-β-catenin signalling is a crucial pathway that determines MSC fate, playing dual roles in adipocyte and osteoblast development (Christodoulides, *et al*., 2006). In the canonical Wnt-β-catenin signalling pathway, the transmembrane protein Frizzled (FZD) and its co-receptors, LRP5/6 (low-density lipoprotein receptor-related proteins 5 and 6), are activated by Wnt

ligands binding to FZD. This initiates a signal transduction cascade that involves recruitment of three proteins (GSK3β, Axin and APC), the so-called 'destruction complex', to FZD and LRP5/6 at the cell membrane (Christodoulides, *et al*., 2009). This prevents cytosolic β-catenin from phosphorylation and degradation via the proteasome, leading to an increase in intracellular β-catenin. Active, non-phosphorylated β-catenin then translocates to the nucleus where it forms a complex with T-cell factor/lymphoid enhancer factor (TCF/LEF) transcription factors; this induces expression of Wnt target genes such as Axin2 (axis inhibition protein 2) (Bennett, *et al*., 2002) (Christodoulides, *et al*., 2009). Axin2 maintains preadipocytes in an undifferentiated state by inhibiting C/EBPβ activity (de Winter & Nusse, 2021). It also acts as a negative regulator of Wnt signalling by targeting β-catenin for degradation in the absence of Wnt ligands, thereby reducing β-catenin levels in a negative feedback loop.

Other key regulators of Wnt signalling include secreted extracellular Wnt antagonists, such as members of the secreted Frizzled-related proteins (SFRPs) and dickkopf (DKK) protein families (Christodoulides, *et al*., 2009). SFRPs inhibit Wnt signalling by binding to Wnts and preventing their interaction with FZD receptors, whereas DKK proteins act on the LRP5/6 co-receptors, which targets them for internalisation (MacDonald, *et al*., 2009). This process is dependent on KREMEN1, which forms a complex with DKK1 and *LRP5*/6.

In the RNA-seq dataset, several genes involved in Wnt signalling were differentially expressed in the LMNA-R482W cells (vs. EGFP), particularly in gluteal. These included genes encoding Wnt antagonists (*DKK1*, *DKK2*, *SFRP1*), which were significantly upregulated at D7 in gluteal mutant cells. DKK1 inhibits canonical Wnt signalling, which typically promotes adipogenesis (Christodoulides, *et al*., 2006), whereas it was recently suggested that DKK2 functions as a beige adipokine that can inhibit adipogenesis (Yang & Shi, 2021). At D0, gluteal mutant DEGs included Wnt receptor genes (*KREMEN1*, *ROR2*), along with several others encoding Wnt ligands (*WNT16*, *WNT2*, *WNT7B*).

Wnt signalling is traditionally considered anti-adipogenic in preadipocytes. However, our own group's research has shown its effects on adipogenesis are complex and vary by depot, depending on levels of β-catenin transcriptional activity (Loh, *et al*., 2015). In our group's previous study, *in vitro LRP5* KD experiments revealed distinct effects on abdominal and gluteal preadipocyte biology. LRP5 KD enhanced adipogenesis in abdominal preadipocytes, whereas differentiation was decreased in gluteal. Dose-dependent suppression of adipogenesis was observed in gluteal preadipocytes using a β-catenin specific inhibitor. In contrast, in abdominal cells, low levels of β-catenin inhibition promoted adipogenesis, while higher levels suppressed it.

Therefore, the increased *DKK* expression in gluteal LMNA-R482W cells could result in reduced LRP5 activity, lowering β-catenin levels. I hypothesise that this could mimic the effects of LRP5 deficiency and impair adipogenesis to a greater extent in gluteal cells, as opposed to abdominal, depending on the level of β-catenin reduction (Loh, *et al*., 2015). These questions could be addressed using Western blotting to determine expression levels of active β-catenin protein in the LMNA mutant cells, against EGFP control cells.

Intriguingly, loss- or gain- of function (LoF or GoF) mutations in *LRP5* are linked to altered body fat distribution (Loh, *et al*., 2025). Specifically, LoF *LRP5* mutations are associated with increased storage of abdominal fat, osteoporosis and increased risk of T2D (Saarinen, *et al*., 2010). Conversely, individuals with rare GoF *LRP5* mutations show increased lower-body fat accumulation, higher bone mass and improved insulin sensitivity (Loh, *et al*., 2025) (Little, *et al*., 2002). In investigation of LRP5's effects on fat distribution, Loh *et al*. (2015) also found a negative correlation between *LRP5* mRNA expression in gluteal depots and upper-body fat accumulation in females (n = 47).

Given that rare LoF *LRP5* mutations are associated with osteoporosis, it is valid to consider whether FPLD2 patients have reduced bone mass. Indeed, Corsa *et al*. (2021) found that FPLD2 patients (n = 24) carrying LMNA R482 mutations have reduced bone mass and bone mineral density compared to healthy controls.

Impaired Wnt/β-catenin signalling has been reported in different models of laminopathies, for example in mice with LMNA-related cardiomyopathy (Le Dour, *et al*., 2017b) and HGPS (Hernandez, *et al*., 2010). Overexpression of LMNA increased nuclear β-catenin levels in human MSCs, supporting a regulatory role of lamin A in Wnt signalling (Bermeo, *et al*., 2015). These cells displayed reduced adipogenic and increased osteogenic differentiation potential. Overall, further investigation into Wnt signalling, which is a key player in preadipocyte differentiation, should be considered for investigating FPLD2.

6.4.4 Lipid metabolism and Wnt signalling-associated genes were consistently downregulated during adipogenesis in gluteal mutant cells

Identification of a core subset of genes altered by the LMNA mutant showed that *ELOLV2* expression was consistently downregulated in gluteal cells during adipogenesis. In contrast, in abdominal cells, *ELOVL2* expression was upregulated. ELOLV2 catalyses the rate-limiting step of long-chain polyunsaturated fatty acid (LC-PUFA) elongation, making it crucial for synthesis of omega-3 FAs such as docosahexaenoic acid (DHA) (22:6n-3) (Chen, *et al*., 2020). Interestingly, DHA inhibits preadipocyte differentiation and reduces body fat accumulation in various cell and animal models, by promoting apoptosis and lipolysis (Kim, *et al*., 2006) (Bian, *et al*., 2024).

Laminopathies are generally considered a disease of early cellular aging, with HGPS as the most extreme example. Methylation of the *ELOVL2* promoter is recognised as a key component of the ‘aging epigenetic clock’ (Garagnani, *et al*., 2012), consistent across multiple tissue types (Slieker, *et al*., 2018). Therefore, the opposite effect of LMNA R482W on *EVOLV2* expression (increased in abdominal and decreased in gluteal) may be related to DNA methylation changes or cellular senescence.

Another notable gene in the gluteal set was *ACKR3* (also known as *CXCR7*), encoding for a scavenger receptor of chemokines, mainly CXCL12. ACKR3's role in the regulation of adipose tissue lipid levels, using an adipocyte-specific KO mouse model, has been reported (Gencer, *et al*., 2021). ACKR3 internalises chemokines, targeting them for lysosomal degradation, thereby reducing chemokine availability in the extracellular space. As an adipokine, CXCL12 acts as a chemoattractant for monocytes and has been linked to inflammation and insulin resistance in obesity (Kim, *et al*., 2014).

To link the RNA-seq results to *in vivo* studies, it would be interesting to measure circulating CXCL12 levels, as well as secretion from specific adipose depots, in FPLD2 patients. I hypothesise that secreted CXCL12 levels will be elevated in femoral adipose depots of FPLD2 subjects, due to reduced clearance by ACKR3. In line with this, Araújo-Vilar *et al*. (2012) previously observed increased $CD68^+$ macrophage and $CD3^+$ lymphocyte infiltration in lipodystrophic adipose tissue samples. Furthermore, higher circulating levels of the pro-inflammatory adipokine MCP-1 have been reported in FPLD2 patients compared to obese subjects (Treiber, *et al*., 2023). In summary, if ACKR3 expression is reduced *in vivo*, this could cause impaired chemokine clearance resulting in inflamed and dysfunctional adipose tissue, with depot-specific effects in gluteal.

Another core gluteal mutant gene was *ROR2*, encoding for a tyrosine kinase receptor that plays a complex role in Wnt signalling (Guo & Xing, 2022). This receptor binds to a variety of Wnt ligands and can activate both canonical β-catenin-dependent and non-canonical β-catenin-independent Wnt signalling pathways. In osteoblastic cells, ROR2 was reported to inhibit Wnt1 and Wnt3-mediated stabilisation of β-catenin (Billiard, *et al*., 2005). More recently, in muscle mesenchymal progenitor cells, it was shown that ROR2 binds Wnt11 to mediate non-canonical Wnt signalling, with effects on cell proliferation, adipogenic differentiation and senescence (Kamizaki, *et al*., 2024). The authors observed nuclear blebbing following KD of ROR2 or Wnt11; this was linked to perinuclear actin stress fibre formation, due to increased cellular senescence (occurring via the cGAS-STING pathway). It is currently unknown whether

downregulation of ROR2 expression in depot-specific preadipocytes has similar consequences and contributes to the previously observed nuclear blebbing in gluteal cells (**Chapter 5**).

6.4.5 Clues from PCDH10 expression – a possible link between LMNA, HOTAIR and PRC2?

Although not discussed in detail in this chapter, the most significantly upregulated DEG in D0 and D7 gluteal LMNA-WT vs. EGFP cells was *PCDH10* (protocadherin 10). Interestingly, the gluteal fat depot-specific *HOTAIR* acts as a repressor of *PCDH10* expression by methylating the promoter of this gene (Kuo, *et al*., 2022) (Seo, *et al*., 2021). In line with this, *PCDH10* expression was higher in abdominal EGFP cells compared to gluteal, i.e. in the cells with lower *HOTAIR* expression (abdominal), *PCDH10* expression was increased.

Elevated *PCDH10* expression in gluteal LMNA-WT cells suggests that *HOTAIR* recruitment to the promoter region of this gene is somehow perturbed. This may be due to increased physical interactions between overexpressed WT lamin A and PRC2 (Cesarini, *et al*., 2015), which is also known to interact with *HOTAIR* (Kuo, *et al*., 2022) (**Figure 6.16**). A scaffolding role for *HOTAIR* in PRC2 recruitment has been previously demonstrated (Tsai, *et al*., 2010).

In contrast, *PCDH10* expression was downregulated in gluteal LMNA mutant cells. This opposite effect in mutant cells may indicate increased methylation by *HOTAIR*-PRC2 complex at the *PCDH10* promoter. I speculate this could occur if, based on previous evidence for lamin A R482W disrupting PRC2 recruitment (Briand, *et al*., 2018b), this would increase the amount of free PRC2 available for *HOTAIR* interaction. The higher levels of 'available' PRC2 could then act cooperatively with *HOTAIR*, in gluteal cells, to increase suppression of *PCDH10*, potentially explaining these findings.

Our group previously investigated the role of *HOTAIR* in gluteal preadipocytes and found it is essential for maintaining the gluteal adipocyte transcriptome (Kuo, *et al*., 2022). Interestingly,

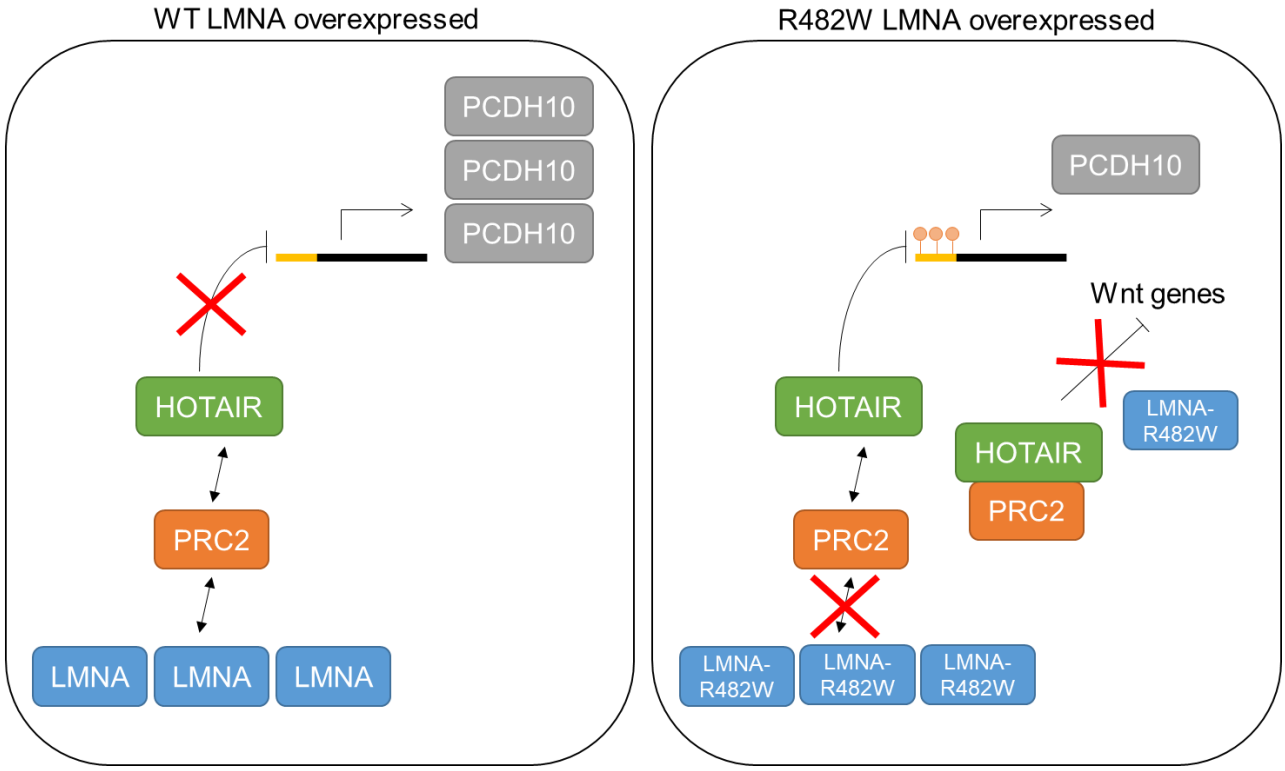
gluteal preadipocytes with *HOTAIR* KO displayed elevated *PCDH10* expression, mirroring my observation of this in gluteal LMNA-WT cells. In *HOTAIR* KO cells, there was decreased occupancy of a PRC2 subunit (SUZ12), as well as reduced H3K27me3 levels, at the *PCDH10* promoter, indicating impaired PRC2 recruitment (Kuo, *et al*., 2022). PRC2 and *HOTAIR* were shown to act cooperatively to regulate expression of Wnt genes in gluteal preadipocytes, facilitating their differentiation. This is intriguing given my observation of the changes in Wnt-related gene expression in gluteal LMNA-R482W cells.

Given the low level of *HOTAIR* expression in abdominal adipose tissue, these results raise further questions as to whether there is a requirement of WT LMNA for PRC2/*HOTAIR* function to maintain the gluteal adipocyte transcriptome. In gluteal cells carrying the dominant-negative LMNA mutation, due to the presence of *HOTAIR*, these interactions are potentially altered, resulting in dysregulation of certain genes such as Wnt (**Figure 6.16**).

However, it should be noted that *HOTAIR* can silence genes independent of PRC2 (Portoso, *et al*., 2017), highlighting the complexity of these processes. Whilst not investigated in my work, studying the relationship between *HOTAIR*, lamin A (WT or R482W) and PRC2, is a research question that could be addressed using these cell models.

a **GLUT**

In nFPLD2 cells, high HOTAIR = low PCDH10



b **ABDO**

In nFPLD2 cells, low HOTAIR = high PCDH10

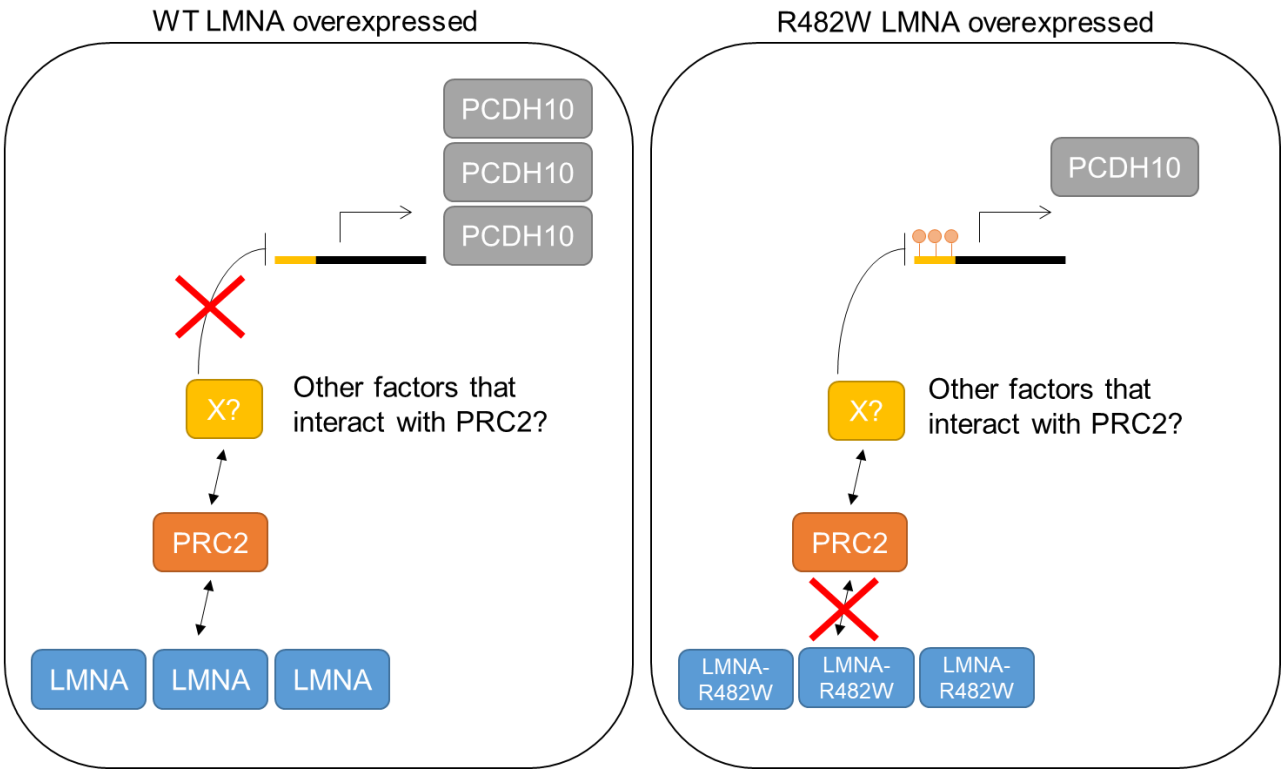


Figure 6.16. Potential mechanism of PRC2 regulation and Wnt signalling in regional LMNA R482W-expressing adipose cells. *HOTAIR* is a depot-specific lncRNA that interacts with PRC2 to maintain the gluteal transcriptome. (**a**) In gluteal adipose cells, LMNA R482W expression may disrupt recruitment of PRC2, enabling *HOTAIR*/PRC2 to increase suppression of the protocadherin 10 (*PCDH10*) gene. *HOTAIR*/PRC2 is important for Wnt gene regulation in gluteal adipocytes (Kuo, *et al*., 2022), however in the presence of the LMNA mutation this function may be perturbed, altering expression of Wnt genes (observed in gluteal mutant cells in this thesis). (**b**) In contrast, in abdominal adipose cells with lower *HOTAIR* expression, *PCDH10* expression may be regulated by PRC2 and/or unknown epigenetic factor(s), since abdominal cells displayed similar patterns in *PCDH10* expression in the RNA-seq results. In these cells, Wnt gene regulation may be affected differently in the presence of LMNA R482W, potentially due to lack of *HOTAIR*. An alternative hypothesis is that Wnt gene dysregulation occurs due to the LMNA mutation in both depots, however the effect of Wnt signalling on adipogenesis in each depot is more nuanced and depends on levels of β-catenin transcriptional activity. This has been shown to have distinct effects on adipogenesis and proliferation in abdominal and gluteal preadipocytes (Loh, *et al*., 2015). nFPLD2, non-familial partial lipodystrophy type 2.

6.4.6 Summary

In summary, this work investigated the ‘gene expression’ hypothesis by performing transcriptional profiling of regional human adipose cells carrying the lipodystrophy-linked LMNA R482W mutation, identifying several genes distinct to the mutant cells. The functional significance of these targets could be further investigated for exploring the depot-specific effects of FPLD2, such as altered Wnt signalling (canonical and non-canonical) in gluteal adipocytes, or the development of fibrosis in abdominal preadipocytes during adipogenesis.

Future work using these cell models could include experiments assessing DNA methylome changes or chromatin accessibility via assay for transposase-accessible chromatin with sequencing (ATAC-seq), to gain a detailed understanding of epigenetic changes induced by LMNA R482W. LAD identification by DamID or ChiP-seq could be used to map changes in the genome-NL interactions during cell commitment to differentiation. If cells were analysed at the same time points, these results could be integrated into the RNA-seq data presented herein. This would provide a better understanding of how the altered transcriptome in LMNA mutant cells is linked to changes in spatial chromatin organisation and histone modifications.

7 General discussion and future perspectives

At the start of my DPhil, there was a lack of *in vitro* 3D adipose models featuring high-throughput automation. Whilst some studies have successfully developed and characterised different 3D adipose models, few of these have been applied to investigate genes associated with adipose tissue development and function. Therefore, the primary aim of this thesis was to develop, optimise and characterise 3D adipose cultures that could support automated workflows for further reproducibility, and functional testing of genes implicated in adipose tissue dysfunction. These models were designed to serve as a more physiologically relevant and scalable tool for the study of adipose biology, with potential applications in metabolic disease research.

7.1 Automation of 3D adipose spheroid production

A key outcome of this thesis was the development of an automated platform for the generation of adipose spheroid models using primary preadipocytes derived from murine subcutaneous WAT (**Chapter 3**). By adapting a previously manual spheroid generation protocol (Graham, *et al*., 2019), this work introduced a nanolitre-scale liquid handling system to automate the droplet dispensing process, addressing a major limitation in the existing method.

The use of primary SVF cells, a heterogeneous cell mixture containing physiologically relevant preadipocytes, enhanced the biological relevance of the model compared to monoculture systems that rely on a single immortalised cell line. This approach better recapitulates the cellular complexity of *in vivo* adipose tissue, thereby enhancing the biological relevance of downstream studies.

The adoption of a 96-well plate format and nanolitre dispensing technology offered several notable advantages. Firstly, the system allowed for increased scalability and statistical power, critical for high-throughput screening applications. Secondly, automation led to reduced inter-

sample variability of the spheroid size and cell numbers, important parameters influencing adipocyte differentiation outcomes. This also allowed more precise control over the spheroid sizes to minimise spheroid necrosis. Lastly, the workflow improvements as a result of automation reduced manual sample handling time, increasing both speed and throughput.

Although the system demonstrated several benefits, the initial cost of the equipment may pose a barrier for other researchers or commercial groups seeking to adopt this approach. However, the financial investment required for nanolitre dispensing technology could be offset by the long-term efficiency gains and increased reproducibility of results. Moreover, alternative low-volume liquid handling systems or the development of custom-built solutions may offer more cost-effective options while retaining the core benefits of the automated system.

7.2 Validation of the murine adipose spheroid model

The 3D adipose system was validated using SVF cells isolated from *Rreb1* heterozygous knockout mice, a gene associated with T2D risk and ectopic fat distribution through GWA studies (Mahajan, *et al*., 2014) (Chu, *et al*., 2017). Previous work had implicated *Rreb1* in the regulation of brown adipocyte gene expression through recruitment of the histone demethylase Jmjd3 (Pan, *et al*., 2015) and more recent unpublished work (Yu, *et al*., 2024) has shown a clear WAT phenotype in a mouse model, that required further investigation in a cellular system. To investigate this, I performed histological analysis of WAT sections from *Rreb1*$^{+/-}$ knockout mice (**Chapter 3**), revealing sex- and diet-dependent changes in adipocyte size within subcutaneous and visceral depots; this indicated that *Rreb1* haploinsufficiency disrupts hypertrophic and/or hyperplastic processes in these tissues.

The 3D spheroid system provided a suitable *in vitro* platform to explore the role of *Rreb1* in adipogenesis. Compared to wild-type controls, spheroids generated from *Rreb1* haploinsufficient cells displayed significantly smaller sizes and impaired lipid accumulation during differentiation, indicating a functional defect in adipogenesis. These results supported

the hypothesis that Rreb1 contributes to white adipocyte differentiation and growth, and demonstrated the usefulness of the spheroid model in revealing functional gene effects relevant to adipose biology.

The automated 3D culture system offered several key advantages in this scenario. The high-throughput format enabled large numbers of replicates to be generated and analysed by high-content imaging, improving statistical power and confidence in observed effects, which may be subtle when examining GWA study variants (Frayling, 2014). Additionally, the increased physiological relevance of the 3D environment, including endogenous ECM production and cell spatial organisation, allowed for the detection of subtle morphological and functional differences that may go undetected in 2D cultures. Precise control of spheroid size and cell number through automation also minimised experimental variability, further enhancing reproducibility. Together, these features made the spheroid model a robust and sensitive tool for investigating gene function in an adipose tissue-like model.

7.3 Depot-specific human 3D adipose models

Current research in human adipose biology relies predominately on *in vitro* models derived from a single anatomical depot, most commonly abdominal subcutaneous fat obtained during surgical procedures. However, this approach does not account for the inherent heterogeneity between depots, which differ widely in their cellular composition, morphology and metabolic function. These differences can have significant implications for metabolic health, and findings obtained from one depot may not necessarily translate to others.

To address this gap, I developed automated 3D adipose spheroid models using human preadipocytes from anatomically distinct depots (**Chapter 4**), with the aim of using the model for the study of human genetic disorders affecting adipose tissue function. These depot-specific 3D models were designed to more closely replicate the biological and functional

characteristics of abdominal and gluteal adipose tissues. They demonstrated key differences consistent with the known *in vivo* behaviour of these depots. For instance, adipose spheroids derived from gluteal preadipocytes contained larger lipid droplets than those from the abdominal depot, aligning with the established morphological features observed *in vivo*.

Staining of nuclei and lipid droplets in 3D culture revealed further differences in tissue expandability between the depots, with gluteal spheroids containing twice as much lipid content as abdominal spheroids, despite both spheroids expanding to a similar extent. This suggests that gluteal preadipocytes expanded via hyperplasia and hypertrophy during *in vitro* differentiation, while abdominal spheroids expanded predominately via hyperplasia.

These features are particularly relevant in the context of metabolic disease, as the mode of adipose tissue expansion is closely linked to insulin sensitivity, inflammation and metabolic disease risk. Hyperplastic expansion, as typically seen in the gluteal depot, is generally considered more metabolically favourable than hypertrophy alone, which is associated with elevated cellular stress and inflammation. Therefore, the ability of these models to maintain depot-specific traits provide a unique tool to investigate how different genetic modifications influence regional fat distribution and contribute to metabolic disease susceptibility.

Importantly, some of these depot-specific features are difficult to capture in 2D cultures, where the flat environment restricts cell proliferation, migration and spatial organisation. In contrast, the spheroid system adopted provided an environment that enabled the emergence of physiologically relevant features, such as tissue expansion and ECM remodelling.

Overall, these findings reinforce the importance of having different models to study the unique responses of individual adipose depots. The tools developed represent a significant step forward for mechanistic studies of human adipose tissue biology, and offers a foundation for exploring how factors affecting regional fat distribution influence metabolic disease. It also

provides a suitable model system to examine disease mechanisms affecting specific depots, as seen in partial lipodystrophy.

7.4 Depot-specific effects of the LMNA R482W mutation in FPLD2

I applied the human adipose spheroid model by selecting one of the most striking monogenic disorders of regional adipose tissue dysfunction: familial partial lipodystrophy type 2 (FPLD2) caused by the LMNA *p*.R482W mutation. Although monogenic lipodystrophies are rare, they offer a powerful model for investigating the underlying causes of regional adipocyte failure (Mann & Savage, 2019). It is poorly understood why subcutaneous gluteofemoral and abdominal adipose depots are disproportionately affected in FPLD2. Whilst previous studies have implicated altered transcriptional and epigenetic regulation (Vadrot, *et al*., 2015) (Oldenburg, *et al*., 2017), most of these have been limited to adipose cells derived from a single anatomical depot. To address this, I employed the depot-specific preadipocyte models to investigate how LMNA R482W differentially affects adipose cells derived from the two main depots.

In **Chapter 5**, preliminary experiments were performed in 2D culture for ease of manipulation and characterisation, with the intention of validating key findings in the spheroid model. This work revealed distinct effects of the mutation in abdominal and gluteal cells on a range of biological processes, including preadipocyte proliferation, nuclear morphology, adipogenic differentiation, and the expression of genes involved in lipid metabolism.

For example, expression of *LPL*, a key regulator of fatty acid uptake, was significantly reduced in gluteal LMNA mutant preadipocytes during differentiation, while remaining unchanged in abdominal mutant cells. This is consistent with the pattern of fat loss in patients and aligns with previous findings reported by Araújo-Vilar *et al*. (2009), who demonstrated reduced *LPL*

expression (assessed using qPCR) specifically in femoral adipose tissue biopsies from FPLD2 subjects.

Given the importance of this enzyme in adipose tissue lipid uptake, decreased LPL activity in the gluteofemoral region would result in reduced clearance and uptake of chylomicron-derived fatty acids. As a result, lipids that would normally be safely stored in this depot would be redirected to other tissues, including abdominal adipose depots and non-adipose organs. This would promote ectopic fat accumulation, elevate circulating triglyceride levels, and contribute to systemic insulin resistance, which are all characteristic features of FPLD2. Reduced LPL activity in the gluteal depot would likely result in worse metabolic health outcomes for females, given the importance of this depot as a 'metabolic sink', reflecting clinical observations of female FPLD2 patients suffering worse metabolic effects (Garg, 2000).

7.4.1 FPLD2: a gene expression model, structural model, or a combination of both?

To gain a more comprehensive understanding of the global gene expression changes in FPLD2, RNA-sequencing analysis of 2D cultures was performed (**Chapter 6**). This data revealed both shared and depot-specific pathways affected by the mutation, including novel candidate genes involved in FPLD2 pathogenesis. Notably, abdominal mutant cells displayed increased expression of genes linked to ECM components, particularly collagens, suggesting early fibrotic changes in this depot. This was supported by histological analysis of adipose spheroids, with abdominal mutant cultures showing enhanced collagen accumulation, indicative of a fibrotic tissue environment that limits adipose expansion and promotes inflammation. In contrast, gluteal mutant cells showed minimal evidence of increased collagen accumulation, suggesting that early fibrosis may be less prevalent in this depot.

RNA-sequencing analysis revealed that the LMNA R482W mutation altered the expression of multiple Wnt pathway genes, potentially through disruption of PRC2 activity. Supporting this,

Wang *et al*. (2010) demonstrated that Ezh2, the catalytic subunit of PRC2, is essential for adipogenesis through repression of Wnt gene expression. In their study, *Ezh2*-deficient murine brown preadipocytes showed impaired adipogenesis, upregulation of Wnt genes and increased cytosolic accumulation of β-catenin protein. Given that our group has previously shown that β-catenin activation downstream of the LRP5 receptor elicits depot-specific responses in human preadipocytes (Loh, *et al*., 2015), it is plausible that in FPLD2, aberrant Wnt/β-catenin signalling, driven by disruption of Ezh2 function by mutant LMNA, may differentially impair adipogenesis depending on fat depot location. This mechanism would contribute to the characteristic pattern of regional lipoatrophy.

Measuring Dickkopf and β-catenin protein levels could form the initial approach to assess Wnt signalling in the LMNA mutant cells. However, caution should be taken when comparing Wnt pathways in 2D and 3D culture, as secreted extracellular Wnt antagonists may be partially retained within the hydrogel-matrix but lost during media changes in 2D culture, potentially influencing adipogenic outcomes. Further work would be required to quantify and characterise the presence of secreted factors within the hydrogel-matrix compared to conditioned media collected from 2D samples.

Although fewer transcriptional changes were observed in gluteal cells, imaging of mutant preadipocytes from this depot revealed alterations in nuclear morphology during proliferation. Nuclear blebbing, a marker of nuclear envelope instability, was predominantly observed in gluteal preadipocytes overexpressing LMNA R482W. In confluent non-proliferating cells, increased nuclear blebbing was not present in either depot. These findings suggest that the mutation specifically affects nuclear architecture in gluteal cells during cell division, potentially through disrupted nuclear lamina remodelling. *In vivo*, this could lead to increased nuclear fragility and DNA damage, thereby reducing the pool of gluteal adipocyte precursors available for differentiation.

Together, these results indicate that LMNA R482W exerts distinct effects on regional preadipocyte biology. In abdominal preadipocytes, the mutation primarily caused

transcriptional dysregulation during adipogenesis, supporting the gene expression model. By contrast, gluteal preadipocytes displayed more structural abnormalities during proliferation, indicating greater loss of nuclear mechanical integrity consistent with the structural model.

7.4.2 Effect of substrate stiffness on *LMNA* expression and mechanosignalling pathways

Lamin A performs several essential functions, including serving as a mechanosensor that counteracts external mechanical forces, protecting the genome (Cho, *et al*., 2019). Its expression levels vary according to the mechanical properties of the cell's extracellular environment, typically being lower in softer tissues (such as adipose and brain) and elevated in stiffer tissues (such as bone) (Swift, *et al*., 2013). Consequently, the use of rigid plastic substrates in 2D culture may have artificially elevated LMNA expression levels compared to *in vivo*.

Furthermore, Elosegui-Artola *et al*. (2017) demonstrated that cells cultured on stiff 2D substrates experience increased cytoskeletal tension and nuclear flattening, which stretches nuclear pores and enhances import of yes-associated protein (YAP), a transcriptional regulator responsive to ECM stiffness and mechanical strain. In contrast, the agarose-based hydrogel used in my work for spheroid culture, with a Young's modulus of ~118 Pa (Graham, *et al*., 2019), is well below the reported stiffness threshold of ~5 kPa required to trigger actin stress fibre formation and strong YAP nuclear translocation (Elosegui-Artola, *et al*., 2017). As a result, nuclear morphology in 3D culture tends to remain more rounded, and YAP signalling is more balanced.

Moreover, lamin A overexpression has been previously shown to impair nuclear flattening and decrease YAP nuclear localisation (Swift, *et al*., 2013), which may partly explain the increased roundness of nuclei in WT LMNA-overexpressing cells I observed in 2D culture (**Chapter 5**),

despite the stiff substrate. How substrate stiffness affects the influence of lamin A R482W on nuclear morphology remains unclear but this could be investigated using high-resolution 3D confocal imaging to quantify nuclear morphology, such as circularity and volume, in cleared spheroid samples. This could be done in conjunction with immunofluorescence staining for lamin A and YAP distribution to analyse potential differences in mechanosignalling pathways.

The functional consequences of nuclear blebbing in gluteal cells is not fully known. Future work could explore the relationship between nuclear structure and gene regulation. To achieve this, immunofluorescence labelling could be employed to examine the organisation of the nuclear lamina and chromatin, particularly within gluteal nuclear blebs. For example, staining for heterochromatin (H3K27me3, H3K9me3) and euchromatin (H3K4me3, H3K9ac) markers could identify depot-dependent differences in chromatin state associated with LMNA R482W. Changes in H3K27me3 marks would provide further evidence supporting PRC2 dysfunction in FPLD2.

7.5 Future perspectives

7.5.1 Functional validation of FPLD2 candidate genes

Future studies should aim to functionally validate the key FPLD2 candidate genes identified through transcriptomic analysis using gene knockdown (e.g. siRNA or CRISPR interference) or overexpression techniques. Employing the 3D culture system would provide a physiologically relevant platform for testing whether altered expression of targets contributes directly to impaired cellular phenotypes, such as altered (pre)adipocyte growth, lipid accumulation or fibrosis. Genes that displayed contrasting expression patterns between depots would be strong candidates for further investigation.

For example, the functional consequences of downregulated *ELOVL2* expression in differentiating gluteal preadipocytes, in contrast to its upregulation in abdominal cells, remain

unclear. *ELOVL2* stands out due to its vital role in lipid homeostasis, with its methylation status considered a biomarker of chronological age (its expression decline with age) (Garagnani, *et al*., 2012). This supports altered DNA methylation patterns in the LMNA R482W cells. Determining whether variations in *ELOVL2* expression across depots impact lipid profiles, adipogenic capacity or cellular aging phenotypes may provide valuable insights into the region-specific susceptibility observed in FPLD2. To further investigate this, lipidomic analyses to assess shifts in very long chain fatty acid (VLCFA) profiles, as well as cellular senescence assays, such as the β-galactosidase (β-Gal) assay, could be carried out.

7.5.2 Increasing the cellular complexity of the 3D adipose model

Despite the advantages of the current 3D platform, further complexity could be introduced through incorporating additional adipose tissue cell types. Adding macrophages or endothelial cells that form microvascular structures would make the system more representative of *in vivo* tissue. This is important given the diversity of cell types that contribute to adipose tissue function, and the reported effects of LMNA mutations on non-adipocyte populations. However, the current static model would still lack an element of cell and tissue organisation due to a lack of media perfusion (reflecting blood flow).

As previously mentioned, endothelial cell dysfunction has been implicated in FPLD2 patients (Bidault, *et al*., 2013), suggesting that impaired communication between vascular and adipose compartments may play a role in disease pathogenesis. Likewise, the consistent finding of raised immune cell infiltration in lipodystrophic adipose tissue, as demonstrated by histological analysis, further justifies adding macrophages in studies of inflammatory responses. Once characterised, this more complex 3D co-culture system may be used to study a wider range of candidate genes and investigate depot-specific responses.

7.6 Concluding remarks

Overall, this thesis provides valuable new insights into the molecular mechanisms driving regional adipose tissue dysfunction in FPLD2 and I have established a robust 3D culture platform for future mechanistic studies. Candidate genes identified through transcriptional profiling provide a strong foundation for follow-up research, and the disease models characterised here can be used to advance knowledge of partial lipodystrophy and support the development of future treatments.

8 References

Agrawal S, Luan J, Cummings BB, Weiss EJ, Wareham NJ, Khera AV. Relationship of Fat Mass Ratio, a Biomarker for Lipodystrophy, With Cardiometabolic Traits. Diabetes. 2024;73(7):1099-111.

Ahler E, Sullivan WJ, Cass A, Braas D, York AG, Bensinger SJ, *et al*. Doxycycline alters metabolism and proliferation of human cell lines. PLoS One. 2013;8(5):e64561.

Akhmanova M, Osidak E, Domogatsky S, Rodin S, Domogatskaya A. Physical, Spatial, and Molecular Aspects of Extracellular Matrix of In Vivo Niches and Artificial Scaffolds Relevant to Stem Cells Research. Stem Cells Int. 2015;2015:167025.

Alagna NS, Thomas TI, Wilson KL, Reddy KL. Choreography of lamina-associated domains: structure meets dynamics. FEBS Lett. 2023;597(22):2806-22.

Alvarez JD, Yasui DH, Niida H, Joh T, Loh DY, Kohwi-Shigematsu T. The MAR-binding protein SATB1 orchestrates temporal and spatial expression of multiple genes during T-cell development. Genes Dev. 2000;14(5):521-35.

Andres V, Gonzalez JM. Role of A-type lamins in signaling, transcription, and chromatin organization. J Cell Biol. 2009;187(7):945-57.

Araujo-Vilar D, Lattanzi G, Gonzalez-Mendez B, Costa-Freitas AT, Prieto D, Columbaro M, *et al*. Site-dependent differences in both prelamin A and adipogenic genes in subcutaneous adipose tissue of patients with type 2 familial partial lipodystrophy. J Med Genet. 2009;46(1):40-8.

Araujo-Vilar D, Victoria B, Gonzalez-Mendez B, Barreiro F, Fernandez-Rodriguez B, Cereijo R, *et al*. Histological and molecular features of lipomatous and nonlipomatous adipose tissue in familial partial lipodystrophy caused by LMNA mutations. Clin Endocrinol (Oxf). 2012;76(6):816-24.

Arner P, Lithell H, Wahrenberg H, Bronnegard M. Expression of lipoprotein lipase in different human subcutaneous adipose tissue regions. J Lipid Res. 1991;32(3):423-9.

Arner P, Ryden M. Human white adipose tissue: A highly dynamic metabolic organ. J Intern Med. 2022;291(5):611-21.

Ashapkin VV, Kutueva LI, Kurchashova SY, Kireev, II. Are There Common Mechanisms Between the Hutchinson-Gilford Progeria Syndrome and Natural Aging? Front Genet. 2019;10:455.

Backdahl J, Franzen L, Massier L, Li Q, Jalkanen J, Gao H, et al. Spatial mapping reveals human adipocyte subpopulations with distinct sensitivities to insulin. Cell Metab. 2021;33(11):2301.

Bellanger A, Madsen-Osterbye J, Galigniana NM, Collas P. Restructuring of Lamina-Associated Domains in Senescence and Cancer. Cells. 2022;11(11).

Bennett CN, Ross SE, Longo KA, Bajnok L, Hemati N, Johnson KW, *et al*. Regulation of Wnt signaling during adipogenesis. J Biol Chem. 2002;277(34):30998-1004.

Bereziat V, Cervera P, Le Dour C, Verpont MC, Dumont S, Vantyghem MC, *et al*. LMNA mutations induce a non-inflammatory fibrosis and a brown fat-like dystrophy of enlarged cervical adipose tissue. Am J Pathol. 2011;179(5):2443-53.

Bermeo S, Vidal C, Zhou H, Duque G. Lamin A/C Acts as an Essential Factor in Mesenchymal Stem Cell Differentiation Through the Regulation of the Dynamics of the Wnt/beta-Catenin Pathway. J Cell Biochem. 2015;116(10):2344-53.

Bian C, Yuan X, Zeng C, Sun J, Kaneko G, Ji H. Docosahexaenoic acid (DHA) inhibits abdominal fat accumulation by promoting adipocyte apoptosis through PPARgamma-LC3-BNIP3 pathway-mediated mitophagy. Biochim Biophys Acta Mol Cell Biol Lipids. 2024;1869(1):159425.

Bidault G, Garcia M, Vantyghem MC, Ducluzeau PH, Morichon R, Thiyagarajah K, *et al*. Lipodystrophy-linked LMNA p.R482W mutation induces clinical early atherosclerosis and in vitro endothelial dysfunction. Arterioscler Thromb Vasc Biol. 2013;33(9):2162-71.

Billiard J, Way DS, Seestaller-Wehr LM, Moran RA, Mangine A, Bodine PV. The orphan receptor tyrosine kinase Ror2 modulates canonical Wnt signaling in osteoblastic cells. Mol Endocrinol. 2005;19(1):90-101.

Briand N, Cahyani I, Madsen-Osterbye J, Paulsen J, Ronningen T, Sorensen AL, *et al*. Lamin A, Chromatin and FPLD2: Not Just a Peripheral Menage-a-Trois. Front Cell Dev Biol. 2018a;6:73.

Briand N, Collas P. Lamina-associated domains: peripheral matters and internal affairs. Genome Biol. 2020;21(1):85.

Briand N, Guenantin AC, Jeziorowska D, Shah A, Mantecon M, Capel E, *et al*. The lipodystrophic hotspot lamin A p.R482W mutation deregulates the mesodermal inducer T/Brachyury and early vascular differentiation gene networks. Hum Mol Genet. 2018b;27(8):1447-59.

Cao YH. Angiogenesis and Vascular Functions in Modulation of Obesity, Adipose Metabolism, and Insulin Sensitivity. Cell Metabolism. 2013;18(4):478-89.

Capanni C, Cenni V, Mattioli E, Sabatelli P, Ognibene A, Columbaro M, *et al*. Failure of lamin A/C to functionally assemble in R482L mutated familial partial lipodystrophy fibroblasts: altered intermolecular interaction with emerin and implications for gene transcription. Exp Cell Res. 2003;291(1):122-34.

Capanni C, Mattioli E, Columbaro M, Lucarelli E, Parnaik VK, Novelli G, *et al*. Altered pre-lamin A processing is a common mechanism leading to lipodystrophy. Hum Mol Genet. 2005;14(11):1489-502.

Capell BC, Erdos MR, Madigan JP, Fiordalisi JJ, Varga R, Conneely KN, *et al*. Inhibiting farnesylation of progerin prevents the characteristic nuclear blebbing of Hutchinson-Gilford progeria syndrome. Proc Natl Acad Sci U S A. 2005;102(36):12879-84.

Carracedo A, Cantley LC, Pandolfi PP. Cancer metabolism: fatty acid oxidation in the limelight. Nat Rev Cancer. 2013;13(4):227-32.

Cattin ME, Wang J, Weldrick JJ, Roeske CL, Mak E, Thorn SL, *et al*. Deletion of MLIP (muscle-enriched A-type lamin-interacting protein) leads to cardiac hyperactivation of Akt/mammalian target of rapamycin (mTOR) and impaired cardiac adaptation. J Biol Chem. 2015;290(44):26699-714.

Cawthorn WP, Scheller EL, Learman BS, Parlee SD, Simon BR, Mori H, et al. Bone marrow adipose tissue is an endocrine organ that contributes to increased circulating adiponectin during caloric restriction. Cell Metab. 2014;20(2):368-75.

Cesarini E, Mozzetta C, Marullo F, Gregoretti F, Gargiulo A, Columbaro M, *et al*. Lamin A/C sustains PcG protein architecture, maintaining transcriptional repression at target genes. J Cell Biol. 2015;211(3):533-51.

Chan LS, Wells RA. Cross-Talk between PPARs and the Partners of RXR: A Molecular Perspective. PPAR Res. 2009;2009:925309.

Chavan A, Isenhart R, Nguyen SC, Kotb NM, Harke J, Sintsova A, *et al*. A nuclear architecture screen in Drosophila identifies Stonewall as a link between chromatin position at the nuclear periphery and germline stem cell fate. Genes Dev. 2024;38(9-10):415-35.

Chavey C, Mari B, Monthouel MN, Bonnafous S, Anglard P, Van Obberghen E, *et al*. Matrix metalloproteinases are differentially expressed in adipose tissue during obesity and modulate adipocyte differentiation. J Biol Chem. 2003;278(14):11888-96.

Chen D, Chao DL, Rocha L, Kolar M, Nguyen Huu VA, Krawczyk M, *et al*. The lipid elongation enzyme ELOVL2 is a molecular regulator of aging in the retina. Aging Cell. 2020;19(2):e13100.

Cheng NC, Wang S, Young TH. The influence of spheroid formation of human adipose-derived stem cells on chitosan films on stemness and differentiation capabilities. Biomaterials. 2012;33(6):1748-58.

Chiquette E, Oral EA, Garg A, Araujo-Vilar D, Dhankhar P. Estimating the prevalence of generalized and partial lipodystrophy: findings and challenges. Diabetes Metab Syndr Obes. 2017;10:375-83.

Cho S, Vashisth M, Abbas A, Majkut S, Vogel K, Xia Y, *et al*. Mechanosensing by the Lamina Protects against Nuclear Rupture, DNA Damage, and Cell-Cycle Arrest. Dev Cell. 2019;49(6):920-35 e5.

Christodoulides C, Lagathu C, Sethi JK, Vidal-Puig A. Adipogenesis and WNT signalling. Trends Endocrinol Metab. 2009;20(1):16-24.

Christodoulides C, Laudes M, Cawthorn WP, Schinner S, Soos M, O'Rahilly S, *et al*. The Wnt antagonist Dickkopf-1 and its receptors are coordinately regulated during early human adipogenesis. J Cell Sci. 2006;119(Pt 12):2613-20.

Chu AY, Deng X, Fisher VA, Drong A, Zhang Y, Feitosa MF, *et al*. Multiethnic genome-wide meta-analysis of ectopic fat depots identifies loci associated with adipocyte development and differentiation. Nat Genet. 2017;49(1):125-30.

Chun TH. Peri-adipocyte ECM remodeling in obesity and adipose tissue fibrosis. Adipocyte. 2012;1(2):89-95.

Church C, Horowitz M, Rodeheffer M. WAT is a functional adipocyte? Adipocyte. 2012;1(1):38-45.

Coelho M, Oliveira T, Fernandes R. Biochemistry of adipose tissue: an endocrine organ. Arch Med Sci. 2013;9(2):191-200.

Cohen CA, Shea AA, Heffron CL, Schmelz EM, Roberts PC. Intra-abdominal fat depots represent distinct immunomodulatory microenvironments: a murine model. PLoS One. 2013;8(6):e66477.

Columbaro M, Capanni C, Mattioli E, Novelli G, Parnaik VK, Squarzoni S, *et al*. Rescue of heterochromatin organization in Hutchinson-Gilford progeria by drug treatment. Cell Mol Life Sci. 2005;62(22):2669-78.

Constantin A, Filippi A, Alexandru N, Nemecz M, Georgescu A. Extracellular Vesicles from Adipose Tissue Stem Cells in Diabetes and Associated Cardiovascular Disease; Pathobiological Impact and Therapeutic Potential. Int J Mol Sci. 2020;21(24).

Corsa CAS, Walsh CM, Bagchi DP, Foss Freitas MC, Li Z, Hardij J, *et al*. Adipocyte-Specific Deletion of Lamin A/C Largely Models Human Familial Partial Lipodystrophy Type 2. Diabetes. 2021;70(9):1970-84.

Corvera S. Cellular Heterogeneity in Adipose Tissues. Annu Rev Physiol. 2021;83:257-78.

Csoka AB, English SB, Simkevich CP, Ginzinger DG, Butte AJ, Schatten GP, *et al*. Genome-scale expression profiling of Hutchinson-Gilford progeria syndrome reveals widespread transcriptional misregulation leading to mesodermal/mesenchymal defects and accelerated atherosclerosis. Aging Cell. 2004;3(4):235-43.

Daquinag AC, Souza GR, Kolonin MG. Adipose tissue engineering in three-dimensional levitation tissue culture system based on magnetic nanoparticles. Tissue Eng Part C Methods. 2013;19(5):336-44.

Dariolli R, Nir R, Mushlam T, Souza GR, Farmer SR, Batista ML, Jr. Optimized scaffold-free human 3D adipose tissue organoid culture for obesity and disease modeling. SLAS Discov. 2025;31:100218.

de Winter TJJ, Nusse R. Running Against the Wnt: How Wnt/beta-Catenin Suppresses Adipogenesis. Front Cell Dev Biol. 2021;9:627429.

Dechat T, Adam SA, Goldman RD. Nuclear lamins and chromatin: when structure meets function. Adv Enzyme Regul. 2009;49(1):157-66.

Dechat T, Pfleghaar K, Sengupta K, Shimi T, Shumaker DK, Solimando L, *et al*. Nuclear lamins: major factors in the structural organization and function of the nucleus and chromatin. Genes Dev. 2008;22(7):832-53.

Decker ML, Chavez E, Vulto I, Lansdorp PM. Telomere length in Hutchinson-Gilford progeria syndrome. Mech Ageing Dev. 2009;130(6):377-83.

Denton N, Pinnick KE, Karpe F. Cartilage oligomeric matrix protein is differentially expressed in human subcutaneous adipose tissue and regulates adipogenesis. Mol Metab. 2018;16:172-9.

Deolal P, Mishra K. Regulation of diverse nuclear shapes: pathways working independently, together. Commun Integr Biol. 2021;14(1):158-75.

Dhe-Paganon S, Werner ED, Chi YI, Shoelson SE. Structure of the globular tail of nuclear lamin. J Biol Chem. 2002;277(20):17381-4.

Diaz-Lopez EJ, Sanchez-Iglesias S, Castro AI, Cobelo-Gomez S, Prado-Morana T, Araujo-Vilar D, *et al*. Lipodystrophic Laminopathies: From Dunnigan Disease to Progeroid Syndromes. Int J Mol Sci. 2024;25(17).

Dittmer TA, Misteli T. The lamin protein family. Genome Biol. 2011;12(5):222.

Divoux A, Sandor K, Bojcsuk D, Talukder A, Li X, Balint BL, *et al*. Differential open chromatin profile and transcriptomic signature define depot-specific human subcutaneous preadipocytes: primary outcomes. Clin Epigenetics. 2018;10(1):148.

Dong CH, Jiang T, Yin H, Song H, Zhang Y, Geng H, *et al*. LMNB2 promotes the progression of colorectal cancer by silencing p21 expression. Cell Death Dis. 2021;12(4):331.

Dorner D, Vlcek S, Foeger N, Gajewski A, Makolm C, Gotzmann J, *et al*. Lamina-associated polypeptide 2alpha regulates cell cycle progression and differentiation via the retinoblastoma-E2F pathway. J Cell Biol. 2006;173(1):83-93.

Dunne LW, Huang Z, Meng W, Fan X, Zhang N, Zhang Q, *et al*. Human decellularized adipose tissue scaffold as a model for breast cancer cell growth and drug treatments. Biomaterials. 2014;35(18):4940-9.

Duval K, Grover H, Han LH, Mou Y, Pegoraro AF, Fredberg J, *et al*. Modeling Physiological Events in 2D vs. 3D Cell Culture. Physiology (Bethesda). 2017;32(4):266-77.

Dyer L, Parker A, Paphiti K, Sanderson J. Lightsheet Microscopy. Curr Protoc. 2022;2(7):e448.

Elosegui-Artola A, Andreu I, Beedle AEM, Lezamiz A, Uroz M, Kosmalska AJ, *et al*. Force Triggers YAP Nuclear Entry by Regulating Transport across Nuclear Pores. Cell. 2017;171(6):1397-410 e14.

Emont MP, Yu H, Jun H, Hong X, Maganti N, Stegemann JP, *et al*. Using a 3D Culture System to Differentiate Visceral Adipocytes In Vitro. Endocrinology. 2015;156(12):4761-8.

Endo K, Sato T, Umetsu A, Watanabe M, Hikage F, Ida Y, *et al*. 3D culture induction of adipogenic differentiation in 3T3-L1 preadipocytes exhibits adipocyte-specific molecular expression patterns and metabolic functions. Heliyon. 2023;9(10):e20713.

Eriksson M, Brown WT, Gordon LB, Glynn MW, Singer J, Scott L, *et al*. Recurrent de novo point mutations in lamin A cause Hutchinson-Gilford progeria syndrome. Nature. 2003;423(6937):293-8.

Eskeland R, Leeb M, Grimes GR, Kress C, Boyle S, Sproul D, *et al*. Ring1B compacts chromatin structure and represses gene expression independent of histone ubiquitination. Mol Cell. 2010;38(3):452-64.

Farmer SR. Transcriptional control of adipocyte formation. Cell Metab. 2006;4(4):263-73.

Fiorenza CG, Chou SH, Mantzoros CS. Lipodystrophy: pathophysiology and advances in treatment. Nat Rev Endocrinol. 2011;7(3):137-50.

Foss-Freitas MC, Gilio D, da Rocha AM, Pais L, O'Leary MC, Rehm HL, *et al*. Early B-cell transcription factor-2 defect as a novel cause of lipodystrophy: disruption of the adipose tissue character and integrity. medRxiv. 2024.

Frayling TM. Genome-wide association studies: the good, the bad and the ugly. Clin Med (Lond). 2014;14(4):428-31.

Fretz JA, Nelson T, Xi Y, Adams DJ, Rosen CJ, Horowitz MC. Altered metabolism and lipodystrophy in the early B-cell factor 1-deficient mouse. Endocrinology. 2010;151(4):1611-21.

Friesen M, Cowan CA. FPLD2 LMNA mutation R482W dysregulates iPSC-derived adipocyte function and lipid metabolism. Biochem Biophys Res Commun. 2018;495(1):254-60.

Galarraga M, Campion J, Munoz-Barrutia A, Boque N, Moreno H, Martinez JA, *et al*. Adiposoft: automated software for the analysis of white adipose tissue cellularity in histological sections. J Lipid Res. 2012;53(12):2791-6.

Gamwell JM, Paphiti K, Hodson L, Karpe F, Pinnick KE, Todorcevic M. An optimised protocol for the investigation of insulin signalling in a human cell culture model of adipogenesis. Adipocyte. 2023;12(1):2179339.

Gao Z, Zhang J, Bonasio R, Strino F, Sawai A, Parisi F, *et al*. PCGF homologs, CBX proteins, and RYBP define functionally distinct PRC1 family complexes. Mol Cell. 2012;45(3):344-56.

Garagnani P, Bacalini MG, Pirazzini C, Gori D, Giuliani C, Mari D, *et al*. Methylation of ELOVL2 gene as a new epigenetic marker of age. Aging Cell. 2012;11(6):1132-4.

Garg A. Gender differences in the prevalence of metabolic complications in familial partial lipodystrophy (Dunnigan variety). J Clin Endocrinol Metab. 2000;85(5):1776-82.

GBD 2021 Adult BMI Collaborators. Global, regional, and national prevalence of adult overweight and obesity, 1990-2021, with forecasts to 2050: a forecasting study for the Global Burden of Disease Study 2021. Lancet. 2025;405(10481):813-38.

Gencer S, Doring Y, Jansen Y, Bayasgalan S, Schengel O, Muller M, *et al*. Adipocyte-Specific ACKR3 Regulates Lipid Levels in Adipose Tissue. Biomedicines. 2021;9(4).

Gesson K, Rescheneder P, Skoruppa MP, von Haeseler A, Dechat T, Foisner R. A-type lamins bind both hetero- and euchromatin, the latter being regulated by lamina-associated polypeptide 2 alpha. Genome Res. 2016;26(4):462-73.

Gesta S, Tseng YH, Kahn CR. Developmental origin of fat: tracking obesity to its source. Cell. 2007;131(2):242-56.

Goldman RD, Shumaker DK, Erdos MR, Eriksson M, Goldman AE, Gordon LB, *et al*. Accumulation of mutant lamin A causes progressive changes in nuclear architecture in Hutchinson-Gilford progeria syndrome. Proc Natl Acad Sci U S A. 2004;101(24):8963-8.

Gong Z, Zhang X, Su K, Jiang R, Sun Z, Chen W, *et al*. Deficiency in AIM2 induces inflammation and adipogenesis in white adipose tissue leading to obesity and insulin resistance. Diabetologia. 2019;62(12):2325-39.

Graham AD, Pandey R, Tsancheva VS, Candeo A, Botchway SW, Allan AJ, *et al*. The development of a high throughput drug-responsive model of white adipose tissue comprising adipogenic 3T3-L1 cells in a 3D matrix. Biofabrication. 2019;12(1):015018.

Guo R, Xing QS. Roles of Wnt Signaling Pathway and ROR2 Receptor in Embryonic Development: An Update Review Article. Epigenet Insights. 2022;15:25168657211064232.

Guo W, Zhang KM, Tu K, Li YX, Zhu L, Xiao HS, *et al*. Adipogenesis licensing and execution are disparately linked to cell proliferation. Cell Res. 2009;19(2):216-23.

Hegele RA. Premature atherosclerosis associated with monogenic insulin resistance. Circulation. 2001;103(18):2225-9.

Helfer G, Wu QF. Chemerin: a multifaceted adipokine involved in metabolic disorders. J Endocrinol. 2018;238(2):R79-R94.

Hernandez L, Roux KJ, Wong ES, Mounkes LC, Mutalif R, Navasankari R, *et al*. Functional coupling between the extracellular matrix and nuclear lamina by Wnt signaling in progeria. Dev Cell. 2010;19(3):413-25.

Hill JT, Demarest B, Gorsi B, Smith M, Yost HJ. Heart morphogenesis gene regulatory networks revealed by temporal expression analysis. Development. 2017;144(19):3487-98.

Hishida T, Naito K, Osada S, Nishizuka M, Imagawa M. peg10, an imprinted gene, plays a crucial role in adipocyte differentiation. FEBS Lett. 2007;581(22):4272-8.

Hodson L, Skeaff CM, Fielding BA. Fatty acid composition of adipose tissue and blood in humans and its use as a biomarker of dietary intake. Prog Lipid Res. 2008;47(5):348-80.

Hsiao AY, Okitsu T, Teramae H, Takeuchi S. 3D Tissue Formation of Unilocular Adipocytes in Hydrogel Microfibers. Adv Healthc Mater. 2016;5(5):548-56.

Ioannidou A, Alatar S, Schipper R, Baganha F, Ahlander M, Hornell A, *et al*. Hypertrophied human adipocyte spheroids as in vitro model of weight gain and adipose tissue dysfunction. J Physiol. 2022b;600(4):869-83.

Ioannidou A, Fisher RM, Hagberg CE. The multifaceted roles of the adipose tissue vasculature. Obes Rev. 2022a;23(4):e13403.

Ivorra C, Kubicek M, Gonzalez JM, Sanz-Gonzalez SM, Alvarez-Barrientos A, O'Connor JE, *et al*. A mechanism of AP-1 suppression through interaction of c-Fos with lamin A/C. Genes Dev. 2006;20(3):307-20.

Jaaskelainen I, Petaisto T, Mirzarazi Dahagi E, Mahmoodi M, Pihlajaniemi T, Kaartinen MT, *et al*. Collagens Regulating Adipose Tissue Formation and Functions. Biomedicines. 2023;11(5).

Jacob KN, Garg A. Laminopathies: multisystem dystrophy syndromes. Mol Genet Metab. 2006;87(4):289-302.

Janssen AFJ, Breusegem SY, Larrieu D. Current Methods and Pipelines for Image-Based Quantitation of Nuclear Shape and Nuclear Envelope Abnormalities. Cells. 2022;11(3).

Jensen C, Teng Y. Is It Time to Start Transitioning From 2D to 3D Cell Culture? Front Mol Biosci. 2020;7:33.

Jespersen NZ, Larsen TJ, Peijs L, Daugaard S, Homoe P, Loft A, *et al*. A classical brown adipose tissue mRNA signature partly overlaps with brite in the supraclavicular region of adult humans. Cell Metab. 2013;17(5):798-805.

Jimenez MA, Akerblad P, Sigvardsson M, Rosen ED. Critical role for Ebf1 and Ebf2 in the adipogenic transcriptional cascade. Mol Cell Biol. 2007;27(2):743-57.

Johnson BR, Nitta RT, Frock RL, Mounkes L, Barbie DA, Stewart CL, *et al*. A-type lamins regulate retinoblastoma protein function by promoting subnuclear localization and preventing proteasomal degradation. Proc Natl Acad Sci U S A. 2004;101(26):9677-82.

Kamizaki K, Katsukawa M, Yamamoto A, Fukada SI, Uezumi A, Endo M, *et al*. Ror2 signaling regulated by differential Wnt proteins determines pathological fate of muscle mesenchymal progenitors. Cell Death Dis. 2024;15(10):784.

Karastergiou K, Fried SK, Xie H, Lee MJ, Divoux A, Rosencrantz MA, *et al*. Distinct developmental signatures of human abdominal and gluteal subcutaneous adipose tissue depots. J Clin Endocrinol Metab. 2013;98(1):362-71.

Karbiener M, Glantschnig C, Pisani DF, Laurencikiene J, Dahlman I, Herzig S, *et al*. Mesoderm-specific transcript (MEST) is a negative regulator of human adipocyte differentiation. Int J Obes (Lond). 2015;39(12):1733-41.

Karpe F, Pinnick KE. Biology of upper-body and lower-body adipose tissue--link to whole-body phenotypes. Nat Rev Endocrinol. 2015;11(2):90-100.

Kershaw EE, Flier JS. Adipose tissue as an endocrine organ. J Clin Endocr Metab. 2004;89(6):2548-56.

Kim D, Kim J, Yoon JH, Ghim J, Yea K, Song P, *et al*. CXCL12 secreted from adipose tissue recruits macrophages and induces insulin resistance in mice. Diabetologia. 2014;57(7):1456-65.

Kim HK, Della-Fera M, Lin J, Baile CA. Docosahexaenoic acid inhibits adipocyte differentiation and induces apoptosis in 3T3-L1 preadipocytes. J Nutr. 2006;136(12):2965-9.

Kim JY, Garcia-Carbonell R, Yamachika S, Zhao P, Dhar D, Loomba R, *et al*. ER Stress Drives Lipogenesis and Steatohepatitis via Caspase-2 Activation of S1P. Cell. 2018;175(1):133-45 e15.

Kim YH, Barclay JL, He J, Luo X, O'Neill HM, Keshvari S, *et al*. Identification of carboxypeptidase X (CPX)-1 as a positive regulator of adipogenesis. FASEB J. 2016;30(7):2528-40.

Kind J, Pagie L, Ortabozkoyun H, Boyle S, de Vries SS, Janssen H, *et al*. Single-cell dynamics of genome-nuclear lamina interactions. Cell. 2013;153(1):178-92.

Klingelhutz AJ, Gourronc FA, Chaly A, Wadkins DA, Burand AJ, Markan KR, *et al*. Scaffold-free generation of uniform adipose spheroids for metabolism research and drug discovery. Sci Rep. 2018;8(1):523.

Kolb T, Maass K, Hergt M, Aebi U, Herrmann H. Lamin A and lamin C form homodimers and coexist in higher complex forms both in the nucleoplasmic fraction and in the lamina of cultured human cells. Nucleus. 2011;2(5):425-33.

Kolberg L, Raudvere U, Kuzmin I, Adler P, Vilo J, Peterson H. g:Profiler-interoperable web service for functional enrichment analysis and gene identifier mapping (2023 update). Nucleic Acids Res. 2023;51(W1):W207-W12.

Kongsuphol P, Gupta S, Liu Y, Bhuvanendran Nair Gourikutty S, Biswas SK, Ramadan Q. In vitro micro-physiological model of the inflamed human adipose tissue for immune-metabolic analysis in type II diabetes. Sci Rep. 2019;9(1):4887.

Krassowski, M. ComplexUpset: Create Complex UpSet Plots Using ggplot2 Components. 2020.

Krimm I, Ostlund C, Gilquin B, Couprie J, Hossenlopp P, Mornon JP, *et al*. The Ig-like structure of the C-terminal domain of lamin A/C, mutated in muscular dystrophies, cardiomyopathy, and partial lipodystrophy. Structure. 2002;10(6):811-23.

Kuo FC, Neville MJ, Sabaratnam R, Wesolowska-Andersen A, Phillips D, Wittemans LBL, *et al*. HOTAIR interacts with PRC2 complex regulating the regional preadipocyte transcriptome and human fat distribution. Cell Rep. 2022;40(4):111136.

Kusminski CM, Bickel PE, Scherer PE. Targeting adipose tissue in the treatment of obesity-associated diabetes. Nat Rev Drug Discov. 2016;15(9):639-60.

Lazarescu O, Ziv-Agam M, Haim Y, Hekselman I, Jubran J, Shneyour A, *et al*. Human subcutaneous and visceral adipocyte atlases uncover classical and nonclassical adipocytes and depot-specific patterns. Nat Genet. 2025;57(2):413-26.

Le Dour C, Macquart C, Sera F, Homma S, Bonne G, Morrow JP, *et al*. Decreased WNT/beta-catenin signalling contributes to the pathogenesis of dilated cardiomyopathy caused by mutations in the lamin a/C gene. Hum Mol Genet. 2017b;26(2):333-43.

Le Dour C, Wu W, Bereziat V, Capeau J, Vigouroux C, Worman HJ. Extracellular matrix remodeling and transforming growth factor-beta signaling abnormalities induced by lamin A/C variants that cause lipodystrophy. J Lipid Res. 2017a;58(1):151-63.

Lefterova MI, Zhang Y, Steger DJ, Schupp M, Schug J, Cristancho A, *et al*. PPARgamma and C/EBP factors orchestrate adipocyte biology via adjacent binding on a genome-wide scale. Genes Dev. 2008;22(21):2941-52.

Lema C, Varela-Ramirez A, Aguilera RJ. Differential nuclear staining assay for high-throughput screening to identify cytotoxic compounds. Curr Cell Biochem. 2011;1(1):1-14.

Li Y, Zhang P, Zhang X, Bi X, Wu M, Zou J, *et al*. Adipose matrix complex: a high-rigidity collagen-rich adipose-derived material for fat grafting. Aging (Albany NY). 2021;13(11):14910-23.

Lijnen HR. Angiogenesis and obesity. Cardiovasc Res. 2008;78(2):286-93.

Liszewski J, Klingelhutz A, Sander EA, Ankrum J. Development and analysis of scaffold-free adipose spheroids. Adipocyte. 2024;13(1):2347215.

Little RD, Carulli JP, Del Mastro RG, Dupuis J, Osborne M, Folz C, *et al*. A mutation in the LDL receptor-related protein 5 gene results in the autosomal dominant high-bone-mass trait. Am J Hum Genet. 2002;70(1):11-9.

Liu Y, Rusinol A, Sinensky M, Wang Y, Zou Y. DNA damage responses in progeroid syndromes arise from defective maturation of prelamin A. J Cell Sci. 2006;119(Pt 22):4644-9.

Lloyd DJ, Trembath RC, Shackleton S. A novel interaction between lamin A and SREBP1: implications for partial lipodystrophy and other laminopathies. Hum Mol Genet. 2002;11(7):769-77.

Loh NY, Minchin JEN, Pinnick KE, Verma M, Todorcevic M, Denton N, *et al*. RSPO3 impacts body fat distribution and regulates adipose cell biology in vitro. Nat Commun. 2020;11(1):2797.

Loh NY, Neville MJ, Marinou K, Hardcastle SA, Fielding BA, Duncan EL, *et al*. LRP5 regulates human body fat distribution by modulating adipose progenitor biology in a dose- and depot-specific fashion. Cell Metab. 2015;21(2):262-73.

Loh NY, Vasan SK, Rosoff DB, Roberts E, van Dam AD, Verma M, *et al*. LRP5 promotes adipose progenitor cell fitness and adipocyte insulin sensitivity. Commun Med (Lond). 2025;5(1):51.

Longo M, Zatterale F, Naderi J, Parrillo L, Formisano P, Raciti GA, *et al*. Adipose Tissue Dysfunction as Determinant of Obesity-Associated Metabolic Complications. Int J Mol Sci. 2019;20(9).

Lonn M, Mehlig K, Bengtsson C, Lissner L. Adipocyte size predicts incidence of type 2 diabetes in women. FASEB J. 2010;24(1):326-31.

Loos RJF, Kilpelainen TO. Genes that make you fat, but keep you healthy. J Intern Med. 2018;284(5):450-63.

Loskill P, Sezhian T, Tharp KM, Lee-Montiel FT, Jeeawoody S, Reese WM, *et al*. WAT-on-a-chip: a physiologically relevant microfluidic system incorporating white adipose tissue. Lab Chip. 2017;17(9):1645-54.

Louis F, Pannetier P, Souguir Z, Le Cerf D, Valet P, Vannier JP, *et al*. A biomimetic hydrogel functionalized with adipose ECM components as a microenvironment for the 3D culture of human and murine adipocytes. Biotechnol Bioeng. 2017;114(8):1813-24.

Lundgren M, Svensson M, Lindmark S, Renstrom F, Ruge T, Eriksson JW. Fat cell enlargement is an independent marker of insulin resistance and 'hyperleptinaemia'. Diabetologia. 2007;50(3):625-33.

MacDonald BT, Tamai K, He X. Wnt/beta-catenin signaling: components, mechanisms, and diseases. Dev Cell. 2009;17(1):9-26.

Maddika S, Ande SR, Wiechec E, Hansen LL, Wesselborg S, Los M. Akt-mediated phosphorylation of CDK2 regulates its dual role in cell cycle progression and apoptosis. J Cell Sci. 2008;121(Pt 7):979-88.

Madsen MS, Siersbaek R, Boergesen M, Nielsen R, Mandrup S. Peroxisome proliferator-activated receptor gamma and C/EBPalpha synergistically activate key metabolic adipocyte genes by assisted loading. Mol Cell Biol. 2014;34(6):939-54.

Madsen-Osterbye J, Abdelhalim M, Baudement MO, Collas P. Local euchromatin enrichment in lamina-associated domains anticipates their repositioning in the adipogenic lineage. Genome Biol. 2022;23(1):91.

Maenhaut N, Van de Voorde J. Regulation of vascular tone by adipocytes. Bmc Medicine. 2011;9.

Mahajan A, Go MJ, Zhang W, Below JE, Gaulton KJ, Ferreira T, *et al*. Genome-wide trans-ancestry meta-analysis provides insight into the genetic architecture of type 2 diabetes susceptibility. Nat Genet. 2014;46(3):234-44.

Malashicheva A, Perepelina K. Diversity of Nuclear Lamin A/C Action as a Key to Tissue-Specific Regulation of Cellular Identity in Health and Disease. Front Cell Dev Biol. 2021;9:761469.

Mann JP, Savage DB. What lipodystrophies teach us about the metabolic syndrome. J Clin Invest. 2019;129(10):4009-21.

Manolopoulos KN, Karpe F, Frayn KN. Gluteofemoral body fat as a determinant of metabolic health. Int J Obes (Lond). 2010;34(6):949-59.

Margueron R, Reinberg D. The Polycomb complex PRC2 and its mark in life. Nature. 2011;469(7330):343-9.

Marquez MP, Alencastro F, Madrigal A, Jimenez JL, Blanco G, Gureghian A, *et al*. The Role of Cellular Proliferation in Adipogenic Differentiation of Human Adipose Tissue-Derived Mesenchymal Stem Cells. Stem Cells Dev. 2017;26(21):1578-95.

Mattis KK, Krentz NAJ, Metzendorf C, Abaitua F, Spigelman AF, Sun H, *et al*. Loss of RREB1 in pancreatic beta cells reduces cellular insulin content and affects endocrine cell gene expression. Diabetologia. 2023;66(4):674-94.

McClintock D, Ratner D, Lokuge M, Owens DM, Gordon LB, Collins FS, *et al*. The mutant form of lamin A that causes Hutchinson-Gilford progeria is a biomarker of cellular aging in human skin. PLoS One. 2007;2(12):e1269.

McCord RP, Nazario-Toole A, Zhang H, Chines PS, Zhan Y, Erdos MR, *et al*. Correlated alterations in genome organization, histone methylation, and DNA-lamin A/C interactions in Hutchinson-Gilford progeria syndrome. Genome Res. 2013;23(2):260-9.

McQuaid SE, Humphreys SM, Hodson L, Fielding BA, Karpe F, Frayn KN. Femoral adipose tissue may accumulate the fat that has been recycled as VLDL and nonesterified fatty acids. Diabetes. 2010a;59(10):2465-73.

McQuaid SE, Manolopoulos KN, Dennis AL, Cheeseman J, Karpe F, Frayn KN. Development of an arterio-venous difference method to study the metabolic physiology of the femoral adipose tissue depot. Obesity (Silver Spring). 2010b;18(5):1055-8.

Merrick D, Sakers A, Irgebay Z, Okada C, Calvert C, Morley MP, *et al*. Identification of a mesenchymal progenitor cell hierarchy in adipose tissue. Science. 2019;364(6438).

Meuleman W, Peric-Hupkes D, Kind J, Beaudry JB, Pagie L, Kellis M, *et al*. Constitutive nuclear lamina-genome interactions are highly conserved and associated with A/T-rich sequence. Genome Res. 2013;23(2):270-80.

Morgani SM, Su J, Nichols J, Massague J, Hadjantonakis AK. The transcription factor Rreb1 regulates epithelial architecture, invasiveness, and vasculogenesis in early mouse embryos. Elife. 2021;10.

Moseti D, Regassa A, Kim WK. Molecular Regulation of Adipogenesis and Potential Anti-Adipogenic Bioactive Molecules. Int J Mol Sci. 2016;17(1).

Muller S, Ader I, Creff J, Lemenager H, Achard P, Casteilla L, *et al*. Human adipose stromal-vascular fraction self-organizes to form vascularized adipose tissue in 3D cultures. Sci Rep. 2019;9(1):7250.

Munekata K, Sakamoto K. Forkhead transcription factor Foxo1 is essential for adipocyte differentiation. In Vitro Cell Dev Biol Anim. 2009;45(10):642-51.

Myllyharju J. Prolyl 4-hydroxylases, key enzymes in the synthesis of collagens and regulation of the response to hypoxia, and their roles as treatment targets. Ann Med. 2008;40(6):402-17.

Naderi N, Wilde C, Haque T, Francis W, Seifalian AM, Thornton CA, *et al*. Adipogenic differentiation of adipose-derived stem cells in 3-dimensional spheroid cultures (microtissue): implications for the reconstructive surgeon. J Plast Reconstr Aesthet Surg. 2014;67(12):1726-34.

Naetar N, Georgiou K, Knapp C, Bronshtein I, Zier E, Fichtinger P, *et al*. LAP2alpha maintains a mobile and low assembly state of A-type lamins in the nuclear interior. Elife. 2021;10.

Nagarajan SR, Cross E, Johnson E, Sanna F, Daniels LJ, Ray DW, *et al*. Determining the temporal, dose, and composition effects of nutritional substrates in an in vitro model of intrahepatocellular triglyceride accumulation. Physiol Rep. 2022;10(20):e15463.

Nakae J, Kitamura T, Kitamura Y, Biggs WH, 3rd, Arden KC, Accili D. The forkhead transcription factor Foxo1 regulates adipocyte differentiation. Dev Cell. 2003;4(1):119-29.

Nazer E. To be or not be (in the LAD): emerging roles of lamin proteins in transcriptional regulation. Biochem Soc Trans. 2022;50(2):1035-44.

Neville MJ, Collins JM, Gloyn AL, McCarthy MI, Karpe F. Comprehensive human adipose tissue mRNA and microRNA endogenous control selection for quantitative real-time-PCR normalization. Obesity (Silver Spring). 2011;19(4):888-92.

Nishijima-Matsunobu A, Aoki S, Uchihashi K, Fujimoto K, Toda S. Three-dimensional culture model for analyzing crosstalk between adipose tissue and hepatocytes. Cell Tissue Res. 2013;352(3):611-21.

Oldenburg A, Briand N, Sorensen AL, Cahyani I, Shah A, Moskaug JO, *et al*. A lipodystrophy-causing lamin A mutant alters conformation and epigenetic regulation of the anti-adipogenic MIR335 locus. J Cell Biol. 2017;216(9):2731-43.

Oldenburg AR, Delbarre E, Thiede B, Vigouroux C, Collas P. Deregulation of Fragile X-related protein 1 by the lipodystrophic lamin A p.R482W mutation elicits a myogenic gene expression program in preadipocytes. Hum Mol Genet. 2014;23(5):1151-62.

Olswang Y, Cohen H, Papo O, Cassuto H, Croniger CM, Hakimi P, *et al*. A mutation in the peroxisome proliferator-activated receptor gamma-binding site in the gene for the cytosolic form of phosphoenolpyruvate carboxykinase reduces adipose tissue size and fat content in mice. Proc Natl Acad Sci U S A. 2002;99(2):625-30.

Orlov SV, Kuteykin-Teplyakov KB, Ignatovich IA, Dizhe EB, Mirgorodskaya OA, Grishin AV, *et al*. Novel repressor of the human FMR1 gene - identification of p56 human (GCC)(n)-binding protein as a Kruppel-like transcription factor ZF5. FEBS J. 2007;274(18):4848-62.

Osmanagic-Myers S, Foisner R. The structural and gene expression hypotheses in laminopathic diseases-not so different after all. Mol Biol Cell. 2019;30(15):1786-90.

Pan D, Huang L, Zhu LJ, Zou T, Ou J, Zhou W, *et al*. Jmjd3-Mediated H3K27me3 Dynamics Orchestrate Brown Fat Development and Regulate White Fat Plasticity. Dev Cell. 2015;35(5):568-83.

Parlee SD, Lentz SI, Mori H, MacDougald OA. Quantifying size and number of adipocytes in adipose tissue. Methods Enzymol. 2014;537:93-122.

Passaro A, Miselli MA, Sanz JM, Dalla Nora E, Morieri ML, Colonna R, *et al*. Gene expression regional differences in human subcutaneous adipose tissue. BMC Genomics. 2017;18(1):202.

Pastel E, Price E, Sjoholm K, McCulloch LJ, Rittig N, Liversedge N, *et al*. Lysyl oxidase and adipose tissue dysfunction. Metabolism. 2018;78:118-27.

Patni N, Garg A. Congenital generalized lipodystrophies--new insights into metabolic dysfunction. Nat Rev Endocrinol. 2015;11(9):522-34.

Patro R, Duggal G, Love MI, Irizarry RA, Kingsford C. Salmon provides fast and bias-aware quantification of transcript expression. Nat Methods. 2017;14(4):417-9.

Paulsen J, Sekelja M, Oldenburg AR, Barateau A, Briand N, Delbarre E, *et al*. Chrom3D: three-dimensional genome modeling from Hi-C and nuclear lamin-genome contacts. Genome Biol. 2017;18(1):21.

Payne VA, Au WS, Lowe CE, Rahman SM, Friedman JE, O'Rahilly S, *et al*. C/EBP transcription factors regulate SREBP1c gene expression during adipogenesis. Biochem J. 2009;425(1):215-23.

Payne VA, Grimsey N, Tuthill A, Virtue S, Gray SL, Dalla Nora E, et al. The human lipodystrophy gene BSCL2/seipin may be essential for normal adipocyte differentiation. Diabetes. 2008;57(8):2055-60.

Pellegrinelli V, Carobbio S, Vidal-Puig A. Adipose tissue plasticity: how fat depots respond differently to pathophysiological cues. Diabetologia. 2016;59(6):1075-88.

Piekarowicz K, Machowska M, Dratkiewicz E, Lorek D, Madej-Pilarczyk A, Rzepecki R. The effect of the lamin A and its mutants on nuclear structure, cell proliferation, protein stability, and mobility in embryonic cells. Chromosoma. 2017;126(4):501-17.

Pinnick KE, Nicholson G, Manolopoulos KN, McQuaid SE, Valet P, Frayn KN, *et al*. Distinct developmental profile of lower-body adipose tissue defines resistance against obesity-associated metabolic complications. Diabetes. 2014;63(11):3785-97.

Portoso M, Ragazzini R, Brencic Z, Moiani A, Michaud A, Vassilev I, *et al*. PRC2 is dispensable for HOTAIR-mediated transcriptional repression. EMBO J. 2017;36(8):981-94.

Rantalainen M, Herrera BM, Nicholson G, Bowden R, Wills QF, Min JL, *et al*. MicroRNA expression in abdominal and gluteal adipose tissue is associated with mRNA expression levels and partly genetically driven. PLoS One. 2011;6(11):e27338.

Ritchie ME, Phipson B, Wu D, Hu Y, Law CW, Shi W, *et al*. limma powers differential expression analyses for RNA-sequencing and microarray studies. Nucleic Acids Res. 2015;43(7):e47.

Robino JJ, Plekhanov AP, Zhu Q, Jensen MD, Scherer PE, Roberts CT, *et al*. Adipose Tissue Analysis Toolkit (ATAT) for automated analysis of adipocyte size and extracellular matrix in white adipose tissue. Obesity (Silver Spring). 2024;32(4):723-32.

Robinson MD, McCarthy DJ, Smyth GK. edgeR: a Bioconductor package for differential expression analysis of digital gene expression data. Bioinformatics. 2010;26(1):139-40.

Robinson MD, Oshlack A. A scaling normalization method for differential expression analysis of RNA-seq data. Genome Biol. 2010;11(3):R25.

Ronningen T, Shah A, Oldenburg AR, Vekterud K, Delbarre E, Moskaug JO, *et al*. Prepatterning of differentiation-driven nuclear lamin A/C-associated chromatin domains by GlcNAcylated histone H2B. Genome Res. 2015;25(12):1825-35.

Rosen ED, Walkey CJ, Puigserver P, Spiegelman BM. Transcriptional regulation of adipogenesis. Genes Dev. 2000;14(11):1293-307.

Rowland LA, Guilherme A, Henriques F, DiMarzio C, Munroe S, Wetoska N, *et al*. De novo lipogenesis fuels adipocyte autophagosome and lysosome membrane dynamics. Nat Commun. 2023;14(1):1362.

Rubino F, Cummings DE, Eckel RH, Cohen RV, Wilding JPH, Brown WA, *et al*. Definition and diagnostic criteria of clinical obesity. Lancet Diabetes Endocrinol. 2025;13(3):221-62.

Ruiz de Eguino G, Infante A, Schlangen K, Aransay AM, Fullaondo A, Soriano M, *et al*. Sp1 transcription factor interaction with accumulated prelamin a impairs adipose lineage differentiation in human mesenchymal stem cells: essential role of sp1 in the integrity of lipid vesicles. Stem Cells Transl Med. 2012;1(4):309-21.

Ruiz-Ojeda FJ, Mendez-Gutierrez A, Aguilera CM, Plaza-Diaz J. Extracellular Matrix Remodeling of Adipose Tissue in Obesity and Metabolic Diseases. Int J Mol Sci. 2019;20(19).

Rullens PMJ, Kind J. Attach and stretch: Emerging roles for genome-lamina contacts in shaping the 3D genome. Curr Opin Cell Biol. 2021;70:51-7.

Saarinen A, Saukkonen T, Kivela T, Lahtinen U, Laine C, Somer M, *et al*. Low density lipoprotein receptor-related protein 5 (LRP5) mutations and osteoporosis, impaired glucose metabolism and hypercholesterolaemia. Clin Endocrinol (Oxf). 2010;72(4):481-8.

Sakers A, De Siqueira MK, Seale P, Villanueva CJ. Adipose-tissue plasticity in health and disease. Cell. 2022;185(3):419-46.

Santoro A, McGraw TE, Kahn BB. Insulin action in adipocytes, adipose remodeling, and systemic effects. Cell Metab. 2021;33(4):748-57.

Saponaro C, Gaggini M, Carli F, Gastaldelli A. The Subtle Balance between Lipolysis and Lipogenesis: A Critical Point in Metabolic Homeostasis. Nutrients. 2015;7(11):9453-74.

Scheja L, Heeren J. The endocrine function of adipose tissues in health and cardiometabolic disease. Nature Reviews Endocrinology. 2019;15(9):507-24.

Schwalie PC, Dong H, Zachara M, Russeil J, Alpern D, Akchiche N, *et al*. A stromal cell population that inhibits adipogenesis in mammalian fat depots. Nature. 2018;559(7712):103-8.

Scott CC, Vossio S, Rougemont J, Gruenberg J. TFAP2 transcription factors are regulators of lipid droplet biogenesis. Elife. 2018;7.

Seo SI, Yoon JH, Byun HJ, Lee SK. HOTAIR Induces Methylation of PCDH10, a Tumor Suppressor Gene, by Regulating DNMT1 and Sponging with miR-148b in Gastric Adenocarcinoma. Yonsei Med J. 2021;62(2):118-28.

Shackleton S, Lloyd DJ, Jackson SN, Evans R, Niermeijer MF, Singh BM, *et al*. LMNA, encoding lamin A/C, is mutated in partial lipodystrophy. Nat Genet. 2000;24(2):153-6.

Shah PP, Lv W, Rhoades JH, Poleshko A, Abbey D, Caporizzo MA, *et al*. Pathogenic LMNA variants disrupt cardiac lamina-chromatin interactions and de-repress alternative fate genes. Cell Stem Cell. 2021;28(5):938-54 e9.

Shen JX, Couchet M, Dufau J, de Castro Barbosa T, Ulbrich MH, Helmstadter M, *et al*. 3D Adipose Tissue Culture Links the Organotypic Microenvironment to Improved Adipogenesis. Adv Sci (Weinh). 2021;8(16):e2100106.

Shimano H, Sato R. SREBP-regulated lipid metabolism: convergent physiology - divergent pathophysiology. Nat Rev Endocrinol. 2017;13(12):710-30.

Shin JY, Worman HJ. Molecular Pathology of Laminopathies. Annu Rev Pathol. 2022;17:159-80.

Simon JA, Kingston RE. Mechanisms of polycomb gene silencing: knowns and unknowns. Nat Rev Mol Cell Biol. 2009;10(10):697-708.

Slieker RC, Relton CL, Gaunt TR, Slagboom PE, Heijmans BT. Age-related DNA methylation changes are tissue-specific with ELOVL2 promoter methylation as exception. Epigenetics Chromatin. 2018;11(1):25.

Soneson C, Love MI, Robinson MD. Differential analyses for RNA-seq: transcript-level estimates improve gene-level inferences. F1000Res. 2015;4:1521.

Spalding KL, Arner E, Westermark PO, Bernard S, Buchholz BA, Bergmann O, *et al*. Dynamics of fat cell turnover in humans. Nature. 2008;453(7196):783-7.

Speakman JR, Elmquist JK. Obesity: an evolutionary context. Life Metab. 2022;1(1):10-24.

Speakman JR. The evolution of body fatness: trading off disease and predation risk. J Exp Biol. 2018;221(Pt Suppl 1).

Stephens AD, Liu PZ, Banigan EJ, Almassalha LM, Backman V, Adam SA, *et al*. Chromatin histone modifications and rigidity affect nuclear morphology independent of lamins. Mol Biol Cell. 2018;29(2):220-33.

Strawford A, Antelo F, Christiansen M, Hellerstein MK. Adipose tissue triglyceride turnover, de novo lipogenesis, and cell proliferation in humans measured with 2H2O. Am J Physiol Endocrinol Metab. 2004;286(4):E577-88.

Stringer C, Wang T, Michaelos M, Pachitariu M. Cellpose: a generalist algorithm for cellular segmentation. Nat Methods. 2021;18(1):100-6.

Sullivan T, Escalante-Alcalde D, Bhatt H, Anver M, Bhat N, Nagashima K, *et al*. Loss of A-type lamin expression compromises nuclear envelope integrity leading to muscular dystrophy. J Cell Biol. 1999;147(5):913-20.

Supek F, Bosnjak M, Skunca N, Smuc T. REVIGO summarizes and visualizes long lists of gene ontology terms. PLoS One. 2011;6(7):e21800.

Swift J, Ivanovska IL, Buxboim A, Harada T, Dingal PC, Pinter J, *et al*. Nuclear lamin-A scales with tissue stiffness and enhances matrix-directed differentiation. Science. 2013;341(6149):1240104.

Taylor J, Sellin J, Kuerschner L, Krahl L, Majlesain Y, Forster I, *et al*. Generation of immune cell containing adipose organoids for in vitro analysis of immune metabolism. Sci Rep. 2020;10(1):21104.

Tchoukalova YD, Votruba SB, Tchkonia T, Giorgadze N, Kirkland JL, Jensen MD. Regional differences in cellular mechanisms of adipose tissue gain with overfeeding. Proc Natl Acad Sci U S A. 2010;107(42):18226-31.

Tiwari M, Roumane A, Sommer N, Han W, Delibegovic M, Rochford JJ, *et al*. Preclinical evaluation of tissue-selective gene therapies for congenital generalised lipodystrophy. Gene Ther. 2024;31(9-10):445-54.

Todorcevic M, Hilton C, McNeil C, Christodoulides C, Hodson L, Karpe F, *et al*. A cellular model for the investigation of depot specific human adipocyte biology. Adipocyte. 2017;6(1):40-55.

Tong Q, Dalgin G, Xu H, Ting CN, Leiden JM, Hotamisligil GS. Function of GATA transcription factors in preadipocyte-adipocyte transition. Science. 2000;290(5489):134-8.

Tontonoz P, Spiegelman BM. Fat and beyond: the diverse biology of PPARgamma. Annu Rev Biochem. 2008;77:289-312.

Treiber G, Gonthier MP, Guilleux A, Medjane S, Bonfanti O, Cogne M, *et al*. Familial partial lipodystrophy type 2 and obesity, two adipose tissue pathologies with different inflammatory profiles. Diabetol Metab Syndr. 2023;15(1):77.

Tsai CC, Hong YJ, Lee RJ, Cheng NC, Yu J. Enhancement of human adipose-derived stem cell spheroid differentiation in an in situ enzyme-crosslinked gelatin hydrogel. J Mater Chem B. 2019;7(7):1064-75.

Tsai MC, Manor O, Wan Y, Mosammaparast N, Wang JK, Lan F, *et al*. Long noncoding RNA as modular scaffold of histone modification complexes. Science. 2010;329(5992):689-93.

Tu Y, Sanchez-Iglesias S, Araujo-Vilar D, Fong LG, Young SG. LMNA missense mutations causing familial partial lipodystrophy do not lead to an accumulation of prelamin A. Nucleus. 2016;7(5):512-21.

Vadrot N, Duband-Goulet I, Cabet E, Attanda W, Barateau A, Vicart P, *et al*. The p.R482W substitution in A-type lamins deregulates SREBP1 activity in Dunnigan-type familial partial lipodystrophy. Hum Mol Genet. 2015;24(7):2096-109.

van Steensel B, Belmont AS. Lamina-Associated Domains: Links with Chromosome Architecture, Heterochromatin, and Gene Repression. Cell. 2017;169(5):780-91.

Vantyghem MC, Pigny P, Maurage CA, Rouaix-Emery N, Stojkovic T, Cuisset JM, *et al*. Patients with familial partial lipodystrophy of the Dunnigan type due to a LMNA R482W mutation show muscular and cardiac abnormalities. J Clin Endocrinol Metab. 2004;89(11):5337-46.

Vasandani C, Li X, Sekizkardes H, Brown RJ, Garg A. Phenotypic Differences Among Familial Partial Lipodystrophy Due to LMNA or PPARG Variants. J Endocr Soc. 2022;6(12):bvac155.

Vigouroux C, Auclair M, Dubosclard E, Pouchelet M, Capeau J, Courvalin JC, *et al*. Nuclear envelope disorganization in fibroblasts from lipodystrophic patients with heterozygous R482Q/W mutations in the lamin A/C gene. J Cell Sci. 2001;114(Pt 24):4459-68.

Vijay J, Gauthier MF, Biswell RL, Louiselle DA, Johnston JJ, Cheung WA, *et al*. Single-cell analysis of human adipose tissue identifies depot and disease specific cell types. Nat Metab. 2020;2(1):97-109.

Vogel MAA, Wang P, Bouwman FG, Hoebers N, Blaak EE, Renes J, *et al*. A comparison between the abdominal and femoral adipose tissue proteome of overweight and obese women. Sci Rep. 2019;9(1):4202.

Wabitsch M, Brenner RE, Melzner I, Braun M, Moller P, Heinze E, *et al*. Characterization of a human preadipocyte cell strain with high capacity for adipose differentiation. Int J Obes Relat Metab Disord. 2001;25(1):8-15.

Wagner A, Lautaoja-Kivipelto JH, Pehkonen K, Hassinen A, Kuusela M, Röttger L, *et al*. In vitro model of human subcutaneous adipocyte spheroids for studying mitochondrial dysfunction and mitochondria activating compounds. bioRxiv. 2025.

Wahrenberg H, Lonnqvist F, Arner P. Mechanisms underlying regional differences in lipolysis in human adipose tissue. J Clin Invest. 1989;84(2):458-67.

Wang L, Jin Q, Lee JE, Su IH, Ge K. Histone H3K27 methyltransferase Ezh2 represses Wnt genes to facilitate adipogenesis. Proc Natl Acad Sci U S A. 2010;107(16):7317-22.

Wang X, Yu H, Gao R, Liu M, Xie W. A comprehensive review of the family of very-long-chain fatty acid elongases: structure, function, and implications in physiology and pathology. Eur J Med Res. 2023;28(1):532.

Wernstedt Asterholm I, Tao C, Morley TS, Wang QA, Delgado-Lopez F, Wang ZV, *et al*. Adipocyte inflammation is essential for healthy adipose tissue expansion and remodeling. Cell Metab. 2014;20(1):103-18.

Weyer C, Foley JE, Bogardus C, Tataranni PA, Pratley RE. Enlarged subcutaneous abdominal adipocyte size, but not obesity itself, predicts type II diabetes independent of insulin resistance. Diabetologia. 2000;43(12):1498-506.

Wojtanik KM, Edgemon K, Viswanadha S, Lindsey B, Haluzik M, Chen W, *et al*. The role of LMNA in adipose: a novel mouse model of lipodystrophy based on the Dunnigan-type familial partial lipodystrophy mutation. J Lipid Res. 2009;50(6):1068-79.

Wolff A, Frank M, Staehlke S, Peters K. A Comparative Study on the Adipogenic Differentiation of Mesenchymal Stem/Stromal Cells in 2D and 3D Culture. Cells. 2022;11(8).

World Health Organization, 2025. Obesity and overweight. [Online] Available at: https://www.who.int/news-room/fact-sheets/detail/obesity-and-overweight [Accessed 16 September 2025].

Worman HJ. Nuclear lamins and laminopathies. J Pathol. 2012;226(2):316-25.

Wronska A, Kmiec Z. Structural and biochemical characteristics of various white adipose tissue depots. Acta Physiol (Oxf). 2012;205(2):194-208.

Wu J, Bostrom P, Sparks LM, Ye L, Choi JH, Giang AH, *et al*. Beige adipocytes are a distinct type of thermogenic fat cell in mouse and human. Cell. 2012;150(2):366-76.

Yang A, Mottillo EP. Adipocyte lipolysis: from molecular mechanisms of regulation to disease and therapeutics. Biochem J. 2020;477(5):985-1008.

Yang J, Shi BY. Dickkopf (Dkk)-2 is a beige fat-enriched adipokine to regulate adipogenesis. Biochem Biophys Res Commun. 2021;548:211-6.

Yang X, Lu X, Lombes M, Rha GB, Chi YI, Guerin TM, *et al*. The G(0)/G(1) switch gene 2 regulates adipose lipolysis through association with adipose triglyceride lipase. Cell Metab. 2010;11(3):194-205.

Ye RZ, Richard G, Gevry N, Tchernof A, Carpentier AC. Fat Cell Size: Measurement Methods, Pathophysiological Origins, and Relationships With Metabolic Dysregulations. Endocr Rev. 2022;43(1):35-60.

Yu GZ, Krentz NAJ, Bentley L, Zhao M, Paphiti K, Sun H, *et al*. Loss of RREB1 reduces adipogenesis and improves insulin sensitivity in mouse and human adipocytes. bioRxiv. 2024.

Yu YH, Ginsberg HN. Adipocyte signaling and lipid homeostasis: sequelae of insulin-resistant adipose tissue. Circ Res. 2005;96(10):1042-52.

Zammouri J, Vatier C, Capel E, Auclair M, Storey-London C, Bismuth E, *et al*. Molecular and Cellular Bases of Lipodystrophy Syndromes. Front Endocrinol (Lausanne). 2021;12:803189.

Zhang H, Kieckhaefer JE, Cao K. Mouse models of laminopathies. Aging Cell. 2013;12(1):2-10.

Zhang Y, Padalecki SS, Chaudhuri AR, De Waal E, Goins BA, Grubbs B, *et al*. Caspase-2 deficiency enhances aging-related traits in mice. Mech Ageing Dev. 2007;128(2):213-21.

Zhu J, He J, Verano M, Brimmo AT, Glia A, Qasaimeh MA, *et al*. An integrated adipose-tissue-on-chip nanoplasmonic biosensing platform for investigating obesity-associated inflammation. Lab Chip. 2018;18(23):3550-60.

Zou P, Liu L, Zheng L, Liu L, Stoneman RE, Cho A, *et al*. Targeting FoxO1 with AS1842856 suppresses adipogenesis. Cell Cycle. 2014;13(23):3759-67.

Zwick RK, Guerrero-Juarez CF, Horsley V, Plikus MV. Anatomical, Physiological, and Functional Diversity of Adipose Tissue. Cell Metab. 2018;27(1):68-83.